VAIDOTAS GUDŽIŪNAS

DEVELOPMENT OF AN ADAPTIVE SYSTEM FOR HUMAN POSTURAL CONTROL ASSESSMENT

DOCTORAL DISSERTATION

Kaunas
2026

KAUNAS UNIVERSITY OF TECHNOLOGY

VAIDOTAS GUDŽIŪNAS

DEVELOPMENT OF AN ADAPTIVE SYSTEM FOR HUMAN POSTURAL CONTROL ASSESSMENT

Doctoral dissertation
Technological Sciences, Mechanical Engineering (T 009)

2026, Kaunas

This dissertation has been prepared at the Institute of Mechatronics of Kaunas University of Technology in 2020–2025.

The doctoral right has been granted to Kaunas University of Technology together with Vytautas Magnus University.

Research supervisor:
Assoc. Prof. Dr. Aurelijus DOMEIKA (Kaunas University of Technology, Technological Sciences, Mechanical Engineering, T 009).

Edited by: English language editor Dovilė Blaudžiūnienė (Publishing House *Technologija*), Lithuanian language editor Rita Malikėnienė (Publishing House *Technologija*).

Dissertation Defence Board of Mechanical Engineering Science Field:
Prof. Dr. Hab. Vytautas OSTAŠEVIČIUS (Kaunas University of Technology, Technological Sciences, Mechanical Engineering, T 009) – **chairperson**;
Prof. Dr. Renata BALNYTĖ (Lithuanian University of Health Sciences, Medical and Health Sciences, Medicine, M 001).
Prof. Dr. Giedrius JANUŠAS (Kaunas University of Technology, Technological Sciences, Mechanical Engineering, T 009);
Prof. Dr. Vytautas JURĖNAS (Kaunas University of Technology, Technological Sciences, Mechanical Engineering, T 009);
Prof. Dr. Aleksejs KATAŠEVS (Riga Technical University, Latvia, Technological Sciences, Mechanical Engineering, T 009).

The dissertation defence will be held on 28 August 2026, at 11 a.m. at the Rectorate Hall of Kaunas University of Technology in the meeting of the Dissertation Defence Board of Mechanical Engineering Science Field.

Address: K. Donelaičio 73-402, LT-44249 Kaunas, Lithuania.
Phone: +370 608 28 527; e-mail doktorantura@ktu.lt

The doctoral dissertation was sent out on 28 July 2026.
The dissertation is available on the website http://ktu.edu, at the Library of Kaunas University of Technology (Gedimino 50, Kaunas) and at the Library of Vytautas Magnus University (K. Donelaičio 52, Kaunas).

© V. Gudžiūnas, 2026

KAUNO TECHNOLOGIJOS UNIVERSITETAS

VAIDOTAS GUDŽIŪNAS

ADAPTYVIOS SISTEMOS KŪRIMAS ŽMOGAUS POSTURALINĖS KONTROLĖS TYRIMAMS

Daktaro disertacija
Technologijos mokslai, mechanikos inžinerija (T 009)

Kaunas, 2026

Disertacija rengta 2020–2025 metais Kauno technologijos universiteto Mechatronikos institute.

Doktorantūros teisė Kauno technologijos universitetui suteikta kartu su Vytauto Didžiojo universitetu.

Mokslinis vadovas:
doc. dr. Aurelijus DOMEIKA (Kauno technologijos universitetas, technologijos mokslai, mechanikos inžinerija, T 009).

Redagavo: anglų kalbos redaktorė Dovilė Blaudžiūnienė (leidykla „Technologija“), lietuvių kalbos redaktorė Rita Malikėnienė (leidykla „Technologija“).

Mechanikos inžinerijos mokslo krypties disertacijos gynimo taryba:
prof. habil. dr. Vytautas OSTAŠEVIČIUS (Kauno technologijos universitetas, technologijos mokslai, mechanikos inžinerija, T 009) – **pirmininkas**;
prof. dr. Renata BALNYTĖ (Lietuvos sveikatos mokslų universitetas, medicinos ir sveikatos mokslai, medicina, M 001);
prof. dr. Giedrius JANUŠAS (Kauno technologijos universitetas, technologijos mokslai, mechanikos inžinerija, T 009);
prof. dr. Vytautas JURĖNAS (Kauno technologijos universitetas, technologijos mokslai, mechanikos inžinerija, T 009);
prof. dr. Aleksejs KATAŠEVS (Rygos technikos universitetas, Latvija, technologijos mokslai, mechanikos inžinerija, T 009).

Disertacija bus ginama viešame Mechanikos inžinerijos mokslo krypties disertacijos gynimo tarybos posėdyje 2026 m. rugpjūčio 28 d. 11 val. Kauno technologijos universiteto Rektorato salėje.

Adresas: K. Donelaičio g. 73-402, LT-44249 Kaunas, Lietuva.
Tel. +370 608 28 527; el. paštas doktorantura@ktu.lt

Disertacija išsiųsta 2026 m. liepos 28 d.
Su disertacija galima susipažinti interneto svetainėje http://ktu.edu, Kauno technologijos universiteto bibliotekoje (Gedimino g. 50, Kaunas) ir Vytauto Didžiojo universiteto bibliotekoje (K. Donelaičio g. 52, Kaunas).

© V. Gudžiūnas, 2026

CONTENT

LIST OF TABLES

LENTELIŲ SĄRAŠAS

LIST OF FIGURES

PAVEIKSLŲ SĄRAŠAS

LIST OF ABBREVIATIONS AND TERMS

95% CI area – 95% CI ellipse area (planar COP or segment analysis);
AP – Anteroposterior axis;
AP/ML – Anteroposterior / Mediolateral axes (pair);
BMI – Body Mass Index;
BOS – Base of Support;
CI – Confidence Interval (typically 95%);
COM – Center of Mass;
COP – Center of Pressure;
COP TMV – COP Total Mean Velocity;
EV95% – 95% CI ellipsoid volume (3D sway envelope);
FRT – Functional Reach Test (anterior limit of stability);
IL – Instability Level (mechanical setting of the platform);
IMU – Inertial Measurement Unit (wearable 9-axis sensor);
IP – Inverted Pendulum model of upright stance;
IQR – Interquartile Range (Q3–Q1);
LL – Limb length (ASIS → medial malleolus);
LOS – Limit of Stability;
mCTSIB – Modified Clinical Test of Sensory Integration and Balance;
ML – Mediolateral axis;
MoCap – Optical motion capture (e.g., Qualisys);
RII – Relative Instability Index;
RK4 – Fourth-order Runge–Kutta numerical integration method;
RMS – Root Mean Square (magnitude of a varying signal);
SIS – Sensory Information Strategy (Basic, Proprioceptive, Visual, Vestibular);
TMV – Total Mean Velocity (3D resultant speed of a segment or COP path);
ToF – Time-of-Flight distance sensor (e.g., VL53L1X);
VAS – Visual Analogue Scale (task difficulty, 0–10);
WBB – Wii Balance Board (force platform for COP);
YBT – Y Balance Test (ANT, PM, PL; composite normalized by limb length).

INTRODUCTION

Human postural balance is a multifaceted control process integrating sensory inputs (visual, vestibular, somatosensory) with motor and biomechanical elements, and it is also influenced by higher-level cognitive factors. Effective balance requires the coordination of anticipatory and reactive mechanisms: anticipatory postural adjustments stabilize the body in a feedforward manner before voluntary movements, while reactive postural responses (e.g., reflexive stepping or grasping) are the last line of defense when stability is perturbed unexpectedly. Notably, the ability to execute rapid reactive balance reactions is critical for fall prevention, as it ultimately determines whether a loss of balance can be arrested or results in a fall.

At the same time, cognitive load and attentional capacity can modulate postural control, and impairments in cognition (e.g., executive function deficits) are associated with degraded balance and greater risk of fall in older or neurologically affected individuals. In summary, balance control emerges from a complex interplay of sensory-motor systems and cognitive influences, and it encompasses both proactive (anticipatory) strategies and reactive (compensatory) responses to maintain the body's center of mass over the base of support in varied conditions.

Current tests of human postural control are insufficient to adequately assess an individual's postural control limits, because they fail to provide balance perturbations with a physiologically natural, graded, and quantifiable level of complexity.

Research aim and objectives

The aim of this research is to develop an individualized and automated postural control assessment system which, by gradually increasing the complexity of postural control perturbations, objectively determines the functional limit of human postural control.

To achieve this aim, the following objectives have been formulated:

1. To investigate, using static and dynamic modeling, how the suspension geometry of the platform board affects the dynamic interaction between the platform and an inverted pendulum placed on it.
2. To experimentally determine the mechanical factors that shape the levels of instability (force threshold for platform board movement and damping characteristics).
3. To evaluate the effect of different levels of instability on the biomechanics of human stance during voluntary movements.
4. To assess the influence of the interaction between mechanical instability levels and sensory strategies (visual, proprioceptive, vestibular) on the effectiveness of postural control.
5. To implement and verify the functionality of a prototype adaptive, automated apparatus for standardized postural-control testing.

Research methods

Experimental and theoretical investigations were carried out at the Kaunas University of Technology (KTU) Institute of Mechatronics.

In the modeling phase, analytical and numerical modeling was used to study how suspension geometry affects the mechanical behavior of the platform and its interaction with an inverted pendulum representing the standing human body. The modeling results were complemented by experimental testing and mechanical characterization of the platform.

In the mechanical analysis, static tests were performed to determine the horizontal force threshold required to initiate platform displacement, and dynamic tests were performed to quantify oscillation damping. These mechanical characteristics were used to define distinct instability levels (IL) as a combined description of platform behavior rather than a single-parameter measure.

Biomechanical evaluation was conducted under graded instability conditions during controlled voluntary movements, using three-dimensional motion capture to quantify body and platform kinematics relevant to balance control.

A neurobiomechanical study was conducted with healthy young adults to evaluate postural control during quiet standing under standardized combinations of mechanical instability levels (IL0–IL3) and sensory information strategies (SIS). Kinematic data and center-of-pressure (COP) signals were recorded, and postural-control outcomes were quantified using segmental and COP-based variability and dispersion measures.

Finally, a fully functional mechatronic prototype platform was developed and implemented. The control architecture supports automatic calibration, progressive instability control, and real-time safety logic based on predefined warning and critical thresholds.

Scientific novelty

A combination of mechanical parameters of a mechatronic platform defining different levels of instability is determined.

The proposed passive equilibrium destabilization method allows modulation of the complexity of disturbances.

Practical value

1. A prototype of a postural control assessment device was developed, which gradually increases the complexity of balance disturbances, and records the subject's balance parameters in real time.

2. An adaptive postural control assessment and training system has been developed, enabling the defined and repeatable selection of balance perturbation mechanisms.

3. An automated algorithm has been proposed which applies the center of pressure (COP) velocity warning and critical thresholds in real time and automatically stops the test, ensuring safe and uniform execution of the procedure and easy reproducibility of results.

Statements for the defence

1. Changing the length of the suspension systematically changes the force threshold required to displace the board and the vibration damping coefficient;

2. Different levels of mechanical instability create different modes of interaction between the body's center of mass and the base of support;

3. Combining levels of mechanical instability with sensory information restriction can significantly increase postural control impairments without additional external mechanical perturbations;

4. A prototype of an adaptive, automated postural control testing device automatically adjusts instability levels and captures changes in biomechanical parameters in real time.

Structure of the dissertation

The dissertation consists of an introduction, six chapters, a list of 111 references, a list of author's publications, curriculum vitae, acknowledgements, and annexes. The volume of the dissertation is 192 pages, 67 figures, and 60 tables. The total length of the dissertation is 328 595 characters including spaces, which corresponds to 81.5% of the maximum allowable dissertation length according to the Kaunas University of Technology doctoral thesis preparation requirements.

1. LITERATURE REVIEW

1.1. The concept of postural control and stability principles

Postural control refers to maintaining both postural stability (preventing a fall) and postural orientation (maintaining a task- and gravity-referenced body configuration) [1–3]. In engineering terms, balance is a continuous control objective: the neuromuscular system regulates the whole-body center of mass (COM) while compensating physiological noise, micro-movements of the support, and self-initiated actions [1]. Accordingly, standing can be modeled as a constrained closed-loop control problem with safety limits rather than as fixed posture [4–7].

The COM–base of support (BOS) relationship captures the primary geometric constraint of standing. The BOS is the support polygon defined by foot–ground contact. If the vertical projection of COM leaves the BOS and the BOS is not changed (i.e., without stepping), gravity produces a net toppling moment that cannot be counteracted by available contact forces [1]. "COM projection inside BOS" is a necessary condition for quasi-static stability but is insufficient for dynamic stability, because COM velocity determines whether the body can be decelerated before reaching the BOS boundary. This provides the rationale for dynamic stability constructs that incorporate a velocity-weighted COM (e.g., extrapolated COM and margin of stability) [8–11]. In practice, boundary approach is state-dependent: at the same COM position, higher COM velocity implies less remaining control authority and a higher probability of strategy transition (e.g., stepping) [12–15].

The center of pressure (COP) explains how stabilizing moments are generated at the support interface. COP is the point location of the resultant ground reaction force and can be modulated through ankle/hip torques and plantar pressure redistribution [16]. Under an inverted-pendulum approximation of quiet stance (useful for small-amplitude sway), the horizontal COP–COM distance is proportional to horizontal COM acceleration: shifting COP relative to COM generates a restoring moment that accelerates COM toward a safer BOS region [16–18]. Because COP excursions are bounded by foot geometry and contact conditions, constrained COP range (e.g., narrow BOS, compliant/unstable support, reduced friction) increases the likelihood that stability must be maintained via other kinematic strategies (hip motion, stepping, grasping) [8,19–21].

Instrumented assessments often focus on COP because it is measurable at high temporal resolution and reflects continuous regulation effort. Static posturography summarizes COP trajectories using spatial dispersion (e.g., 95% confidence ellipse area, EV95%), temporal variability, and velocity-based metrics [22]. Mean COP velocity (often reported as total mean velocity, TMV) is widely used because it tracks the intensity and frequency of corrective actions and is sensitive to increased postural-control demand [23–25]. In control terms, COP velocity approximates "control activity": how rapidly COP must be repositioned to manage COM dynamics [23]. However, COP metrics are protocol-dependent (trial duration, sampling frequency, filtering), so threshold proposals require disciplined and consistent instrumentation [22,26–31].

Static versus dynamic balance should be treated as a shift in the dominant stability constraint, not a categorical split between “standing” and “moving”. In static tasks, COM position relative to BOS often dominates and stability can be maintained via small COP shifts within the feasible pressure range [1]. In dynamic tasks, COM velocity and time-to-boundary become decisive, and strategy transitions (ankle → hip → step/grasp) emerge as functional limits are approached [8].

This distinction matters here because the experimental platform alters BOS mechanics and the feasibility of COP modulation, thereby changing how participants approach a stability boundary [12,14].

COM–BOS–COP stability logic in standing: BOS defines the geometric support region; COM projection must remain within BOS for geometric stability; COP modulation generates restoring moments that accelerate COM toward safer regions [8,16,19].

Stability in standing can be conceptualized as regulating COM state within BOS-related constraints via COP modulation, with dynamic stability depending on both COM position and velocity [8]. However, purely ordinal clinical tests and quasi-static “stable/unstable” interpretations can overlook the continuous, state-dependent approach to a stability boundary [32].

This dissertation combines controllable mechanical destabilization (instability level, IL) and sensory manipulation (sensory information strategy, SIS) within an IL×SIS framework to drive the system toward a measurable boundary; in this dissertation, COP-derived parameters (e.g., TMV and dispersion measures such as EV95%) are used to operationalize objective warning/critical thresholds [12,14,33,34].

Sensory-integration mechanisms provide the physiological rationale for SIS (sensory information strategy) as a controlled method for increasing task difficulty without external push/pull perturbations [35].

1.2. Neurophysiological basis of postural control (sensory integration)

Postural control relies on concurrent cues from vision, vestibular input, and somatosensory/proprioceptive input [1]. Each channel provides a partially redundant estimate of body orientation and motion, but with different dynamics, noise, and reference frames. The central nervous system (CNS) therefore combines these cues to form a usable state estimate for feedback control of posture [36]. Because the channels differ in reliability and processing characteristics, multisensory combination is itself a control-relevant challenge [4,36,37].

Vision provides an external spatial reference (e.g., optic flow, visual vertical) that supports slow sway correction and orientation relative to the environment [38]. Its contribution increases when other cues are uncertain, but it can be degraded by low illumination, moving scenes, and processing delays [37,38].

Vestibular input supplies inertial cues about head motion and head orientation relative to gravity, and becomes critical when vision is absent and somatosensory cues are unreliable (e.g., compliant support) [39]. However, vestibular signals alone do not specify whole-body COM state because they are referenced to the head; effective balance therefore requires integration with body and surface information to generate appropriate corrective torques [1,4].

Somatosensory and proprioceptive inputs provide fast information about joint angles, muscle-tendon stretch, and foot–ground interaction forces, enabling inference of the relationship between the body, the support surface, and BOS boundaries [1]. On rigid support these cues often dominate quiet-stance regulation, yet their reliability is systematically distorted on compliant or moving surfaces [36,37].

The CNS combines sensory channels by weighting them according to context-dependent reliability ("sensory reweighting") [36]. When a channel becomes noisy or inconsistent, it is down-weighted while alternative cues are up-weighted, supporting robust balance across environments [40]. Control-oriented models emphasize that reweighting directly affects closed-loop stability margins by changing effective feedback gains and delays, not only perception [37,41,42].

Operationally, SIS can be implemented through structured sensory conditions that selectively reduce a channel's contribution. The simplest manipulations are eyes open versus eyes closed (reducing visual input) and firm versus compliant support (reducing somatosensory reliability) [43]. This logic aligns with the modified Clinical Test of Sensory Interaction on Balance (mCTSIB) and related sensory-organization approaches while remaining feasible in an engineering test-bed [44]. In this dissertation, SIS is defined as an ordinal progression of sensory availability [45–48]:

- SIS0 (Basic): eyes open, firm support.
- SIS1 (Visual reduction): eyes closed, firm support.
- SIS2 (Somatosensory reduction): eyes open, compliant support (e.g., foam).
- SIS3 (Combined reduction / vestibular-reliant): eyes closed, compliant support.

Figure 1 summarizes the control logic underlying the present dissertation: sensory inputs are integrated by the CNS, reweighted according to context, and translated into motor output that regulates COM relative to BOS. In the proposed framework, SIS acts on the reliability of sensory inputs, whereas IL acts on the mechanical properties of the support, and both manipulations increase postural-control demand in a complementary manner.

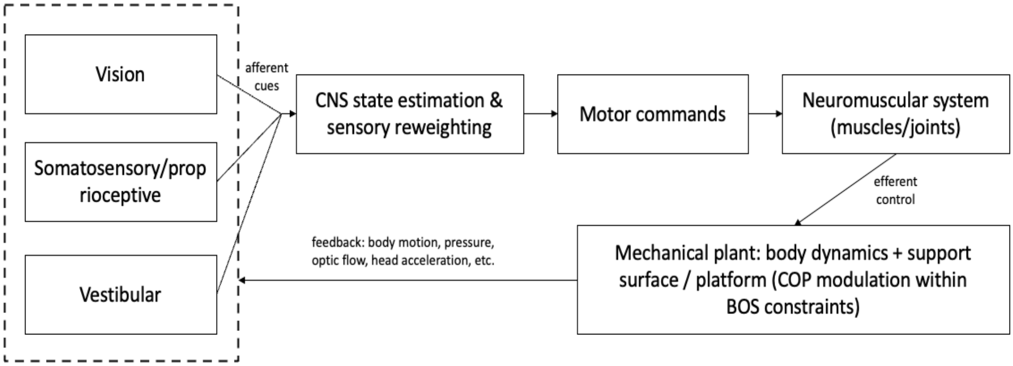

Figure 1 Sensory inputs → CNS state estimation and sensory reweighting → motor output → COM/BOS regulation. SIS manipulates sensory reliability while IL manipulates the mechanical plant, jointly increasing control demand. Source: adapted from sensorimotor integration and reweighting frameworks

This ordering intentionally shifts control from multi-cue regulation toward conditions where vestibular cues and internal models contribute proportionally more to state estimation [36,42].

Postural control is best described as a multisensory closed-loop process in which the CNS reweights visual, vestibular, and somatosensory cues based on context-dependent reliability [40]. A limitation of many standard sensory-integration assessments is that they employ only a small number of fixed conditions, which constrains graded and individualized progression of difficulty [44]. In this dissertation, SIS is used as a physiologically grounded difficulty axis that, when combined with mechanically controlled IL, can increase task demand and elicit stronger reactive control without external perturbations [37,42].

1.3. Postural strategies

As mechanical instability (IL) increases and/or sensory information availability (SIS) decreases, postural-control solutions are expected to shift across ankle, hip, and change-in-support strategies; the main strategies and their expected transitions are summarized below.

Postural strategies can be viewed as families of muscle synergies and joint-coordination patterns that achieve the same objective – keeping COM compatible with BOS constraints – under different task and environmental conditions [1]. The ankle–hip–step taxonomy remains useful because each strategy provides corrective moments under different requirements for available COP range and time-to-boundary [4,14,49].

The ankle strategy is typically the default in quiet stance and under small disturbances on rigid support [49]. Mechanically, it approximates the body as an inverted pendulum rotating mainly about the ankle, where COP modulation acts as the primary actuator to restore COM toward the BOS interior [16]. It is effective while COP can be shifted within foot-support limits; as COP approaches its boundary, in-place ankle torque becomes insufficient and additional degrees of freedom (hip motion or stepping) are recruited [8,19,20].

The hip strategy becomes more prominent when ankle-based COP control is insufficient, such as under larger-amplitude disturbances, narrow BOS, or higher-frequency sway [50]. Here, trunk and pelvis rotations alter segmental inertial forces and shift whole-body COM indirectly, enabling correction even when COP modulation is saturated [49]. Evidence suggests ankle–hip coordination transitions gradually with task constraints rather than switching discretely [4,14,51].

Stepping and other change-in-support actions maintain balance by enlarging BOS rather than controlling COM within a fixed BOS [52]. Protective stepping is expected when COM approaches a state where in-place torque modulation cannot prevent balance loss, or when time-to-boundary becomes too short for in-place correction [8]. Upper-limb support (“grasp” or “reach-to-grasp”) plays an analogous role by rapidly creating a new support constraint [14,52,53].

Strategy transitions provide a functional marker of approaching an individual stability boundary. Increasing IL reduces the robustness of ankle-only control by changing plant dynamics and/or limiting effective COP modulation [49]. Reducing sensory information (lower SIS) degrades state estimation and increases uncertainty, which can trigger more conservative, higher-amplitude corrections (greater hip involvement, earlier stepping) even at comparable kinematic states [37,40,42].

Ankle, hip, and change-in-support strategies represent alternative control solutions for regulating COM relative to BOS constraints, and transitions between them are expected as stability margins decrease [8]. Much of the existing strategy literature is based on discrete perturbations or a limited set of support-surface manipulations, which complicates direct translation to continuously graded difficulty [32]. The graded IL×SIS paradigm in this dissertation is designed to provoke controlled strategy transitions, enabling boundary detection without abrupt perturbations [14,33,34].

1.4. Anticipatory vs Reactive postural control

Anticipatory postural adjustments (APA) and reactive postural control (RPC) represent complementary stabilization regimes; distinguishing them is important for interpreting how an IL×SIS approach-to-instability paradigm moves an individual toward a stability boundary.

APA are feedforward adjustments that occur before a predictable voluntary movement or self-initiated perturbation (e.g., pre-activating trunk/leg muscles before arm movement or step initiation). Their role is to reduce expected COM displacement and keep COM within a safe BOS region despite the planned action. APA therefore depend on prediction and motor planning and are most evident when the task is sufficiently predictable [54,55].

RPC are feedback-driven corrective actions triggered after an unexpected disturbance or when the current state estimate indicates imminent instability (e.g., rapid in-place torque modulation, hip corrections, stepping, grasping) [1]. They include coordinated whole-body synergies that redistribute COP and segmental angular momentum to restore COM to a stable region [56]. RPC tends to dominate when time-to-boundary is short and prediction is limited by sensory uncertainty or support dynamics [8,12,14,53].

APA and RPC coexist, but they dominate different parts of the task space. In low-demand stance, stability can often be maintained through small continuous corrections and APA during predictable actions [36]. As task difficulty increases (less reliable sensory information and/or more challenging support mechanics), prediction becomes less effective and corrections are increasingly driven by error growth and boundary proximity, raising the relative contribution of RPC [37,40,42].

Many clinical balance tests have limited ability to isolate reactive control capacity [32]. For safety and feasibility, protocols often avoid strong perturbations and may not push participants into a regime where reactive recovery must be expressed measurably. Ordinal scoring and ceiling effects can further mask changes that occur mainly in reactive recovery rather than gross task completion [33,34,57,58].

APA and RPC can be treated as distinct regimes: feedforward stabilization during predictable actions versus feedback-driven recovery near instability, with the relative contribution of RPC increasing as time-to-boundary decreases [8]. Standard clinical tests often under-sample this reactive regime because they avoid perturbations and can saturate due to ceiling effects [32]. In the IL×SIS approach-to-instability paradigm used here, task difficulty is increased without external push/pull perturbations, but up to a threshold where reactive control intensifies and can be monitored with objective criteria [12,14,33].

1.5. Factors influencing postural control and population differences

Several factors – including age, pathology, cognitive load, and anthropometry – modulate postural control and influence how assessment outcomes should be interpreted, with direct implications for protocol design and generalizability.

Age consistently modulates postural control by affecting both sensory reliability and motor execution. Meta-analytic evidence links age-related degradation of somatosensory afferences and multisensory integration to larger sway and reduced balance performance, especially under challenging sensory conditions. From a control perspective, ageing increases sensory noise and delays, reducing feedback robustness and shifting strategy selection toward more conservative solutions (e.g., earlier stepping) [1]. Because IL×SIS intentionally manipulates sensory reliability, age is particularly relevant for translation to older populations [33,55].

Pathology can reduce stability margins by affecting either state estimation (sensory integration) or actuation (motor output), thereby changing baseline sway and responses to instability [1]. In clinical translation, different conditions may shift which component becomes rate-limiting (sensorimotor, biomechanical, cognitive), altering which parts of the IL×SIS space remain tolerable [13,59].

Cognitive load also matters because postural control shares attentional resources with concurrent tasks. Reviews in healthy adults show that dual-tasking can increase sway, slow corrective responses, and amplify instability, particularly when sensory cues are reduced [60–62]. Accordingly, any boundary or threshold derived from an assessment protocol is context-dependent: the functional “limit” can shift with attentional demands even if the mechanical plant is unchanged.

Anthropometry influences postural dynamics through geometry and inertia: stature, mass distribution, and foot placement change the effective pendulum length and available BOS, affecting sway amplitude and COP metrics. This can confound between-participant comparisons and bias any instability level defined purely by platform mechanics. Therefore, the assessment system requires normalization of mechanical difficulty so that thresholds reflect control capability rather than body size. In this dissertation, this normalization is implemented via the relative instability index (RII).

Measurable postural-control outputs depend on sensory reliability, cognitive resources, and body geometry; these factors jointly shape stability margins and strategy selection [1]. Without anthropometric scaling and context control, between-subject comparisons can therefore reflect mechanical/geometry differences rather than true differences in control capability [63]. To support comparable individualized thresholds under standardized sensory conditions, this dissertation uses RII alongside IL×SIS [26,29,33].

1.6. Postural control assessment methods

Postural-control assessment methods are reviewed here to clarify why many existing approaches do not provide a graded, objective identification of an individual functional boundary, motivating an instrumented protocol with controllable task difficulty (IL and SIS) and objective real-time monitoring.

A practical classification separates clinical/functional tests from instrumented measurements, and then divides instrumented approaches into (a) static posturography and (b) dynamic/perturbation-based paradigms [32]. This reflects a feasibility–resolution trade-off: clinical tests are accessible but low-resolution, whereas instrumented methods provide continuous metrics but require equipment and protocol control [64]. For this dissertation, the key design requirement is gradual difficulty progression with objective termination criteria rather than subjective judgment [26,29,33].

Within instrumented methods, difficulty can be increased via sensory manipulation (e.g., eyes closed, compliant surface, moving visual surround) or via mechanical destabilization/perturbation (e.g., platform translation/tilt, unstable support dynamics, unexpected pulls/pushes, slips/trips) [1]. Most protocols emphasize one axis at a time; only a subset offers (i) graded, continuously controllable progression and (ii) objective real-time metrics suitable for automated stop criteria [4,14,26,32].

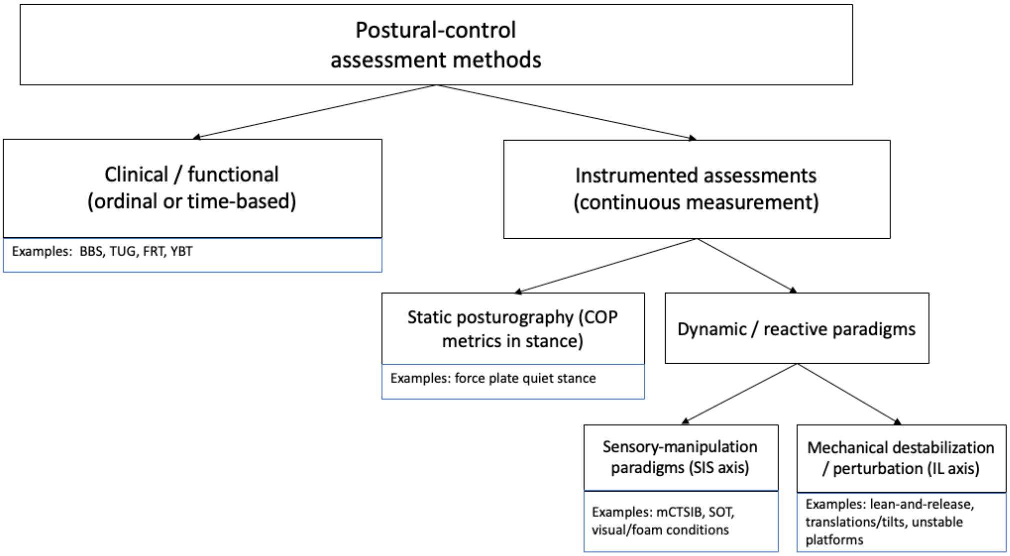

Figure 2. Conceptual classification of assessment methods: (1) clinical versus instrumented; (2) instrumented static versus dynamic/perturbation; (3) dynamic sensory-manipulation versus mechanical-destabilization paradigms. Source: adapted from clinical–instrumented assessment frameworks and posturography clinical-utility reviews 22)

Figure 2 shows that balance-assessment methods can be classified not only by instrumentation level, but also by the mechanism used to increase task difficulty. The methodology proposed in this dissertation belongs to the instrumented branch and combines two complementary difficulty axes: sensory manipulation and mechanical destabilization.

1.6.1. Clinical tests

Clinical tests are widely used because they are low-cost, quick, and feasible across settings [32]. Examples include the Berg Balance Scale (BBS), Timed Up and Go (TUG) [65], Functional Reach Test (FRT), and dynamic reach tests such as the Y-Balance Test (YBT) [32,66]. They serve as global indicators of balance or mobility, but compress complex behavior into a score or time, limiting mechanistic interpretation [32–34,58].

Resolution and subjectivity are persistent limitations: many scales use ordinal scoring rather than continuous measurement [32]. Meaningful strategy changes (e.g., greater hip use, earlier stepping, higher-frequency corrections) may not shift the score unless a category boundary is crossed [32]. Even time-based outcomes can be dominated by non-balance factors (strength, gait speed, turning strategy, motivation), complicating interpretation when the target is postural-control capacity rather than global function [33,34,67].

Measurement breadth and ceiling effects are additional limitations. Ceiling effects and low sensitivity to change have been reported across widely used tools, limiting discrimination in higher-functioning individuals and potentially underestimating intervention effects [57,68,69]. Reliability can also vary across the score range, so group-level reliability does not guarantee sensitivity to modest within-individual change at higher functional levels [70]. For boundary-oriented methodology development, these effects obscure where an individual approaches a functional limit [33,58].

Reactive postural control is also sampled weakly in many clinical protocols. For safety and standardization, many clinical protocols avoid unexpected perturbations and therefore may not evoke protective stepping, grasping, or rapid recovery responses [32]. Consistent with this limitation, TUG shows limited predictive ability for falls in community-dwelling older adults when used alone [67]. Dynamic reach tests such as YBT probe voluntary limits and can be reliable in active populations, but remain self-paced and anticipatory, with predictive value depending on population-specific cut points [71].

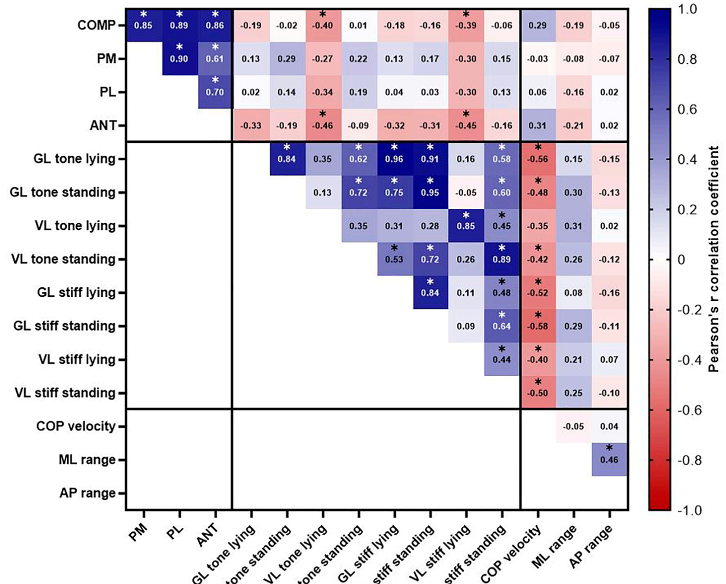

Figure 3. Correlation matrix for associations between muscle mechanical properties and static and dynamic balance, where values indicate Pearson's r correlation coefficient. *Indicates statistically significant correlation ($p < .05$). Shading indicates strength of relationship (blue = positive correlation, red = negative correlation). Note. ANT, anterior reach distance; AP, anteroposterior COP range; COMP, composite reach score; COP, center of pressure; GL, lateral gastrocnemius; ML, mediolateral COP range; PL, posterolateral reach distance; PM, posteromedial reach distance; Stiff, stiffness; VL, vastus lateralis [72]. Reproduced Hill et al., Frontiers in Physiology (2023) - doi:10.3389/fphys.2023.1168314. Included for scholarly (non-commercial) use in this dissertation; copyright remains with the original rights holder

Figure 3 illustrates that associations between muscle mechanical properties and balance outcomes are task-specific and non-uniform. This supports the methodological decision taken in the present dissertation to use multiple biomechanical indicators rather than rely on a single clinical score or one isolated posturographic parameter.

Clinical tests remain practical for screening, but their outcomes are often low-resolution and may not yield a mechanistically interpretable quantitative indicator of an individual stability boundary [32]. Ceiling effects, ordinal scoring, and the avoidance of perturbations can further mask the shift from anticipatory to reactive control that is central for boundary-based assessment [57]. These limitations motivate the objective stability-threshold assessment approach in this dissertation: an instrumented, controllable paradigm with objective metrics for warning/critical thresholds and reproducible difficulty progression [33,34,58].

1.6.2. Static posturography

Static posturography uses force platforms to measure ground reaction forces and derive COP trajectories during standardized standing tasks [22]. Its key advantage is continuous, high-resolution measurement, which can reveal subtle control changes invisible to ordinal clinical scoring [22]. Common metrics include dispersion (e.g., EV95%), directional variability, and velocity-based measures (TMV or path length per unit time) [22]. Conceptually, COP is not COM: COP reflects the control action at the support interface, whereas COM is the controlled state. COP metrics therefore describe control effort and neuromechanical coupling more directly than COM motion [16,19,26,29].

As illustrated in **Figure 4**, force-platform posturography transforms corner load-cell signals into COP time series in the AP and ML directions and into a planar COP trajectory. These outputs form the basis of the spatial and velocity-based parameters used throughout this dissertation, especially COP area and COP mean velocity.

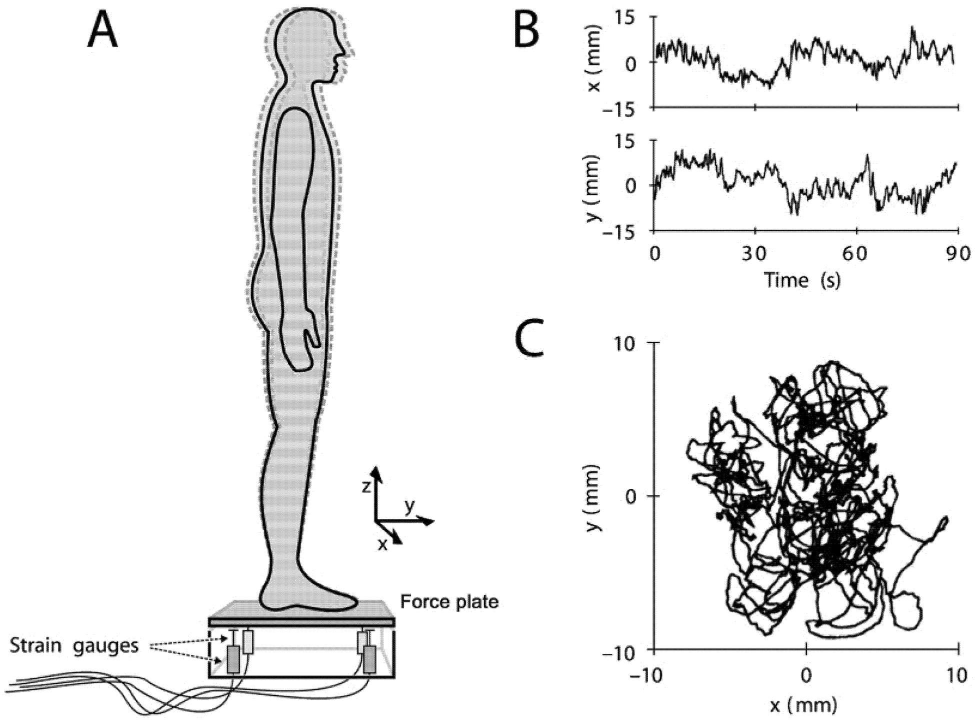

Figure 4. Change of the center of pressure (COP) calculated through the force plate. (A) Stand statically on the force plate for the postural sway test. The dotted line of the humanoid outline indicates spontaneous sway. The force plate is usually arranged with strain gauges at the four corners below the supporting plate, which can calculate the ground reaction force and COP trajectory. (B) COP time series in ML(x) and AP(y) directions. (C): The trajectory of COP [22]. Reproduced: Chen et al., Int J Environ Res Public Health (2021) "Review of the Upright Balance Assessment Based on the Force Plate" – doi:10.3390/ijerph18052696. Included for scholarly (non-commercial) use in this dissertation; copyright remains with the original rights holder

COP velocity is particularly informative because it is sensitive to both correction amplitude and timing. COP can change rapidly even when sway area remains moderate, so velocity can reveal escalating corrective activity earlier than purely spatial measures [23]. For threshold-based monitoring, this motivates using COP velocity/TMV as a candidate real-time signal for warning/termination criteria (e.g., increasing TMV), potentially before overt balance loss [23]. Comparability across devices is feasible only when sampling and filtering are controlled [22,26–28].

A critical constraint is method sensitivity: reliability depends on trial duration, sampling frequency, filtering, stance width, and instruction set. Empirical evaluations show that measurement error and reliability differ across posturographic parameters and that some parameters are unstable unless protocols are standardized and repeated measures are used [73]. Static posturography becomes "objective" only when the measurement chain and protocol are explicitly controlled and metric selection is justified by reliability/sensitivity evidence [26–29,73]. Instrumented COP assessment is increasingly accessible: low-cost force plates and portable systems have been evaluated for validity and test–retest reliability, enabling objective balance measurement outside specialized laboratories [74,75]. This shifts the primary challenge from feasibility to methodological design—how to use objective metrics to approach and detect an individual boundary safely and comparably [76–79].

Interpretation still requires caution because COP is a control variable rather than a direct proxy for COM kinematics; similar COP patterns can correspond to different COM dynamics depending on anthropometry and strategy (ankle-dominant vs hip-dominant) [16]. Dispersion and velocity are best treated as objective indicators of control effort/regulation demand under standardized tasks, not as standalone surrogates of a universal stability limit [19,21,22,29].

Static tasks also have a structural limitation: quiet stance may not elicit the reactive regime of interest. Participants can remain within BOS using small continuous corrections without approaching a boundary that requires protective responses [1]. Accordingly, static COP metrics may differentiate groups yet still map weakly to functional limits unless tasks probe the relevant control subsystems [64,80–83]. Static COP measurement is therefore necessary for objective quantification, but not sufficient for objective boundary identification [26,82].

Static posturography provides objective, continuous measures of the support-interface control action (COP), and COP velocity/TMV is particularly practical for real-time quantification of escalating corrective activity [23]. At the same time, COP metrics are protocol-sensitive and quiet stance may not elicit reactive regimes, limiting boundary identification unless task difficulty is manipulated [73]. Within this proposed objective stability-threshold assessment framework, COP-derived parameters are therefore used as warning/critical thresholds only when embedded in a paradigm that systematically reduces stability margins via mechanical and/or sensory manipulation [26,28,29].

1.6.3. Dynamic posturography and reactive tests

Dynamic posturography extends static measurement by manipulating context so the control system must adapt and, ideally, approach a limit where reactive recovery is required [1]. Two families are central to the dissertation logic: (i) sensory-organization paradigms that alter sensory reliability and (ii) mechanical destabilization/perturbation paradigms that challenge support mechanics or inject disturbances [14,26,59].

Sensory-organization approaches align with SIS. Computerized dynamic posturography can implement discrete sensory conditions by altering visual input and/or support-surface properties, often with a harness for safety [64]. They allow within-subject comparison across sensory reliabilities (vision, somatosensation, vestibular), providing an operational window into sensory reweighting and control adaptation [36]. Measured responses can be interpreted through reweighting models in which sensory weighting and control gains change with context [40]. Clinically, such systems offer richer information than simple tests because they force adaptation and yield continuous platform-derived metrics [37,42,59,64].

A widely used example is the Sensory Organization Test (SOT) in computerized dynamic posturography (CDP), where participants stand on a force platform while visual and/or support-surface conditions are varied across a small standardized set of trials (commonly six) [64]. Typical conditions combine eyes open/closed, sway-referenced visual surround, and sway-referenced support (platform motion coupled to sway to reduce reliable sensory error) [59].

SOT/CDP outputs summarize stability across sensory contexts and can infer relative reliance on visual, somatosensory, or vestibular inputs [36]. From a research standpoint this is valuable because it standardizes sensory manipulation and enables within-subject comparison [36]. From a boundary-detection standpoint, the same standardization (fixed discrete conditions) limits fine-grained difficulty scaling: performance is sampled in a few contexts rather than ramped continuously toward an individual threshold [37,42].

Simplified protocols such as mCTSIB apply the same principle (visual removal and compliant support) with minimal equipment and acceptable test–retest reliability, confirming sensory manipulation as a practical lever for changing demand [43]. However, they remain categorical and do not define a mechanical instability index suitable for device-to-device comparison or real-time adaptive scaling [45–48].

Sensory-organization paradigms face three boundary-relevant limitations: (i) difficulty is typically discrete, limiting fine-grained difficulty scaling; (ii) the mechanical plant is largely fixed, preventing a general mechanical instability index comparable across devices; and (iii) many systems are proprietary and expensive, constraining dissemination and customization [26,29,59,64].

Perturbation-based and mechanically destabilizing tests probe reactive control by imposing rapid changes that require recovery. Reactive paradigms include manual pull/push-release tests, lean-and-release, motorized translation/tilt platforms, and treadmill or walkway slips/trips [52]. Their advantage is that they elicit protective stepping, grasping, and fast hip corrections—behaviors that demarcate the boundary between recoverable instability and balance loss [52]. Reactive stepping can change after perturbation-based interventions, indicating trainability and supporting these paradigms for studying adaptation [84,85]. Because reactive responses also adapt with repeated exposure, boundary estimation benefits from protocols with graded difficulty and explicit stop criteria [14,53].

Lean-and-release and related pull/push-release procedures approximate a graded threshold concept by starting from a controlled lean or preload and then releasing support, requiring rapid recovery (often stepping) [86]. Step onset timing, step length, and recovery success/failure provide objective markers, and difficulty can be tuned via lean angle or applied load [87]. Such tests can reveal reactive deficits hidden in voluntary or quasi-static tasks by forcing time-constrained recovery [32]. However, grading is typically implemented as discrete perturbation magnitudes and the disturbance is external rather than a continuous change in support dynamics [14,53].

Mechanically destabilizing platforms modify the plant itself rather than injecting a brief impulse (e.g., compliant/unstable supports, tilting/rolling platforms, devices that change the mapping between sway and support reaction forces) [1]. This class aligns with the IL concept because it alters stability properties (e.g., effective stiffness/damping, controllable COP range) and can, in principle, be adjusted continuously [88]. Yet applied literature often uses unstable supports qualitatively ("wobble board", "foam", "unstable") without a standardized, comparable instability index, limiting cross-system metrology [14,29,64].

Safety and automation are central design constraints. Perturbation tests often rely on harnesses and conservative procedures, but stopping rules are frequently procedural (clinician judgment, fixed trial counts) rather than based on real-time objective signals [64]. Gradual difficulty progression (via plant instability and/or sensory reliability) can enable explicit "warning" and "critical" thresholds based on continuous measures such as TMV and dispersion (e.g., EV95%); in this dissertation, these thresholds are implemented as part of the safety/automation logic [23]. Objective thresholds can support standardized termination and reduce operator dependence when approaching an individual boundary [26–28].

Reactive-test literature supports the value of measuring recovery behavior, but also shows why controlled approach-to-instability remains underdeveloped: many reactive tests rely on discrete perturbation steps or complex infrastructure, and many sensory-organization tests do not manipulate mechanical instability in a metrologically comparable way [26,32,33,64].

Perturbation paradigms also face practical barriers: high-quality platforms and treadmills are costly; manual perturbations can be difficult to standardize; and safety concerns require harnesses, trained staff, and conservative protocols [64]. Outcome measures vary (step latency/length, COM displacement, success/failure), complicating comparison across studies and systems. Standardized reactive stepping measures exist and have been applied in neurological populations, but are less common in routine screening [53,86].

Another boundary-relevant limitation is that many perturbation paradigms increase difficulty by injecting larger disturbances rather than by continuously adjusting underlying support dynamics [89–91]. This can probe reactive capacity but complicates controlled threshold identification and may require exposing participants to abrupt perturbations. External impulses can also confound COP-based thresholds because measured responses reflect both participant control action and the imposed disturbance.

The assessment literature highlights a methodological gap: many systems manipulate sensory information or impose mechanical perturbations, but few combine graded mechanical instability and graded sensory restriction with real-time objective monitoring and explicit safety termination criteria [32]. Without a graded controllable difficulty axis, an individual functional boundary cannot be defined as a reproducible point on a continuous scale; without objective real-time metrics, automated warning/termination rules cannot be implemented safely [14,26,29].

Dynamic posturography and reactive tests can probe sensory dependence and recovery behaviors that are not accessible in purely static assessments, making them the closest existing analogs to boundary-focused evaluation [1,64]. However, most implementations use discrete difficulty steps or rely on externally injected perturbations; relatively few combine graded mechanical instability with graded sensory restriction under real-time objective monitoring and explicit safety thresholds [32,64]. IL×SIS is designed to address this gap by combining scalable mechanical instability (IL) with physiologically justified sensory manipulation (SIS) and by applying objective parameters (e.g., TMV and dispersion) for warning/critical thresholds and automatic stop/progression rules [14,22,23,26,53,59].

1.6.4. Existing equipment/systems for balance assessment

To complement the overview of assessment methods, this subsection summarizes representative clinical tests and instrumented systems used to quantify balance in research and practice. The comparison highlights (i) what each approach measures, (ii) the instability/impairment range it can typically address, and (iii) limitations relevant to objective identification of an individual postural-control boundary.

Table 1. Comparison of balance assessment methods and representative instrumented systems

Method/System	Domain/Outcome	Instability level	Key limitations
Timed Up and Go (TUG) [67,92]	Time to stand up, walk 3 m, turn, and sit. Functional mobility and dynamic balance during gait.	Mild–moderate (ambulatory).	Global performance metric influenced by strength, gait speed, and strategy; limited insight into sensory/reactive components.
Berg Balance Scale (BBS) [93]	Ordinal score (0–56) across 14 tasks (static/anticipatory balance, transfers, reaching).	Low–moderate (frail to moderately impaired).	Ceiling effect in higher-functioning individuals; limited reactive balance and gait-related challenges.
Functional Reach Test (FRT) [94]	Maximal forward reach distance without stepping; limits of stability (anticipatory control).	Mild–moderate (standing, anticipatory control).	Primarily probes a single task dimension (reach); does not assess gait or reactive stepping; potential learning/strategy effects.

Method/System	Domain/Outcome	Instability level	Key limitations
Four Square Step Test (FSST) [95]	Time to step in a square pattern over obstacles; multidirectional stepping and change-of-direction control.	Mild–moderate (requires independent stepping).	Safety constraints in high instability; single-time outcome offers limited mechanistic detail.
Dynamic Gait Index (DGI) / Functional Gait Assessment (FGA) [96,97]	Scores on gait tasks (head turns, obstacles, stairs, narrow BOS, etc.); walking balance under challenge.	Mild–moderate (ambulatory).	Focus on gait; limited quantification of stance control and reactive responses to unexpected perturbations.
Balance Error Scoring System (BESS) [98,99]	Count of observable balance "errors" across stance conditions (firm/foam; eyes closed).	Mild deficits (e.g., sport-related, subtle instability).	Subjective scoring and inter-rater variability; floor effects in moderate–severe impairment; limited dynamic/reactive content.
Static posturography (force plate COP sway) [22,82]	Objective COP metrics during quiet stance (e.g., velocity/TMV, path length, area) under EO/EC and firm/foam variants.	Broad (as long as standing is feasible).	Protocol-sensitive (duration, sampling, filtering); quiet stance may not elicit reactive control; functional/fall relevance depends on context.
Low-cost force plate: Wii Balance Board (WBB) [100,101]	COP-derived sway metrics using a low-cost platform; typically for static stance protocols.	Mild–moderate (static stance).	Accuracy depends on data acquisition and processing; not designed for controlled perturbations; limited standardization across implementations.
Low-cost balance plate: BTrackS [75]	Portable COP measurement; validated against laboratory force plates for COP accuracy/reliability.	Mild–moderate (static stance).	Primarily static/limited task set; boundary identification requires an external paradigm to scale challenge safely.

Method/System	Domain/Outcome	Instability level	Key limitations
Computerized Dynamic Posturography (CDP – SOT) [59]	Equilibrium scores across standardized sensory conditions (moving platform/visual surround); sensory integration profiling.	Mild–severe (with safety harness).	High cost and specialized infrastructure; typically discrete condition set (limited continuous difficulty ramping); limited gait/real-world specificity.
Biodex Balance System (unstable platform + LOS) [102]	Stability indices (overall/AP/ML), limits-of-stability (LOS), and related protocols (incl. mCTSIB variants).	Mild–moderate (difficulty can be adjusted).	Device-specific indices can be hard to translate to daily function; not primarily designed for reactive stepping thresholds.
Wearable accelerometer/IMU posturography [103]	Body-sway metrics (e.g., RMS, normalized path length) from wearable sensors in community or clinic settings.	Mild–moderate (static stance; some protocols extend to walking).	Signal processing and sensor placement affect comparability; limited capacity to impose controlled mechanical perturbations.
Reactive stepping (lean-and-release paradigms) [104]	Reactive stepping thresholds/strategies (single vs multiple steps) under induced forward loss of balance.	Moderate–high (requires harness and safety procedures).	Protocol heterogeneity; external perturbation paradigms can be logistically demanding and are not always standardized.
Instrumented treadmill perturbations [105]	Controlled belt perturbations with balance measures and test-retest reliability metrics.	Moderate–high (harnessed, perturbation-based).	High equipment complexity/cost; perturbations differ from standing-based destabilization; clinical accessibility can be limited.

Method/System	Domain/Outcome	Instability level	Key limitations
Stepping Threshold Test (STT) [87]	Gradually increasing platform perturbations in multiple directions; single- and multiple-step thresholds.	Moderate–high (harnessed, perturbation-based).	Emerging protocols; normative thresholds and fall-discrimination performance vary by implementation and population.

1.7. Practical and clinical significance of postural control assessment

Postural-control assessment is valuable beyond diagnosis, particularly for dosing rehabilitation/training, monitoring progression, and managing fall risk.

Assessment is valuable because postural control is context-dependent and multi-dimensional: a single clinical score often does not indicate which subsystem is limiting (sensory integration, motor output, biomechanical constraints) or provide sufficient resolution for individualized progression [32]. Instrumented metrics can complement screening by providing objective continuous parameters tracked over time and under controlled difficulty manipulation [22,26,29,33].

One application is dosing and monitoring balance training/rehabilitation. Adaptive systems that quantify performance under progressively more difficult conditions can support graded exposure and overload within a safety envelope. Clinically, titrating challenge is generally important: too little challenge may limit adaptation, while excessive challenge may increase fall risk and reduce adherence [106–108]. Objective metrics also improve feedback by making change visible in continuous variables (e.g., COP velocity, success/failure boundaries) rather than only in ordinal categories [26,106,107].

Postural-control assessment is also used for fall-risk evaluation. Falls reflect sensory deficits, cognition, and environmental exposure, so no single test is sufficient; nevertheless, objective balance measures and standardized protocols can, in some contexts, improve stratification relative to observation alone. Posturography-based parameters can contribute to prediction and monitoring, but clinical utility depends in part on standardization and selection of metrics that generalize across tasks and populations [64,82,83]. Syntheses linking somatosensory deficits to impaired balance further support assessments that probe sensory-dependent conditions rather than only basic stance [33,58,82].

Postural-control assessment supports objective dosing of training/rehabilitation, monitoring of progress, and more informative fall-risk evaluation than purely observational tests in some contexts [64,82,83]. A recurring limitation is that many existing assessments do not always increase difficulty in a standardized, safe, and individualized manner up to a clearly defined functional boundary [32]. This motivates the development of a system that can increase difficulty in a standardized way to an individual threshold while preserving safety [26,33,82].

1.8. Literature review summary and identified gaps

The key findings of this literature review are summarized below, followed by gaps that motivate the dissertation, with emphasis on an engineering outcome: a graded, instrumented, and safe approach to determining an individual functional stability boundary.

Several recurring principles appear across the reviewed literature. Stability in standing can be treated as regulating COM state within BOS-related constraints via COP modulation, with dynamic stability depending on COM position and velocity [8]. Postural control is multisensory and adapts via sensory reweighting; controlled sensory restriction can increase task demand without external perturbations [36]. As stability margins decrease, strategies transition (ankle → hip → step/grasp) and reactive control becomes more dominant, creating a regime where an individual boundary is observable [49]. Existing assessments rarely combine graded mechanical destabilization with graded sensory manipulation while using objective real-time metrics and explicit safety stop criteria [4,12,14,26,29,32,37,42,53,59,64].

Against this background, five gaps are apparent and directly motivate the dissertation structure:

Gap 1. Mechanical modeling gap → Chapter 3 (Modeling). Existing work on dynamic posturography and perturbation platforms often emphasizes translation/tilt actuation or sway-referenced surfaces and reports outcomes as test scores rather than parametric comparisons of mechanical configuration [64]. As a result, quantitative comparison of how platform suspension geometry (e.g., predominantly vertical versus predominantly angular behavior) alters coupled human–platform dynamics and recovery mechanisms is still relatively limited [1]. Chapter 3 models the human–platform system to isolate how geometric design parameters influence dynamics and stability restoration pathways [26,59].

Gap 2. Mechanical gap → Chapter 2 (Mechanical analysis). Even when mechanical destabilization devices are used, there is limited consensus on universally defined, comparable mechanical instability indices for cross-platform comparison [64]. Without such indices, difficulty is often described qualitatively or in device-specific terms, making reproducible dosing and cross-study comparability more difficult [22]. Chapter 2 develops and analyzes mechanically defined indices (including IL and related normalization) to enable controlled progression across configurations [26,29].

Gap 3. Biomechanical interaction gap → Chapter 4 (Biomechanics). Many models and assessments assume a fixed BOS and analyze COP under that assumption [16]. Platforms with bounded motion create a dynamic and limited BOS, producing distinct COM–BOS interaction regimes (e.g., phases of effective coupling versus decoupling that require different recovery mechanisms) [8]. Chapter 4 defines and quantifies COM–BOS interaction modes relevant to the proposed platform and links them to observable outcomes [12,19,21].

Gap 4. Neurobiomechanical interaction gap → Chapter 5 (IL×SIS interaction). Sensory-organization paradigms quantify sensory dependence and perturbation paradigms probe reactive recovery; however, interactions between graded mechanical instability and graded sensory restriction are rarely quantified, particularly in protocols that do not use external push/pull perturbations [32,36]. Literature typically varies sensory conditions or applies perturbations, but less often uses a controlled continuous progression in which plant stability and sensory reliability are both manipulated to escalate reactive control demand. Chapter 5 quantifies IL×SIS interactions using objective metrics and determines how sensory restriction shifts instability thresholds [14,42,46].

Gap 5. Engineering/system gap → Chapter 6 (Adaptive system and safety logic; prototype implementation). Many existing assessments do not include an adaptive control loop that changes difficulty in real time, logs objective parameters continuously, and applies mechanistically justified safety thresholds or automatic termination rules [22,23]. Without automation and threshold logic, protocols can remain discrete/rigid or depend on operator judgment, limiting reproducibility and scalability [32]. Chapter 6 implements an adaptive system that adjusts IL, logs indicators (e.g., TMV and EV95), and applies warning/critical thresholds with automatic stopping to preserve safety while approaching an individual functional boundary [26–29].

2. MECHANICAL ANALYSIS

This chapter defines quantitative mechanical metrics for balance-perturbation difficulty, enabling comparison of instability levels between studies and participants.

2.1. Angled suspension platform

The mathematical model of the angled suspension platform, introduced in Chapter 3, was based on a simplified two-dimensional scheme with idealised assumptions, such as frictionless joints and chains restricted to a single plane. It is effective for comparing suspension layouts and assessing chain-length effects but does not fully represent the real apparatus.

This section experimentally determines two key mechanical properties of the *Abili Balance* © platform: (i) the horizontal force needed to displace the board from neutral (force threshold) and (ii) the decay rate of free oscillations (oscillation damping).

Figure 5 shows a steel frame with four vertical columns supporting a 0.60 × 0.50 m board suspended on chains.

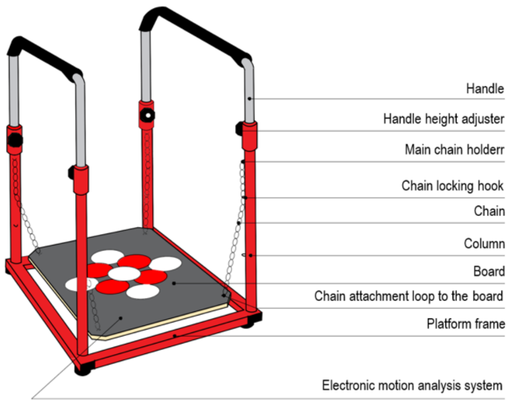

Figure 5. *Abili Balance* apparatus – schematic of the angled-suspension platform with frame, vertical columns, adjustable chain holders, suspension chains, and instrumented board

Each column has three attachment brackets, providing discrete instability levels (**Figure 6).** Chain lengths and the perpendicular distance between the board and column brackets are summarised in **Table 2**.

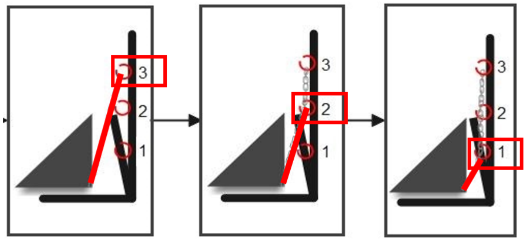

Figure 6. Stepwise adjustment of the suspension chain: moving the hook from bracket 3 to 2 to 1 shortens the active chain and increases stability (from IL 3 to IL 1)

Table 2. Geometric parameters for the three preset instability levels of the *Abili Balance* platform

Instability level	Chain length (m)	Perpendicular distance between the board and the attachment to the support column (m)
3	0.445	0.435
2	0.255	0.24
1	0.125	0.115

Note: For each instability level the table lists the active chain (holder) length l (Figure 7) and perpendicular distance c (Figure 7) to the attachment point on the support column.

The chains are anchored at a 45° inward angle toward the board's corners (**Figure 7**).

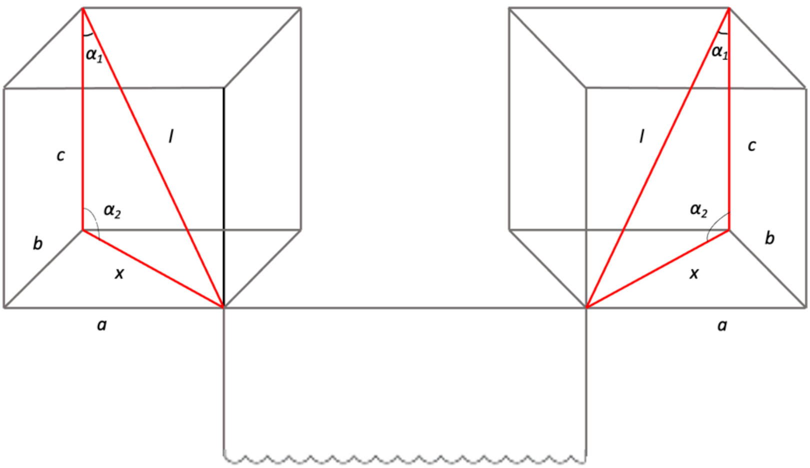

Figure 7. Spatial schematic of the angled four-chain suspension: the chains attach to the support columns at 45° toward the board corners, allowing three-axis freedom while providing a restoring force in the anterior–posterior direction

The 3-D chain geometry allows free oscillation while still producing a restoring force. The analysis therefore focuses on the anterior–posterior displacement component (**Figure 8**), where chain-angle variation is greatest.

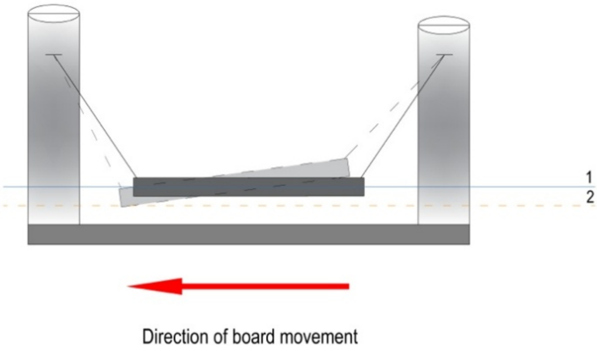

Figure 8. Anterior–posterior board movement. Solid line: neutral position; dashed line: anterior displacement and board tilt. Level 1 marks equilibrium board height; Level 2 the lowered leading-edge height as it approaches the frame

2.2. Methodology

2.2.1. Horizontal Stiffness Measurement

Board displacement was measured with the system's centre of mass fixed. Horizontal stiffness k was measured using test masses of 10, 20, 30, and 40 kg placed at the board centre. A custom auxiliary steel frame positioned posterior to the platform (**Figure 10**) supported a linear sliding rail with a digital force transducer (Mecmesin, RS-232 output; range 10–2500 N; accuracy ± 0.25 %) connected to the board by a non-elastic cable to avoid torsional artefacts. Board-centre displacement was referenced to the platform-frame centre, with neutral position defined as zero. The force required to maintain static equilibrium was recorded at 0.05 m displacement intervals until the leading edge approached the frame. The procedure was repeated for each instability level (IL1–IL3) in the anterior–posterior direction (**Figure 9**)

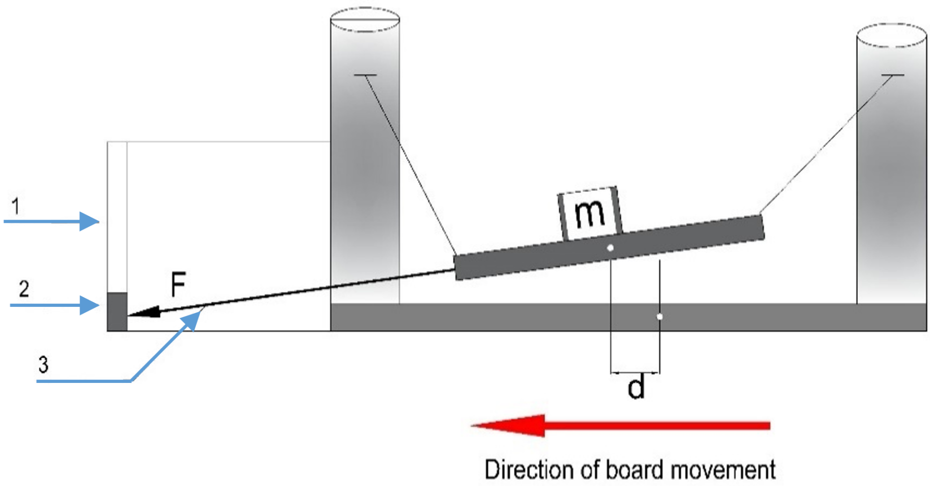

Figure 9. Static force–displacement test set-up. An auxiliary frame (1) supports a digital force transducer (2) that applies and measures horizontal force F. The board is pulled by a non-elastic cable (3) to impose anterior displacement d while load mass m is centred on the board. Force was recorded at 0.05 m displacement intervals. Labels: (1) auxiliary frame; (2) digital force transducer; (3) non-elastic cable

Figure 10. Custom-built auxiliary frame used to apply controlled horizontal force during static force–displacement testing

Figure 11 defines the variables governing the horizontal force required to maintain a prescribed anterior displacement: board load mass m, active chain length l, chain angle α, and horizontal displacement x. These determine the equilibrium force F.

For a symmetrically angled, two-chain suspension, force balance in the sagittal plane gives

$$Vertical\ equilibrium: 2T\cos\alpha = mg \quad (1)$$

$$Horizontal\ equilibrium: 2T\sin\alpha = F \quad (2)$$

where T is chain tension and g is gravitational acceleration. Eliminating T between Equations 1 and 2 yields

$$F = mg\ \tan\alpha \quad (3)$$

For small displacements ($\alpha \ll 1\, rad.$) the small-angle relation $\tan\alpha \simeq x/l$ is appropriate, giving the linear approximation

$$F \simeq \frac{mg}{l}x \quad (4)$$

Equation 3 gives the exact non-linear dependence of holding force on chain angle; Equation 4 provides a first-order estimate sufficient for the ≤ 10 cm displacements investigated in this study.

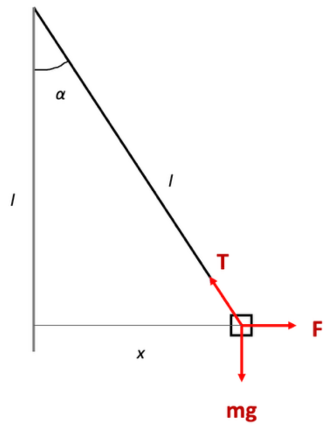

Figure 11. Free-body schematic of the parameters affecting the external force needed to statically displace the board: mass m, chain length l, chain angle α, horizontal displacement x, gravitational force m g, chain tension T, and horizontal force F

2.2.2. Oscillatory Damping Measurement

To characterise attenuation of free vibrations, the damping ratio (ζ) was evaluated for each instability level. In each test the board was displaced anteriorly from neutral and released to oscillate. Test conditions are summarised in Table 3. For IL 3 and IL 2, the board was retracted until its leading edge approached the inner contour of the platform frame (displacement ≈ 4.8 cm); for IL 1, geometric constraints limited retraction to 1.6 cm. Displacement was recorded with an integrated triaxial accelerometer (*Abili Balance*, 100 Hz sampling frequency). The dimensionless damping ratio ζ describes how rapidly oscillation amplitude decays toward steady state; systems with $\zeta < 1$ are underdamped. Under the small-amplitude assumption, the platform can be modelled as a damped mathematical pendulum, with parameters defined in Equations 5–11.

Because the platform has no dedicated damping elements, attenuation is expected to be small and arises mainly from friction at the suspension interfaces (hook–bracket contact, chain-link articulation, and attachment bearings) and, to a lesser extent, aerodynamic drag. Under the small swing angles and low oscillation velocities of the free-decay tests, the system is therefore lightly damped ($\zeta \ll 1$). Higher damping ratios with shorter chains are consistent with greater tension and contact forces, which slightly increase frictional losses per cycle.

The platform can be modelled as a damped mathematical pendulum. The composite attenuation parameter κ, combining chain-length-dependent stiffness and damping per unit mass, is defined in Equation 5:

$$\kappa = \frac{kLD}{3m} + \frac{c}{m} \tag{5}$$

Substituting κ into the free-body balance yields the small-angle equation of motion (Equation 6):

$$\ddot{\theta} + \kappa\dot{\theta} + \frac{g}{l}\theta = 0 \tag{6}$$

For reference, the ideal undamped period is given by Equation 7; in the present 3-D chain geometry, this value is only indicative:

$$T = 2\pi\sqrt{\frac{L}{g}} \tag{7}$$

In subsequent calculations, the period is taken from the recorded vibrograms; deviations from T_0 reflect the shorter effective length of the 3-D chain geometry and additional bearing friction. The corresponding natural angular frequency is calculated from Equation 8:

$$\omega = 2\pi f \tag{8}$$

where f denotes the measured oscillation frequency. The critical damping constant is then given by Equation 9:

$$C_c = 2m\omega_0 \tag{9}$$

The dimensionless damping ratio, computed from the logarithmic decrement δ, is expressed in Equation 10:

$$\xi = \frac{\sigma}{\sqrt{(2\pi)^2 + \sigma^2}} \tag{10}$$

The effective damping coefficient is obtained from Equation 11:

$$C = C_c\,\xi \tag{11}$$

These relations quantify oscillation damping at each instability level.

Table 3. Test conditions for damping evaluation

Instability level	Chain length l (m)	Initial board-center displacement x_0 (cm)	Holding force F_0 (N)	Recording duration (s)
3	0.445	4.8	132	60
2	0.255	4.8	196	60
1	0.125	1.6	310	60

2.3. Results

2.3.1. Horizontal Stiffness evaluation

With centre of mass fixed, the static force–displacement tests showed a linear relation between holding force and anterior displacement from neutral (**Figure 12**).

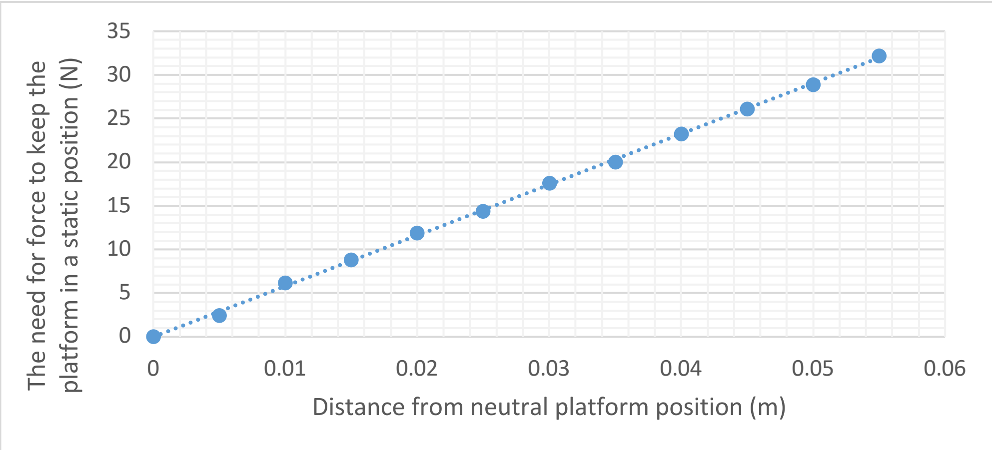

Figure 12. Static force–displacement response of the angled-suspension platform (IL 3; mass 20 kg). Holding force increases linearly with anterior displacement from neutral.

The horizontal force required to stabilise the board increased with applied mass. At instability level 2 (IL 2), heavier loads produced steeper force–displacement curves, as shown in **Figure 13**.

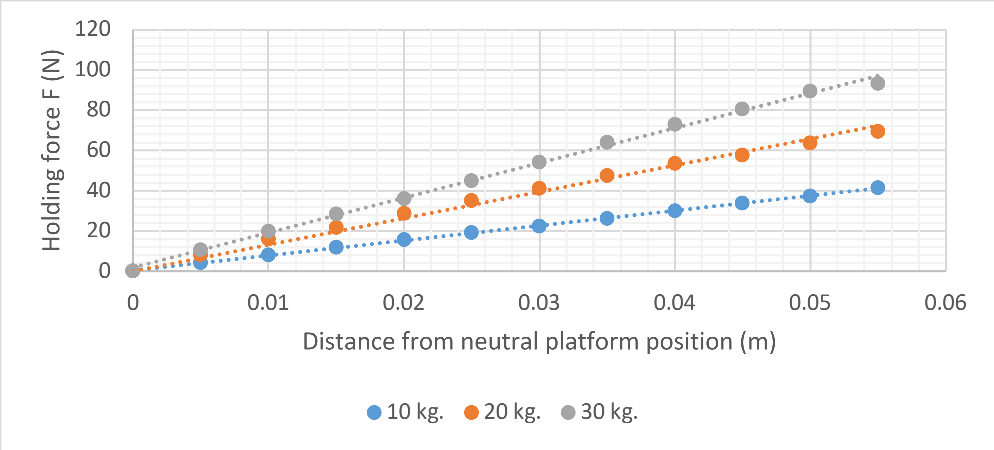

Figure 13. Static force–displacement curves at IL 2 for board loads of 10, 20, and 30 kg. Increasing mass increases holding force at a given anterior displacement

Figure 13 shows that the force–displacement slope k increases with board load. This slope, hereafter termed the stiffness coefficient, is defined as the incremental ratio (Equation 12):

$$k = \frac{\Delta F}{\Delta x} \tag{12}$$

Under the small-angle assumption, the ideal theoretical value is given by Equation 13:

$$k_{theor} = \frac{g\, m}{l} \tag{13}$$

Figure 13 shows that increasing the load from 10 kg to 30 kg increased k from 754 N m^{-1} to 1 797 N m^{-1}. Slopes for each instability level and load are listed in **Table 4**; the ratios between instability levels are given in **Table 6**.

Table 4. Experimentally determined stiffness coefficients $k = \Delta F / \Delta x$ of the static force–displacement curves at three instability levels and four board loads

IL	Board load weight (kg)	Stiffness coefficient (k)
3	10	352.8
	20	579.7
	30	846.2
	40	1066.4
2	10	753.6
	20	1316.1
	30	1797.4
	40	2397.2
1	10	1971.7
	20	3382.3
	30	4803.3
	40	6277.6

Note: Lower IL (shorter chains) or larger mass produces a steeper slope and higher force requirement per unit displacement.

To assess agreement with the small-angle prediction of Equation 13, the slopes measured at the reference 20 kg load were compared with the theoretical value $k_{theor} = mg/l$.

As shown in **Table 5**, the force–displacement relationship remains linear, but the absolute slope exceeds the idealised estimate by +31% at IL 3, +71% at IL 2, and +115% at IL 1. The increasing divergence with shorter chains suggests that 3-D suspension geometry and joint friction raise effective stiffness, especially at the shortest-chain setting. Equation 13 therefore provides a conservative lower bound for experimental horizontal stiffness k.

Table 5. Comparison between theoretical and experimental stiffness coefficients k at a 20 kg load

IL	**Chain length l (m)**	**Theoretical slope $k_{theor} = mg/l$ (N m⁻¹) ***	**Experimental slope k_{exp} (N m⁻¹) †**	**Relative deviation (%)**
3	0.445	442	579.7	+31 %
2	0.255	769	1 316	+71 %
1	0.125	1 570	3 382	+115 %

NOTE: * Calculated from Equation 13 using m=20 kg and g=9.81 m s^{-2}. † Experimental slopes from **Table 4**.

Table 6. Ratios of stiffness coefficients k between instability levels

IL exchange (from / to)	**3**	**2**	**1**
3	–	0.46	0.17
2	2.18	–	0.38
1	5.76	2.64	–

Note: Each entry gives the average change in force–displacement slope when moving from the IL in the left-hand column to that in the header across all four board loads. Values < 1 indicate reduced stiffness, whereas values > 1 indicate increased stiffness.

2.3.2. Oscillatory Damping evaluation

Damping was quantified from the free-decay vibrograms recorded at each instability level (IL 1 – IL 3). The key oscillatory parameters—period, logarithmic decrement, damping ratio ζ, and damping coefficient—are summarised in **Table 7**. As shown in **Figure 14**, amplitude envelopes for all three instability levels show exponential decay, consistent with lightly damped second-order behaviour. In every case $0 < \zeta < 0.05$, confirming underdamped behaviour. The damping ratio decreased from IL 1 to IL 3 (ζ_IL1 > ζ_IL2 > ζ_IL3), indicating that longer suspension chains provide progressively smaller inherent damping.

Table 7. Oscillation and damping characteristics of the angled-suspension platform at the three preset IL

Characteristic	IL 1	IL 2	IL 3
Chain length (m)	0.125	0.255	0.445
Displacement of the center of the board relative to the center of the platform frame (cm)	3.500	4.000	4.000
The force required to keep the board in a stable retracted position before the fluctuations began (N)	310	196	132
Period (s)	0.502	1.007	1.238
Number of cycles (n)	20	20	20
Remaining amplitude from baseline after n cycles	0.143	0.500	0.700
Measured natural angular frequency (ω_o) [rad·s⁻¹]	10.649	6.243	5.077
Logarithmic decrement (δ) over n cycles	1.946	0.693	0.357
Logarithmic decrement during cycle 1	0.097	0.035	0.018
Damping ratio (ζ)	0.015	0.006	0.003
Damping constant (C_c)	1064.95	624.26	507.73
Damping coefficient (C)	16.49	3.44	1.44
Damped natural angular frequency (ω_d) [rad·s⁻¹]	10.65	6.24	5.08

Note: The table lists chain length l, initial board displacement x_0, holding force F_0, period T, number of cycles n, residual amplitude after n cycles, measured natural angular frequency ω_0 (from T), logarithmic decrement δ, damping ratio ζ, critical damping constant Cc, effective viscous damping coefficient C, and damped natural angular frequency $\omega_d = \omega_0 \sqrt{(1-\zeta^2)}$ Values correspond to a total board load of m = 50 kg (≈ 40 kg external load + ~10 kg board mass).

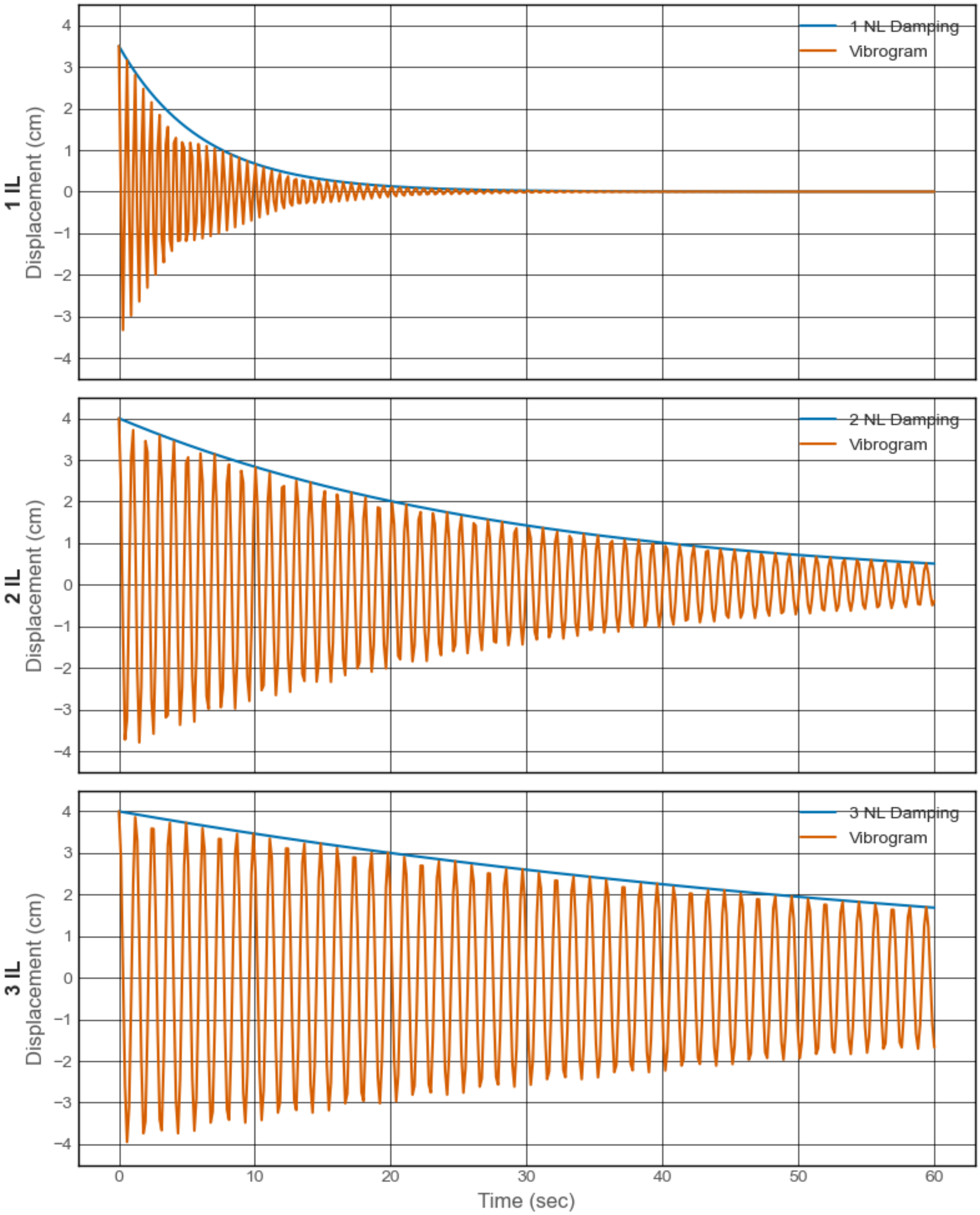

Figure 14. Free-decay vibrograms for the three instability levels (top – IL 1; middle – IL 2; bottom – IL 3). Orange traces show measured anterior–posterior displacement and blue curves the fitted single-exponential envelopes used to extract damping ratio ζ. All responses are lightly damped ($\zeta < 0.05$), but decay time changes systematically across instability levels

2.3.3. Horizontal Stiffness as a Quantitative Instability Metric

Although static tests covered only 10–40 kg board loads, the platform is intended for users weighing 60–120 kg. Predicting behaviour for these heavier participants therefore requires extrapolation of the experimental results. A strict theoretical extrapolation is unreliable because measured stiffness k_{exp} is consistently, and increasingly, higher than that predicted by idealised two-dimensional models, especially at shorter chain lengths (**Table 5**). Any predictive model must therefore be empirical rather than purely theoretical.

Measured horizontal stiffness k_{exp} scales approximately linearly with board load m (**Table 4**), motivating the use of a mass-normalized stiffness coefficient K_{IL} for each instability level.

In the ideal small-angle model, $k_{theor} = \frac{gm}{l}$, so $k/m = g/l$ is mass-invariant. In the real platform, however, measured stiffness exceeds the ideal prediction (**Table 5**) because of 3-D suspension geometry and joint/friction effects, and the ratio k_{exp}/m retains a small dependence on calibration load, especially at the lowest tested load.

For extrapolation to user masses (60–120 kg), K_{IL} is treated as a first-order constant for each instability level; the remaining deviations are treated as experimental scatter and non-ideal effects rather than changes in the stability setting.

$$K_{IL} = \frac{gm}{l} \tag{14}$$

Using the IL 3, 20 kg data from **Table 4** gives (calculation 15):

$$K_{IL} = \frac{k_{exp}}{m} = a_{IL}\,\frac{\mathrm{g}}{l} \tag{15}$$

Here $a_{IL} = \frac{k_{exp}}{k_{theor}}$ is an empirical stiffness multiplier (dimensionless) identified from the reference quasi-static tests (**Table 5**). For IL 3, $\alpha_3 = 1.31$ and $l = 0.445$ m, giving $K_{IL} = 1.31 \cdot \frac{9.81}{0.445} = 28.9\mathrm{N{\cdot}m^{-1}kg^{-1}}$, consistent with $579.7/20 = 29.0\mathrm{N}\cdot\mathrm{m}^{-1}\cdot\mathrm{kg}^{-1}$ from **Table 4**.

This empirically derived $K_{IL} =$ serves as a robust constant for each instability setting (**Table 8**) and enables a first-order prediction of absolute stiffness k_{pred} for any user of mass m (Equation 16):

$$k_{pred}(m, IL) = K_{IL}\, m \tag{16}$$

This model predicts the platform's horizontal stiffness for any user mass without relying on idealised 2-D assumptions.

The reference load of 20 kg was selected as a mid-range calibration condition within 10–40 kg and is used consistently in **Table 5**. Applying Eq. (16) to other calibration loads (30–40 kg) keeps the discrepancy between k_{pred} and measured k_{exp} below ~10% across instability levels; the largest absolute difference (≈500 N/m) occurs at IL 1 and remains a single-digit relative error. These discrepancies are therefore not considered significant for defining and extrapolating the instability-level stiffness constants.

Table 8. Empirical stiffness multipliers and derived mass-normalized stiffness (20 kg static tests)

Instability level	**Chain length l_{IL} (m)**	**Empirical stiffness multiplier a_{IL}**	**Mass - Normalized stiffness $\boldsymbol{K_{IL}}$(N m^{-1} kg^{-1})**
3	0.445	1.31	28.9
2	0.255	1.71	65.8
1	0.125	2.15	168.7

Note: $a_{IL} = k_{exp}/k_{theor}$was computed at the reference load $m_{ref} = 20$ kg using $k_{theor} = gm/l$ (Eq. 13) and the measured slopes in summarised in **Table 5**. The derived mass-normalized stiffness is $K_{IL} = \alpha_{IL}\, g/l$ (Eq. 15).

For IL 2, $K_{IL\,2} =\ 65.8$ N m^{-1} kg$^{-1:}$

70 kg participant: $k_{exp} = K_{IL\,2}m =\ 65.8\ x\ 70\ \approx\ 4602$ N m^{-1}

110 kg participant: $k_{exp} = K_{IL\,2}m =\ 65.8\ x\ 110\ \approx\ 7240$ N m^{-1}

The heavier user therefore experiences a force-displacement gradient about 1.6-fold steeper, reflecting a stiffer and less easily displaced platform. In general, lower k_{exp} values indicate easier board movement under anterior force, whereas higher values indicate greater mechanical stability.

The preceding analysis characterises the platform's intrinsic properties by modelling the user as a passive inertial load. It does not, however, account for the subject's active neuromuscular control as an inverted pendulum generating corrective torques. The Mass-Normalized Stiffness K_{IL} therefore quantifies the external perturbation but not the subject's anthropometrically determined capacity to counteract it.

A subject-specific instability metric should therefore relate platform resistance to the passive gravitational effect of body mass at centre-of-mass height. The platform's resistance is governed by horizontal stiffness k_{exp}, whereas the body's applied force can be modelled as that of an inverted pendulum of mass m and centre-of-mass height h_{COM}; for small sway angles θ, its horizontal component is given by Equation (17):

$$F_{body} \gg \frac{m\ g\ x}{h_{COM}} = m\ g\ \sin\theta \tag{17}$$

Here, $m\ g\ /\ h_{COM}$ is the proportionality between horizontal displacement x and the passive gravitational force applied to the platform. Their ratio defines the dimensionless Relative Instability Index (RII) (Equation 18):

$$RII = \frac{k_{exp}}{m\ g\ /\ h_{COM}} = \frac{K_{IL}m}{m\ g\ /\ h_{COM}} = \frac{K_{IL}\ h_{COM}}{g} = \frac{\left(a_{IL}\frac{g}{l_{IL}}\right)h_{COM}}{g} = a_{IL}\ \frac{h_{\mathrm{COM}}}{l_{IL}} \tag{18}$$

RII normalises the platform's mechanical challenge by the subject's geometric leverage. Because body mass influences both the platform's resistance and the body's applied gravitational load equally, m cancels out, leaving the ratio governed only by platform stiffness and h_{COM}.

The ratio reduces the human–platform interaction to two opposing mechanical properties (Equation 19):

$$RII \approx \frac{\text{Platform}'\text{sMechanicalResistance}}{\text{Gravitational Force Applied by the Body}} \tag{19}$$

A high RII indicates dominance of platform stiffness over the passive gravitational effect of the subject's body, whereas a low RII indicates a highly sensitive system prone to small displacements.

2.3.4. Oscillatory Damping as a Quantitative Instability Metric

The measurements summarised in **Table 7** were obtained with board loads of 10 – 40 kg.

For each load the platform was displaced horizontally by approximately 10 mm, released, and the half-settling time $T_{1/2}$—the interval required for the oscillation amplitude to fall to 50% of its initial value—was recorded.

The decay is governed by viscous friction in the hinge bearings and chain links. Because these hardware properties do not vary with board mass, larger masses settle more slowly because of greater inertia. In practice, the relation is described by Equation (20).

$$T_{1/2}(m, IL) = \psi_{IL} m \tag{20}$$

where $T_{1/2}$ is half-settling time (s), m the total board load (kg), IL the selected instability level (defined by chain length/configuration), and $\psi_{IL}(\text{s kg}^{-1})$ the damping index (slope).

For each instability level, ψ_{IL} is obtained from the slope of the linear fit of $T_{1/2}$ versus m (Equation 21):

$$\psi_{IL} = \frac{\Delta T_{1/2}}{\Delta m}\ [s\ kg^{-1}] \tag{21}$$

The empirical slope ψ_{IL} characterises the rate at which oscillations decay per kilogram of board load at a given instability level. Because it depends only on mechanical configuration, not user mass, it serves as a practical index of the platform's intrinsic damping capacity. Once ψ_{IL} is determined, the expected half-settling time for any subject can be estimated from Equation (20).

Example: Table 9 lists half-settling times obtained from a 20 kg calibration load and the corresponding damping indices for each instability level.

Table 9. Half-settling time $\Delta T_{1/2}$ and damping index ψ_{IL} (20 kg load)

Instability level	**Board load m (kg)**	**Half-settling time $T_{1/2}$ (s)**	**Damping index** $\psi_{IL} = \frac{\Delta T_{1/2}}{\Delta m}$ $[s\ kg^{-1}]$
IL 1	20	7	0.35
IL 2	20	15	0.75
IL 3	20	30	1.50

As shown in **Table 9**, the half-settling time recorded at IL 2 with a 20 kg load is 15 s. The corresponding damping index is therefore

$$\psi_{IL2} = \frac{15\ s}{20\ kg} = 0.75\ [s\ kg^{-1}]$$

This index can be used to predict settling for other board loads:

$$T_{1/2}\,(60\ kg) = 0.75\ x\ 60 = 45\ s.$$

$$T_{1/2}\,(90\ kg) = 0.75\ x\ 90 = 67.5\ s.$$

Accordingly, a 60 kg participant is expected to settle in about 45 s, whereas a 90 kg participant would require about 68 s.

2.4. Conclusions

1. Static force–displacement tests showed that horizontal stiffness increases as chain length decreases; longer suspension chains therefore allow easier board displacement.
2. The effect of shortening suspension chains is more accurately evaluated in space than in a plane, because the real suspension acts in a 3-D geometry with non-ideal joints.
3. Oscillations are lightly underdamped: $0 < \zeta < 0.05$ for all levels. The low damping is mainly due to friction in the suspension interfaces (chain links / hook-bracket contacts / bearings) and weak aerodynamic drag.
4. Damping scales linearly with load. Half-settling time T1/2 increased with board mass, and ψ_{IL} remained constant within each level: 0.35 s kg^{-1} (IL 1), 0.75 s kg^{-1} (IL 2), 1.50 s kg^{-1} (IL 3).
5. Biomechanically, higher instability (IL 3) combines a low force threshold with slow decay, demanding precise, sustained neuromuscular control; IL 1 is more forgiving but provides weaker stimulation.
6. The ordered pair (ψ_{IL}) specifies passive platform behaviour (threshold and decay) independent of user mass, while the Relative Instability Index (RII) relates task difficulty to the participant and enables comparison across sizes and statures.

3. MODELLING

In human balance research, understanding how test-platform suspension geometry generates the mechanical instability experienced by a person standing on the board is crucial. Numerical modelling is therefore used as a first step.

The dynamic analysis integrates these data into two-degree-of-freedom models to compare how platforms generating different levels of mechanical instability affect the inverted pendulum mounted on them.

3.1. **Static Analysis of Suspension Configurations**

This subsection identifies the static mechanical parameters that determine mechanical instability levels and clarifies their influence. Accordingly, three static force components were evaluated:

1. External push force required to displace the platform board.
2. Chain tensions after board displacement, including left-right asymmetry.
3. Horizontal restoring forces in the chains after displacement, including asymmetry.

Balance-assessment devices employ different suspension geometries for the platform board **Figure 15**:

a) ⦀ **Vertical suspension** – the support chains form a 0° angle with the attachment point when the board is in the neutral position.

b) ∠ **Angled suspension** – the support chains form a finite angle with the attachment point in the neutral position.

Differences in suspension type, chain length and neutral-position angle lead to unequal board forces. The two suspension types differ in two principal respects:

A. The neutral-position angle between each chain and its attachment point.

B. During board translation, chain angles either increase symmetrically (vertical suspension) or become asymmetric (angled suspension).

To characterize the angled suspension, an otherwise identical vertical suspension was also analyzed for comparison.

To keep the theoretical analysis general (i.e., representative of a class of suspended balance platforms rather than a 1:1 replica of a single device), the simulations use three nominal suspension lengths l: 0.18 m, 0.24 m, and 0.43 m. These values span a practical short–medium–long stability range of commercially available platforms (e.g., Shuttle Balance™ in a vertical configuration and Abili Balance Analyzer™ in an angled configuration) and are rounded to two decimals for clarity.

The mechanical experiments in Chapter 2 were performed on the Abili Balance platform, where the three discrete holder brackets resulted in measured device-specific chain lengths l_{exp}= 0.125 m, 0.255 m, and 0.445 m (Table 2). The shortest experimental setting (0.125 m) lies in the regime where 3-D geometry and joint friction cause the largest deviation from idealised 2-D predictions (see Table 5); therefore, the generic modelling uses 0.18 m as the representative "short" setting. Throughout this chapter, IL1–IL3 denote relative stability levels (short, medium, long) used in the model, while the exact chain lengths are device-specific.

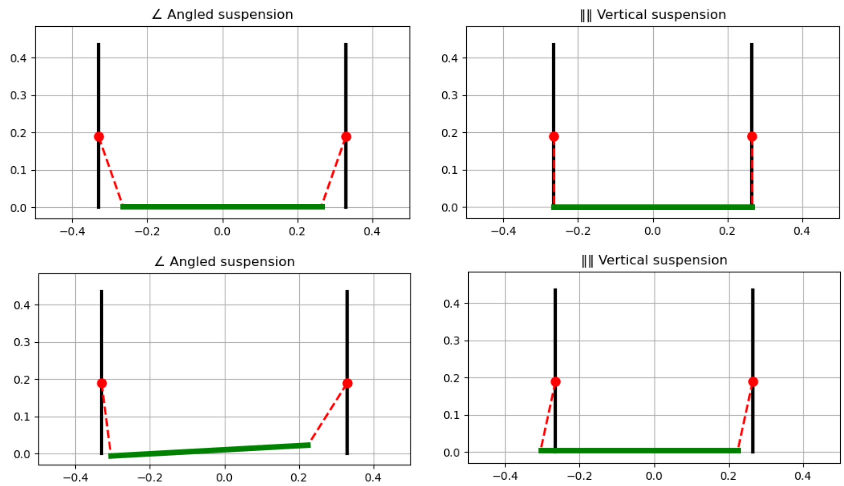

Figure 15. Schematic illustration. A comparison of different suspension geometries and their changes during platform translation. The figure contrasts vertical and angled suspension configurations. The top row shows the platforms in a neutral position, while the bottom row presents the situation when the platform is displaced by −0.04 m to the left (with suspension length fixed at 0.43 m in all cases)

3.1.1. Methodology and Governing Equations

3.1.1.1. Static Equilibrium Model

When the platform board is hung in an ∠ angled suspension, each chain is attached to its own support column. In the neutral position the chain tensions are balanced. Once the board is displaced, the chain angles become asymmetric: one side becomes steeper, the other more oblique. This changes each chain's horizontal support force, so even with symmetric column placement a displacement from neutral produces unequal chain tensions.

The following formulation models the system's static equilibrium by relating the chain angles to the board displacement x and the total system mass $(M + m)$. The resulting model allows theoretical estimation of the external push force $F(x)$ needed to create (and statically maintain) a board displacement of $\pm x$, and to quantify left-right force asymmetries that are relevant for later kinetic/dynamic analysis.

A system of two equations. Let T_{left} – tension in the left chain, T_{right} – tension in the right chain, $\alpha(x)$ and $\beta(x)$ – chain angles as functions of board displacement x. Definitions of variables and geometry parameters:

Here, m is the mass of the platform board (kg) and M is the additional load placed on the board (kg), so the total suspended mass is $(M + m)$.

In Eq. (22), h and c are geometric parameters used to express the chain angles as the board translates:

– Lower anchor spacing – distance between the two lower chain attachment points on the board (in this dissertation 0.53 m);

– Upper anchor spacing – distance between the two upper suspension anchors on the frame (0.53 m for the vertical setup and 0.66 m for the angled setup);

– h – per-side horizontal offset between upper and lower anchors in the neutral position, defined as h = (upper anchor spacing − lower anchor spacing)/2. Thus $h = 0$ for vertical; and $h \approx 0.067$ m for angled);

– c – vertical separation between the upper and lower anchors in the neutral position. For a fixed chain length l, the neutral geometry satisfies $l^2 = c^2 + h^2$ (Angles α and β are measured from the vertical; x denotes the board horizontal translation.)

$$\alpha\,(x) = \tan^{-1}\left(\frac{h-x}{c}\right),\ \beta(x) = \tan^{-1}\left(\frac{h+x}{c}\right) \tag{22}$$

Vertical equilibrium (supporting the total mass $M + m$)

$$T_{left}\cos\big(\alpha(x)\big) \ + T_{right}\cos\big(\beta(x)\big) \ = (M+m)g \tag{23}$$

Horizontal equilibrium, including the external push force $F(x)$ that compensates for the difference between horizontal projections

$$T_{left}\sin\big(\alpha(x)\big) \ - T_{right}\sin\big(\beta(x)\big) \ - F(x) = 0 \tag{24}$$

Solution for chain T_{left}, T_{right} tensions

$$T_{right} = \frac{(M+m)g - \cos[\alpha\,(x)]}{\cos[\alpha(x)]\,cos[\beta(x)] + \sin[\alpha(x)]\,sin[\beta(x)]}$$

$$T_{left} = \frac{(M+m)g - \cos[\beta\,(x)]}{\cos[\alpha(x)]\,cos[\beta(x)] + \sin[\alpha(x)]\,sin[\beta(x)]} \tag{25}$$

External horizontal force $\boldsymbol{F(x)}$

$$F(x) = T_{left}\sin\big(\alpha(x)\big) \ - T_{right}\sin\big(\beta(x)\big) \tag{26}$$

This expression specifies the force $F(x)$ required to keep the board statically balanced at a displacement x, given the chain angles $\alpha(x)$ and $\beta(x)$, chain length, and the total weight $(M + m)\,g$.

3.1.1.2. Static Displacement Simulation

One parameter that distinguishes IL's is the force necessary to achieve a given board displacement. Here the required external push force was calculated to hold the board at horizontal displacements x = 0–5 cm from neutral.

Initial conditions:

- Two total masses were analyzed (board mass (m) + added mass (M)): 25 kg and 100 kg.
- Three IL's, defined by non-elastic rope lengths: 0.18 m, 0.24 m, 0.43 m.
- Two suspension geometries were compared: vertical suspension and ∠ angled suspension.
- Board displacement x in the anterior–posterior direction ranged from 0 cm to 5 cm.

These calculations provide baseline forces for characterizing mechanical instability across typical platform configurations.

3.1.1.3. Python script for the static – equilibrium calculations

The full source listing that produced the static results – push-force curves, chain-tension asymmetries and instability-level comparisons – is reproduced verbatim in Appendix A.

The script follows three steps (**Figure 16**):

1. Geometry solver – for each prescribed x, finds the board tilt φ and vertical displacement Y that keep the two chains the same length.
2. Static-equilibrium solver – using these geometrical values, balances horizontal and vertical forces and moments to obtain left- and right-chain tensions and any external push force F.
3. Parameter sweep – repeats the procedure over a range of displacements and exports the resulting tables and quick-look plots.

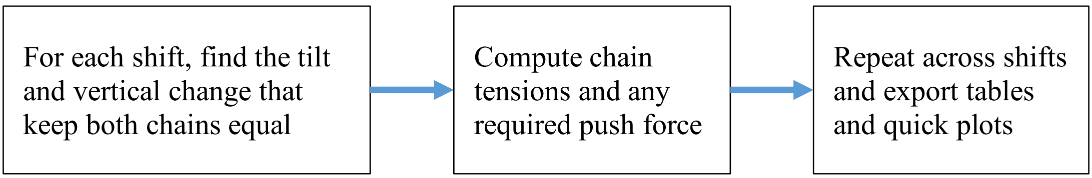

Figure 16 Three-step workflow of the static-equilibrium script: geometry solution, force–moment balance, and parameter sweep with export

Default sliders (**Figure 17**) allow the reader to explore alternative chain lengths, anchor spacing and body mass without changing a single line of code.

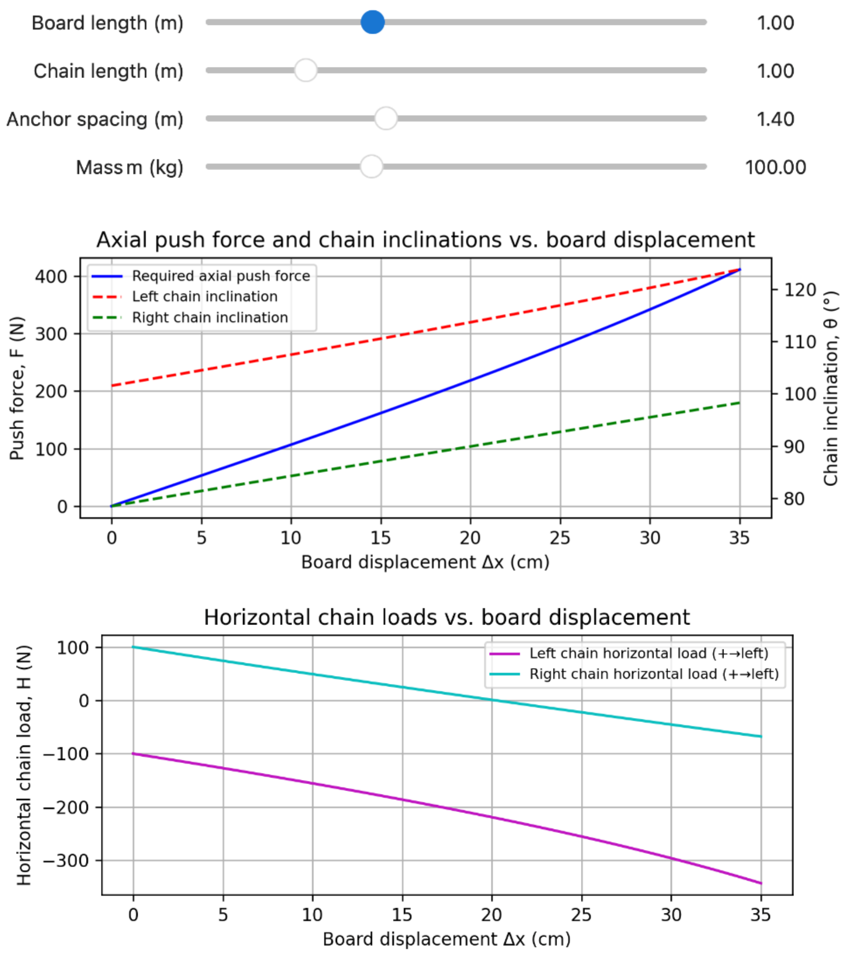

Figure 17. Interactive output from the static-analysis script.
The upper panel shows the external push force and chain angles as the board is shifted; the lower panel displays the corresponding horizontal forces transmitted through each chain. Sliders on the left let the user adjust geometric and mass parameters in real time

The static-analysis results are organized in three steps:

1. Force requirement – external push force vs. board displacement shows, for each suspension geometry, chain length and total mass, the horizontal force needed to hold the board at increasing displacements.
2. Load distribution – tension and horizontal forces at two key positions compare the neutral position with a 5 cm displacement, showing how force is shared between the left and right chains: nearly symmetrically in the vertical setup and strongly asymmetrically in the angled setup.

3. Instability effect – the effect of IL tracks the same quantities across the three chain lengths. Longer chains progressively magnify the left-right imbalance.

Thus, the sequence moves from total force to force distribution, to the effect of higher instability.

3.1.2. Results

3.1.2.1. External push force vs. board displacement

The findings are summarized in **Table 10** and illustrated in **Figure 18.** As expected, smaller board displacements correspond to proportionally lower external push force values, whereas the required external push force rises markedly with increasing x. Chain length strongly modulates this relationship: the shortest chain (0.18 m) demands the highest force to achieve the same displacement, whereas the longest chain (0.43 m) requires the lowest force because its horizontal restoring component is smaller. In addition, the ∠ angled suspension consistently necessitates more force than the ⦀ vertical suspension for an equivalent board displacement.

Table 10. External horizontal force required for board displacement (0.01–0.05 m), compared across different chain lengths and system weights

x (m)	⦀ Vertical suspension (25 kg)			⦀ Vertical suspension (100 kg)			∠ Angled suspension (25 kg)			∠ Angled suspension (100 kg)		
	0.18 m	0.24 m	0.43 m	0.18 m	0.24 m	0.43 m	0.18 m	0.24 m	0.43 m	0.18 m	0.24 m	0.43 m
0.01	13.6	10.2	5.6	54.5	40.9	22.5	17.4	11.6	5.8	69.62	46.7	23.4
0.02	27.4	20.5	11.2	109.6	82.0	45.1	35.2	23.4	11.7	140.8	93.8	46.9
0.03	41.4	30.9	16.9	165.8	123.5	67.8	53.8	35.4	17.6	215.5	141.8	70.5
0.04	55.9	41.4	22.6	223.5	165.8	90.5	74.0	47.8	23.5	296.0	191.2	94.3
0.05	70.9	52.2	28.3	283.6	208.9	113.5	96.5	60.6	29.5	386.1	242.5	118.2

Note. Values are given in newtons. Each row represents the external push force necessary to maintain a prescribed board displacement (*x*). Columns show how this requirement varies with chain configuration, chain length and total system mass. Color scale: green = low force, red = high force. The chain lengths shown in the column headers (0.18/0.24/0.43 m) are nominal modelling values; the measured Abili Balance® chain lengths used in the mechanical experiments were 0.125/0.255/0.445 m (Table 2).

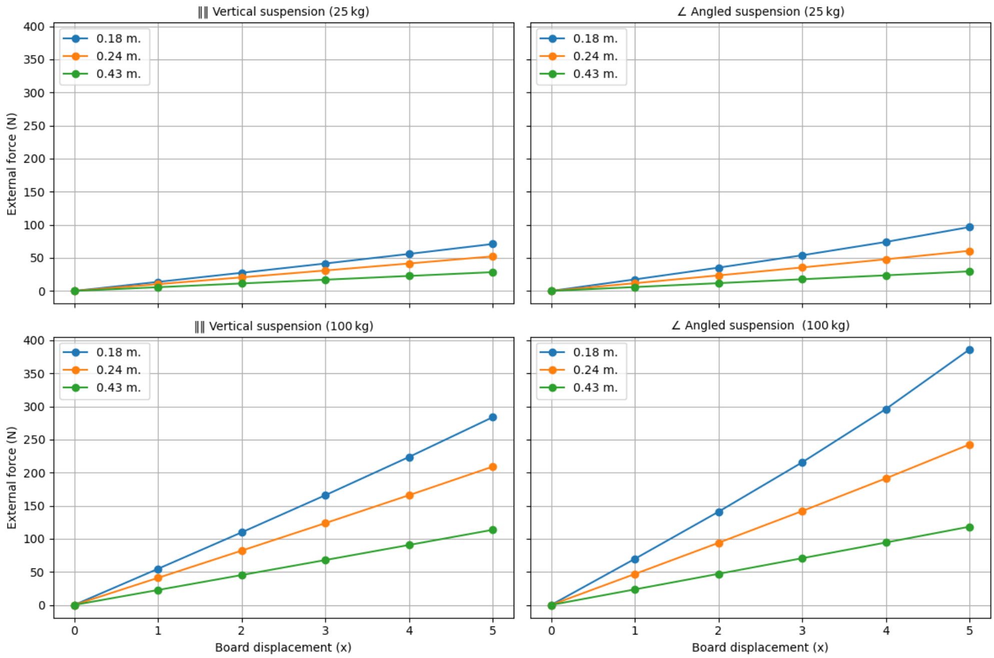

Figure 18. External push force requirement for board displacement under different suspension configurations and weights. This figure compares the external push force needed to displace the balance board (0.00–0.05 m) under two chain configurations (vertical vs. angled), at three nominal model chain lengths (0.18 m, 0.24 m, 0.43 m), and for two total masses (25 kg, 100 kg). Each sub-plot illustrates how the external push force increases with board displacement x, depending on the chain setup and system weight. For comparison, the Abili Balance® experimental chain lengths were 0.125 m, 0.255 m and 0.445 m (**Table 2**)

3.1.2.2. Tension and horizontal forces at two key positions

The suspension geometry – and the angles that result from it – dictates how much force is required to produce a given board displacement. With a ⦀ vertical suspension the left and right chain angles remain symmetric as the board moves; with an ∠ angled suspension a pronounced angular asymmetry appears (see **Figure 15**).

During the simulations, the total suspended mass was set to 100 kg, consisting of the board mass m and an additional load M ($\mathrm{m} + \mathrm{M} = 100$ kg). The chain length was $l = 0.43$ m.

The distance between the two lower chain attachment points on the board was 0.53 m. The distance between the two upper suspension anchors was 0.53 m for the vertical configuration and 0.66 m for the angled configuration.

In Equation (22), the corresponding per-side horizontal offset is h – per-side horizontal offset between upper and lower anchors in the neutral position, defined as h = (upper anchor spacing − lower anchor spacing)/2. Thus $h = 0$ for vertical; and $h \approx 0.067$ m for angled); The parameter c denotes the vertical separation between the upper and lower anchors in the neutral position (with $l^2 = \mathrm{c}^2 + \mathrm{h}^2$).

Table 11 presents the required external push force F, the left- and right-chain angles, and the corresponding chain tensions at two board positions – neutral (x = 0 m) and displaced (x = 0.05 m) – for both suspension geometries (⫴ vertical and ∠ angled).

⫴ Vertical suspension. In the neutral position (x = 0 m) the chains are perfectly vertical and exert no horizontal components (0 N); therefore, no external push force is required to keep the board stable (**Figure 19)**.

When the board is displaced by 0.05 m, an external push force of approximately 119 N is needed. The left and right chain angles remain identical (6.92°), and the horizontal restoring component on each side is ±59.5 N. Their sum (119 N) balances the pulling force (**Figure 20).**

∠ Angled suspension. Even in the neutral position (x = 0 m) a considerable horizontal projection exists: both chains generate ≈ 78 N in opposite directions, cancelling each other so that F = 0 (**Figure 21**).

At a 5 cm displacement the required external push force is ≈ 125 N – slightly higher than for the vertical suspension. However, the horizontal component is highly asymmetric: ~18 N on the left chain and ~142 N on the right, so almost the entire horizontal support is carried by one side (**Figure 22**).

These results confirm that the angled suspension produces substantial tension and horizontal-force asymmetries, whereas the vertical suspension remains near-symmetric over comparable displacements.

Table 11. Lists, for both geometries, the external push force F, the left and right chain angles, and the corresponding chain tensions at two board positions: neutral and displaced (x = 0.05 m)

Board displacement x (m)	**External F (N)**	**α (°)**	**β (°)**	**Left chain tension T_{left} (N)**	**Right chain tension T_{right} (N)**	**Left chain horizontal component H_{left}, x (N)**	**Right chain horizontal component H_{right}, x (N)**
‖ Vertical suspension							
0	0	0	0	490.5	490.5	0	0
0.05	119.06	6.92	6.92	494.1	494.1	+59.53	+59.53
∠ Angled suspension							
0	0	9.01	9.01	496.63	496.63	-77.79	+77.79
0.05	124.53	2.09	16.11	488.4	513.05	-17.8	+142.32

Note (sign convention): Chain tensions T_{left} and T_{right} are reported as magnitudes (always positive). Horizontal components H_{left}, x and H_{right}, x are signed with respect to the global x-axis shown in Figure 19 – Figure 22 (positive to the right, negative to the left). The external force F in this table is reported as magnitude; its direction is opposite to the net horizontal force produced by the chains.

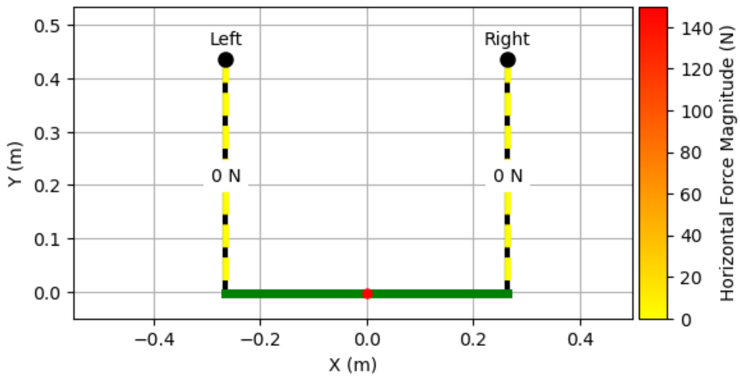

Figure 19. Vertical suspension, neutral position (x = 0 m). Both chains are perfectly vertical; horizontal force components are absent, and no external push force is required to stabilize the board

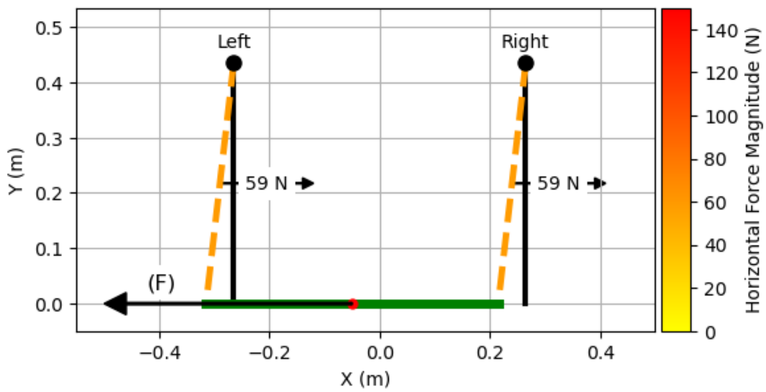

Figure 20. Vertical suspension, displaced position (x = 0.05 m). Chain angles are symmetric (6.92°). Equal horizontal restoring forces (± 59.5 N) balance the 119 N external pull applied to hold the board

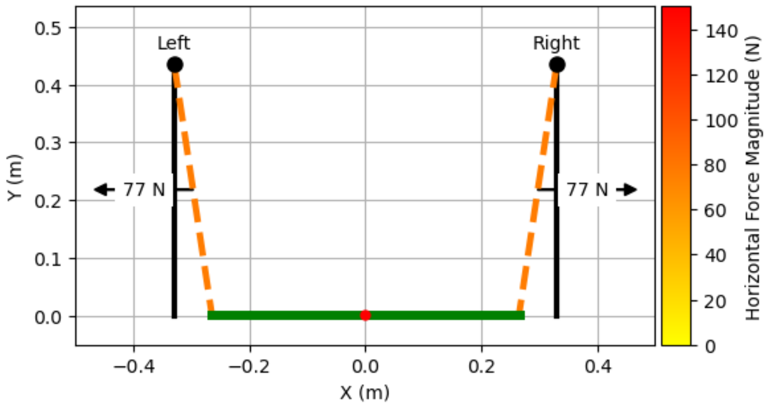

Figure 21. Angled suspension, neutral position (x = 0 m). Initial chain angles (9.01°) generate opposite horizontal forces (~ 78 N each) that cancel one another, so the net external push force is zero

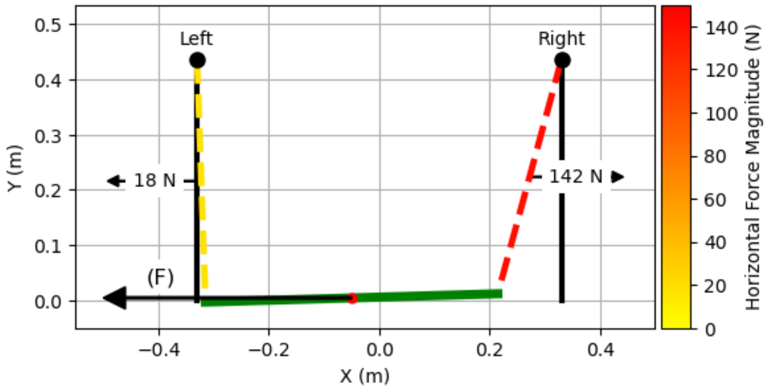

Figure 22. Angled suspension, displaced position (x = 0.05 m). Chain angles become asymmetric (2.09° vs. 16.11°), producing highly unequal horizontal components (17.8 N left vs. 142.3 N right) and requiring an external stabilizing force of ~ 125 N

3.1.2.3. Effect of instability level (chain length)

This section examines how chain length (usually defining IL), together with total system mass, affects left- and right-side chain tension as the board moves from center. Because forces remain symmetric in the vertical suspension, the graphs focus on the angled suspension.

Figure 23 shows chain tensions for an angled suspension at three chain lengths (0.18 m, 0.24 m, 0.43 m) and two total masses (25 kg, 100 kg). As x increases, one chain tension rises while the other falls. Divergence is greatest for short chains and smallest for long chains.

Figure 24 shows the corresponding horizontal restoring forces for a 100 kg system at x = 3.5 cm under three ILs of the angled suspension.

For comparison, **Figure 25** shows the corresponding forces for a vertical suspension under identical conditions. These comparisons show that IL, determined mainly by chain length, strongly affects the magnitude and symmetry of chain tensions and horizontal forces, thereby modulating the mechanical challenge to postural control.

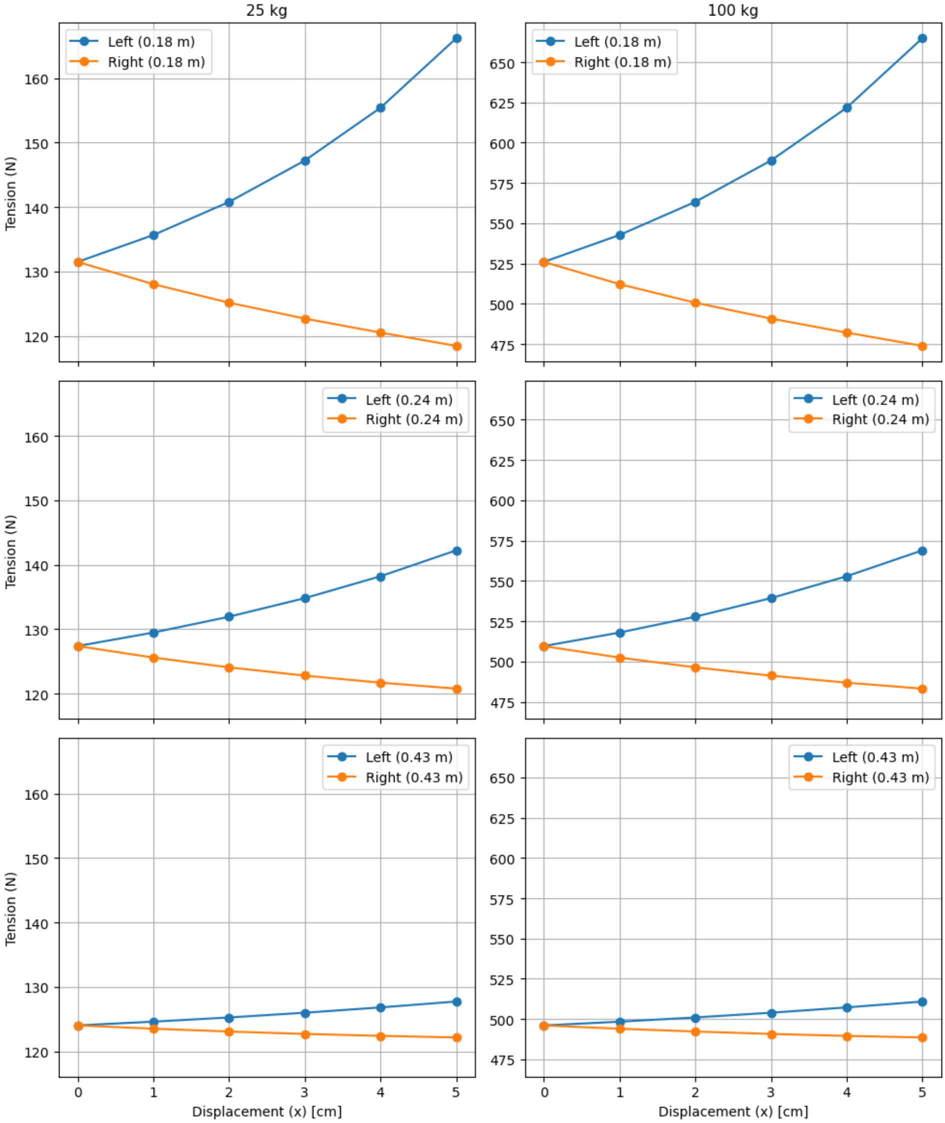

Figure 23. Left and right chain tension versus board displacement in an ∠ angled suspension ("stable position" configuration). Each subplot represents one chain length (0.18 m, 0.24 m, 0.43 m) and compares two total masses (25 kg, 100 kg). Increasing asymmetry indicates the combined influence of geometry and mass on equilibrium

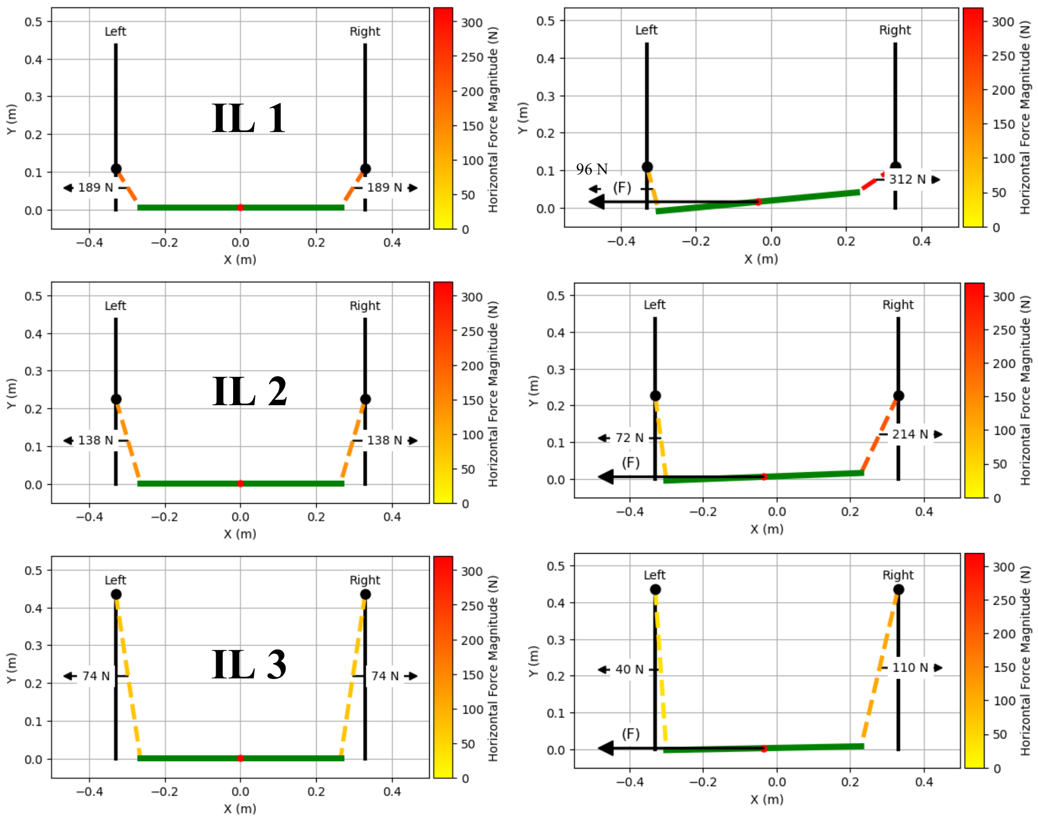

Figure 24. Horizontal restoring forces in an ∠ angled suspension at three instability levels (chain lengths 0.18 m, 0.24 m, 0.43 m; total mass = 100 kg; board displacement = 0.035 m)

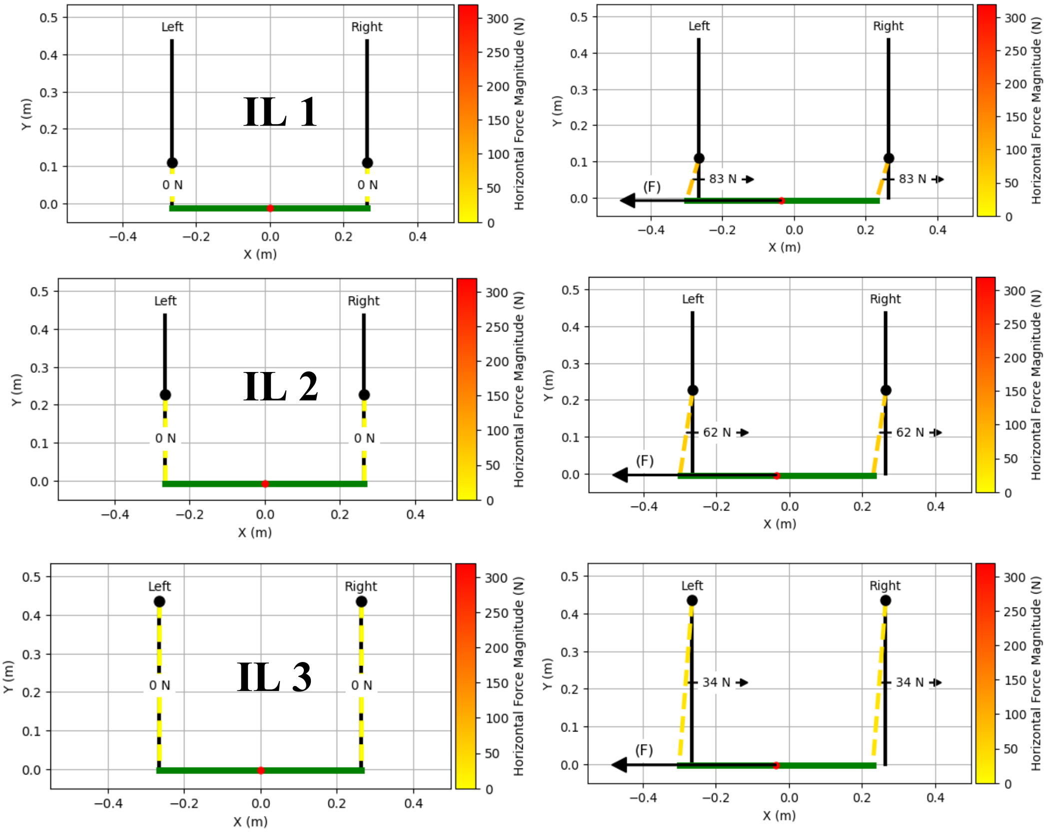

Figure 25. Horizontal restoring forces in a ||| vertical suspension at three instability levels (chain lengths 0.18 m, 0.24 m, 0.43 m; total mass = 100 kg; board displacement = 0.035 m)

3.1.3. Discussion of results

An ∠ angled suspension exhibits large chain-angle differences already in the neutral position, so each chain carries a greater horizontal component. Even small board displacements further amplify the asymmetry, and one chain may absorb almost the entire horizontal load.

Thus, even a small displacement x substantially unbalances the horizontal forces and increases mechanical instability. By contrast, with a ||| vertical suspension a 5 cm displacement remains approximately symmetric: chain angles stay equal and the horizontal restoring force is shared almost evenly. Such a configuration is less prone to “run away” because both chains maintain similar tensile forces. Accordingly, the angled suspension is mechanically less stable because of the one-sided horizontal counterforce.

Biomechanically, highly asymmetric horizontal forces mean that, when a person stands on the platform:

- A slight error in body center-of-mass position can abruptly shift the board, sharply increasing the horizontal force in one chain while decreasing it in the other.
- The person must rapidly reorganize muscular activity to compensate for the changing board inclination.
- This creates a subjective feeling of instability, as the platform tends to slide toward one edge unless constant corrections are applied.

Because the vertical-suspension platform remains largely symmetric, it is less likely to provoke large corrective reactions.

Thus, an initial chain angle more readily creates horizontal-force asymmetry during small board displacements. Mechanically this means greater instability; biomechanically it demands greater effort or faster corrective actions to avoid loss of balance.

3.2. Dynamic Analysis – Board–Pendulum Interaction

A fall occurs when the body's center of mass (COM) moves outside the base of support (BOS) and the COM-BOS relationship can no longer be dynamically restored. Avoiding a fall requires corrective actions that return the COM to the BOS; quantifying their effectiveness and reserve is therefore central to objective balance assessment.

On a balance platform the COM-BOS interaction is continuous: physiological sway moves the COM while the horizontally translating board moves the BOS. Different ILs determine the amplitude and speed of board translation. At all levels, stability requires precise force dosing so that their separation never exceeds a critical threshold.

A theoretical sliding-board-inverted-pendulum model is valuable because it permits simulation of conditions that would be difficult, unsafe or unethical to induce experimentally, especially imminent falls or limits of compensatory balance recovery.

To characterize different ILs, the simulation focused on a common mechanism of postural-control failure: the slip, in which COM and BOS suddenly diverge because the support surface unexpectedly moves.

The simulation therefore evaluates how different ILs affect the compensatory mechanisms that restore balance after such divergence.

Dynamically, loss of balance can be viewed as a state transition in the closed system comprising the inverted pendulum (body) and the sliding board. In the mathematical model:

- (x, θ) are the board position and pendulum angle,
- $(\dot{x}, \dot{\theta})$ are their velocities, and
- $(\ddot{x}, \ddot{\theta})$ are the accelerations generated by the interaction of inertial and/or external push forces (springs, suspension angles, gravity, pendulum inertia).

Balance is considered lost when the board displacement $|x|$ exceeds a predefined limit $\pm x_{max}$ or the pendulum angle $|\theta|$ exceeds its limit $\pm\theta_{max}$.

3.2.1. Methodology and Governing Equations

3.2.1.1. Model Simplification and Coordinate Definition

To represent the human-platform system in a tractable form, the dynamics are approximated by a cart-and-inverted-pendulum model subjected to external push forces acting on the cart. In this context, these forces correspond to the horizontal reactions generated by the board's suspension chains.

To make dynamic analysis tractable, complex geometry-dependent chain forces are replaced by a linear Hookean approximation. The equivalent spring constant (k) captures the core behaviour while simplifying the governing equations.

Empirical or geometric calculations provide the horizontal force $F(x)$ produced by the loaded board (total mass $(m + M)$ at a given lateral displacement $\pm x$. In static conditions the chain-derived horizontal force

$$F_{chains}\ (x) \tag{27}$$

rises from 0 to some value F^* over a displacement Δx. This relation can be approximated by Hooke's law

$$F \approx\ k\,x \tag{28}$$

$$k \approx \frac{F^*}{\Delta x} \tag{29}$$

becomes an equivalent spring constant. The real angle dependencies $\alpha_i(x)$ and $\beta_i(x)$ are therefore replaced by a simpler spring model

$$F_{springs}\ (x) \approx\ k\,x \tag{30}$$

with k (or k_{left}, k_{right} when asymmetry is present) chosen to replicate the actual horizontal action of the chains. In practice, the total horizontal force equals the sum of two springs: one representing the left-side increase $F_{left}(x)$, the other the right-side increase $F_{right}(x)$.

After performing the static evaluation at a loaded board position, we obtain a two-spring substitute system that mechanically reproduces the chain-generated horizontal force growth with displacement $\pm x$.

Consequently, a two-degree-of-freedom dynamic model (cart + pendulum with side springs) can replace explicit tracking of each chain angle $\alpha_i(x)$, $\beta_i(x)$. In other words, the displacement-induced variation in horizontal force is mapped onto the corresponding spring reaction:

$$\begin{cases} x \leftrightarrow\ \text{cart translation} \\ \theta \leftrightarrow\ \text{inverted pendum angle} \\ F_{springs}(x) \leftrightarrow \text{chain horizontal} F_{chain}(x) \end{cases} \tag{31}$$

The approach removes the need for continuous recalculation of $\alpha_i(x)$ and $\beta_i(x)$ and $\beta_i(x)$, yet preserves the key non-linearity: the farther the board moves, the larger the opposing spring force.

The resulting system comprises a cart of mass M (the sliding board) that moves horizontally between two side springs (k), and an inverted pendulum of mass m, length L, and angle θ mounted on the cart. The two external horizontal forces supplied by the springs emulate the real suspension chains, whose projected angles generate unequal horizontal reactions. Thus, the actual chain geometry (α, β) is replaced by the displacement-dependent spring forces $F_{springs}(x)$. If the geometry is asymmetric, the spring constants differ on the left and right.

Because the two springs link horizontal board motion $\pm x$ to the pendulum angle θ, the model exhibits coupled non-linear dynamics. Two state variables are selected:

1. x – horizontal translation of the board (anterior–posterior axis),
2. θ – angle of the inverted pendulum relative to the vertical ($\theta = 0$ denotes upright).

This simplified framework mimics human balance on a moving platform: $\theta \approx 0$ signifies upright posture, while $\pm x$ represents board deviation from center. No damping is included $c\_demping = 0$, so oscillations persist indefinitely unless limited by boundary constraints (e.g., maximum board travel or angular limits).

With this two-DOF model (**Figure 26**) we can test how different horizontal-force configurations (spring constants, pre-loads, asymmetries) influence the likelihood of pendulum destabilization, as reflected in changes in oscillation amplitude and pattern.

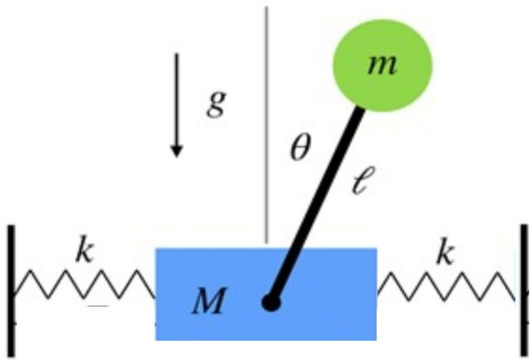

Figure 26. Depicts the two-degree-of-freedom system: a cart of mass M translates horizontally against two side springs (k), while an inverted pendulum of mass m and length ℓ pivots at angle θ. Gravity g acts downward; the springs provide the horizontal restoring force proportional to cart displacement, yielding coupled motion in x and θ

3.2.1.2. Derivation of Board – Pendulum Dynamic Equations

Derivation of the Board Translation Equation

In this subsection the horizontal (x) and angular (θ) equations of motion are derived using Newtonian mechanics; below we focus on the horizontal board equation.

System description

- Cart (sliding board) mass: M
- Inverted pendulum (human surrogate) mass: m, length L, angle θ

Only anterior–posterior translation is allowed; the coordinate is x. Horizontal forces consist of

- the external horizontal restoring force from the side springs, $F_{springs}(x)$ and
- inertial + gravitational components generated by the pendulum.

Effective mass term

Because part of the pendulum mass projects horizontally, the effective inertia is

$$(M + m\,sin^2\theta)\,\ddot{x} \tag{32}$$

where $\sin^2(\theta)$ is the projection factor.

Additional horizontal terms

- Centrifugal (inertial) term: $mL\left(\dot{\theta}\right)^2 sin(\theta)$
- Gravity projection: $m\,g\,sin\theta\,cos\theta$

Horizontal force balance

Applying Newton's second law gives

$$(M + m\,sin^2\theta)\,\ddot{x} + mL\left(\dot{\theta}\right)^2 sin(\theta) - mgsin\theta cos\theta = F_{springs}(x) \tag{33}$$

Term interpretation

The physical interpretation of each term appearing in Equation (33) is summarised in **Table 12**.

Table 12. Interpretation of individual terms in the board-translation equation (33).

Term	**Physical meaning**
$(M + m\,sin^2\theta)\,\ddot{x}$	Effective horizontal inertia of cart + pendulum
$mL\left(\dot{\theta}\right)^2 sin(\theta)$	Inertial coupling from pendulum angular velocity
$m\,g\,sin\theta\,cos\theta$	Horizontal component of pendulum weight
$F_{springs}(x)$	Restoring force produced by the side springs

Equation 33 shows that board dynamics are not a simple $M\ddot{x}$ term: non-linear θ – dependent components strongly couple translational and angular motion. Even small changes in θ can significantly affect horizontal displacement and, reciprocally, the pendulum's subsequent behavior.

Derivation of the Pendulum Motion Equation. To obtain the angular equation of motion for the inverted pendulum (mass $\boldsymbol{m}$, length $\boldsymbol{L}$, angle $\boldsymbol{\theta}$), Newton's second law for rotation – or, equivalently, the Lagrange formalism – is applied. A key feature of the system is that the pendulum experiences not only gravity but also the horizontal acceleration $\ddot{x}$ of the moving board.

General coordinate. θ is measured about the pivot fixed to the board; $\theta = 0$ corresponds to the perfectly upright position. $\theta > 0$ – clockwise angle, $\theta < 0$ – counter-clockwise angle.

Two principal torques acting about the pivot:

1. Gravitational torque: $mgL\sin(\theta)$ tends to restore (or further overturn) the pendulum.
2. Inertial torque from board acceleration: $-mL\cos(\theta)\,\ddot{x}$. The horizontal acceleration of the support produces an inertial force on the pendulum mass; applied at a distance L above the pivot, it becomes a moment of magnitude opposing the direction of $\ddot{x}$.

Angular equation of motion. Dividing the net torque by the pendulum's moment of inertia mL^2 yields

$$\ddot{\theta} = \frac{(g\sin(\theta) - \cos(\theta)\,\ddot{x})}{L} \tag{34}$$

Interpretation of the terms. The physical meaning of the terms in Equation (34) can be explained as follows. The term $g\sin(\theta)$ represents the gravitational component acting on the pendulum. Depending on the chosen sign convention, this component may be interpreted as a restoring or overturning effect. The term $\cos(\theta)\ddot{x}$ represents the inertial contribution caused by the horizontal acceleration of the board.

If the board suddenly accelerates to the right ($\ddot{x} > 0$), the resulting inertial effect acts to the left on the pendulum mass. This creates a moment opposite to the positive x-direction. Since the effective lever arm is $L\cos(\theta)$, the influence of the board acceleration depends on the current pendulum angle.

Non-linearity. Both $sin\theta$ and $cos\theta$ are non-linear, and $\ddot{x}$ itself depends on θ through Equation (33). Consequently, Equation (34) is non-linear, and the coupled system can exhibit complex, even irregular, oscillations in response to modest initial disturbances.

Equation (34) makes clear that temporal changes in θ respond directly to the board's horizontal motion: the gravitational term ($g\sin(\theta)$) drives the pendulum toward upright, whereas the inertial term ($-\cos(\theta)\,\ddot{x}$) can either stabilise or destabilise the pendulum, depending on the sign and magnitude of $\ddot{x}$ relative to the current pendulum angle.

Coupling of the Equations. The horizontal-translation equation (33) and the angular-rotation equation (34) form a coupled, non-linear system; the accelerations $\ddot{x}$ and $\ddot{\theta}$ depend on each other through the trigonometric factors $\sin\theta$, $sin^2\theta$, $cos\theta$, $(\dot{\theta})^2$. Because of these couplings no classical closed-form solution exists; numerical integration (e.g., Euler or Runge–Kutta schemes) is therefore required. At every time-step the current value of θ must be used to evaluate the trigonometric terms, after which both equations are solved simultaneously to update the state trajectory.

Mutual influence of the coordinates

- The board experiences a variable effective mass $(M + m\,sin^2\theta)$ and additional inertial/gravitational terms $mL\left(\dot{\theta}\right)^2 sin(\theta)$ and $m\; g\; sin\theta\; cos\theta$
- The pendulum continuously senses the board acceleration $\ddot{x}$, which can destabilise (or stabilise) the pendulum depending on the sign of θ and $cos\theta$

This bidirectional interaction means that even a small initial disturbance can generate large-amplitude oscillations, especially in the absence of damping.

Algebraic substitution. Starting from equation (33) solve for $\ddot{x}$:

$$\ddot{x} = \frac{F_{springs}(x) + m\; g\; sin\theta\; cos\theta - mL\left(\dot{\theta}\right)^2 sin(\theta)}{M + m\,sin^2\theta} \tag{35}$$

Insert equation (35) into equation (34):

$$\ddot{\theta} = \frac{g\sin(\theta) - \cos(\theta)\left[\dfrac{F_{springs}(x) + m\; g\; sin\theta\; cos\theta - mL\left(\dot{\theta}\right)^2 sin(\theta)}{M + m\,sin^2\theta}\right]}{L} \tag{36}$$

Equations (35) and (36) constitute the two-degree-of-freedom non-linear model to be integrated numerically:

$$\begin{cases} \ddot{x} = \dfrac{F_{springs}(x) + m\; g\; sin\theta\; cos\theta - mL\left(\dot{\theta}\right)^2 sin(\theta)}{M + m\,sin^2\theta} \\ \ddot{\theta} = \dfrac{(g\sin(\theta) - \cos(\theta)\,\ddot{x})}{L} \end{cases} \tag{37}$$

Solving system Equation (37) with a time-integration scheme provides the accelerations $\ddot{x}\,(t)$ and $\ddot{\theta}\,(t)$; double integration then yields the complete time histories $x\,(t)$ and $\theta\,(t)$, revealing the full non-linear dynamics of the board–pendulum pair.

The computational flow just described is summarized schematically in **Figure 27**, which shows how the current state is propagated through spring-force evaluation, acceleration computation, numerical integration (RK4), and boundary checking.

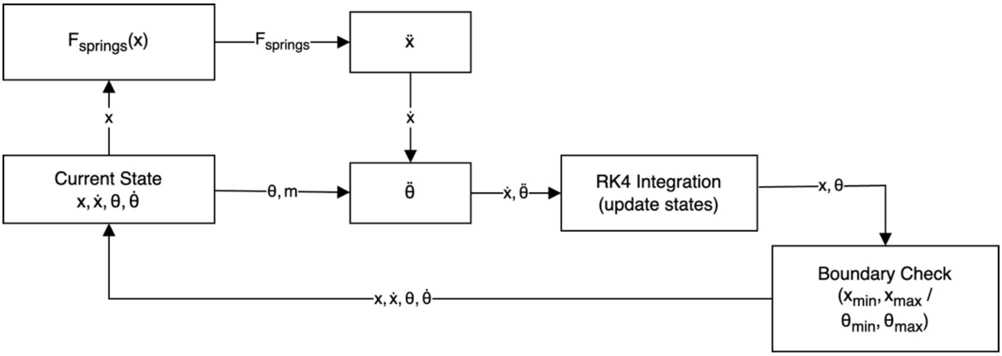

Figure 27. Dynamic block diagram of the coupled cart–pendulum simulation. Each block denotes a fundamental computational element – from the current state variables x, $\dot{x}$, θ, $\dot{\theta}$ through spring-force calculation $F_{springs}$ and acceleration derivation $\ddot{x}$, $\ddot{\theta}$, to RK4 integration and boundary checks. Arrows indicate the direction of data flow, clarifying how state variables are updated and how boundary conditions are enforced at every time-step

3.2.1.3. Initial and Boundary Conditions

The idealized assumptions used in the numerical simulation are summarized in **Table 13.**

Table 13. Initial and boundary conditions imposed on the cart–pendulum simulation

Condition	Formal statement	Purpose / comment
No damping	$c\_demping = 0$	Eliminates energy dissipation so that pure, undamped oscillations can be studied
Pendulum-angle limit	$\lvert\theta(t)\rvert \leq 10°$, $\dot{\theta}(\,t_{hit}^{+}) = -\dot{\theta}(\,t_{hit}^{-})$	When the angle reaches 10°, the angular velocity is instantaneously reversed ("boom" reflection)
Board-translation limit	$\lvert x(t)\rvert \leq\ 0.1\,m,$ $\dot{x}\big(\,t_{edge}^{+}\big) = -\dot{x}\big(\,t_{edge}^{-}\big)$	When the board reaches ±0.10 m, its horizontal velocity is instantaneously reversed ("boom" reflection)
Initial state (board)	$x(0) = 0, \dot{x}(0) = 0$	Board starts from the centered neutral position with zero velocity
Horizontal motion only	$y \equiv const, \dot{y}(t) = 0$	Vertical translation and any rotations about other axes are neglected.
Initial state (pendulum)	$\theta(0) = 1°, \dot{\theta}(0) = 0$	A small initial angle is introduced without angular momentum
Symmetric spring preload	$F_{left(0)} + F_{right(0)} = 0$ when $x = 0$	The horizontal spring forces cancel in the neutral position; for $x \neq 0$ they grow or diminish according to their individual stiffnesses k and pre-loads $\pm \mathrm{F}_0$
Vertical moments ignored		Any pitching moment induced by the pendulum in the vertical plane is omitted

These constraints define the initial board and pendulum states, cap the admissible amplitudes, and allow undamped oscillations. The "boom" reflection guarantees that neither θ nor x exceeds its respective limit, yet the system continues to oscillate, enabling the analysis of how often and under what conditions the pendulum and board approach the in boundaries.

3.2.1.4. Modelling Instability Levels with Spring Parameters

Four parameters define the horizontal spring forces so that the model reproduces different suspension behaviours.

The numerical values assigned to L_0, R_0, Fleft_at_0.1, Fright_at_0.1 for each IL are listed in **Table 14** .

Table 14. Spring-force parameters (L_0, R_0, Fleft_at_0.1, Fright_at_0.1) defining the eight simulated ILs

Parameter	Definition	Physical meaning in the spring analogue
L_0	Left-side preload force at $x = 0$	Baseline horizontal force (or projection) exerted by the left spring/chain when the board is in the neutral position.
R_0	Right-side preload force at $x = 0$	Baseline horizontal force exerted by the right spring/chain at $x = 0$
Fleft_at_0.1	Left-side horizontal force at $x = +0.1\ m$	Indicates how much the left-side force has grown or decreased after a 0.10 m rightward displacement.
Fright_at_0.1	Right-side horizontal force at $x = +0.1\ m$	Same for the right side.

Example: if $L_0 = -75$ N and $\mathrm{Fleft}_{\mathrm{a}}\mathrm{t}_{0}1 = -125\mathrm{N}$, the left-side force has increased by 50 N when the board is displaced 0.10 m to the right.

By adjusting these four values, the horizontal-force scenario can emulate several ILs, from completely unconstrained (“Free”) through symmetric or asymmetric spring pairs to a very stiff (“Rigid”) support.

The numerical spring-force presets used for each IL are summarized in **Table 15**.

Table 15. Parameter presets defining the eight simulated ILs

	Free	Rigid	1 IL∠	2 IL∠	3 IL∠	1 IL⦀	2 IL⦀	3 IL⦀
L_0	0	0	-189	-138	-74.1	0	0	0
R_0	0	0	189	138	74.1	0	0	0
Fleft_at_01	0	5000	-20	-64	-38	327	224	115
Fright_at_01	0	5000	-2898	-501	-203	327	224	115

Note: Symbols and abbreviations. ∠ = angled suspension; ⦀ = vertical suspension. IL1–IL3 refer to the nominal model suspension lengths used in Chapter 3 (0.18 m, 0.24 m, 0.43 m). Free denotes a fully unconstrained environment with no horizontal resistance; Rigid denotes an immovable support whose stiffness is effectively infinite.

These parameter sets capture how chain geometry alters horizontal force as the board (BOS) translates. They are then used to examine how much corrective effort is required to keep the COM aligned with the BOS under each IL.

3.2.2. Baseline Simulation Setup

Neutral position with no horizontal displacement or velocity: $x(0) = 0, \dot{x}(0) = 0$.

The inverted pendulum is released from a forward angle of $\theta(0) = -20°$ (negative sign indicates the chosen direction); it has no initial angular velocity: $\dot{\theta}(0) = 0$.

The cart–pendulum system starts from rest, but any preload defined by the spring parameters $L_0,\ R_0$ is already present, establishing the initial horizontal tension in the support chains.

3.2.2.1. Simulation Protocol and Performance Metric

For each instability IL, determine the minimum initial centripetal acceleration $a_{c0,min}$, that allows the pendulum, released from a hazardous forward angle of $\theta = -20°$, to regain the upright position $\theta = 0°$ before the board reaches the horizontal-displacement limit $x\ = +10$ m.

This mimics a real-world slip in which a person must generate sufficient corrective muscle impulse to recover balance before the support surface moves too far.

The resulting $a_{c0,min}$ represents the minimal corrective reserve required to recover from the critical $-20°$ angle.

Because the entire protocol is executed under every IL (**Table 15**), the set of $a_{c0,min}$values provide a direct, quantitative comparison of how mechanical instability alters the corrective effort needed to prevent a fall.

3.2.2.2. Numerical procedure

1. **Apply trial acceleration.** At $t\ = 0$, the model applies a candidate centripetal acceleration toward upright and integrates Equation (37) with a fixed-step RK-4 scheme.
2. **Failure test condition 1** – worsening pendulum angle. If at any time
$$\theta(\mathrm{t}) < \ -20°$$
the angle is increasing; the run terminates and is marked unsuccessful.
3. **Failure test condition 2** – board runaway. If the board displacement reaches
$$x(\mathrm{t}) \geq 0$$
Before the pendulum angle crosses zero, the board has left the BOS; the run is unsuccessful.
4. **Success test.** A run is successful when the first zero-crossing
$$\theta(t_{cross}) = \ 0°, \theta(\mathrm{t}) < 0 \text{ for } t < t_{cross}$$
occurs with $x(t_{cross}) < \ 0.1$ m. At that instant the state vector $\{x, \dot{x}, \dot{\theta},\ t_{cross}\}$ is recorded.

Search for $a_{c0,min}$ A bisection or grid search iteratively reduces a_{c0} until it meets the success criterion.

3.2.2.3. Python script for the coupled cart–pendulum simulation

The full Python script used for every dynamic simulation is reproduced verbatim in Appendix B. **Table 16** summarizes its key elements so that the reader can understand the workflow without inspecting each line of source.

Figure 28 shows a frame from the real-time visualisation generated by the script. This animation makes it easy to verify qualitative behavior (e.g., board reversal under vertical suspension) before exporting the quantitative results used in **Table 17, Figure 29**, and **Figure 30**.

The Python script serves three purposes:

1. Verification. By reproducing the analytically derived trajectories, the script provides an independent check on Equations (35–37).
2. Result generation. All numerical values reported in **Table 17** and **Figure 29**, and **Figure 30** were obtained directly from these simulations.
3. Research platform. Because the code is annotated and modular, it can readily be adapted. For example, to investigate alternative control algorithms, introduce damping, or replace the single-segment pendulum with a multi-segment model.

Table 16. Key features of the Python cart–pendulum simulation script

Item	**Description**
Language & libraries	Python 3.10; core packages – NumPy, Math, Pandas, Matplotlib (static plots + HTML5 animation) and the standard-library CSV
Model equations	Implements Equations (14–16); helper routine derivatives returns $(\dot{x}, \dot{\theta}, \ddot{x}, \ddot{\theta})$.
Integrator	Classical fourth-order Runge–Kutta (rk4_step) with fixed time-step dt = 0.01 s (default)
Spring calibration	Reads L_0, R_0, $\mathrm{Fleft}_{\mathrm{at}_0}$, $\mathrm{Fright}_{\mathrm{at}_0 1}$, from **Table 15** and converts them to linear spring constants k_{left}, k_{right}
Initial conditions	Set through header variables (e.g., initial_centrip_acc, theta, x, x_dot). If initial_centrip_acc > 0, the script computes the matching angular velocity
Mechanical limits	Rail end-stops (x_min, x_max) and angle bounds (theta_min, theta_max) enforce the same "boom" reflection logic used in the analytical model
Outputs	(1) Real-time animation of board, springs and pendulum; (2) CSV log (path set by csv_path) containing time, kinematics, spring forces, and diagnostic energy terms at every step
Re-use	Self-contained; after editing the header block for a desired IL the script runs in any standard Python or Jupyter environment.

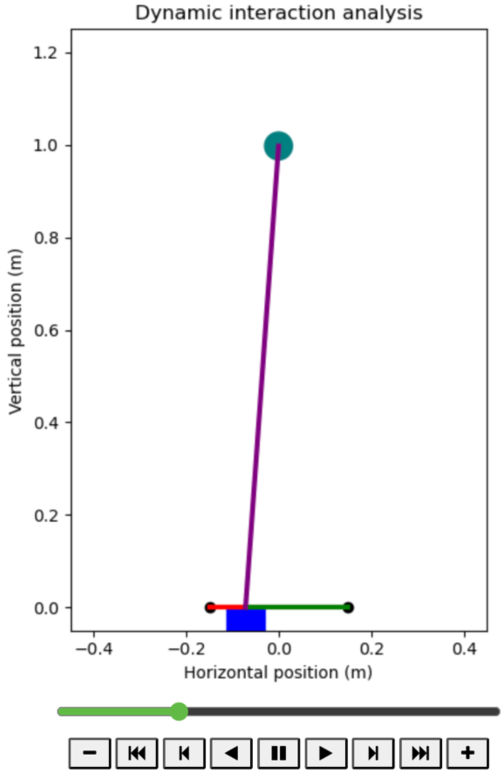

Figure 28. Representative frame from the interactive animation generated by the cart–pendulum Python script. The blue rectangle depicts the translating board, red and green lines depict the left- and right-side springs, and the purple rod with teal bob represent the inverted pendulum. The slider and playback buttons allowing to pause, step, or scrub through the simulation in real time

The complete listing in Appendix A may be copied into any standard Python Jupiter environment, allowing other researchers to replicate the present findings or extend the model to address new questions.

3.2.3. Results

Table 17 summarizes the outcomes for each IL. For each IL it lists:

- $a_{c0,minimal}$ – the minimal centripetal acceleration that fulfils the recovery criterion,
- $t_{\theta=0}$ – the time elapsed until the first zero-crossing of the angle
- $x\ (t_{\theta=0})$ – board position at that instant,
- $\dot{x}\ (t_{\theta=0})$ – board velocity, and
- $\dot{\theta}(t_{\theta=0})$ – pendulum angular velocity.

Figure 29 and **Figure 30** present the same data from two perspectives: **Figure 29** compares the two suspension geometries; **Figure 30** compares the three ILs within each geometry.

Table 17. Minimal corrective acceleration and kinematic variables at first upright crossing for each IL

	Free	**Rigid**	**1 IL∠**	**2 IL∠**	**3 IL∠**	**1 IL‖**	**2 IL‖**	**3 IL‖**
$a_{c0,minimal}$	**6.8**	**1.5**	**9.6**	**8.5**	**7.8**	**1.6**	**1.8**	**4.5**
$t_{\theta=0}$ (s)	0.19	0.47	0.13	0.16	0.17	0.49	0.34	0.24
$x\ (t_{\theta=0})$ (m)	0.09	0.00	0.03	0.08	0.09	0.01	-0.05	0.08
$\dot{x}\ (t_{\theta=0})$ (m s^{-1})	0.88	0.00	1.38	2.10	1.56	-1.16	-0.89	-0.76
$\dot{\theta}(t_{\theta=0})$ (rad s^{-1})	1.46	0.78	1.52	0.59	1.00	1.66	1.51	2.51

Note: Abbreviations: ∠ – angled suspension, ‖ – vertical suspension; IL1/IL2/IL3 correspond to the nominal model chain lengths used in this chapter (≈0.18 m, 0.24 m, 0.43 m). Free = no horizontal resistance, Rigid = effectively infinite stiffness.

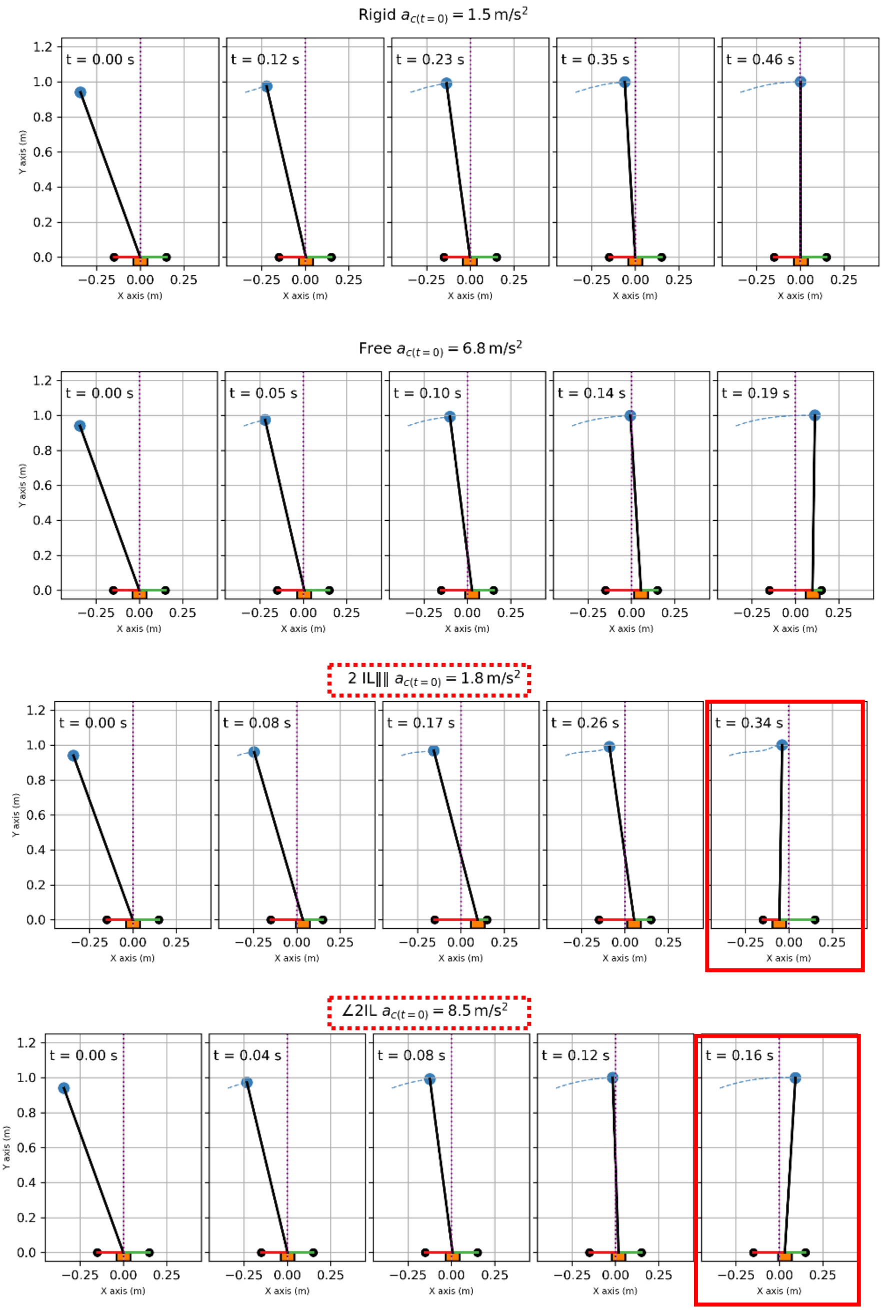

Figure 29. The effect of suspension geometry on recovery. Vertical suspension requires a smaller initial acceleration but follows a different recovery pattern: the board first moves away from center and returns only after θ approaches 0°, whereas in the angled case a larger impulse is needed and θ must “chase” a board that never comes back toward center

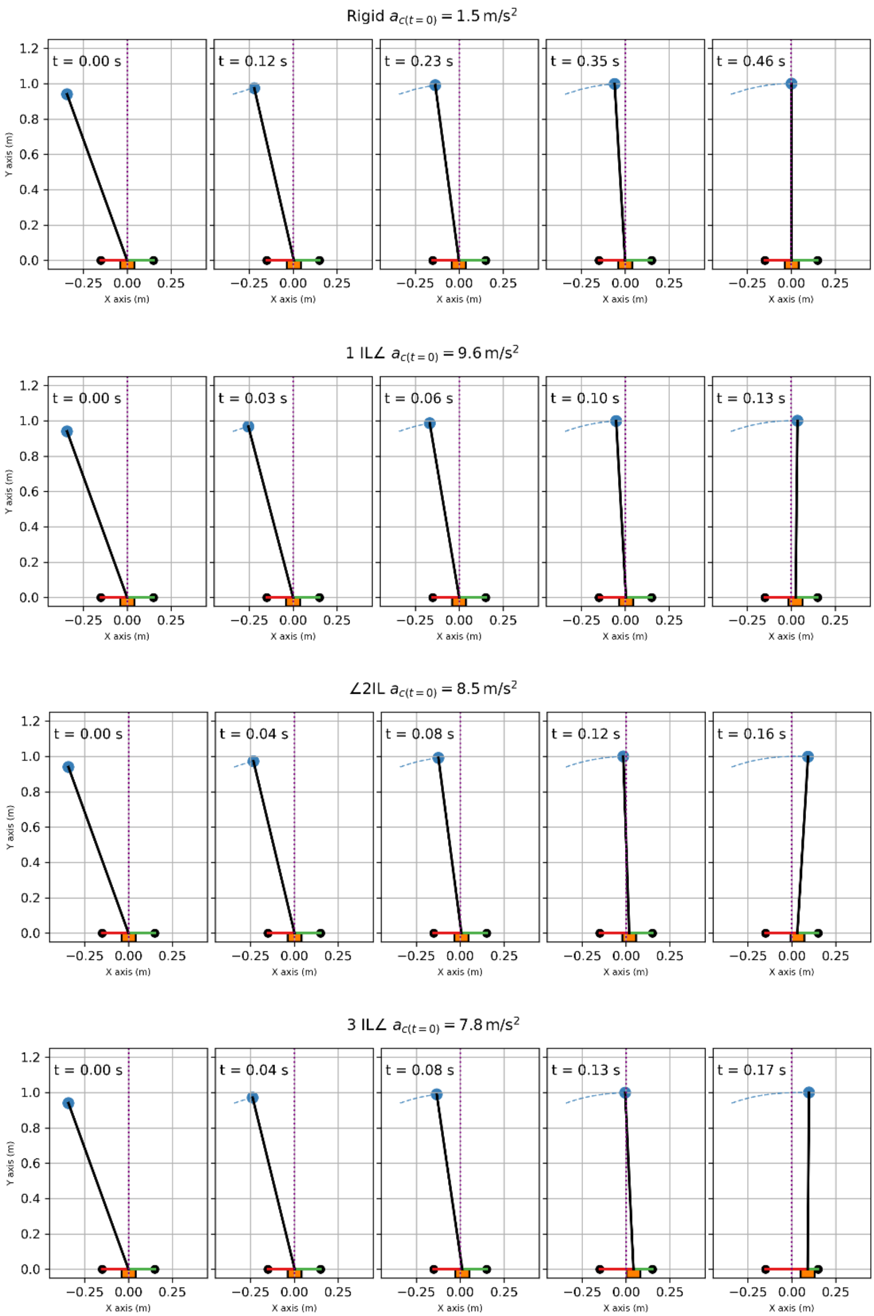

Figure 30. Effect of instability level on recovery. Higher instability (longer chains) reduces the necessary initial acceleration but lengthens the recovery time and yields a larger off-center board position at the upright crossing

The results in **Table 10**, **Figure 29**, and **Figure 30** reveal how the required corrective impulse and the ensuing kinematics depend on suspension geometry and mechanical IL.

3.2.3.1. Influence of suspension geometry

Angled suspension (∠) demands the largest initial centripetal accelerations (7.8–9.6 m s^{-2}) and produces rapid board drift (up to ≈ 0.09 m from center, 1.4–2.1 m s^{-1}). The pendulum therefore must deliver a short, high-magnitude impulse while continuously “chasing” an ever-departing base of support.

Vertical suspension (‖), by contrast, distributes horizontal forces symmetrically. After the initial impulse the board often reverses toward the body, so the BOS approaches the COM instead of the COM chasing the BOS. This raises the pendulum’s angular velocity (up to ≈ 2.5 rad s^{-1} for IL3‖) but shortens the final phase of correction.

Rigid support represents the lower bound of corrective demand (1.5 m s^{-2}), whereas the Free surface lies between the vertical and angled cases, with moderate impulse (6.8 m s^{-2}) and moderate board speed (≈ 0.9 m s^{-1}).

3.2.3.2. Influence of instability level

For either suspension geometry, increasing the chain length, from IL1 to IL3, diminishes the effective restoring force, which in turn lowers the minimal corrective acceleration $a_{c0,minimal}$ needed for recovery. This benefit is displacement by two drawbacks: the correction takes longer, and the board reaches a larger off-center displacement at the moment of success. Should the perturbation persist, this greater excursion could endanger balance despite the lower initial impulse.

3.2.3.3. Practical relevance

Angled suspension combines strong force asymmetry with high board velocities, making balance recovery more difficult. Vertical suspension benefits from the board’s natural return toward center, easing the impulse requirement despite slightly higher angular speeds. A free surface spreads inertia between body and board, so a moderate impulse is sufficient.

In sum, suspension geometry and IL jointly determine the magnitude and timing of the corrective action needed to avert a fall, informing the design of balance-training platforms and the selection of difficulty settings in clinical or athletic contexts.

3.3. Conclusions

1. Static analysis showed that suspension geometry shapes the horizontal force field acting on the board. Over the analysed displacement range, restoring demand increased with displacement and was highest for the shortest chains (0.18 m).
2. Vertical suspension maintained near-symmetric chain tensions and horizontal components, producing balanced restoring responses on both sides.
3. Angled suspension introduced preload and pronounced left-right asymmetry during board translation; shorter chains again produced the stiffest response.
4. The static force-displacement behaviour was translated into effective stiffness parameters for the dynamic model.
5. Dynamic analysis extended these insights to a two-degree-of-freedom cart-pendulum system with nonlinear coupling between board acceleration and pendulum motion.
6. Numerical simulations identified the minimal corrective centripetal acceleration $a_{c0,minimal}$ required to recover from an initial pendulum angle of $-20°$ before the board exceeded ±0.10 m.
7. Geometry effects were consistent across domains: angled suspension produced the highest corrective demand, while rigid support formed the lower bound; free surface and vertical suspension lay between these extremes.
8. Instability level (chain length) acted as a stiffness-like tuning parameter; however, its impact on $a_{c0,minimal}$ was geometry-dependent, indicating that recovery demand is governed by coupled kinematics rather than horizontal stiffness alone.

4. BIOMECHANICAL ANALYSIS

Previous mechanical characterisation showed that link length and hinge geometry define three discrete instability levels (IL1–IL3).

Unlike standing on solid ground, where the base of support (BOS) remains stationary, any tilt of this platform displaces the BOS. Thus, the same forward center of mass (COM) displacement can produce different COM–BOS configurations across instability levels.

This analysis quantified the relationship between p-COM displacement and BOS displacement across IL1–IL3 during voluntary forward leaning.

4.1. **Methodology**

A single-participant experiment was conducted at IL1, IL2, and IL3 to measure forward COM displacement, corresponding platform (BOS) displacement, and the point at which the platform board stopped moving.

One healthy male volunteer (author; height = 183 cm, mass = 85 kg) participated. According to anthropometric tables, his standing COM is located ≈ 55 % of body height above the support surface; this anthropometric COM mark is denoted p-COM.

Platform instability was adjusted mechanically to IL1, IL2, and IL3 by changing the supportlink length (details in Section 4.1). A Qualisys Mocap® system (Qualisys AB, Göteborg, Sweden) recorded three retroreflective markers (COM, platform board center, ground reference) at 100 Hz.

The participant stood barefoot on the platform with feet hip-width apart, knees and hips extended, arms akimbo. At the start of each trial, the COM, board and ground markers were aligned vertically. Only ankle motion was permitted; heel lift, hip/knee flexion or arm movement were not allowed. Two familiarisation trials preceded data capture. During the recorded trial, the participant performed three slow forward–backward sways, self-terminating each sway when further flexion would violate the posture constraints (classical limit-of-stability paradigm performed on an unstable surface; see **Figure 31**).

For each instability level, forward BOS displacement was measured when the platform board reached its forward stop (terminal inclination). The corresponding COM position marked the transition from the coupled phase, in which BOS and COM moved together, to the uncoupled phase, in which the BOS remained fixed while the COM continued forward. Total forward COM displacement (from start to maximal lean) was divided into coupled- and uncoupled-phase components, and a COM–BOS linkage coefficient was computed as the ratio of COM displacement to BOS displacement during the coupled phase.

1. BOS displacement (cm): forward BOS movement at the end of the coupled phase.
2. Total p-COM displacement (cm): total forward displacement of the COM's projection from start to peak lean.
3. p-COM displacement (coupled phase, cm): forward COM travel from start until the BOS stops moving.

4. p-COM displacement (uncoupled phase, cm): remaining forward COM travel after the BOS has stopped.

5. p-COM-per-BOS coefficient (–): ratio of COM displacement to BOS displacement during the coupled phase.

Figure 31. Experimental task. Start: vertical alignment of p-COM (yellow), BOS center – the platform board center (blue), and a fixed ground reference (red). The participant performs a controlled forward lean using ankle motion only. Two phases are shown: coupled – p-COM and BOS move together while the board tilts; uncoupled – once the board stops tilting (BOS no longer displaces), p-COM continues forward while BOS remains fixed. Left to right: initial alignment → coupled phase → uncoupled phase. The sequence illustrates the single permitted degree of freedom at the ankle

4.2. **Results**

The relationship between forward COM displacement and platform (BOS) displacement was quantified at each instability level (IL1–IL3) (Figure 32). Key outcome metrics for a representative trial at each IL are summarised in **Table 18**.

In each trial, two distinct movement phases were observed: (A) coupled, in which the COM and platform moved together with forward BOS displacement, and (B) uncoupled, in which the COM continued to move forward after the platform reached its forward stop. The instant when the board stopped tilting (t*) marked the transition between phases.

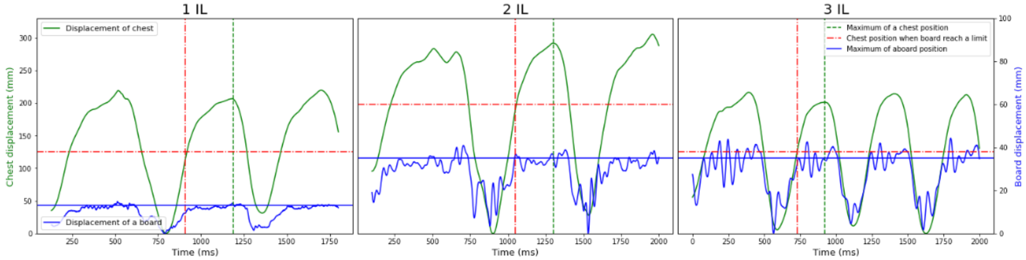

Figure 32 Coupling of p-COM and BOS displacement across instability levels (left → right: IL1, IL2, IL3). Green: p-COM displacement (projected COM surrogate; chest marker, left y-axis). Blue: BOS displacement (platform board centre, right y-axis). Time (ms), displacement (mm). The red vertical dashed line marks t*, the moment when the board reaches its forward travel limit and stops. Before t* both p-COM and BOS increase together (coupled phase); after t* BOS remains constant while p-COM continues to increase (uncoupled phase). The green vertical dashed line marks the time of peak p-COM. Horizontal reference lines indicate the BOS maximum and the p-COM values at t* and at peak. With increasing IL (IL1 → IL3), t* tends to occur earlier and a larger proportion of total p-COM occurs in the uncoupled phase

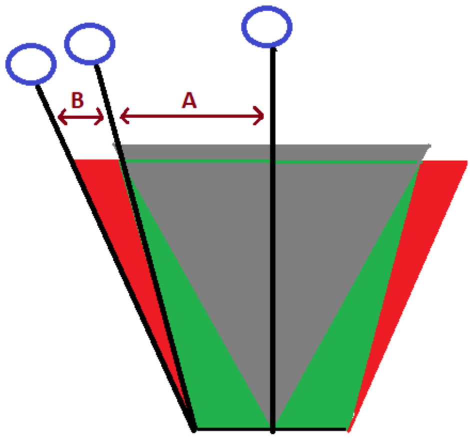

Figure 33. Phase segmentation. In the coupled phase, p-COM and BOS (platform board center) move together; once the platform stops (t*), the BOS remains fixed and p-COM continues forward. The vertical dashed line marks t* and the point at which BOS displacement is recorded, distinguishing the coupled- and uncoupled-phase p-COM components

4.2.1. Board response metrics

Forward BOS displacement increased with instability, from about 7.0 cm at IL1 to 15.5 cm at IL3, whereas total forward COM (p-COM) displacement remained in a similar range (approximately 16–19 cm) across all three conditions.

4.2.2. COM strategy across ILs

Although total COM displacement changed little with instability, its distribution between the two phases changed markedly. At IL1, about 78% of the forward COM motion occurred during the coupled phase, whereas at IL3 only about 56% occurred in the coupled phase, indicating that a smaller forward lean was needed for the platform to reach its stop at the highest instability level.

4.2.3. Mechanical gain

Mechanical coupling between COM and BOS also differed across instability levels. At IL1, the p-COM-per-BOS coefficient was approximately 2.0, indicating COM excursion about twice the BOS movement. By IL3, this coefficient dropped to roughly 0.6, indicating greater BOS movement for the same COM displacement. Thus, platform motion was amplified at higher ILs, and the same body sway caused a much larger BOS displacement at IL3 than at IL1.

Table 18 Key stability metrics at IL1–IL3 in the single-participant leaning trials

Metric	IL1	IL2	IL3
BOS displacement (cm)	7.0	12.5	15.5
Total p-COM displacement (cm)	18	19	16
p-COM displacement (coupled phase) (cm)	14	16	9
p-COM displacement (uncoupled phase) (cm)	4	3	7
p-COM-per-BOS coefficient (cm/cm)	2.00	1.28	0.58

4.3. **Single-participant demonstration**

As instability increased, the mechanical coupling between the p-COM and BOS was amplified, so the platform reached its movement limit with a smaller forward lean. At IL3, for example, the board stopped after only ~9 cm of p-COM movement (versus ~14 cm at IL1), so the uncoupled phase began earlier. Consequently, a larger portion of the lean occurred with the BOS fixed, increasing the p-COM–BOS mismatch (**Figure 34**).

In summary, increasing the instability level (IL) augments the BOS movement caused by a given COM excursion and triggers the uncoupled phase sooner, making balance maintenance more challenging and increasing corrective effort.

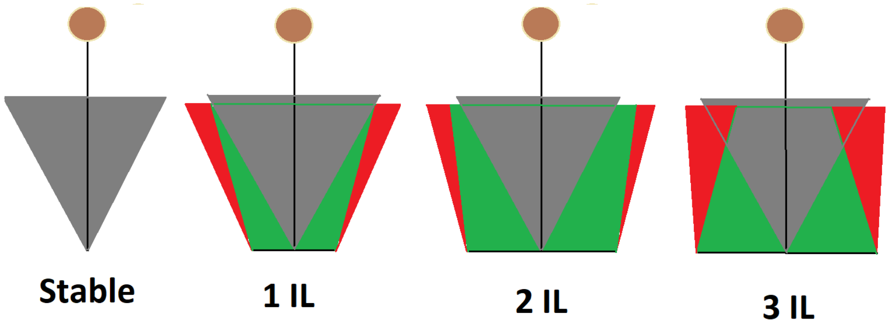

Figure 34. p-COM–BOS geometry across instability levels (Stable, IL1–IL3). Grey triangles = stable-ground p-COM sway envelope; green areas = p-COM travel while BOS moves with it (**coupled phase**); red areas = additional p-COM travel after the platform stops (**uncoupled phase**). Black outline = BOS; brown circle = p-COM. As IL increases (left → right), the uncoupled phase begins earlier and the uncoupled portion of p-COM grows, producing a marked anterior BOS displacement relative to p-COM at IL3

5. NEUROBIOMECHANICAL ANALYSIS

Reactive postural control (RPC) is the capacity to restore stability after an unexpected disturbance, and it is fundamental for safe mobility. Balance is preserved when the center of mass remains within the base of support through coordinated muscular actions shaped by gravity and inertia. This regulation depends on multisensory estimation: the central nervous system (CNS) integrates visual, vestibular, and proprioceptive signals to infer body state and issue corrective commands. Deficits in any part of this loop increase fall risk, especially in environments with reduced sensory reliability or mechanical instability (e.g., slippery or compliant surfaces).

5.1. Methodology

5.1.1. Participant Recruitment and Inclusion Criteria

Twenty-five healthy young adults (13 women, 12 men) were enrolled. A structured questionnaire and brief interview verified eligibility and safety before testing. Inclusion criteria were: (i) no recent trauma or surgery; (ii) no chronic dizziness or balance complaints; and (iii) self-reported good or excellent general health. Habitual physical activity was documented with a standardized questionnaire.

Prespecified exclusion criteria were diagnosed neurological, musculoskeletal, or vestibular disorders; injury or surgery likely to affect balance or postural control within the previous six months; current use of medications known to influence balance; or any condition judged by the investigators to make participation unsafe or unduly uncomfortable. Demographic descriptors and essential anthropometrics were recorded for later analyses and normalization.

All participants provided informed consent before taking part in the study, in accordance with the principles of the Declaration of Helsinki [109].

5.1.2. Baseline Participant Characterisation

5.1.2.1. Anthropometric Measurements

Anthropometric profiling described interparticipant morphology and enabled length-Normalized scoring of the baseline tests. Measurements were taken barefoot, in light clothing, by the same assessor using a calibrated stadiometer (0.1 cm resolution), a digital scale (0.1 kg), and a non-elastic anthropometric tape (0.1 cm). Each dimension was recorded three times and averaged; a fourth trial was taken if any pair differed by > 0.5 cm.

Height and body mass. Standing height was recorded with the head in the Frankfurt plane and heels together. Body mass was measured immediately afterward on level ground; BMI was computed for sample description.

Upper-limb length. Arm length was measured bilaterally from the lateral acromion to the distal end of the third metacarpal with the shoulder at ~90° flexion, elbow fully extended, and wrist neutral. This metric provided an optional normalizer for upper-body reach measures and was reported alongside raw values in the baseline description.

Lower-limb length. In accordance with the Y-Balance Test composite scoring convention, limb length was measured bilaterally in the supine position from the anterior superior iliac spine (ASIS) to the distal tip of the medial malleolus along the anterior aspect of the limb. The tape was aligned to the skin without slack or indentation. Lengths were recorded separately for each limb and used to normalise reach distances for the YBT Composite score.

All measurements followed a standard operating procedure, with landmarks palpated and marked before recording. If postural asymmetries impeded landmark alignment, measurements were repeated after repositioning to ensure neutral alignment.

5.1.2.2. Participant Normalized Mechanical Indices (RII and Damping Index)

To relate platform mechanics to each participant's body geometry, two dimensionless, participant-Normalized factors were computed: the Relative Instability Index (RII) and the damping index ψ_{IL} Both build on the bench-characterised behavior of the suspended platform at each instability level (IL) and on subject-specific anthropometrics, most importantly whole-body center of mass height h_{COM}.

Mass-Normalized horizontal stiffness. Static force–displacement tests yielded an experimental horizontal stiffness k_{exp} for each IL. Because k_{exp} scaled linearly with applied mass, we expressed stiffness in mass-Normalized form, $k_{exp} = K_{IL}\, m$ where K_{IL} $\mathrm{N \cdot m^{-1}\, kg^{-1}}$ is an instability level-specific geometric constant obtained from the bench tests (monotonically decreasing from IL1 to IL3).

Relative Instability Index (RII). RII compares platform resistance to the participant's gravitational restoring gradient about the ankle. Defining RII as the ratio of platform stiffness to this gradient gives a mass-independent, dimensionless index (Equation 38):

$$RII = \frac{K_{IL}\, h_{COM}}{g} = \frac{\left(a_{IL}\frac{g}{l_{IL}}\right) h_{COM}}{g} = a_{IL}\frac{h_{\mathrm{COM}}}{l_{IL}} \tag{38}$$

Higher RII denotes a relatively stiffer support for that person (i.e., an easier mechanical context), whereas lower RII denotes greater relative instability.

Damping index. Free-decay recordings after a small horizontal release provided the half-settling time $\Delta T_{1/2}$. For each IL, $\Delta T_{1/2}$ increased approximately linearly with added static mass; the damping index was defined as the slope (Equation 39):

$$\psi_{IL} = \frac{\Delta T_{1/2}}{\Delta m}\ [s\ kg^{-1}] \tag{39}$$

which compactly captures how quickly oscillations decay per unit mass at that IL. Larger ψ_{IL} indicates slower decay (more lightly damped behavior). For every participant and IL: (i) h_{COM} from anthropometrics; (ii) read $K_{IL}$and $\psi_{IL}$from the bench-characterisation library; (iii) evaluate RII. These factors were then used in downstream analyses linking mechanics to IL×SIS outcomes.

5.1.3. Baseline Balance Assessment

5.1.3.1. Functional Reach Test – Upper-Body Limit of Stability

To characterize upper-body limits of stability at baseline, the Functional Reach Test (FRT) was administered using the standard protocol for forward reach in standing [24]. A rigid measuring scale was mounted horizontally at each participant's acromion height. Participants stood side-on to the wall without contact, feet hip-width apart, knees comfortably extended, and the dominant arm at 90° shoulder flexion with the elbow extended and hand in a fist. The starting position was the horizontal projection of the third metacarpal head on the scale.

On the verbal cue "reach," participants leaned forward and reached as far as possible without stepping, moving the feet, lifting the heels, touching the wall, or grasping external support. After briefly holding the end position, they returned to the start. Three valid trials were performed with the dominant arm; invalid attempts (step, foot displacement, heel lift, loss of balance, or failure to return under control) were discarded and immediately repeated. Reach distance (cm) was the difference between end- and start-position readings, and the best of three valid trials was retained. Raw trial values were archived for quality control and sensitivity analyses.

This procedure yields a single task-level index of anterior stability margin dominated by trunk-and-shoulder control and was used as a clinical baseline for later interpretation of IL×SIS outcomes.

5.1.3.2. Y-Balance Test – Lower-Limb Dynamic Control

Dynamic postural control of the lower limbs was assessed with the Y Balance Test (YBT). Participants performed three recorded trials in each reach direction—anterior (ANT), posteromedial (PM), and posterolateral (PL)—while standing on the contralateral limb. Standardized instructions and a visual demonstration were provided before testing; direction order was kept constant within participants to minimize procedural variance.

For each trial, the participant maintained a single-leg stance while reaching with the free limb along the marked direction to the maximal controllable distance. Trials were invalid and repeated if there was loss of balance, stance-foot movement or heel lift, use of the reaching foot for weight support, or failure to return the reaching limb under control. The best of three valid trials per direction was retained. Direction-specific asymmetry was the absolute side-to-side difference in centimeters (e.g., |rightANT − leftANT|).

Reach distances were normalized to limb length. Limb length (LL) was measured in supine from the anterior superior iliac spine to the distal tip of the medial malleolus with a flexible tape, consistent with YBT standardization and the composite-score method [23]. The YBT Composite score for each limb was then calculated as (Equation 40):

$$Composite\ score = \frac{(ANT + PM\ +\ PL)}{(LL\ \times 3)} \times 100 \tag{40}$$

Together with upper-body measures reported elsewhere in this chapter, YBT provided an independent lower-limb index of dynamic balance capacity that is sensitive to side-to-side differences and limb-length normalization [20–23].

5.1.4. Experimental Balance Assessment Under IL×SIS Conditions

5.1.4.1. Mechanical Instability Levels (IL)

Mechanical instability was manipulated with a single-plane suspension platform (Abili Balance®, Ltd Abili, Kaunas, Lithuania). The suspended board is supported by an inward-angled four-chain geometry; increasing chain length reduces horizontal stiffness and makes the base more compliant, whereas shortening the chains increases stiffness and stability. Detailed derivations of platform mechanics (static stiffness K_{IL} and decay slope ψ_{IL}) and their mass-Normalized forms are presented in the Mechanical Analysis; likewise, human–platform coupling and the neuromechanical interpretation are treated in the Biomechanical Analysis. In this subsection we use a simplified instability notation: IL0 denotes quiet standing on a rigid floor, and IL1–IL3 denote progressively more unstable suspension settings (IL1→IL3: increasing chain length, decreasing horizontal stiffness, greater board sensitivity to body sway).

For each task, the platform was preset to the target IL and levelled. Participants stood bipedally with self-selected foot spacing kept constant across trials. No external perturbations were applied; instability arose solely from the passive mechanics of the suspended base.

5.1.4.2. Sensory Information Strategies (SIS)

Sensory conditions were adapted from the Modified Clinical Test of Sensory Integration and Balance (mCTSIB) [24]. Four sensory information strategies (SIS) were crossed with instability levels (IL; 0–3), yielding 16 task conditions. Participants stood barefoot or in thin non-slip socks; for proprioceptive degradation, a foam interface (Airex Balance Pad Cloud®, Airex AG, Sins, Switzerland) was placed under the feet.

5.1.4.3. Condition definitions (mCTSIB-derived SIS):

Basic (eyes open, firm contact) – Full visual, somatosensory, and vestibular input; reference condition.

Visual (eyes closed, firm contact) – Visual input removed; somatosensory and vestibular input available.

Proprioception (eyes open, foam under feet) – Plantar/ankle somatosensory input degraded by the compliant surface; visual and vestibular input available.

Vestibular (eyes closed, foam under feet) – Visual input removed and plantar/ankle somatosensory input degraded, leaving vestibular input as the most reliable source.

5.1.4.4. Postural Control Testing Procedure

Quiet-stance balance was assessed under the full IL×SIS matrix (**Figure 35**). For each condition, participants adopted a standardized stance: feet shoulder-width apart and parallel, knees comfortably extended, arms alongside the trunk. In vision-available SIS (Basic, Proprioception), gaze was fixed on a high-contrast rectangular target ~5 m ahead at eye level; in vision-occluded SIS (Visual, Vestibular), eyes were gently closed. Participants were instructed to minimize whole-body sway and avoid intentional board motions during 40 s of quiet standing.

Each participant completed 16 trials (**Table 19**). Order was fixed by instability blocks: IL0 → IL1 → IL2 → IL3. Within each IL, SIS were administered in the sequence Basic → Visual → Proprioception → Vestibular (four 40-s trials per block). A 5-min seated break separated the instability blocks; brief rests were provided within blocks as needed. Foot position was maintained and rechecked before each trial.

Table 19. Trial sequence across IL×SIS combinations. Cells contain the ordinal number (1–16) of each 40-s quiet-stance trial. Columns are instability blocks (0–IL3), rows are SIS administered in fixed order (Basic → Visual → Proprioception → Vestibular). A 5-min rest was provided between IL blocks

SIS \ IL	**IL 0**	**IL 1**	**IL 2**	**IL 3**
Basic	1	5	9	13
Visual	2	6	10	14
Proprioception	3	7	11	15
Vestibular	4	8	12	16

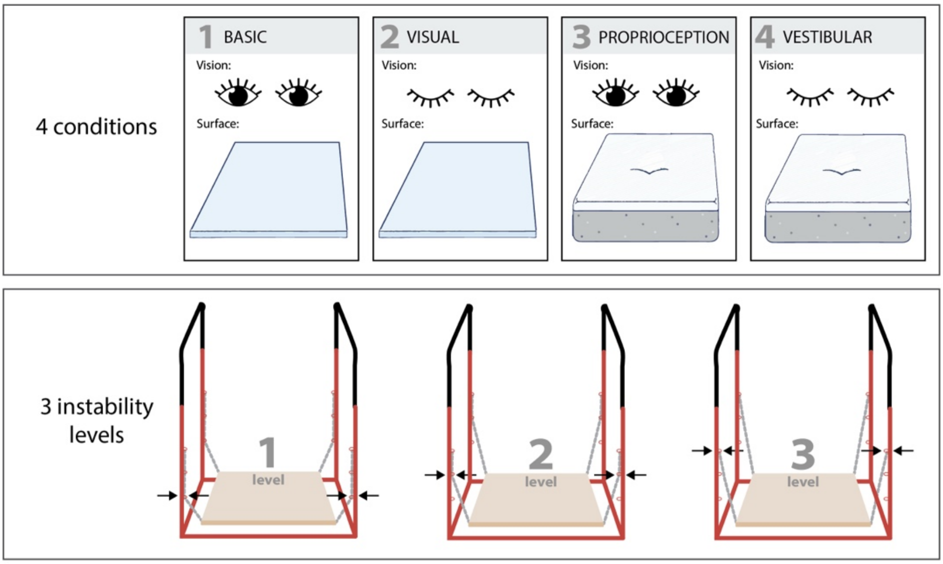

Figure 35. Testing matrix for IL×SIS conditions.
Schematic of the 4 SIS (upper panel) and 3 unstable ILs (lower panel). Icons denote sensory availability: open eye = vision available (Basic, Proprioception); closed eye = vision occluded (Visual, Vestibular). Surface icons: flat surface = firm support; wavy pad = foam to alter plantar/proprioceptive cues. The lower panel illustrates the three suspended platform settings used to create progressively higher mechanical instability; IL0 denotes firm ground (not pictured)

5.1.4.5. Motion Capture Setup

Three-dimensional kinematics were recorded with a motion capture (MoCap) system (Qualisys Mocap®, Qualisys AB, Göteborg, Sweden) sampling at 100 Hz. Multiple infrared cameras tracked retro-reflective markers affixed to standardized anatomical landmarks. Before each session, the volume was calibrated according to the manufacturer's procedure, wand-calibrated to establish the global laboratory frame, and verified for residual error within recommended tolerances. Global axes were anteroposterior (x), mediolateral (y), and vertical (z). A brief static trial was collected to confirm marker visibility and alignment.

Marker placement targeted six regions: head, chest, shoulder, knee, ankle, and the platform surface (**Figure 36**). This minimal set ensured robust visibility under IL×SIS while capturing segmental excursions relevant to postural adjustments. Analyses used reconstructed 3D marker coordinates in the laboratory frame; when required, displacements were expressed relative to the platform marker to separate body from base motion.

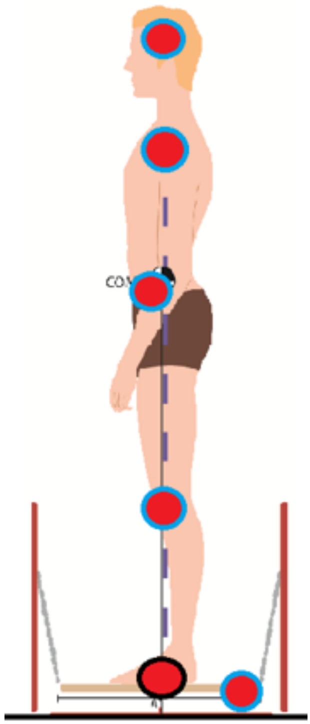

Figure 36. Marker set and global axes used for motion capture.
Schematic of the six-marker configuration (head, chest, shoulder, knee, ankle, platform). Blue rings indicate reflective markers; the dashed vertical line illustrates the laboratory z-axis. The platform marker enables expressing segment motion relative to the base when analyzing IL-induced board excursions

5.1.4.6. Balance Board Platform Setup

Center of pressure (COP) data were acquired with the Nintendo Wii Balance Board (WBB; Nintendo Co., Ltd., Kyoto, Japan), used here as a low-cost force platform to record vertical load distribution and derive COP trajectories. Only COP coordinates in the local board frame (x: mediolateral; y: anteroposterior) and their time series were analyzed; no diagnostic claims are made for the device. The WBB is widely used as an accessible surrogate for laboratory force plates, and here provided COP-based summary measures.

The board was positioned coaxially with the participant's stance and support surface. Taped markers reproduced a shoulder-width, parallel foot posture across trials. COP acquisition was synchronized with motion capture: a custom Python script initiated and terminated WBB logging in parallel with Qualisys acquisition using a shared time stamp and identical trial duration.

Before each session, the board was zeroed without load and checked with a brief quiet-standing calibration.

5.1.4.7. Participant-Rated Task Difficulty

Immediately after each IL×SIS condition, participants rated perceived task difficulty on a 10-point visual analogue scale (VAS). The horizontal scale was labelled 0–10 with integer tick marks; 0 denoted no effort/very easy and 10 maximal difficulty (unable to maintain balance without handrail contact). While still standing on the platform, participants marked a single integer (0–10) before receiving feedback and before the next trial. Previous task results were hidden. If a step or handrail contact occurred, the event was logged separately, but the participant still provided a VAS rating.

5.1.4.8. Post-Testing Expert-Rated Task Difficulty and Safety

To obtain an external criterion for task demand and document safety, all quiet-standing trials were evaluated post hoc from MoCap videos. The dataset comprised 400 recordings (25 participants × 16 IL×SIS conditions). Videos were exported, stripped of condition labels, and presented to the rater in automated random order so that IL, SIS, and participant identity were concealed.

A single trained reviewer scored each trial three times on a 0–100 visual analogue scale, where higher values indicated greater perceived instability/difficulty. The three scores were averaged to yield the expert-rated difficulty for that trial and used in subsequent analyses alongside the objective biomechanical metrics.

In parallel with the numeric score, the rater assigned a safety outcome to each video: (i) safe completion, (ii) instability without fall, or (iii) fall-like event. These labels were derived solely from video evidence and were blind to IL×SIS.

All ratings were performed within a purpose-built interface that randomized videos and recorded scores.

The study did not aim to validate a new subjective scale or assess inter-rater reliability; the goal was to obtain internally consistent, condition-blinded difficulty and safety indices for correlation with kinematic and COP-based measures. Strict blinding and a fixed rater minimized expectancy bias.

5.1.5. Data Acquisition and Collection

Data streams were captured from three sources and stored in native machine-readable formats:

Anthropometry and ratings. Height, mass, limb lengths, and sub-/suprasternal heights; post-trial self-rated task difficulty (0–10 VAS); and expert difficulty/safety scores were logged in a master spreadsheet (Microsoft Excel workbook).

Motion capture (MoCap). For each trial, the 3-D position $(\mathrm{x}, \mathrm{y}, \mathrm{z})$ of six markers (head, chest, shoulder, knee, ankle, and platform) and the derived linear velocity $(\dot{\mathrm{x}}, \dot{\mathrm{y}}, \dot{\mathrm{z}})$ were exported with timestamps as tab-separated values (.tsv).

Balance board (COP). COP–X and COP–Y coordinates with timestamps were exported as comma-separated values (.csv).

Dataset organization (per participant). Each participant's package comprised (i) a demographic/anthropometric sheet and (ii) a 16-condition matrix covering all IL×SIS combinations. For every condition, MoCap provided six markers × (x, y, z) + $(\dot{x}, \dot{y}, \dot{z})$ $= 36$ channels, yielding 576 MoCap columns across the 16 conditions. The force-platform file contributed 32 COP columns (two coordinates × 16 conditions). These structures were preserved for downstream processing and statistical analysis.

5.1.6. Data Processing and Computational Environment

Data were processed in Python 3 using NumPy, Pandas, SciPy, Matplotlib, and Seaborn.

5.1.7. Parameter Extraction and Rationale

To capture complementary aspects of postural control under IL×SIS, four primary metrics were extracted for each participant, condition, and tracked segment (head, chest, shoulder, knee, ankle) and for COP. One dynamic and one quasi-static descriptor were retained at both segmental and COP levels; additional sway metrics were calculated for descriptive checks but excluded from the main inferential analyses.

Segment-level (3D kinematics). Total Mean Velocity (TMV), $\mathrm{cm \cdot s^{-1}}$ – mean magnitude of the resultant 3-D velocity vector of the segment trajectory; herein 'velocity' denotes the magnitude (speed). TMV is a robust indicator of ongoing corrective activity and shows good responsiveness to task difficulty in posturography.

95% CI Ellipsoid Volume (EV95%) ($\mathrm{cm^3}$) – spatial dispersion of the 3D trajectory approximated by the 95% confidence ellipsoid. This summarizes the sway envelope across anteroposterior, mediolateral, and vertical axes and is widely used to characterize stability in clinical and research settings.

COP-level (balance-board platform). COP Total Mean Velocity (COP TMV) (cm/s) – mean speed of the COP path in the horizontal plane, a standard marker of postural demand and corrective effort.

COP 95 % CI Ellipse Area ($\mathrm{cm^2}$) – bivariate (AP–ML) sway area enclosing ≈ 95 % of COP samples, computed from the covariance structure; smaller areas indicate tighter control.

TMV and EV95% provide complementary information: correction speed and spatial dispersion. Combining segment-level and COP-level measures links body-segment kinematics to the neuromechanical interaction with the support surface. Path length and axis-specific range were retained for completeness because they are common in COP literature but were more collinear with the chosen area/volume descriptors and added limited explanatory value.

5.1.8. Statistical Analysis

All analyses were two-tailed with $\alpha = 0.05$. Distributions were checked with the Shapiro–Wilk test; because most parameters violated normality, central tendency is reported as median (IQR) and non-parametric procedures were used. For VAS and expert scores, condition means are shown for the across-condition log fit; medians (IQR).

Within-participant contrasts across instability levels (IL) and sensory strategies (SIS) were tested with the Wilcoxon signed-rank test. Cliff's δ was computed for significant contrasts and summarized in effect-size matrices using conventional small/medium/large thresholds.

To characterize difficulty across the ordered 16 IL×SIS conditions, we fitted a monotonic logarithmic model to self-ratings and expert ratings. Adequacy was evaluated with R^2 and residual inspection; results are shown with IQR bars and the fitted curve.

Associations between IL×SIS metrics and baseline tests were analyzed with Spearman's rank correlation (ρ), given non-normality and outliers. This included YBT direction-specific and composite scores, FRT reach, and the quasi-static/dynamic IL×SIS metrics.

Correlations with mechanical stability indices. Relationships between the mechanical descriptors (Relative Instability Index, RII; damping index, ψ_{IL}) and IL×SIS metrics (EV95%, TMV, COP metrics) were examined with Spearman's ρ within each IL and SIS stratum.

For each condition, we present medians (IQR). Pairwise comparison tables report Wilcoxon p-values and Cliff's δ; correlation matrices report coefficients and p-values. No between-subject pooling was performed without retaining the paired within-subject structure.

5.2. Results

5.2.1. Descriptive Statistics of Participants

Twenty-five healthy adults (13 women, 12 men) completed the study. Mean (± SD) age was 24.5 ± 6.1 years (range 18–39), mean stature 172.8 ± 10.3 cm (155–190), mean body mass 71.2 ± 14.9 kg (47.3–107), and mean BMI 23.5 ± 3.6 kg m^{-2} (18.4–29.3) **Table 20**.

All scheduled tasks were completed, yielding 225 YBT, 75 FRT, and 400 IL×SIS trials. Lower-limb dominance was uniformly right-sided (100%); hand dominance was 23 right and 2 left.

Table 20. Anthropometric characteristics of the participant cohort (n = 25). Values are presented as mean ± standard deviation with observed ranges

Variable	Mean ± SD	Range
Age (years)	24.5 ± 6.1	18 – 39
Height (cm)	172.8 ± 10.3	155 – 190
Mass (kg)	71.2 ± 14.9	47.3 – 107
BMI (kg m^{-2})	23.5 ± 3.6	18.4 – 29.3

5.2.2. Descriptive Statistics of Baseline Postural Control Tests

All participants met the pass thresholds for both baseline tests (YBT composite ≥ 89% of limb length; anterior asymmetry ≤ 4 cm) and thus satisfied current normative injury-risk screening criteria.

5.2.2.1. Y-Balance Test (YBT).

Mean YBT Composite scores were 91.4 ± 5.7% of limb length on the left and 91.8 ± 5.9% on the right (**Table 21**). Anterior asymmetry averaged 3.0 ± 2.0 cm; 84% of participants were below the 4 cm cut-off. Posterolateral and posteromedial asymmetries averaged 4.1 ± 3.7 cm and 3.4 ± 2.6 cm, with 68% below the 4 cm reference in each plane.

5.2.2.2. Functional Reach Test (FRT).

Mean forward reach was 39.9 ± 5.4 cm, exceeding the benchmark reported for healthy young adults (34.1 ± 9.0 cm) (**Table 21**).

Table 21. Baseline YBT and FRT outcomes compared with published normative data for healthy young adults. Values are mean ± SD with observed ranges. †Normative references as reported in prior literature [110,111]

Measure	Study Sample (n = 25)	Normative Values†	% < 4 cm Asymmetry
YBT Composite – Left (% LL)	91.4 ± 5.7 (81.8–104.7)	94.7 ± 7.0	-
YBT Composite – Right (% LL)	91.8 ± 5.9 (81.8–102.8)	94.7 ± 7.0	-
YBT Anterior Asymmetry (cm)	3.0 ± 2.0 (0.3–8.1)	3.2 ± 3.3	84 %
YBT Posterolateral Asymmetry (cm)	4.1 ± 3.7 (0.3–14.9)	3.7 ± 2.8	68 %
YBT Posteromedial Asymmetry (cm)	3.4 ± 2.6 (0.1–9.3)	3.1 ± 2.7	68 %
FRT – Anterior Reach (cm)	39.9 ± 5.4 (30–54)	34.1 ± 9.0	-

5.2.3. Participant Self-Rated Task Difficulty

Immediately after each balance trial, participants rated perceived task difficulty on a visual analogue scale. Median and interquartile range (IQR) values for each IL×SIS combination are shown in **Table 22**.

Perceived difficulty increased systematically across IL×SIS conditions. Under Basic, mean ratings remained low across ILs (0.9–2.2). Vestibular produced the highest scores, reaching 6.3 ± 2.5 at IL3, while Visual and Proprioception were intermediate, with most increases emerging between IL1 and IL2.

This progression confirms that participants distinguished task demands and that the IL×SIS matrix modulated perceived challenge as expected.

Table 22. Participant self-rated task difficulty (mean and interquartile range) across all IL×SIS conditions. Difficulty scores were recorded on a visual analogue scale immediately after each task. Higher values reflect greater perceived instability. Color scale (from green to red) denotes relative difficulty, with red indicating highest values

SIS \ IL	IL 0		IL 1		IL 2		IL 3	
	Mean	**IQR**	**Mean**	**IQR**	**Mean**	**IQR**	**Mean**	**IQR**
Basic	0.91	0	1.18	1	2.09	1	2.22	1.625
Visual	1.64	1	1.91	2	4.22	2.25	3.54	2
Proprioception	1.70	1	2.30	2	3.45	1.75	3.45	2.5
Vestibular	2.50	2	4.10	1.5	6.04	3.125	6.27	2.5

5.2.4. IL×SIS Effects on Postural Control Parameters

The combined manipulation of instability level (IL) and sensory strategy (SIS) produced progressive, segment-specific increases in postural sway, captured by EV95% and TMV.

Median chest EV95% increased with IL in every SIS (**Table 23**). Under Basic it rose from 179 cm³ at IL0 to 693 cm³ at IL3 (+386%), whereas under Vestibular it increased from 1 880 cm³ to 12 917 cm³ (+587%). The contrast between Basic IL0 and Vestibular IL3 was 71-fold.

Table 23. Chest EV95% (cm³) across IL×SIS conditions; traffic-light scale (green = low, yellow = moderate, red = high)

SIS \ IL	IL 0		IL 1		IL 2		IL 3	
	Median	IQR	Median	IQR	Median	IQR	Median	IQR
Basic	179.5	261.7	561.5	551.8	771.6	833.6	692.9	855.7
Visual	186.1	188.7	653.5	683.6	3213.8	7806.3	2645.0	3163.6
Proprioception	855.7	726.5	1354.4	1117.9	1725.0	1389.9	1784.7	2104.5
Vestibular	1880.0	1633.2	4604.4	6535.5	9729.0	12,599.6	12,917.0	23,512.2

TMV followed the same rank order. Basic rose from 0.78 cm s^{-1} to 0.98 cm s^{-1}; Vestibular climbed from 2.00 cm s^{-1} to 4.53 cm s^{-1} (+127 %). Distributions and significance markers are displayed in **Figure 37** and **Figure 39**. Median trajectories across the full IL×SIS grid appear in **Figure 38** and **Figure 40**. For visual intuition **Figure 41** shows a single participant's ellipsoid reconstructions; the volumetric inflation from Basic IL 0 to Vestibular IL 3 is readily visible.

Table 24. Chest TMV (cm s^{-1}) across IL×SIS conditions; same colour scale

SIS \ IL	IL 0		IL 1		IL 2		IL 3	
	Median	IQR	Median	IQR	Median	IQR	Median	IQR
Basic	0.78	0.21	0.88	0.18	1.07	0.32	0.98	0.28
Visual	0.86	0.23	1.08	0.46	2.20	2.33	1.93	0.95
Proprioception	1.20	0.18	1.22	0.36	1.46	0.44	1.54	0.35
Vestibular	2.00	0.50	2.95	0.93	4.19	1.77	4.53	1.87

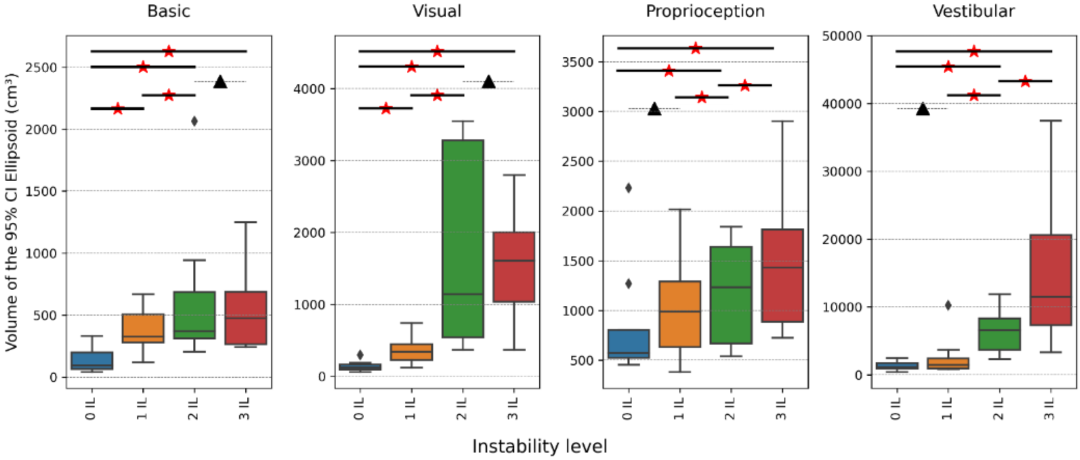

Figure 37. Chest EV95% movement distributions by IL×SIS cell. ★ $p < 0.05$, ▲ not significant, ◊ outliers

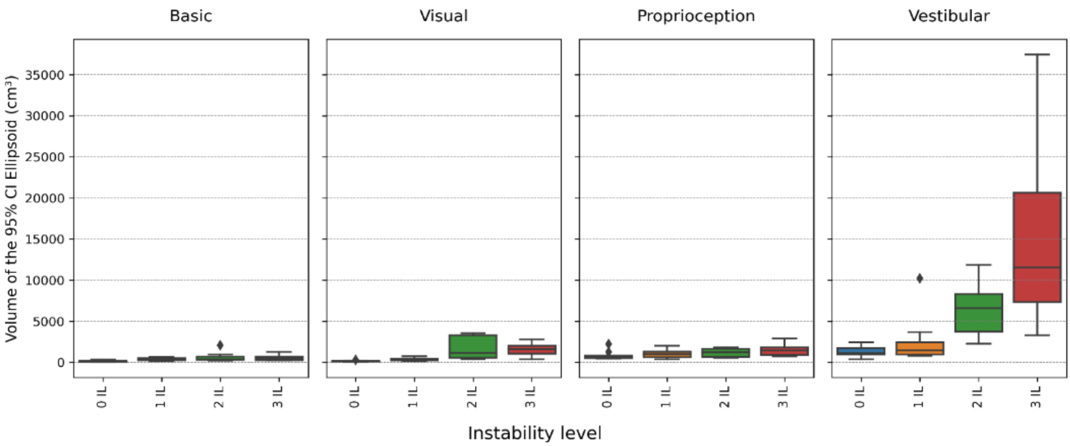

Figure 38. Chest movement EV95% across by IL×SIS cell. ◊ outliers

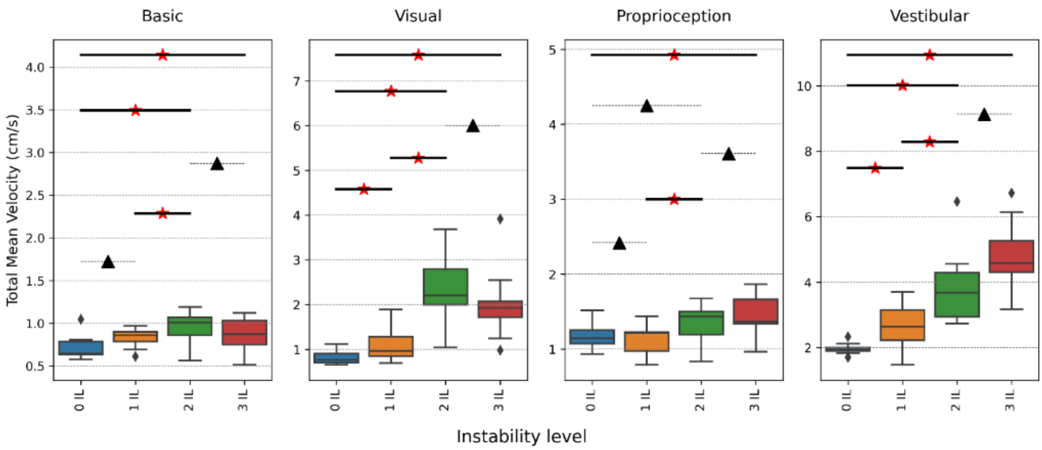

Figure 39. Chest TMV distributions by IL×SIS cell; ★ $p < 0.05$, ▲ not significant., ◊ outliers

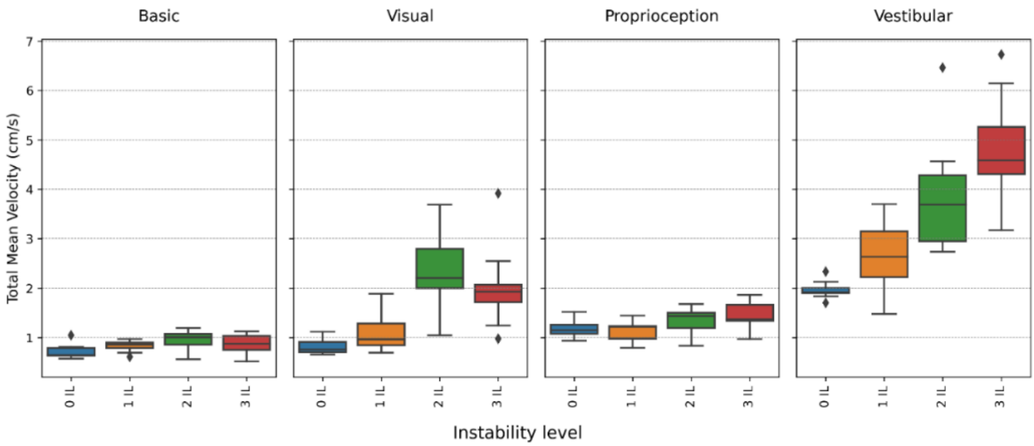

Figure 40. Chest movement TMV across by IL×SIS cell. ◊ outliers

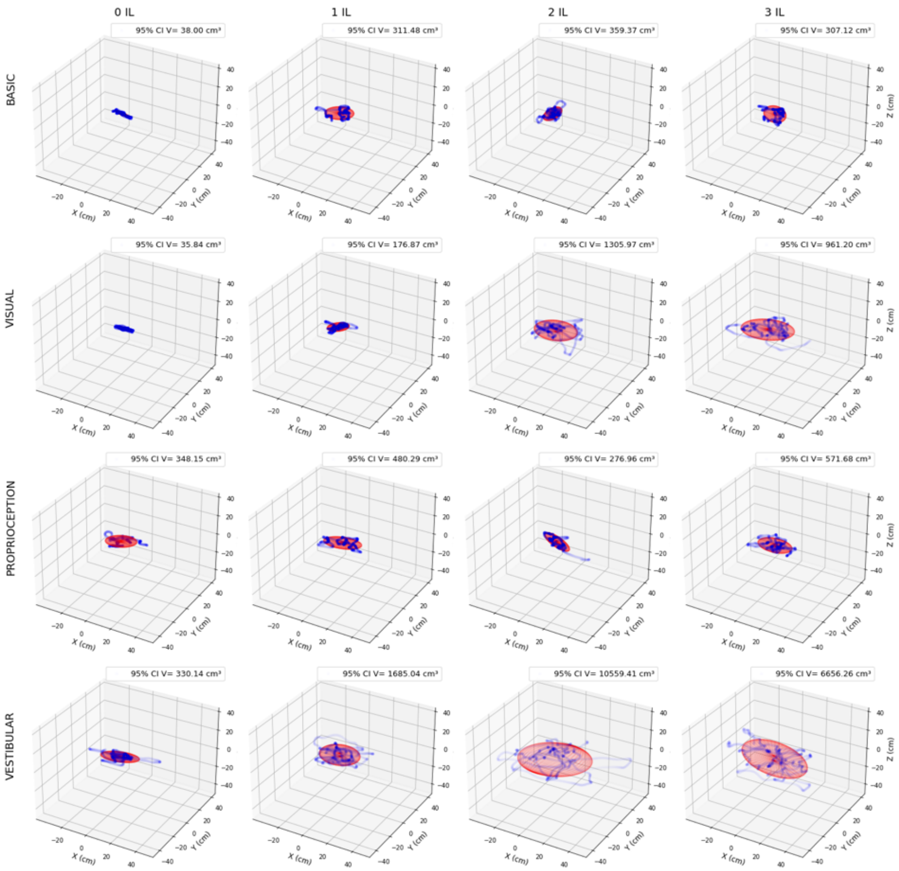

Figure 41. Single participant chest ellipsoids; blue = raw positions, red = 95 % CI

Head EV95% expanded from 318 cm³ (Basic IL 0) to 35 875 cm³ (Vestibular IL 3), while ankle EV95% rose from 0.01 cm³ to 3 410 cm³ (**Table 25 and Table 26**). Corresponding velocities increased six- to eleven-fold (**Table 27** and **Table 28**). Visual and Proprioceptive conditions occupied an intermediate range, consistently positioned between Basic and Vestibular across all ILs. COP sway mirrored segmental behavior (**Table 29** and **Table 30**). The COP 95% CI area increased from 1 cm² (Basic IL0) to 52 cm² (Vestibular IL3), and COP TMV from 0.7 cm s⁻¹ to 5.6 cm s⁻¹

Table 25. Head EV95% (cm³) across IL×SIS conditions

Head EV95%	IL 0		1 IL		IL 2		IL 3	
	Median	**IQR**	**Median**	**IQR**	**Median**	**IQR**	**Median**	**IQR**
Basic	318	487	932	1312	971	2009	1319	1864
Visual	458	558	882	3122	4896	11449	3687	7093
Proprioception	1902	1461	2282	2110	3252	4727	2789	3966
Vestibular	2944	2773	8959	12096	18994	21317	35875	54147

Table 26. Ankle EV95% (cm³) across IL×SIS conditions

Ankle EV95%	IL 0		IL 1		IL 2		IL 3	
	Median	**IQR**	**Median**	**IQR**	**Median**	**IQR**	**Median**	**IQR**
Basic	0.01	0.03	0.32	0.71	4.67	8.70	7.98	13.21
Visual	0.02	0.04	0.60	4.84	71.44	264.71	49.36	118.02
Proprioception	4.13	3.86	15.51	19.43	113.60	107.18	144.93	136.45
Vestibular	9.92	10.91	133.66	161.29	1937.77	3217.46	3409.92	5531.22

Table 27. Head TMV (cm s⁻¹) across IL×SIS conditions

Head TMV	IL 0		IL 1		IL 2		IL 3	
	Median	**IQR**	**Median**	**IQR**	**Median**	**IQR**	**Median**	**IQR**
Basic	0.78	0.24	0.94	0.29	1.17	0.44	1.12	0.45
Visual	0.89	0.22	1.04	0.50	2.51	2.01	2.26	1.10
Proprioception	1.26	0.34	1.34	0.37	1.69	0.54	1.86	0.45
Vestibular	2.20	0.78	3.39	1.21	4.53	1.59	5.37	2.02

Table 28. Ankle TMV (cm s⁻¹) across IL×SIS conditions

Ankle TMV	IL 0		IL 1		IL 2		IL 3	
	Median	**IQR**	**Median**	**IQR**	**Median**	**IQR**	**Median**	**IQR**
Basic	0.9	0.4	0.8	0.5	1.5	1.2	1.4	0.9
Visual	1.0	0.4	1.0	0.9	4.5	8.7	3.0	2.7
Proprioception	1.0	0.6	1.0	0.3	2.4	1.6	3.1	1.3
Vestibular	1.3	0.5	2.3	2.1	8.9	6.0	10.2	5.2

Table 29. COP 95 % CI area (cm²) across IL×SIS conditions

Center of Pressure		IL 0		IL 1		IL 2		IL 3	
Parameter	**mCTSIB**	**Median**	**IQR**	**Median**	**IQR**	**Median**	**IQR**	**Median**	**IQR**
Area (cm^2)	**Bas**	1.0	2.0	0.03	2.0	3.0	8.0	5.0	7.0
	Vis	2.0	2.0	0.04	7.0	18.0	37.0	15.0	22.0
	Prop	7.0	7.0	7.0	9.0	9.0	11.0	11.0	11.0
	Vest	19.0	1.70	27.0	52.0	53.0	49.0	52.0	79.0

Table 30. COP TMV (cm s^{-1}) across IL×SIS conditions

Center of Pressure		IL 0		IL 1		IL 2		IL 3	
Parameter	**mCTSIB**	**Median**	**IQR**	**Median**	**IQR**	**Median**	**IQR**	**Median**	**IQR**
TMV (cm/s)	**Bas**	0.7	0.2	0.9	0.5	1.4	1.0	1.1	0.7
	Vis	0.9	0.4	1.2	0.6	3.4	4.3	2.6	0.1
	Prop	1.4	0.6	1.3	0.6	1.6	0.9	1.5	0.6
	Vest	3.1	1.6	4.2	5.4	4.1	4.1	5.6	4.3

5.2.5. Challenge Progression across IL×SIS

Ordering IL×SIS conditions by ascending median chest EV95% shows a clear progression of task difficulty (**Figure 42**). As the chest motion envelope expands across the ordered set, TMV increases in parallel, with the steepest rise toward the upper end. The largest joint increases occur in IL1–Proprioception, IL3–Proprioception, IL3–Visual, and IL3–Vestibular, indicating disproportionate postural responses when greater mechanical instability is combined with reduced or unreliable sensory input.

The ordered x-axis labels provide a compact challenge ladder: conditions with stable support and full sensory availability produce the smallest EV95% and slowest velocities, whereas conditions at the top—especially Vestibular at high IL—produce the largest EV95% and fastest velocities.

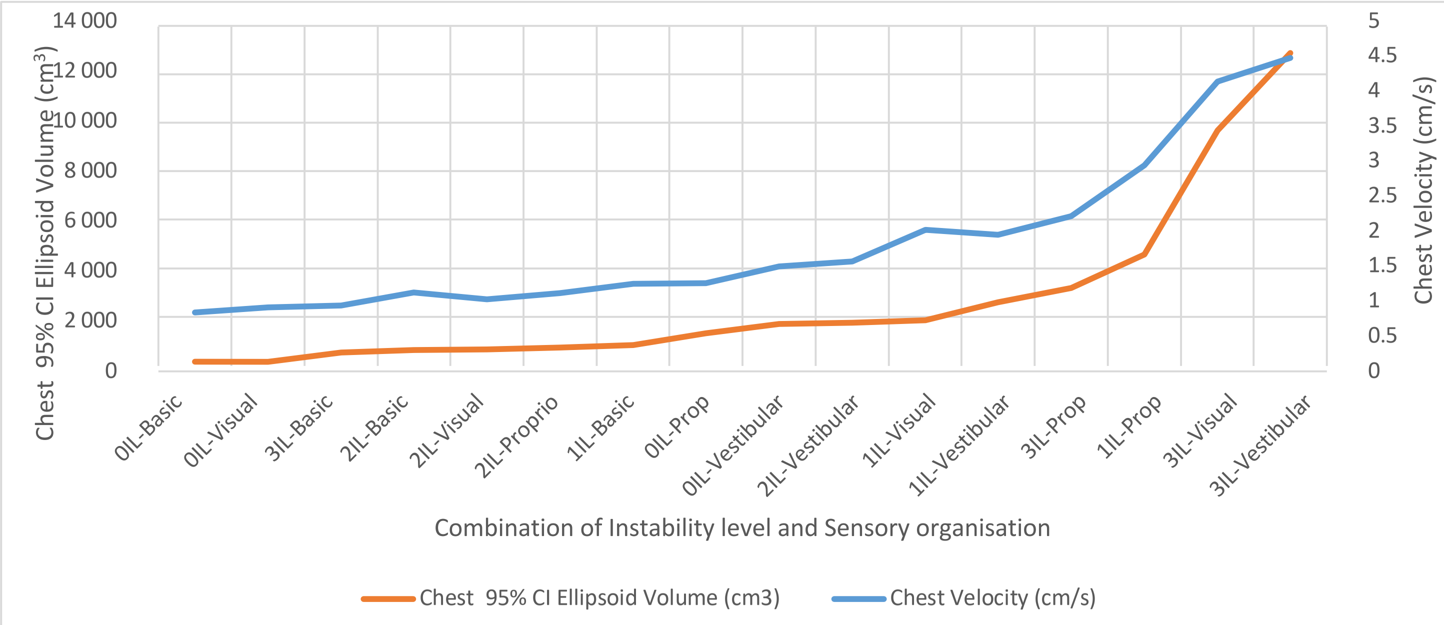

Figure 42. Sequential ranking of IL×SIS conditions by chest sway. Each point corresponds to one IL×SIS combination; the x-axis lists conditions ordered from the smallest to the largest median chest EV95% (cm^3). The two overlaid series plot median chest EV95% and TMV ($cm\ s^{-1}$) for the same conditions.

5.2.6. Effect Size Analysis of Instability Level Contrasts within SIS

Pairwise IL contrasts were tested with the Wilcoxon signed-rank test; Cliff's δ was reported only when $p < 0.05$. Heat-mapped matrices in **Table 31** (chest TMV) and **Table 32** (chest EV95%) summarize the effects; bold p denotes significance and strikethrough denotes non-significance.

A consistent pattern emerged across IL×SIS: Vestibular > Proprioception ≈ Visual > Basic at each IL, with the largest step from IL1 to IL2. By contrast, IL2 to IL3 was predominantly non-significant, indicating a plateau once IL2 was reached under sensory degradation (**Table 31**, **Table 32**).

For chest TMV (**Table 31**), 0→2 effects were large in Basic ($\delta \approx 0.92$, $p < 0.001$), Visual ($\delta = 1.00$, $p < 0.001$), Proprioception ($\delta \approx 0.76$, $p < 0.001$), and Vestibular ($\delta = 1.00$, $p < 0.001$). Within-SIS 1→2 contrasts were also large (e.g., $\delta \approx 0.84$ in Basic, $p < 0.001$; $\delta \approx 0.83$ in Visual, $p < 0.001$), whereas 2→3 was mostly non-significant.

Chest EV95% showed the same hierarchy and break-point (**Table 32** and **Table 31**). Examples include Basic 0→2: $\delta \approx 0.60$ ($p < 0.001$), Visual 0→2: $\delta \approx 0.83$ ($p < 0.001$), Proprioception 0→2: $\delta \approx 0.60$ ($p = 0.001$), and Vestibular 0→2: $\delta = 1.00$ ($p < 0.001$). Again, 2→3 contrasts were mostly non-significant.

Table 31. Effect sizes for chest TMV across IL contrasts within each SIS. Matrix of paired contrasts (0→1, 0→2, 0→3, 1→2, 1→3, 2→3). Bold p marks significance ($\alpha = 0.05$); strikethrough p marks non-significance. Cliff's δ reported only when significant; warmer shading denotes larger δ

From IL→ To IL	Basic		Visual		Proprioception		Vestibular	
	p value	Cliff's delta	p value	Cliff's delta	p value	Cliff's delta	p value	Cliff's delta
0 → 1	**0.032**	0.52	**0**	0.667	~~0.396~~	0.2	**0**	0.826
0 → 2	**0**	0.6	**0**	0.917	**0**	0.52	**0**	1
0 → 3	**0.001**	0.44	**0**	0.917	**0**	0.84	**0**	1
1 → 2	**0**	0.68	**0**	0.75	**0.024**	0.52	**0.001**	0.565
1 → 3	**0.015**	0.6	**0**	0.75	**0**	0.84	**0**	0.739
2 → 3	~~0.141~~		~~0.375~~		~~0.771~~		~~0.142~~	

Table 32. Effect sizes for chest EV95% across IL contrasts within each SIS. Notation and colouring as in Table 31; most 2→3 cells are non-significant, indicating a plateau beyond IL 2

From IL→ To IL	Basic		Visual		Proprioception		Vestibular	
	p value	Cliff's delta	p value	Cliff's delta	p value	Cliff's delta	p value	Cliff's delta
0 → 1	**0.001**	0.76	**0**	0.917	**0.022**	0.36	**0.001**	0.652
0 → 2	**0**	0.76	**0**	0.917	**0**	0.68	**0**	0.913
0 → 3	**0**	0.76	**0**	1	**0**	0.76	**0**	0.913
1 → 2	**0.001**	0.68	**0**	0.75	**0.024**	0.68	**0.02**	0.478
1 → 3	**0.02**	0.36	**0**	0.833	**0.003**	0.52	**0**	0.826
2 → 3	0.979		0.128		0.615		0.142	

This IL-driven scaling extended beyond the chest. Head, chest, and ankle matrices confirmed strong 0→2 and 0→3 effects, especially when vision was removed, whereas 2→3 added little. For TMV (**Table 33**), Visual and Vestibular frequently reached $\delta \geq 0.80$ for 0→2/0→3 across segments (e.g., head/vestibular 0→3: $\delta = 1.00$, $p < 0.001$), with moderate-to-large effects in Basic and Proprioception. For EV95% (**Table 34**), head values were highly sensitive to vision removal (e.g., Visual 0→2: $\delta \approx 0.83$, $p < 0.001$), and ankle values increased markedly once instability exceeded IL1 (e.g., Vestibular 0→3: $\delta \approx 0.91$, $p < 0.001$).

Table 33. TMV (Head, Chest, Ankle): Wilcoxon p and Cliff's δ for all IL contrasts within each SIS. Largest effects occur for 0→2 and 0→3 under Visual/Vestibular; 2→3 is sparse

Velocity / Body part	From IL→ To IL	Basic		Visual		Proprioception		Vestibular	
		p value	Cliff's delta	p value	Cliff's delta	p value	Cliff's delta	p value	Cliff's delta
Head	0 → 1	**0**	0,76	**0**	0,75	**0,027**	0,28	**0**	0,739
	0 → 2	**0**	0,92	**0**	1	**0**	0,76	**0**	1
	0 → 3	**0**	0,84	**0**	1	**0**	1	**0**	1
	1 → 2	**0**	0,84	**0**	0,833	**0,024**	0,76	**0**	0,739
	1 → 3	**0**	0,84	**0**	0,917	**0**	0,92	**0**	0,826
	2 → 3	~~0,12~~		~~0,663~~	0,083		0,04	~~0,142~~	
Chest	0 → 1	**0,032**	0,52	**0**	0,667	~~0,396~~	0,2	**0**	0,826
	0 → 2	**0**	0,6	**0**	0,917	**0**	0,52	**0**	1
	0 → 3	**0,001**	0,44	**0**	0,917	**0**	0,84	**0**	1
	1 → 2	**0**	0,68	**0**	0,75	**0,024**	0,52	**0,001**	0,565
	1 → 3	**0,015**	0,6	**0**	0,75	**0**	0,84	**0**	0,739
	2 → 3	~~0,141~~		~~0,375~~		~~0,771~~		~~0,142~~	
Ankle	0 → 1	~~0,442~~		~~0,966~~		~~0,381~~		**0**	0,826
	0 → 2	**0**	0,6	**0**	0,833	**0**	0,92	**0**	1
	0 → 3	**0**	0,68	**0**	0,833	**0**	1	**0**	1
	1 → 2	**0**	0,76	**0**	0,75	**0,024**	0,92	**0**	0,913
	1 → 3	**0**	0,76	**0**	0,75	**0**	1	**0**	0,913
	2 → 3	~~0,22~~		~~0,055~~		~~0,263~~		~~0,142~~	

Table 34. EV95% (Head, Chest, Ankle): Wilcoxon p and Cliff's δ for all IL contrasts within each SIS. Replicates the stepwise escalation and plateau; head and ankle are especially sensitive when vision is absent

Volume	From IL→ To IL	Basic		Visual		Proprioception		Vestibular	
Body part		p value	Cliff's delta	p value	Cliff's delta	p value	Cliff's delta	p value	Cliff's delta
Head	0 → 1	0	0,68	0,002	0,583	~~0,12~~		0	0,913
	0 → 2	0	0,68	0	0,833	0,001	0,6	0	1
	0 → 3	0	0,92	0	1	0	0,68	0	1
	1 → 2	~~0,141~~		0	0,75	0,024	0,36	0,002	0,739
	1 → 3	~~0,052~~		0,001	0,75	~~0,101~~		0	0,913
	2 → 3	~~0,634~~		~~0,603~~		~~0,653~~		~~0,142~~	
Chest	0 → 1	0,001	0,76	0	0,917	0,022	0,36	0,001	0,652
	0 → 2	0	0,76	0	0,917	0	0,68	0	0,913
	0 → 3	0	0,76	0	1	0	0,76	0	0,913
	1 → 2	0,001	0,68	0	0,75	0,024	0,68	0,02	0,478
	1 → 3	0,02	0,36	0	0,833	0,003	0,52	0	0,826
	2 → 3	~~0,979~~		~~0,128~~		~~0,615~~		~~0,142~~	
Ankle	0 → 1	0	0,84	0	1	0	1	0	1
	0 → 2	0	0,92	0	1	0	1	0	1
	0 → 3	0	0,92	0	1	0	1	0	1
	1 → 2	0	1	0	1	0,024	0,92	0	0,913
	1 → 3	0	1	0	1	0	1	0	1
	2 → 3	0,034	0,36	~~0,128~~		0,016	0,68	~~0,142~~	

COP metrics showed the same ceiling at IL2 (**Table 35**). Under Vestibular, COP TMV yielded 0→2: $\delta \approx 0.81$ and 0→3: $\delta \approx 0.91$ (both $p \leq 0.001$), while 2→3 was usually small or non-significant. An isolated negative effect appeared for COP area in Basic 2→3 ($\delta = -0.429$, $p = 0.05$), consistent with saturation beyond IL2.

Table 35. COP metrics (95% CI area; TMV): Wilcoxon p and Cliff's δ for all IL contrasts within each SIS. Shows strong increases up to IL 2 and limited additional change at IL 3; includes an isolated negative δ (Basic 2→3 for area)

COP	From IL→ To IL	Basic		Visual		Proprioception		Vestibular	
Body part		p value	Cliff's delta	p value	Cliff's delta	p value	Cliff's delta	p value	Cliff's delta
Range (X axis)	0 → 1	0	0.81	0	1	~~0.633~~		0	0.81
	0 → 2	0	0.81	0	1	~~0.393~~	0.333	0	0.81
	0 → 3	0.001	0.619	0	0.905	0.01	0.619	0	0.905
	1 → 2	~~0.32~~		0.001	0.714	0.024	0.429	0.004	0.524
	1 → 3	~~0.708~~		0.003	0.619	~~0.137~~		0	0.714
	2 → 3	0.05	-0.429	~~0.304~~		~~0.585~~		~~0.142~~	
Range (Y axis)	0 → 1	~~0.812~~		~~0.633~~		~~0.473~~		0.05	0.333
	0 → 2	~~0.055~~		0	0.714	~~0.147~~		0	1
	0 → 3	0.042	0.333	0	0.905	0.002	0.619	0	0.81
	1 → 2	0.014	0.429	0.006	0.524	~~0.06~~		~~0.082~~	
	1 → 3	0.004	0.619	0.001	0.81	0.001	0.619	0.003	0.524
	2 → 3	~~0.919~~		~~0.733~~		0.019	0.333	~~0.082~~	
Area	0 → 1	0.006	0.619	0	0.905	~~0.585~~		0.001	0.524
	0 → 2	0.001	0.714	0	0.905	~~0.203~~		0	0.905
	0 → 3	0.001	0.619	0	0.905	0.001	0.619	0	1
	1 → 2	0.019	0.333	0.001	0.619	0.024	0.429	0.019	0.524
	1 → 3	0.01	0.333	0.005	0.619	0.001	0.714	0	0.714
	2 → 3	~~0.517~~		~~0.374~~		~~0.119~~		~~0.142~~	
Total mean velocity	0 → 1	0.006	0.524	0	0.714	~~0.082~~		0.001	0.455
	0 → 2	0	0.905	0	1	~~0.759~~		0	0.818
	0 → 3	0	0.81	0	1	~~0.355~~		0	0.909
	1 → 2	0	0.905	0	0.619	0.024	0.524	~~0.656~~	
	1 → 3	0	0.619	0.001	0.714	0.006	0.429	0	0.545
	2 → 3	0.007	-0.524	0.009	-0.333	~~0.708~~		~~0.142~~	

5.2.7. Correlation Between Anthropometric Characteristics and Postural Control Parameters Under IL×SIS Conditions

Spearman rank correlations (ρ) were computed between anthropometric variables (height, age, weight, BMI) and two postural-control metrics derived from the chest trajectory – chest TMV (cm s^{-1}) and chest EV95% (cm^3) – across all IL×SIS combinations (IL 0–3 × Basic/ Visual/ Proprioception/ Vestibular). Summary correlation matrices are provided in **Table 36** (EV95%) and **Table 37** (TMV).

Age did not correlate with chest TMV or chest EV95% across IL×SIS conditions (all |ρ| small; $p > 0.33$ in the TMV matrix; analogous non-significance for EV95%). Thus, age did not explain inter-individual differences in postural responses in this sample ($n = 25$).

Height showed the only coherent pattern: a positive, mostly moderate correlation with chest EV95% across several IL×SIS conditions (multiple entries $p < 0.05$ in **Table 36**), indicating larger 3D chest displacement envelopes in taller participants. Height–TMV associations were limited to Vestibular IL0 ($\rho = 0.636$, $p = 0.001$) and IL1 ($\rho = 0.504$, $p = 0.010$) and were small and non-significant elsewhere (e.g., Visual IL2: $\rho = 0.141$, $p = 0.500$; Proprioception IL2: $\rho = 0.054$, $p = 0.797$).

Weight and BMI showed only weak, scattered associations. For chest TMV, correlations were uniformly small ($|\rho| \leq 0.28$ in most cells) and non-significant across

ILs and SIS (e.g., BMI under Vestibular IL3: $\rho = 0.200$, $p = 0.385$). The EV95% matrix likewise showed no consistent pattern; isolated $p < 0.05$ values corresponded to small coefficients.

Within this cohort, body size—operationalized by height—was linked mainly to the amplitude of upper-trunk excursions (EV95%), whereas movement speed (TMV) was largely unaffected except under vestibular sensory degradation at IL0–IL1. Age, weight, and BMI did not materially explain between-subject variability in chest-based IL×SIS measures.

Table 36. Spearman correlations (r_s, p) between anthropometric characteristics and chest EV95% across all IL (0–3) and SIS (Basic, Visual, Proprioception, Vestibular) conditions. Cells provide coefficients and p-values; shaded cells in the source indicate stronger effects

Chest 95% CI Volume (cm^3)		**0 IL**		**1 IL**		**2 IL**		**3 IL**	
Correlation	mCTSIB	**Corr. Coef.**	**p**	**Corr. Coef.**	**p**	**Corr. Coef.**	**p**	**Corr. Coef.**	**p**
Height	Bas	0,700	0,000	0,650	0,000	0,630	0,000	0,560	0,000
	Vis	0,370	0,070	0,630	0,000	0,370	0,070	0,320	0,110
	Prop	0,510	0,010	0,560	0,000	0,540	0,010	0,330	0,110
	Vest	0,570	0,000	0,560	0,000	0,320	0,120	0,380	0,080
Age	Bas	0,230	0,340	-0,340	0,150	-0,120	0,630	-0,390	0,100
	Vis	0,080	0,740	0,070	0,790	-0,160	0,510	-0,110	0,660
	Prop	-0,290	0,240	-0,150	0,550	-0,050	0,850	-0,270	0,270
	Vest	-0,040	0,880	0,190	0,440	-0,030	0,910	-0,030	0,910
Weight	Bas	0,490	0,020	0,500	0,020	0,600	0,000	0,440	0,030
	Vis	0,380	0,080	0,390	0,070	0,350	0,100	0,240	0,260
	Prop	0,530	0,010	0,420	0,040	0,310	0,150	0,490	0,020
	Vest	0,360	0,090	0,450	0,030	0,360	0,090	0,320	0,150
BMI	Bas	0,070	0,740	0,270	0,210	0,420	0,040	0,260	0,230
	Vis	0,240	0,280	0,120	0,600	0,240	0,280	0,140	0,520
	Prop	0,430	0,040	0,260	0,220	0,110	0,620	0,480	0,020
	Vest	0,090	0,670	0,250	0,260	0,280	0,190	0,290	0,200

Table 37. Spearman correlations (r_s, p) between anthropometric characteristics and chest TMV across all IL×SIS conditions. Layout mirrors Table 36; significant entries are comparatively sparse

Chest Velocity (cm/s)		0 IL		1 IL		2 IL		3 IL	
Correlation	mCTSIB	Corr. Coef.	p	Corr. Coef.	p	Corr. Coef.	p	Corr. Coef.	p
Height	Bas	0.137	0.515	0.222	0.286	0.229	0.271	0.201	0.335
	Vis	0.069	0.743	0.219	0.304	0.141	0.500	-0.055	0.795
	Prop	0.224	0.282	0.258	0.213	0.054	0.797	0.152	0.468
	Vest	0.636	0.001	0.504	0.010	0.039	0.852	0.324	0.131
Age	Bas	0.099	0.687	-0.127	0.604	-0.163	0.506	-0.243	0.316
	Vis	0.084	0.733	-0.142	0.574	-0.184	0.451	-0.379	0.109
	Prop	-0.013	0.957	-0.034	0.891	0.043	0.860	-0.138	0.574
	Vest	-0.008	0.974	0.169	0.490	-0.137	0.576	-0.105	0.688
Weight	Bas	0.084	0.703	-0.018	0.936	0.119	0.590	0.030	0.893
	Vis	0.136	0.535	-0.015	0.946	0.210	0.337	-0.157	0.474
	Prop	0.224	0.304	0.146	0.506	0.006	0.979	0.154	0.483
	Vest	0.412	0.051	0.429	0.041	0.162	0.460	0.279	0.220
BMI	Bas	-0.068	0.757	-0.179	0.414	0.011	0.961	-0.026	0.907
	Vis	0.128	0.562	-0.135	0.549	0.218	0.317	-0.102	0.644
	Prop	0.099	0.654	0.041	0.854	0.019	0.932	0.112	0.612
	Vest	0.048	0.826	0.203	0.354	0.188	0.391	0.200	0.385

5.2.8. Correlation Between Baseline Postural Control Tests and Postural Control Parameters Under IL×SIS Conditions

We examined whether baseline balance tests—Y-Balance Test (YBT) and Functional Reach Test (FRT)—were associated with chest EV95%, chest TMV, and COP TMV under IL×SIS. Spearman's ρ was used because distributions were non-normal.

The only consistent pattern was a small positive association between chest EV95% and non-dominant-leg YBT Anterior and Posterolateral reaches across several IL×SIS combinations. No reliable association was observed for the Composite score (**Table 38**).

Table 38. Spearman correlations between YBT metrics and chest EV95% across IL×SIS conditions (IL 0–3; Basic, Visual, Proprioception, Vestibular). The matrix reports ρ and p for left/right limbs and ANT/PL/PM directions plus Composite; positive associations are confined to non-dominant ANT and PL

Chest 95% CI Volume (cm^3)		0 IL		1 IL		2 IL		3 IL	
Correlation	mCTSIB	Corr. Coef.	p	Corr. Coef.	p	Corr. Coef.	p	Corr. Coef.	p
Y Balance Test Left Anterior	Bas	0,430	0,030	0,640	0,000	0,680	0,000	0,640	0,000
	Vis	0,440	0,030	0,560	0,000	0,510	0,010	0,400	0,050
	Prop	0,590	0,000	0,440	0,030	0,520	0,010	0,490	0,010
	Vest	0,470	0,020	0,420	0,040	0,480	0,020	0,620	0,000
Y Balance Test Left Posterior-Lateral	Bas	0,400	0,050	0,510	0,010	0,440	0,030	0,320	0,120
	Vis	0,430	0,030	0,490	0,020	0,490	0,010	0,360	0,080
	Prop	0,320	0,120	0,390	0,050	0,480	0,010	0,310	0,140
	Vest	0,450	0,030	0,550	0,000	0,360	0,080	0,570	0,000
Y Balance Test Left Posterior-Medial	Bas	0,340	0,090	0,220	0,290	0,280	0,170	0,240	0,240
	Vis	0,260	0,210	0,190	0,380	0,090	0,680	0,210	0,310
	Prop	0,250	0,240	0,040	0,850	0,330	0,110	0,230	0,260
	Vest	0,100	0,640	0,170	0,430	-0,160	0,450	0,280	0,200
Left Composite Score	Bas	0,010	0,950	0,050	0,820	0,200	0,330	0,160	0,460
	Vis	0,210	0,300	0,150	0,490	0,040	0,860	0,190	0,350
	Prop	0,210	0,310	0,090	0,670	0,330	0,110	0,330	0,110
	Vest	0,030	0,880	0,110	0,590	-0,030	0,880	0,330	0,120
Y Balance Test Right Anterior	Bas	0,400	0,050	0,350	0,080	0,480	0,010	0,440	0,030
	Vis	0,240	0,250	0,370	0,080	0,270	0,190	0,270	0,200
	Prop	0,180	0,390	0,010	0,980	0,240	0,240	0,170	0,400
	Vest	0,250	0,230	0,150	0,480	0,230	0,260	0,360	0,090
Y Balance Test Right Posterior-Lateral	Bas	0,540	0,010	0,330	0,110	0,300	0,140	0,170	0,420
	Vis	0,530	0,010	0,450	0,030	0,220	0,300	0,290	0,170
	Prop	0,040	0,850	0,090	0,660	0,380	0,060	-0,030	0,890
	Vest	0,230	0,270	0,380	0,060	0,000	0,990	0,410	0,050
Y Balance Test Right Posterior-Medial	Bas	0,350	0,080	0,150	0,460	0,170	0,430	0,090	0,660
	Vis	0,400	0,050	0,310	0,140	0,160	0,450	0,150	0,460
	Prop	0,120	0,560	-0,090	0,680	0,330	0,110	0,090	0,660
	Vest	0,040	0,860	0,200	0,340	-0,150	0,480	0,230	0,290
Right Composite Score	Bas	0,070	0,760	-0,230	0,270	-0,060	0,780	-0,150	0,490
	Vis	0,240	0,240	0,020	0,920	-0,140	0,490	0,040	0,850
	Prop	-0,130	0,550	-0,290	0,170	0,090	0,660	0,000	1,000
	Vest	-0,220	0,280	-0,070	0,730	-0,310	0,130	0,140	0,530

No meaningful correlations were observed between chest EV95% and either mean or maximal FRT reach (**Table 39**).

Table 39. Spearman correlations between FRT (mean, max reach) and chest EV95% across IL×SIS conditions. Coefficients are uniformly small and non-significant

Chest 95% CI Volume (cm³)		0 IL		1 IL		2 IL		3 IL	
Correlation	mCTSIB	Corr. Coef.	p	Corr. Coef.	p	Corr. Coef.	p	Corr. Coef.	p
Mean Functional Reach Test	Bas	0,320	0,110	0,000	0,990	0,090	0,680	0,060	0,760
	Vis	0,070	0,750	-0,040	0,870	-0,200	0,340	0,150	0,490
	Prop	0,010	0,980	-0,060	0,790	0,170	0,410	0,060	0,760
	Vest	0,200	0,330	0,070	0,750	-0,020	0,940	0,100	0,650
Max Functional Reach Test	Bas	0,370	0,070	0,050	0,830	0,140	0,500	0,140	0,510
	Vis	0,090	0,680	-0,040	0,860	-0,240	0,250	0,100	0,650
	Prop	0,120	0,560	0,020	0,920	0,210	0,300	0,170	0,410
	Vest	0,250	0,220	0,010	0,960	-0,050	0,800	0,060	0,770

Chest TMV showed no systematic relationship with baseline tests. Scattered nominal p-values did not replicate across ILs or SIS, and the corresponding ρ values were modest, so they were not interpreted as stable effects (**Table 40** and **Table 41**).

Table 40. Spearman correlations between YBT metrics and chest TMV across IL×SIS conditions. Isolated significant cells lack consistency across ILs/SIS; no coherent pattern

Chest Velocity (cm/s)		0 IL		1 IL		2 IL		3 IL	
Correlation	mCTSIB	Corr. Coef.	p	Corr. Coef.	p	Corr. Coef.	p	Corr. Coef.	p
Y Balance Test Left Anterior	Bas	0.120	0.568	0.299	0.147	0.152	0.467	0.282	0.173
	Vis	0.414	0.040	0.297	0.159	0.323	0.115	0.126	0.548
	Prop	0.260	0.209	0.271	0.191	0.148	0.481	0.267	0.197
	Vest	0.414	0.040	0.344	0.092	0.256	0.217	0.543	0.008
Y Balance Test Left Posterior-Lateral	Bas	0.289	0.161	0.292	0.157	0.157	0.453	0.122	0.560
	Vis	0.394	0.052	0.209	0.328	0.261	0.207	-0.038	0.858
	Prop	0.302	0.142	0.258	0.214	0.093	0.659	0.247	0.234
	Vest	0.591	0.002	0.511	0.009	0.152	0.470	0.436	0.038
Y Balance Test Left Posterior-Medial	Bas	0.104	0.621	0.122	0.560	0.024	0.911	-0.131	0.534
	Vis	0.266	0.199	-0.069	0.750	-0.027	0.897	0.139	0.508
	Prop	-0.100	0.636	-0.063	0.764	0.038	0.857	0.131	0.533
	Vest	0.195	0.350	0.102	0.629	-0.162	0.439	0.213	0.330
Left Composite Score	Bas	0.206	0.323	0.270	0.192	-0.123	0.558	0.149	0.479
	Vis	0.529	0.007	0.160	0.455	-0.066	0.753	0.032	0.878
	Prop	0.129	0.538	0.238	0.253	0.155	0.461	0.385	0.058
	Vest	-0.102	0.627	-0.008	0.971	-0.120	0.568	0.205	0.349
Y Balance Test Right Anterior	Bas	0.191	0.384	-0.288	0.183	-0.180	0.448	-0.062	0.785
	Vis	-0.158	0.470	-0.335	0.118	-0.415	0.061	-0.127	0.574
	Prop	0.183	0.404	0.081	0.726	-0.069	0.767	-0.082	0.717
	Vest	-0.004	0.988	0.090	0.683	0.036	0.873	0.005	0.984
Y Balance Test Right Posterior-Lateral	Bas	0.326	0.112	0.329	0.108	0.188	0.368	0.069	0.745
	Vis	0.285	0.167	0.204	0.339	0.085	0.685	0.075	0.723
	Prop	0.132	0.528	0.135	0.520	0.070	0.741	-0.047	0.825
	Vest	0.441	0.028	0.402	0.046	-0.050	0.814	0.366	0.086
Y Balance Test Right Posterior-Medial	Bas	0.243	0.241	0.126	0.550	0.018	0.933	-0.184	0.380
	Vis	0.240	0.248	-0.041	0.848	0.025	0.907	0.126	0.550
	Prop	-0.240	0.248	-0.187	0.370	0.004	0.984	-0.052	0.805
	Vest	0.057	0.785	0.135	0.520	-0.141	0.503	0.236	0.279
Right Composite Score	Bas	0.195	0.351	0.165	0.430	-0.115	0.583	-0.082	0.696
	Vis	0.347	0.089	0.058	0.787	-0.145	0.488	0.056	0.790
	Prop	-0.171	0.414	-0.021	0.922	0.062	0.770	0.067	0.751
	Vest	-0.262	0.205	-0.085	0.685	-0.206	0.323	0.117	0.596

Table 41. Spearman correlations between FRT (mean, max reach) and chest TMV across IL×SIS conditions. No meaningful associations

Chest Velocity (cm/s)		0 IL		1 IL		2 IL		3 IL	
Correlation	mCTSIB	Corr. Coef.	p	Corr. Coef.	p	Corr. Coef.	p	Corr. Coef.	p
Mean Functional Reach Test	Bas	0.313	0.128	0.052	0.804	-0.180	0.389	-0.028	0.896
	Vis	0.329	0.108	-0.050	0.818	-0.245	0.239	-0.053	0.801
	Prop	0.167	0.425	0.096	0.648	-0.082	0.696	0.094	0.656
	Vest	0.105	0.619	0.105	0.619	0.004	0.985	0.100	0.651
Max Functional Reach Test	Bas	0.304	0.140	0.060	0.775	-0.234	0.261	0.006	0.978
	Vis	0.372	0.068	-0.056	0.794	-0.303	0.142	-0.123	0.557
	Prop	0.150	0.473	0.130	0.536	-0.117	0.577	0.135	0.520
	Vest	0.041	0.848	0.019	0.929	-0.066	0.754	0.048	0.830

COP TMV was not related to YBT (**Table 42**) or FRT (**Table 43**) across IL×SIS. Coefficients were near zero and p-values exceeded 0.05 in nearly all cells.

Table 42. Spearman correlations between YBT metrics and COP TMV across IL×SIS conditions

COP Velocity (cm/s)		0 IL		1 IL		2 IL		3 IL	
Correlation	mCTSIB	Corr. Coef.	p	Corr. Coef.	p	Corr. Coef.	p	Corr. Coef.	p
Y Balance Test Left Anterior	Bas	0.689	0.000	0.455	0.029	0.329	0.156	0.457	0.033
	Vis	0.574	0.004	0.405	0.055	0.369	0.100	0.374	0.086
	Prop	0.670	0.001	0.643	0.002	0.460	0.036	0.555	0.007
	Vest	0.526	0.010	0.382	0.072	0.388	0.074	0.476	0.025
Y Balance Test Left Posterior-Lateral	Bas	0.567	0.005	0.470	0.024	-0.093	0.698	0.149	0.508
	Vis	0.657	0.001	0.319	0.138	0.194	0.399	0.080	0.725
	Prop	0.568	0.005	0.650	0.001	0.355	0.114	0.393	0.070
	Vest	0.637	0.001	0.437	0.037	0.185	0.411	0.397	0.068
Y Balance Test Left Posterior-Medial	Bas	0.379	0.074	0.210	0.336	-0.002	0.993	0.203	0.364
	Vis	0.350	0.102	0.131	0.551	0.031	0.896	0.184	0.413
	Prop	0.329	0.125	0.341	0.131	0.245	0.284	0.296	0.181
	Vest	0.216	0.322	-0.089	0.688	0.013	0.954	0.244	0.274
Left Composite Score	Bas	0.186	0.396	0.173	0.430	-0.260	0.268	-0.161	0.474
	Vis	0.263	0.226	0.076	0.730	-0.079	0.733	-0.099	0.662
	Prop	0.118	0.593	0.165	0.475	0.110	0.634	0.098	0.665
	Vest	0.053	0.809	0.001	0.996	-0.197	0.379	-0.046	0.840
Y Balance Test Right Anterior	Bas	0.493	0.017	0.228	0.296	0.439	0.053	0.486	0.022
	Vis	0.339	0.113	0.338	0.115	0.381	0.088	0.440	0.041
	Prop	0.544	0.007	0.374	0.095	0.334	0.139	0.489	0.021
	Vest	0.219	0.316	0.223	0.306	0.295	0.183	0.438	0.041
Y Balance Test Right Posterior-Lateral	Bas	0.438	0.036	0.364	0.088	-0.035	0.885	0.085	0.706
	Vis	0.512	0.013	0.341	0.112	0.094	0.685	0.132	0.559
	Prop	0.363	0.089	0.365	0.104	0.169	0.464	0.301	0.173
	Vest	0.435	0.038	0.384	0.071	0.192	0.392	0.373	0.087
Y Balance Test Right Posterior-Medial	Bas	0.281	0.194	0.124	0.574	0.017	0.942	0.120	0.595
	Vis	0.224	0.305	0.134	0.544	0.108	0.642	0.212	0.344
	Prop	0.181	0.410	0.174	0.452	0.126	0.586	0.344	0.117
	Vest	0.087	0.695	-0.045	0.839	0.129	0.568	0.275	0.215
Right Composite Score	Bas	0.050	0.819	0.024	0.915	-0.277	0.238	-0.283	0.202
	Vis	0.098	0.657	0.059	0.788	-0.155	0.504	-0.141	0.533
	Prop	-0.045	0.840	-0.069	0.767	-0.088	0.704	-0.004	0.986
	Vest	-0.096	0.664	-0.016	0.943	-0.151	0.503	-0.060	0.789

Table 43. Spearman correlations between FRT (mean, max reach) and COP TMV

COP Velocity (cm/s)		0 IL		1 IL		2 IL		3 IL	
Correlation	mCTSIB	Corr. Coef.	p	Corr. Coef.	p	Corr. Coef.	p	Corr. Coef.	p
Mean Functional Reach Test	Bas	0.113	0.609	-0.291	0.179	-0.202	0.394	-0.084	0.710
	Vis	-0.150	0.494	-0.313	0.146	-0.416	0.061	-0.106	0.640
	Prop	0.167	0.446	0.034	0.885	-0.043	0.854	-0.101	0.655
	Vest	0.027	0.904	0.096	0.664	0.059	0.793	0.015	0.946
Max Functional Reach Test	Bas	0.191	0.384	-0.288	0.183	-0.180	0.448	-0.062	0.785
	Vis	-0.158	0.470	-0.335	0.118	-0.415	0.061	-0.127	0.574
	Prop	0.183	0.404	0.081	0.726	-0.069	0.767	-0.082	0.717
	Vest	-0.004	0.988	0.090	0.683	0.036	0.873	0.005	0.984

across IL×SIS conditions. No significant relationships

Baseline functional tests were poor predictors of task-level postural responses under IL×SIS. The only recurring tendency was a weak, direction-specific link between non-dominant-leg YBT reaches (ANT, PL) and chest EV95%; TMV and COP measures showed no robust correspondence to baseline tests.

5.2.9. Correlation Between Mechanical Stability Indices and Postural Control Parameters Under IL×SIS Conditions

Scope and indices. Two mass-normalized mechanical descriptors were analysed against postural outcomes across all Instability Levels (IL) and Sensory Integration Strategies (SIS):

a) the Relative Instability Index (RII), which relates platform resistance to participant ankle-level corrective torque;

b) (ii) the Damping index (level-specific half-settling time per unit mass), representing passive decay characteristics of the platform (mechanical characterisation summarized earlier).

RII showed a consistent inverse association with EV95% at IL1 across SIS. For the chest, coefficients were moderate (≈ −0.40 to −0.56; $p \leq 0.049$), with similar patterns for the head (≈ −0.56 to −0.65; $p \leq 0.004$) and ankle (≈ −0.47 to −0.67; $p \leq 0.018$) (**Table 44**). At IL2 the strength attenuated and statistical significance became inconsistent across SIS (e.g., chest: Basic −0.45, $p = 0.025$; Proprioception −0.54, $p = 0.006$), and by IL3 most SIS were non-significant, with only isolated associations persisting. These findings indicate that RII best explained sway dispersion in the most stable configuration.

Table 44. Spearman correlations between RII and EV95% (head, chest, ankle) across IL×SIS. Coefficients are negative at IL 1 across SIS (moderate magnitude), weaken at IL 2, and are largely non-significant at IL 3, with few exceptions (e.g., Basic chest). Significant entries in the table are highlighted

RII		1 IL		2 IL		3 IL	
Correlation	mCTSIB	Corr. Coef.	p	Corr. Coef.	p	Corr. Coef.	p
Head 95% CI Volume	Bas	-0.555	0.004	-0.447	0.025	-0.557	0.004
	Vis	-0.533	0.007	-0.223	0.284	-0.224	0.282
	Prop	-0.397	0.049	-0.538	0.006	-0.237	0.254
	Vest	-0.535	0.006	-0.365	0.073	-0.289	0.181
Chest 95% CI Volume	Bas	-0.654	0.000	-0.628	0.001	-0.558	0.004
	Vis	-0.626	0.001	-0.374	0.066	-0.324	0.114
	Prop	-0.562	0.004	-0.539	0.005	-0.328	0.109
	Vest	-0.563	0.003	-0.323	0.116	-0.376	0.077
Ankle 95% CI Volume	Bas	-0.470	0.018	-0.394	0.051	-0.288	0.163
	Vis	-0.582	0.003	-0.148	0.482	-0.230	0.270
	Prop	-0.669	0.000	-0.412	0.041	-0.380	0.061
	Vest	-0.586	0.002	-0.090	0.668	-0.326	0.129

RII versus segment velocities. Associations between RII and segment mean velocities were weak and inconsistent. A few negative correlations reached significance at IL 1 (e.g., chest under Vestibular and Proprioception), but there was no stable pattern across SIS or IL, and effects largely dissipated at higher IL (**Table 45**). Overall, movement speed was poorly captured by RII compared with EV95% metrics.

Table 45. Spearman correlations between RII and segment TMV (head, chest, ankle) across IL×SIS

RII		1 IL		2 IL		3 IL	
Correlation	mCTSIB	Corr. Coef.	p	Corr. Coef.	p	Corr. Coef.	p
Head Velocity	Bas	-0.380	0.061	-0.568	0.003	-0.393	0.052
	Vis	-0.471	0.020	-0.157	0.454	-0.150	0.475
	Prop	-0.487	0.014	-0.500	0.011	-0.417	0.038
	Vest	-0.600	0.002	-0.173	0.410	-0.415	0.049
Chest Velocity	Bas	-0.222	0.286	-0.229	0.271	-0.201	0.335
	Vis	-0.219	0.304	-0.141	0.500	0.055	0.795
	Prop	-0.258	0.213	-0.054	0.797	-0.152	0.468
	Vest	-0.504	0.010	-0.039	0.852	-0.324	0.131
Ankle Velocity	Bas	0.011	0.958	-0.305	0.138	-0.358	0.079
	Vis	-0.171	0.424	-0.126	0.549	-0.324	0.115
	Prop	-0.218	0.294	-0.241	0.247	-0.112	0.594
	Vest	-0.380	0.061	-0.025	0.906	-0.317	0.141

RII versus COP metrics. For COP area and COP TMV, RII displayed negative correlations that were clearest at IL1 (multiple SIS $p < 0.05$) and weakened or vanished at IL2–3 (**Table 46**). This pattern mirrors the EV95% results: greater relative platform stability (higher RII) was associated with smaller sway envelopes and slower COP drift, predominantly in the easiest mechanical context.

Table 46. Spearman correlations between RII and COP metrics (area; TMV) across IL×SIS

RII		1 IL		2 IL		3 IL	
Correlation	mCTSIB	Corr. Coef.	p	Corr. Coef.	p	Corr. Coef.	p
COP area	Bas	-0.584	0.003	-0.436	0.055	-0.454	0.034
	Vis	-0.455	0.029	-0.467	0.033	-0.427	0.048
	Prop	-0.750	0.000	-0.580	0.006	-0.571	0.006
	Vest	-0.638	0.001	-0.644	0.002	-0.650	0.001
COP velocity	Bas	-0.525	0.010	-0.353	0.127	-0.467	0.028
	Vis	-0.332	0.122	-0.271	0.235	-0.328	0.137
	Prop	-0.660	0.001	-0.260	0.255	-0.522	0.013
	Vest	-0.437	0.037	-0.341	0.121	-0.437	0.042

Damping index versus EV95%. The Damping index correlated positively with EV95% at IL1 for the chest and head under most SIS ($r \approx 0.46–0.59$; $p \leq 0.024$), with attenuation at IL2 and mostly non-significant results at IL3 (**Table 47**). Thus, slower passive decay (greater damping index) coincided with larger spatial dispersion of sway, especially when instability remained moderate.

Table 47. Spearman correlations between the Damping index and EV95% (head, chest, ankle) across IL×SIS

Damping index		1 IL		2 IL		3 IL	
Correlation	mCTSIB	Corr. Coef.	p	Corr. Coef.	p	Corr. Coef.	p
Head 95% CI Volume	Bas	0.506	0.010	0.551	0.004	0.485	0.014
	Vis	0.460	0.024	0.352	0.084	0.257	0.216
	Prop	0.312	0.129	0.524	0.007	0.367	0.071
	Vest	0.521	0.008	0.447	0.025	0.293	0.176
Chest 95% CI Volume	Bas	0.584	0.002	0.671	0.000	0.479	0.015
	Vis	0.511	0.011	0.449	0.025	0.290	0.160
	Prop	0.523	0.007	0.434	0.030	0.524	0.007
	Vest	0.538	0.006	0.432	0.031	0.444	0.034
Ankle 95% CI Volume	Bas	0.479	0.015	0.242	0.245	0.219	0.292
	Vis	0.391	0.059	0.267	0.197	0.209	0.317
	Prop	0.608	0.001	0.346	0.090	0.352	0.085
	Vest	0.681	0.000	0.223	0.284	0.400	0.058

Damping index versus segment velocities. Correlations with segment velocities were small. A moderate positive association appeared under Vestibular–IL 1 (e.g., chest/head), but across IL×SIS the overall relationship was weak and frequently not significant (**Table 48).**

Table 48. Spearman correlations between the Damping index and segment TMV (head, chest, ankle)

Damping index		1 IL		2 IL		3 IL	
Correlation	mCTSIB	Corr. Coef.	p	Corr. Coef.	p	Corr. Coef.	p
Head Velocity	Bas	0.120	0.566	0.385	0.057	0.276	0.181
	Vis	0.208	0.329	0.287	0.164	0.045	0.832
	Prop	0.339	0.097	0.426	0.034	0.344	0.093
	Vest	0.586	0.002	0.234	0.260	0.437	0.037
Chest Velocity	Bas	0.194	0.353	0.305	0.138	0.224	0.283
	Vis	0.216	0.311	0.297	0.149	-0.084	0.692
	Prop	0.276	0.182	0.206	0.323	0.284	0.170
	Vest	0.531	0.006	0.219	0.294	0.351	0.101
Ankle Velocity	Bas	0.189	0.366	0.048	0.821	0.332	0.105
	Vis	0.127	0.554	0.311	0.131	0.207	0.320
	Prop	0.370	0.069	0.224	0.283	0.129	0.541
	Vest	0.511	0.009	0.239	0.249	0.348	0.104

Damping index versus COP metrics. Unlike segment velocities, COP outcomes tracked the Damping index more robustly. Positive correlations with COP area and COP TMV were observed across several SIS at IL 1–2 (multiple $p < 0.05$), remaining noticeable, though less uniform, at IL3 (**Table 49**). These results indicate that passive decay properties of the platform are most evident in pressure-based sway measures, particularly when sensory information is reduced.

Table 49. Spearman correlations between the Damping index and COP metrics (area; TMV)

Damping index		1 IL		2 IL		3 IL	
Correlation	mCTSIB	Corr. Coef.	p	Corr. Coef.	p	Corr. Coef.	p
COP area	Bas	0.557	0.006	0.454	0.045	0.418	0.053
	Vis	0.450	0.031	0.616	0.003	0.316	0.152
	Prop	0.729	0.000	0.595	0.004	0.681	0.001
	Vest	0.818	0.000	0.722	0.000	0.708	0.000
COP velocity	Bas	0.513	0.012	0.293	0.211	0.418	0.053
	Vis	0.380	0.074	0.436	0.048	0.229	0.305
	Prop	0.821	0.000	0.494	0.023	0.524	0.012
	Vest	0.716	0.000	0.512	0.015	0.543	0.009

Overall, mechanical indices explained only a limited but interpretable share of variance. RII was most related to EV95% and COP excursions at low instability; as instability increased, neuromuscular control and multi-segment coordination dominated and RII–outcome relationships weakened. The Damping index showed a similar pattern for EV95% and its clearest footprint in COP measures. Together, these results are consistent with a shift from passive mechanics-limited to active sensorimotor-limited control as IL×SIS challenge increased.

5.2.10. Expert-rated Task Difficulty Across IL×SIS Conditions

Across 400 trials (25 participants × 16 IL×SIS conditions), the external rater recorded six fall-like events (1.5%), 19 handrail contacts (4.75%), and 375 safe trials (93.75%), indicating high overall safety despite wide variation in task difficulty (**Table 50**).

Table 50. Trial outcomes across all IL×SIS conditions (N = 400)

Type	Count	Percentage of Trials
Fall down	0	0%
Fall imitating behavior (stepping/ grasping)	6	1.5%
Handrail contact	19	4.75%
Safe trials (no event)	375	93.75%
Total	400	100%

Expert difficulty scores increased systematically with IL and SIS (**Figure 43**). Mean ratings rose as tasks combined higher IL with greater sensory degradation, and the logarithmic model fit the across-condition pattern well ($R^2 = 0.943$). IQR bars also widened under the most challenging configurations, indicating greater inter-individual divergence when balancing demands were high.

This ordering was consistent with participants' self-ratings and objective markers of postural challenge, including increases in chest EV95%, segment velocities, and COP metrics with higher IL and reduced sensory input. Together, the expert judgements support the IL×SIS progression as a coherent difficulty ladder.

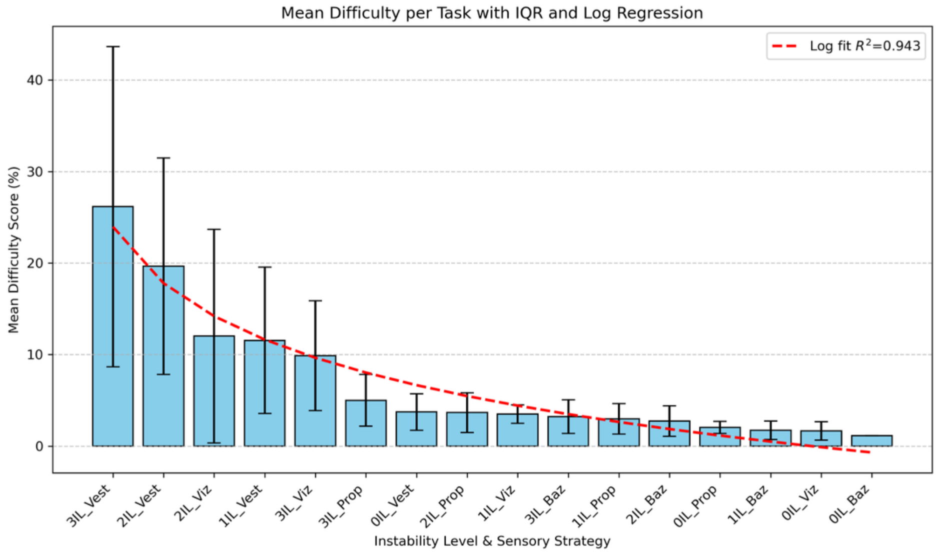

Figure 43. Expert-rated task difficulty across IL×SIS conditions. Bars denote the mean expert score per IL×SIS combination; whiskers show the interquartile range (IQR). The dashed curve is a logarithmic fit to the condition means ($R^2 = 0.943$). Difficulty rises monotonically with higher IL and more restrictive SIS (e.g., Vestibular and Visual), and variance widens under the hardest settings - mirroring the escalation observed in kinematic and COP measures (Blue bars = condition means; dashed red line = log fit)

5.3. **Discussion**

This study examined how mechanical instability (IL) and sensory information strategies (SIS) jointly shape postural control in healthy young adults. Two main patterns emerged: IL alone scaled task difficulty but only modestly perturbed control, whereas combining IL with SIS produced large, condition-dependent increases in dynamic and quasi-static sway.

Increasing instability without sensory manipulation raised segment velocities and EV95% only within a limited range compared with conditions that also altered SIS. Thus, a compliant base alone challenged postural control but, in most young adults, did not drive the system into marked instability. This is consistent with the within-SIS box-plot comparisons, which steepened only when sensory reliability was reduced.

Combining IL with SIS produced pronounced increases in TMV and EV95%. Under visual and vestibular strategies at higher ILs, chest and head metrics rose several-fold relative to the basic eyes-open condition, with changes approaching ~700% over baseline. Sensory down-weighting degrades state estimates, and platform compliance amplifies corrective imprecision, converting small controller errors into larger whole-body excursions. Unlike impulsive external perturbations, SIS scales with the individual and avoids confounding by perturbation tuning, which likely contributed to the monotonic trends.

Despite the high IL×SIS challenge, the protocol remained safe: only six of 400 tasks involved fall-like behavior (1.5%) and 19 required handrail contact (4.75%); 93.75% were completed without events. This supports the suitability of the method for functional balance assessment and automated individualized difficulty progression based on real-time monitoring.

Difficulty increased nonlinearly. Ordering tasks by segment TMV, EV95%, COP TMV, participant self-ratings, and expert ratings produced a clear logarithmic progression, with an excellent fit ($R^2 \approx 0.94$) in the mean-difficulty analysis. This predictable progression may help place submaximal thresholds for testing or training.

Effect-size heatmaps and pairwise tests localized the main transition to IL1 → IL2. Many IL2 ↔ IL3 contrasts were non-significant, suggesting that IL2 already imposed near-maximal challenge for most healthy adults when sensory reliability was reduced. The strongest changes occurred when vision was removed, underscoring its stabilizing role and the burden on vestibulospinal and cerebellar loops when it was unavailable.

Anthropometry had limited influence on IL×SIS outcomes. Age showed no associations, stature related to EV95% at IL1–IL2 but not to dynamic metrics, and body mass showed no consistent associations. These findings argue against routine anthropometric normalization of dynamic measures for this apparatus and suggest that quasi-static EV95% in easier tasks is more susceptible to body-size effects.

Mechanical indices explained performance mainly in the easiest context. RII and the damping index showed their clearest relationships with EV95% at IL1 and weak or absent associations with TMV; these relationships diminished as IL increased and SIS reduced sensory reliability. The inverted-pendulum approximation embedded in RII/damping is reasonable when base motion is small, but as IL rises, COM and BOS motions become tightly coupled and the omission of BOS feedback limits predictive power. COP metrics nevertheless showed negative correlations with RII under harder conditions, consistent with greater relative platform stability constraining sway envelopes and slowing COP drift.

Baseline clinical tests related selectively to IL×SIS performance. Non-dominant-limb YBT Anterior and Posterolateral directions correlated positively with chest EV95% in some conditions, whereas segment velocities and FRT did not. Normalizing YBT by limb length removed the EV95% association, consistent with a body-size effect rather than a shared control mechanism. This distinction likely reflects the fact that IL×SIS tasks require state estimation from degraded sensory streams on a compliant base, whereas YBT/FRT involve goal-directed reach with intact multisensory input and a static BOS. This also helps explain why TMV emerged as a cleaner marker of IL×SIS challenge than EV95%.

Overall, balance challenge was jointly governed by sensory reliability and the mechanical gain of the support surface. As sensory evidence degraded, corrective commands relied more heavily on vestibular and proprioceptive channels; as mechanical gain increased, residual estimation error was magnified at whole-body level. The conceptual model in **Figure 44** summarizes this interplay by linking sensory inflow, neural control, corrective actions, and the attenuating/augmenting role of the platform.

IL×SIS increased EV95% and TMV most steeply when vision was absent at IL2–IL3, indicating that sensory reliability rather than mechanical instability alone governed the challenge. Balance depends on visual, vestibular, and proprioceptive inputs, which the brain integrates to estimate body position and generate corrective adjustments.

At higher instability levels, the platform became more sensitive to body sway: smaller forces produced larger board movements than at lower ILs. This heightened sensitivity underscores the need for precise neuromechanical responses to maintain balance and prevent falls.

Combining instability levels with sensory strategies helps clarify their interaction in postural control. Reduced sensory input and higher instability engage vestibulospinal and cerebellar pathways more strongly within the neural controller. The vestibular system stabilizes posture when visual or proprioceptive input is reduced, proprioception supplies feedback on body position and movement, and the cerebellum integrates these signals and fine-tunes postural adjustments. The increases in chest TMV and EV95%, especially under vestibular conditions at higher instability levels, are consistent with this integrative role. The working mechanism is illustrated in **Figure 44**.

5.4. **Strengths and limitations**

This study has several limitations.

1. The cohort comprised only healthy young adults; direct extrapolation to older or clinical populations is uncertain.
2. External task difficulty and safety were judged by a single expert reviewer; although videos were randomized and the rater was blinded to IL×SIS, rater-specific bias and the absence of inter-rater reliability estimates limit generalizability.
3. Psychometric properties were not established. Test–retest reliability and learning/adaptation effects were not quantified; repeated sessions are needed to characterize within-subject variability, habituation, and minimal detectable change. The present results should not be interpreted as clinical cut-offs.
4. The testing sequence followed a fixed order, so order and carry-over effects cannot be excluded; future work should randomize or counterbalance IL×SIS presentation.
5. Sessions were relatively long, and residual fatigue may have influenced some trials despite scheduled rest. These constraints define the scope of inference and priorities for follow-up studies: broader samples, multi-rater designs, randomized protocols, and formal test–retest evaluation.

Strengths. The protocol combined a full IL×SIS matrix with 3-D kinematics and COP readouts, and triangulated these measures against anthropometry, mechanical indices (RII, damping), and baseline clinical tests (YBT, FRT). This multi-level design separated mechanical from neurosensory contributions and yielded convergent evidence across objective metrics and subjective/expert ratings, supporting the robustness and practical relevance of the findings.

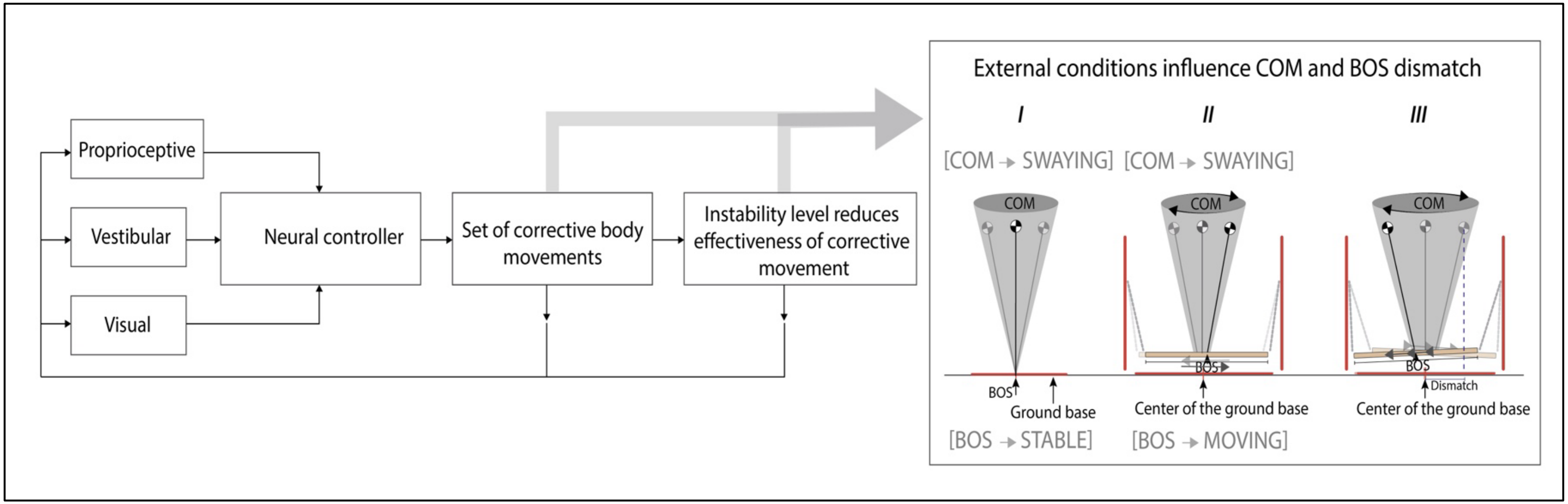

Figure 44. Sensorimotor control of posture under combined sensory information (SIS) and mechanical instability (IL).
Left schematic: visual, vestibular, and proprioceptive inputs are integrated by a neural controller, which issues a set of corrective body movements. The corrective output operates in closed loop (feedback arrow) but its effectiveness is attenuated by IL (rightmost block), because higher IL amplifies platform motion and the consequences of any imprecise correction.
Right schematic (I–III): external conditions shape the mismatch between the center of mass (COM) and the base of support (BOS). In I (stable BOS) the BOS is fixed (red vertical bars and baseline), COM sway remains small (grey envelope), and corrections are effective. In II (moving BOS) the platform translates/tilts so the BOS displace under the body (red arrows/offset baseline), enlarging the COM–BOS mismatch even for similar COM sway; more corrective action is needed. In III (high IL and/or reduced SIS) BOS excursions (ΔBOS) become larger and faster, while sensory information is degraded; the COM–BOS mismatch grows and corrective movements lose efficacy, explaining the empirically observed rises in chest/head TMV and EV95% under IL×SIS conditions.
Graphical conventions: grey regions depict typical COM sway envelopes; red elements mark BOS boundaries and displacement; black arrows indicate sway direction

5.5. Conclusions

1. Mechanical instability alone raised task difficulty in healthy young adults, as shown by self-ratings, objective metrics, and expert scores, but did not produce marked destabilization.
2. Pairing IL with SIS (IL×SIS) produced pronounced increases in dynamic and quasi-static postural demands, with condition-dependent changes reaching ≈700% relative to baseline.
3. Across SIS, the largest increments occurred from IL1 → IL2; IL2 and IL3 were often non-significantly different, indicating that IL2 already imposed near-maximal challenge for most participants.
4. Age showed no associations with IL×SIS outcomes. Stature related to quasi-static EV95% at IL1–IL2 but not to TMV, and these effects weakened at higher ILs.
5. Non-dominant-limb YBT Anterior and Posterolateral directions correlated positively with chest EV95% in some IL×SIS conditions, whereas no associations were observed for TMV or FRT. Normalizing YBT by limb length removed the EV95% association, consistent with a body-size effect.
6. RII and the damping index related to EV95% mainly at IL1 and were weak or absent for TMV; these relationships diminished as instability and sensory degradation increased, indicating limited explanatory power of the mechanical model once neurosensory control dominates.
7. TMV of body segments and COP scaled proportionally with expert-rated difficulty and was minimally confounded by anthropometry, whereas EV95% inflated disproportionately under high IL×SIS. TMV is therefore the more practical quantitative indicator of postural-challenge intensity.

6. CONSTRUCTION AND SYSTEM INTEGRATION

6.1. Introduction

The empirical measurements reported in this dissertation were performed on the commercial Abili Balance® suspended platform (Chapters 2 and 4–5), whereas the parametric modelling in Chapter 3 uses nominal suspension lengths (0.18/0.24/0.43 m) representative of commercial systems; the adaptive mechatronic prototype presented in Chapter 6 is a separate implementation derived from these findings and was not used to collect the reported data.

Healthy adults maintain postural control under low instability levels (IL) even when sensory input is reduced, but as IL increases the system depends more strongly on available sensory information. This is reflected in segmental behavior: chest EV95% rose by 123% from IL1→IL3 under the Basic sensory information strategy (SIS), but by 280% under the Vestibular SIS, indicating a larger compensatory trunk contribution when vestibular cues are emphasized or other inputs are constrained. These differences illustrate sensory reweighting as mechanical demands escalate.

6.2. Potential Application for Postural Control Training and Rehabilitation

The graded increases in chest EV95% across SIS×IL combinations index adaptive recruitment of segmental strategies under instability or sensory limitation. Such adaptations map directly to everyday contexts, e.g., uneven terrain or reduced-visibility environments, where control of larger sway excursions is critical to fall avoidance. Clinical literature likewise supports the relevance of explicit sensory integration in balance rehabilitation.

Some SIS×IL pairings yield comparable control despite different sensory input. For example, IL2–Visual and IL2–Proprioception produced similar postural outcomes, consistent with sensory substitution in healthy individuals. This provides a practical rehabilitation handle: when one sensory channel is compromised, therapists can up-weight or train alternative channels at equivalent mechanical difficulty.

Because the platform permits continuous titration of IL without external perturbations, training intensity can be dosed from minimal to severe destabilization, including levels at which even healthy young participants begin to struggle. This enables safe, progressive overload immediately below each participant's breakdown threshold.

These properties support targeted programs for sensory deficits – vision impairment, peripheral neuropathy, vestibular dysfunction – by selecting SIS×IL regimes that reduce reliance on the impaired modality or train its reintegration. The same framework can identify each patient's breakdown threshold (the SIS×IL region where control fails) and structure progression just below it to improve reserves while minimizing risk. Because the method spans a broad destabilization range, patients can begin at a tolerable setting and advance along a standardized, individualized trajectory.

6.3. Potential Application for Postural Control Assessment

Systematic manipulation of instability level (IL) and sensory information strategy (SIS) provides a controlled means to probe postural control efficiency and reserve. By titrating mechanical demands while selectively weighing visual, proprioceptive, or vestibular information, the platform elicits graded sway responses that reveal sensory allocation and when compensation fails. The point at which balance fails under a given SIS×IL combination operationalizes an individual breakdown threshold and provides an interpretable marker of capacity limits and adaptability.

Because SIS can be varied independently of IL, the assessment can profile sensory dependence by comparing performance across strategies at the same mechanical difficulty. This increases ecological validity: task configurations can mimic common high-risk contexts, such as reduced-visibility navigation, while keeping procedure and scoring standardized. In clinical practice, the same logic can separate modality-specific weaknesses (e.g., impaired proprioception) from general motor insufficiency and document compensatory reliance on spared modalities.

For longitudinal use, the platform supports standardized retesting under identical SIS×IL conditions, enabling objective tracking of change following rehabilitation or athletic training. Controlled SIS×IL manipulations therefore yield an assessment of balance capacity sensitive to both sensory integration and mechanical challenge.

6.4. **Design and Architecture**

The developed platform is intended to assess human postural control under controlled dynamic mechanical perturbations. The design prioritizes (i) biomechanical validity of the standing task, (ii) experimental safety, and (iii) adaptability to different protocols and measurement configurations. Mechanically, it is based on a suspended standing surface whose stability is modulated by controlled changes in suspension geometry. This enables programmable multidirectional instability without imposing rigid, predefined rotations, allowing a load-dependent, physiologically relevant response.

6.5. Main structural components

Support frame. The supporting structure is a modular open-frame assembly built from standardized 30×30 mm aluminum profiles. The frame provides a high stiffness-to-weight ratio while maintaining unobstructed access to the standing area. Its open architecture supports straightforward mounting and routing of experimental components (actuators, sensors, and cabling) and preserves visibility for supervision and external measurement systems.

Suspended platform board. The standing surface is a rigid rectangular board with a non-slip finish to reduce the risk of unintended foot slippage during perturbations. Visual foot placement markers are integrated on the upper surface to standardize initial stance geometry across trials and participants, improving repeatability and comparability of measurements.

Suspension and actuation system. The platform board is suspended from the supporting frame via four steel cables arranged at the corners. Each cable is coupled to a vertically mounted linear actuator (LA10), allowing independent adjustment of the effective suspension length at each corner. Importantly, the actuation principle is not to directly prescribe pitch, roll, or yaw trajectories. Instead, controlled changes in cable length modify the suspension geometry, which passively determines the platform height and orientation under the combined influence of gravity and the participant's load distribution. This architecture enables systematic tuning of instability characteristics (e.g., asymmetry, compliance, and sensitivity to weight shifts) through geometric reconfiguration rather than forced tilting, supporting physiologically meaningful postural responses.

Safety handrails. Two vertically adjustable handrails are integrated into the frame to mitigate fall risk and increase participant confidence, particularly during higher-intensity perturbations or when testing individuals with reduced balance capacity. Height adjustability allows the safety interface to be standardized across participants while keeping the handrails available without obstructing the standing surface.

Modularity and experimental configurability. The platform is designed as a modular rig that can be rapidly prepared for use, repositioned within the laboratory, and reconfigured between protocols. The frame provides flexible mounting opportunities for additional instrumentation (e.g., force sensing elements, motion capture markers, IMUs, or supplementary fixtures) without requiring changes to the core mechanical concept. **Figure 45** illustrates the overall geometry and placement of the principal components, including the suspended board, the corner actuation layout, and the accessible open-frame arrangement.

Hardware and Electronics Components. The mechatronic system developed for the adaptive balance platform integrates sensors, actuators, signal processing, and control logic into a unified architecture. This integration enables real-time generation of mechanical perturbations and simultaneous biomechanical data acquisition. The system is modular, scalable, and designed to support safe experimentation with human subjects.

Figure 45. CAD rendering of the adaptive balance platform. The suspended board hangs on steel cables whose effective lengths are adjusted by four corner-mounted linear actuators to modulate suspension geometry and produce programmable multidirectional instability. A force platform (F-P) is located under the board, and frame-mounted proximity sensors (P-1, P-2) estimate board position in the horizontal plane (x and y coordinates) and quantify displacement. Adjustable safety handrails are integrated into the open aluminum frame. Labels: F-P - force platform; P-1/P-2 - proximity sensors

6.6. Core subsystems and their functional roles

6.6.1. Control and Communication Subsystem

A microcontroller (Arduino ATmega328p) serves as the central I/O hub for low-level control and data acquisition. It receives high-level commands from the computer via USB serial and translates them into PWM and direction signals for each actuator. It also acquires analog input from actuator potentiometers and digital I2C input from proximity sensors.

Computer (running Python) handles high-level tasks, including Bluetooth and serial sensor acquisition, filtering, real-time algorithm execution, graphical display, and decision-making. It receives data from IMUs and the balance board via Bluetooth and communicates with the Arduino via USB serial.

6.6.2. Actuation Subsystem development

Each corner of the platform is actuated by a LA10 linear actuator (12 V DC) with an integrated screw-drive mechanism and built-in position-feedback potentiometer. In the present system, the actuators are used to adjust suspension-cable length rather than to impose a predefined angular trajectory of the platform; their role is to reconfigure suspension geometry and thereby modulate the effective instability level. Position feedback from the integrated potentiometer is read by the Arduino to monitor actuator stroke and platform pose in real time. Technical specifications of the actuator are provided in the manufacturer’s documentation.

Each actuator includes a 3-wire potentiometer. Its wiper signal is read by the Arduino via analog input (A0–A3), allowing continuous monitoring of actuator stroke length and thus platform pose.

Each actuator is controlled through a dedicated BTS7960 H-bridge driver rated for high current (up to 30 A). The driver receives PWM and direction signals from the Arduino and supplies bi-directional power to the actuator motor.

6.6.3. Sensing Subsystem development

Proximity Sensors (VL53L1X ×2) are mounted on the frame to measure the vertical distance to the edges of the suspended platform. Both share a common I2C bus but are individually addressed through dedicated XSHUT pins controlled by the Arduino. They provide real-time height tracking for passive platform monitoring and stability-limit detection.

Inertial Measurement Units (WIT Motion WT901BLECL ×2) are mounted on the subject's chest and foot. These 9-axis IMUs transmit acceleration, angular velocity, and orientation data via Bluetooth directly to the computer at ~100 Hz for analysis of segmental movement strategies and synchronization of body response with platform behavior.

Balance Board (Nintendo Wii Balance Board, model RVL-021) contains four strain gauge-based load cells at each corner. Its embedded analog controller computes the center of pressure (COP) in real time and transmits the data wirelessly over Bluetooth to the computer using third-party Python libraries.

6.6.4. Power Supply Subsystem development

Primary Power Supply (12 V, ≥300 W) powers all four linear actuators via the BTS7960 H-bridges and is sized to maintain sufficient current (≥25 A) during simultaneous actuator movement.

Buck Converter (12 V → 5 V) regulates a 5 V output for the Arduino board, potentiometers, and proximity sensors, supporting logic-level communication and sensor functionality.

All subsystems share a common ground to ensure stable analog referencing and prevent floating-voltage artifacts, especially in potentiometer feedback readings.

6.7. **Signal and Communication Structure**

The platform uses a two-tier closed loop. The host computer (Python) handles wireless sensing, decision-making, time-stamped visualization/logging, and sends setpoints via USB serial; the microcontroller (Arduino ATmega328p) performs deterministic low-level I/O and actuator drive. IMU and COP streams arrive at the host over Bluetooth, while proximity and actuator-position signals are sampled by the microcontroller (I2C for proximity; analog inputs for potentiometers). The host converts sway and pose into target positions and streams them over USB; the microcontroller translates these into PWM + direction signals for H-bridges. A shared 12 V/5 V power domain with common ground supports stable analog referencing. **Figure 46** shows the end-to-end topology.

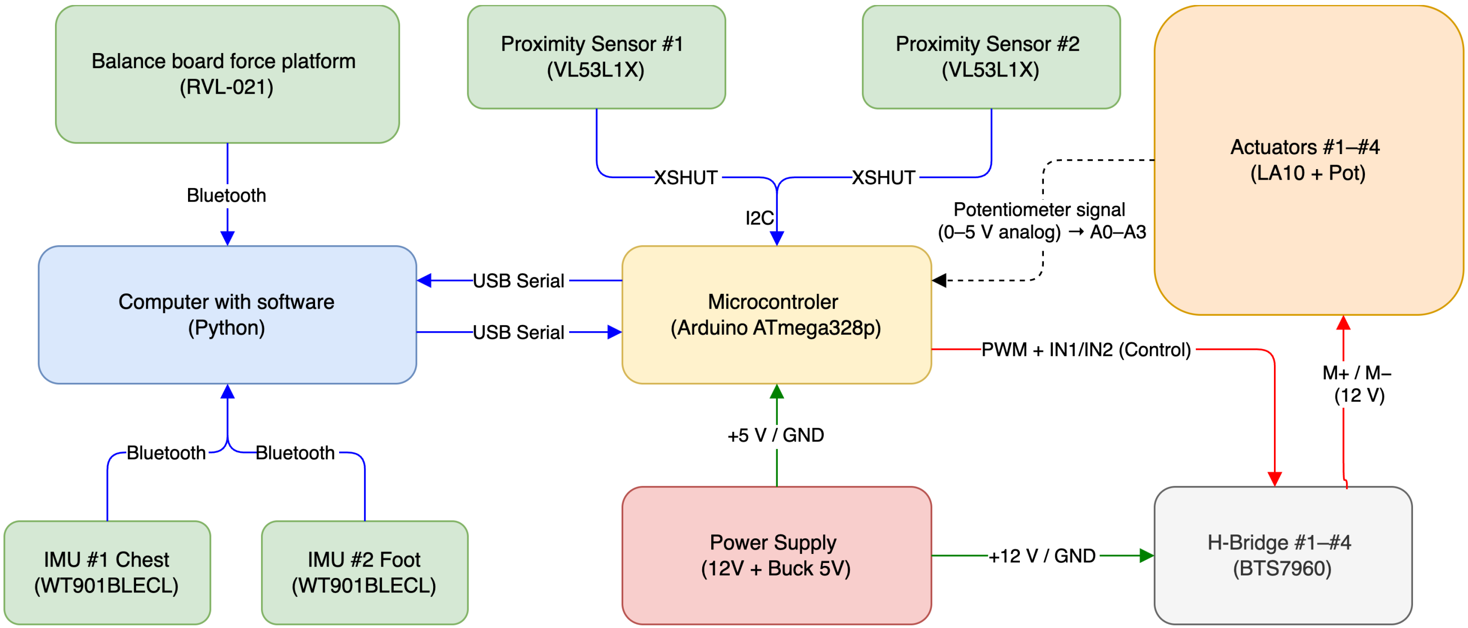

Figure 46. System-level signal and communication topology. Bluetooth delivers IMU and COP data to the host; USB serial connects host microcontroller; I2C links proximity sensors; dashed lines denote analog potentiometer feedback (A0–A3); black arrows show PWM/direction control to H-bridges; red/green paths indicate 12 V motor power and 5 V/GND distribution. The diagram separates sensing, control, and power domains within one closed-loop architecture

6.8. **Software and Logic Integration**

The platform executes a structured, safety-oriented automated testing algorithm that probes human postural responses to progressively increased mechanical destabilization. Execution is partially interactive and based on real-time biomechanical analysis. The procedure terminates automatically once destabilization reaches a predefined hazardous state (COP mean velocity > θ_2 for ≥3 s).

In this dissertation, the individualized outcome is the instability level reached at termination (functional limit) for the given sensory information strategy (SIS); for between-participant comparisons, this endpoint can also be expressed in participant-normalized form using the Relative Instability Index (RII, Eq. 38).

Here, the "functional limit" denotes the operational safety endpoint at which the automated stop criterion is triggered (COP mean velocity > θ_2 for ≥3 s) for a given SIS condition. θ_2 is conservatively defined as the 95th percentile of COP mean velocity from non-fall trials (falls/handrail contact excluded) and is not claimed to represent a physiological stepping/grasping boundary without external validation.

6.8.1. Initialization and calibration

At startup, an on-screen prompt instructs the operator to keep the platform board stationary with the participant off the device.

Potentiometer signals from the four linear actuators (LA10) are read against predefined limits for the initial static pose. If any stroke lies outside bounds, actuators are automatically driven to the target start position.

Two VL53L1X time-of-flight proximity sensors, mounted on opposite edges of the platform, measure the vertical distances from the frame to the board surface. Based on the known sensor placement and platform length, these readings are used to compute the board's vertical displacement and pitch angle relative to the frame. The resulting estimate of the platform's central vertical position is stored as the neutral reference for subsequent control. Roll orientation is not derived from the proximity sensors; instead, it is inferred from the actuator potentiometer feedback, which reports stroke extension at each corner and thus the effective suspension chain lengths.

The operator is prompted to place two WT901BLECL IMUs on the participant (chest and foot).

The system waits until the load on the Wii Balance Board (RVL-021) exceeds 1 kg. At that point, center of pressure (COP) zeroing is initiated: raw corner signals (FL, FR, BL, BR) are captured as baseline compensation values (ZeroX, ZeroY logic in compute_cop()) and subsequently subtracted from incoming data to yield corrected COP. Once the participant stands stably on the board, IMUs auto-calibrate to ensure consistent interpretation of acceleration magnitude throughout the test.

6.8.2. Test execution and safety logic

Before each cycle, the display indicates the sensory information strategy (SIS) to be tested (basic, proprioceptive, visual, vestibular). Upon start, the control loop activates and instability level (IL) increases in 30 s stages while actuators change stroke synchronously under algorithmic control. No additional operator input is required.

Every second, COP mean velocity is computed from the planar COP path length in a 1 s sliding window (rolling_velocity()) and checked against two thresholds: θ_1 (warning) and θ_2 (critical).

The warning (θ_1) and critical (θ_2) thresholds are derived from the non-fall distribution of COP mean velocity (θ_2 set to the 95th percentile; θ_1 set lower, e.g., the 80th percentile). If COP mean velocity exceeds θ_2 for ≥ 3 s, the system emits an audible warning, automatically terminates the current stage, and returns all actuators to the initial pose. For each SIS, three 30 s tasks are executed; after one SIS is completed, the system resets actuator positions, informs the operator, and proceeds to the next SIS.

6.8.3. Data acquisition and logging

All streams are resampled and logged at 30 Hz; analysis uses 1 s sliding windows. Per stage, .csv files record COP coordinates (X, Y), corner forces (FL, FR, BL, BR), COP mean velocity, IMU acceleration magnitude, proximity measurements, and actuator stroke positions. COP mean velocity is the sole criterion for automated safety decisions.

This algorithmic structure keeps test execution standardized, physiologically relevant, safe, and reproducible, and provides the operational basis for objective quantification of postural control reserve. The complete control sequence is depicted in **Figure 47**.

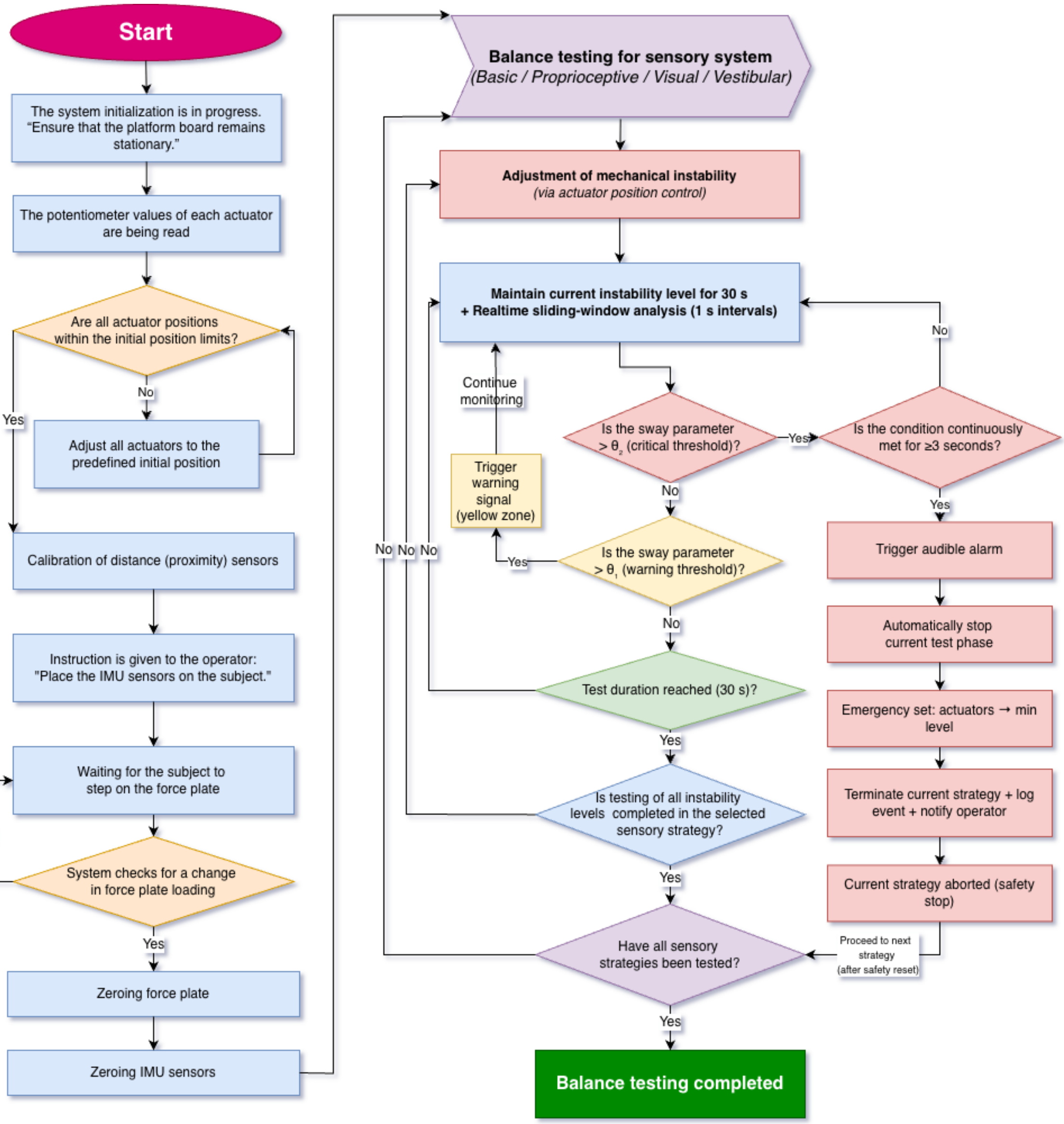

Figure 47. Automated testing algorithm flowchart for adaptive postural control evaluation. The flowchart shows initialization, sensor calibration (balance board zeroing; IMU auto-calibration), 30 s stepwise increases in IL, sliding-window COP mean velocity computation, and threshold-based safety logic (θ_1 warning, θ_2 critical with ≥3 s persistence). Green indicates completion states, yellow the warning zone, red the termination path, and blue process blocks. The algorithm is repeatable across basic, proprioceptive, visual, and vestibular SIS

6.9. **Selection of the Most Informative Parameter**

Correlation analysis between expert-rated task difficulty and biomechanical parameters identified mean velocity as the most consistently associated measure across anatomical locations, with the strongest effect at the platform level and center of pressure (COP). COP mean velocity showed a strong linear relationship with subjective difficulty scores ($r = 0.82$; $R^2 = 0.67$; $p < 0.001$; **Figure 48**), supporting its use as a sensitive real-time indicator of perceived postural challenge.

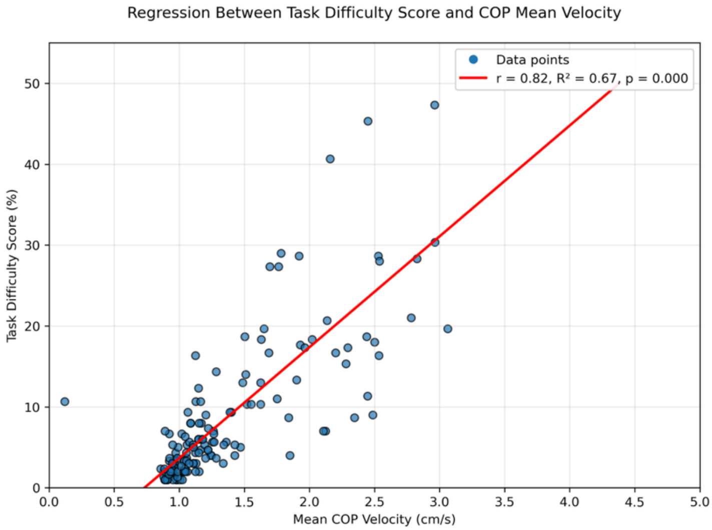

Figure 48. Linear regression between COP mean velocity and expert-rated task difficulty, showing a strong positive correlation ($r = 0.82$, $R^2 = 0.67$, $p < 0.001$)

Pearson correlation coefficients were computed for multiple motion parameters at four anatomical sites (head, chest, knee, platform): trajectory length, mean velocity, displacement range along X and Y axes, 95% confidence ellipsoid volume (EV95%), jerk index, and root mean square (RMS) (**Table 51**). RMS denotes the root mean square of the time-varying displacement signal of the tracked segment within the analyzed trial window. It summarizes the effective magnitude of oscillatory motion irrespective of sign and was included as an auxiliary descriptor of sway intensity in the present correlation analysis.

Subjective difficulty scores were obtained on a 0–100 scale from blinded expert video evaluation, as described in the Neurobiomechanical methodological section.

Table 51. Pearson correlation coefficients (r) between expert-rated task difficulty and biomechanical parameters at four anatomical locations. Stronger correlations are highlighted in red; strikethrough values are not statistically significant ($p \geq 0.05$)

Parameter/Body part	Head	Chest	Knee	Board
Path length	0.82	0.59	0.83	0.81
Mean velocity	0.82	0.58	0.83	0.81
Range X axis	0.71	0.28	0.27	0.78
Range Y axis	0.74	0.55	0.72	0.74
EV 95%	0.55	0.12	0.83	0.70
Jerk index	~~-0.01~~	~~0.08~~	~~0.04~~	0.15
RMS	~~0.06~~	0.14	0.16	0.18

Dynamic parameters such as jerk index and RMS exhibited low, inconsistent correlations across body segments, indicating limited standalone value for estimating perceived balance difficulty. This may reflect the relatively short task duration and the predominance of slower compensatory rather than rapid reactive movements.

The subset of COP-based parameters (trajectory length, mean velocity, X/Y range) was further examined (**Table 52**). COP mean velocity remained the highest-correlating measure, reinforcing its role as a robust indicator of postural challenge intensity.

Table 52. Pearson correlation coefficients (r) between expert-rated task difficulty and COP-derived parameters. Strongest associations are highlighted in red

	Total mean Velocity	Path length	Range X axis	Range Y axis
COP	0.82	0.82	0.83	0.75

These results indicate that mean velocity, particularly COP mean velocity, offers the strongest association with expert-rated task difficulty, making it a practical target for threshold-based control and automated decision-making in balance testing protocols.

6.10. **Determination of Threshold Values for Objective Balance Parameters**

To establish safe real-time monitoring thresholds, only balance tasks completed without loss of stability, defined as absence of falls or handrail contact, were analyzed. This ensured that threshold values reflected high yet tolerable instability levels.

Twenty-five participants completed 16 tasks each, lasting 40 s. Valid trials were segmented into 1 s non-overlapping windows, yielding >16,000 time segments. For each segment, the selected biomechanical parameter, primarily COP mean velocity, was computed. The 95th percentile of the resulting distribution was selected as a conservative safety threshold, representing the upper bound observed in trials completed without overt loss-of-balance events, and used as the real-time cut-off in automated control.

Processing workflow:

1. Participant performs balance tasks.
2. Exclude trials with falls or handrail contact.

3. Segment remaining trials into 1 s windows.
4. Compute biomechanical parameters for each window.
5. Pool and analyze distributions (~16,000 values).
6. Identify 95th percentile as upper safety threshold.

Because 1 s COP mean velocity distributions were positively skewed, the arithmetic mean was not representative of central tendency. The median and mode were therefore used to describe typical sway behavior, with the 95th percentile defining the extreme bound (**Figure 49**). Mean sway velocity differed systematically across body segments, with values at the platform interface exceeding those of the upper body. This supports the interpretation that the platform is the most responsive indicator of mechanical instability, whereas upper-body segments show attenuated sway responses. At the COP level, velocity measures from planar trajectories captured both typical and extreme sway dynamics, providing a sensitive real-time stability metric. These findings are summarized in **Table 53** and **Table 54**, which together provide the basis for selecting COP mean velocity as the principal control parameter in automated balance testing.

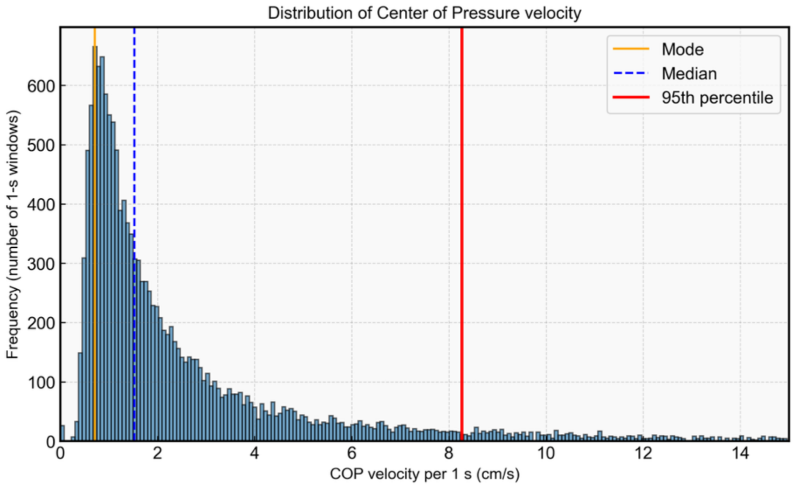

Figure 49. Distribution of COP mean velocity across all non-fall trials, calculated in 1 s non-overlapping windows. The histogram shows a positively skewed distribution with mode, median, and the 95th percentile threshold indicated. Values >15 cm/s were excluded to reflect physiologically plausible sway.

Table 53. Descriptive statistics of mean velocity (cm/s) for different body segments. Values were calculated from 1-second non-overlapping windows. The table presents mode, median, and 95th percentile values for each segment

Segment/ Velocity (cm/s)	Mode	Median	95th Percentile
Head	0.7	1.28	5.37
Chest	1.54	1.09	4.67
Knee	0.95	1.26	6.26
Board	0.73	1.3	10.02

Table 54. Descriptive statistics of Center of Pressure (COP) velocity (cm/s). Values were calculated over 1-second non-overlapping windows from planar COP trajectories. The table presents mode, median, and 95th percentile values across all conditions

Velocity (cm/s)	Mode	Median	95th Percentile
COP	0.76	1.54	8.95

6.11. **System Assembly and Calibration**

The final prototype of the adaptive balance platform was assembled as a complete functional unit comprising the structural frame, suspended platform with four linear actuators, integrated sensing modules, and the dedicated electronics block. The assembled platform, shown in **Figure 51**, shows the final mechanical and sensor configuration used during integration verification and experimental sessions. The electronic control unit, depicted in **Figure 50**, shows the motor drivers, microcontroller, voltage regulation, and control interfaces required for platform operation. This setup represents the final hardware configuration.

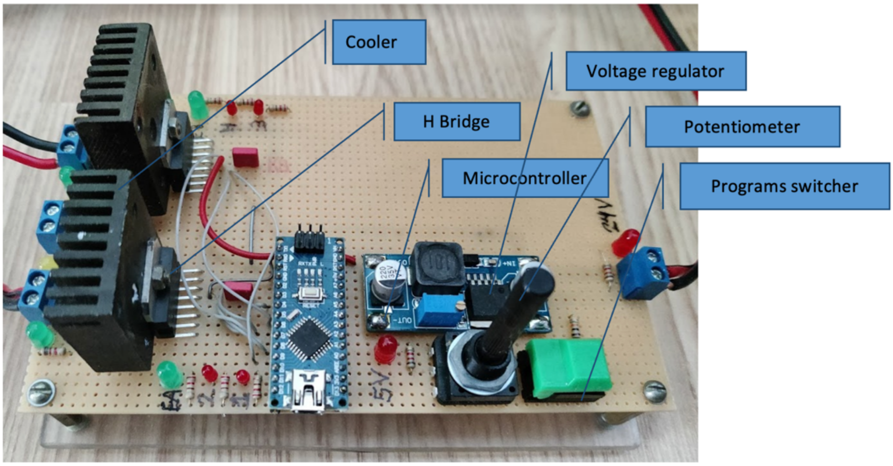

Figure 50. Electronics block of the adaptive balance platform, showing the Arduino ATmega328p microcontroller, four BTS7960 H-bridge motor drivers, 12 V power input, 12 V→5 V buck converter, actuator potentiometer feedback inputs (A0–A3), program selection switch, wiring terminals, and cooling modules

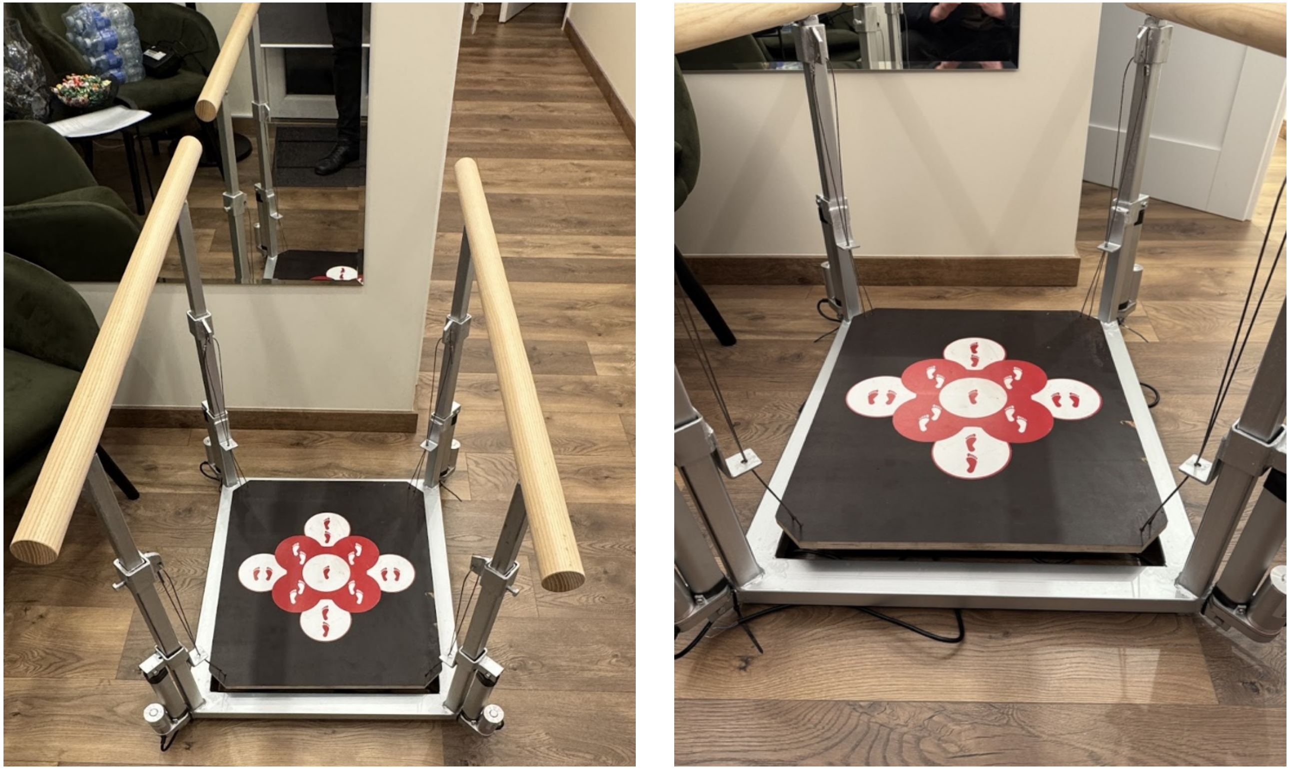

Figure 51. Assembled adaptive balance platform. Front and oblique views of the completed prototype showing the suspended board, four LA10 linear actuators, suspension cables, safety handrails, force platform, and frame-mounted proximity sensors used during all experimental procedures

6.12. **Verification of Integration Functionality**

The developed device is a fully automated mechatronic platform for standardized assessment of human postural control. It couples stepwise mechanical destabilization with selective sensory modulation (visual, proprioceptive, vestibular) to enable comprehensive testing of balance capacity. Operation is autonomous: the system performs automatic calibration, controls progressive instability, and monitors safety in real time with an emergency stop when sway exceeds predefined critical thresholds.

During testing, the software continuously acquires biomechanical signals and provides live graphical feedback. **Figure 53** illustrates center of pressure (COP) velocity over time as instability level (IL1–IL3) and sensory strategy (SIS) change, allowing visual verification of test progression and safety status. Results are stored after each session, enabling longitudinal comparison and visualization against reference values obtained in healthy individuals.

A demonstrative example of the follow-up functionality is provided in **Figure 52**. It shows two sessions of the same participant under identical SIS×IL configurations: Session 1 without cognitive load (single-task stance) and Session 2 with a concurrent color–word Stroop task (dual-task). Although not intended for diagnostic interpretation, the example demonstrates the platform's ability to repeat assessments under controlled conditions, store results, and visualize changes against a normative reference range. Here, higher sway values in the dual-task (Stroop) session than in the single-task session illustrate sensitivity to cognitive–motor interference during longitudinal follow-up under constant mechanical and sensory settings.

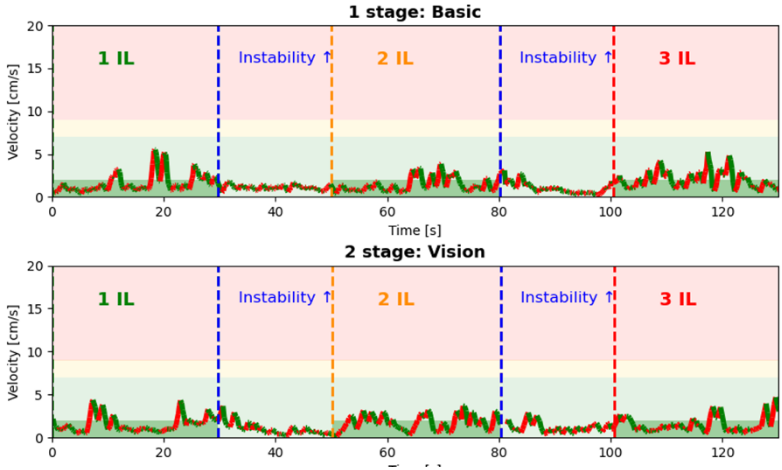

Figure 53. Real-time monitoring of postural sway during balance testing under different instability levels and sensory strategies. Graphs show COP velocity over time for basic (top) and visual (bottom) conditions across IL1–IL3. Colored background zones indicate predefined stability ranges, and vertical dashed lines mark transitions between instability levels

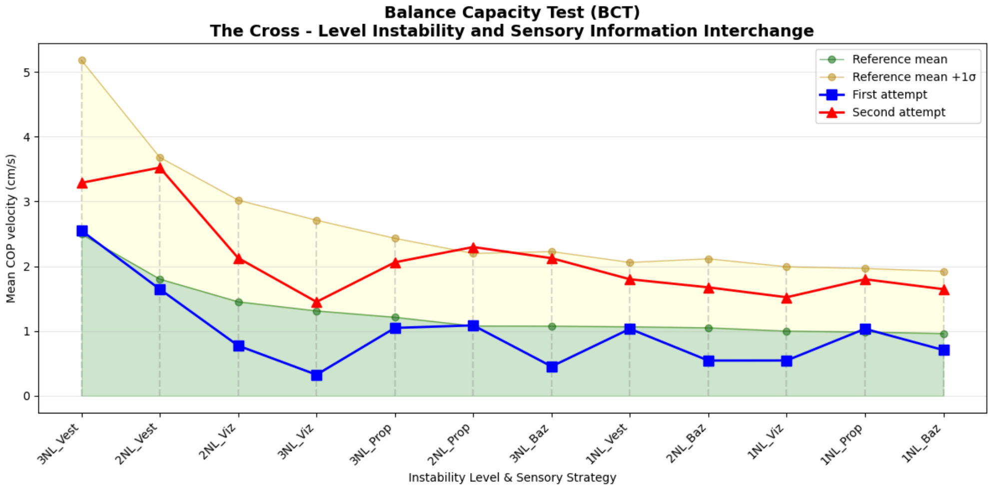

Figure 52. Comparison of COP mean velocity across all test conditions between two sessions of a single participant: Session 1 – single-task (no cognitive load); Session 2 – dual-task with a color–word Stroop task. Reference mean and ±1 SD for healthy individuals are overlaid. Both sessions remain within the normative range, but the dual-task (Stroop) session shows higher sway values than the single-task session. Legend mapping: "First attempt" = single-task; "Second attempt" = dual-task (Stroop)

6.13. Conclusions

1. A complete adaptive balance-testing platform was constructed and integrated, enabling standardized experiments with stepwise mechanical destabilization (IL) under controlled sensory information strategies (SIS).
2. The mechanical structure (open aluminum frame, cable-suspended non-slip board, four corner linear actuators, and adjustable safety handrails) provides programmable multidirectional instability while maintaining safety and modularity.
3. A modular mechatronic architecture integrated actuation, sensing (COP, IMUs, proximity), and a two-tier control scheme (host computer + microcontroller) to support real-time perturbation generation and synchronized biomechanical data acquisition.
4. A standardized, safety-oriented software workflow was developed, including initialization and calibration, automated progression across SIS×IL conditions, and consistent data logging to ensure reproducibility and longitudinal follow-up.
5. COP mean velocity was selected as the primary real-time indicator of task difficulty ($r = 0.82$; $R^2 = 0.67$) and used to define a safety limit (95th percentile of non-fall trials: 8.95 cm/s), implemented as an automatic termination criterion when exceeded for ≥3 s.

CONCLUSIONS

1. Using static and dynamic modeling, it was determined that the suspension geometry significantly affects the platform–pendulum interaction and balance restoration mechanics. An angled suspension produces asymmetric chain tensions and a non-linear increase of the net horizontal restoring force, therefore maintaining the same board displacement and restoring balance requires a larger horizontal corrective force/impulse than with a vertical suspension.

2. During experimental studies, the mechanical parameters of the balance assessment platform were determined and used to create instability indices suitable for comparative analysis and characterization of induced instability. The two main mechanical parameters are the horizontal displacement stiffness coefficient K_{IL} and the free-oscillation damping index ψ_{IL}: $K_{IL1} = 168\,N\,m^{-1}\,kg^{-1}$ $\psi_{IL1} = 0.35\,[s\,kg^{-1}]$, $K_{IL3} = 28.9\,N\,m^{-1}\,kg^{-1}$ $\psi_{IL3} = 1.5\,[s\,kg^{-1}]$. It integrates automatic calibration, stepwise instability-level control, and real-time COP-based safety logic within a two-tier host computer–microcontroller architecture.

3. Biomechanical analysis revealed two phases during voluntary movements on the platform: (1) a coupled phase, during which the body center of mass moves together with the platform board (base of support), and (2) an uncoupled phase, during which only the body center of mass moves while the platform board, having reached its movement limit, remains stationary. The relative duration of these phases and the magnitude of center-of-mass displacement in the uncoupled phase determine the biomechanical effects observed at different instability levels.

4. Gradually increasing mechanical instability and restricting sensory information significantly deteriorated postural stability indicators and increased perceived instability (in the most extreme case, sway volume increased by ~71 times, while movement velocity and perceived task difficulty increased by more than 600% when comparing Basic IL0 with Vestibular IL3). These IL×SIS outcomes did not correlate with conventional functional balance test results, indicating that the methodology assesses a specific neuromechanical reserve not captured by standard tests.

5. An adaptive, automated postural control assessment prototype was developed and validated. The system safely increases task complexity across instability levels, objectively evaluates postural control in real time using COP-based safety logic, and automatically stores and visualizes results, enabling repeated standardized testing and long-term monitoring of postural control (including individualized determination of the functional limit under different sensory conditions).

SANTRAUKA

Įvadas

Esami žmogaus posturalinės kontrolės[1] testai neleidžia gerai įvertinti individualios posturalinės kontrolės ribų[2], nes neužtikrina fiziologiškai natūralaus, dozuojamo ir išmatuojamo pusiausvyros trikdymo[3].

Tyrimo tikslas

Sukurti individualizuotą ir automatizuotą pusiausvyros vertinimo sistemą, kuri, laipsniškai didindama pusiausvyros trikdymo sudėtingumą, objektyviai nustatytų žmogaus funkcinę posturalinės kontrolės ribą.

Tyrimo uždaviniai

1. Eksperimentiškai nustatyti platformos mechaninius parametrus, apibūdinančius jos nestabilumo lygius – horizontalaus poslinkio standumo koeficientą bei laisvųjų svyravimų slopinimo rodiklį.
2. Statinio ir dinaminio modeliavimo būdu ištirti, kaip pusiausvyros vertinimo platformos plokštės pakabinimo geometrija veikia platformos ir ant jos esančios apverstos švytuoklės dinaminę sąveiką.
3. Įvertinti skirtingų nestabilumo lygių poveikį žmogaus stovėsenos valingų judesių biomechanikai.
4. Įvertinti nestabilumo lygių ir sensorinių strategijų sąveikos įtaką posturalinės kontrolės efektyvumui.
5. Sukurti adaptyvaus, automatizuoto įrenginio, skirto standartizuotam žmogaus posturalinės kontrolės vertinimui, prototipą ir patikrinti jo funkcionalumą.

Tyrimo metodai

Atlikti eksperimentiniai ir teoriniai tyrimai. Tyrimai vykdyti Kauno technologijos universiteto Mechatronikos institute.

Atliekant mechaninę analizę naudota pusiausvyros vertinimo platforma ir papildomai sukonstruotas rėmas statinėms jėgoms matuoti. Vykdyti du bandymų tipai: 1) statiniai – nustatyti horizontaliosios jėgos slenkstį ir eksperimentinį standumą k_{exp}; 2) laisvo slopinimo – įvertinti virpesių slopinimą.

[1] Posturalinė kontrolė – nervų ir raumenų sistema, valdanti pusiausvyros palaikymą judesio ir ramybės metu.
[2] Posturalinės kontrolės riba – aukščiausias pusiausvyros trikdymo sudėtingumo lygmuo, kur5 pasiekusi žmogaus nervų ir raumenų sistema dar sugeba stabilizuoti kūno masės centrą atramos ploto atžvilgiu neįjungdama apsauginių (reakcinių) strategijų.
[3] Pusiausvyros trikdymo sudėtingumas – pusiausvyros užduoties struktūrinis lygmuo, nusakantis, kiek ir kokių biomechaninių bei sensorinių veiksnių vienu metu turi kontroliuoti nervų sistema, kad išlaikytų COM–BOS santykį.

Taikant modeliavimą atlikti analitiniai ir skaitiniai tyrimai. Sukurtas dviejų laisvės laipsnių vežimo ir apverstos švytuoklės modelis su šoninėmis „spyruoklėmis“, imituojančiomis pakabos grandinių horizontalias reakcijas. Netiesinės lygtys spręstos ketvirtojo laipsnio Runge–Kutta metodu (Δt = 0,01 s), taikant iš anksto apibrėžtas pradines ir ribines sąlygas. Skaičiavimai vykdyti „Python 3.10“ aplinkoje (NumPy, Pandas, Matplotlib).

Biomechaniniame tyrime dalyvavo sveikas savanoris (autorius; 183 cm, 85 kg). Esant trims nestabilumo lygiams (toliau – IL) IL1–IL3, jis atliko lėtus pasvirimus pirmyn ir atgal, judant tik per čiurnos sąnarį. 3D judesių analizė vykdyta su „Qualisys Mocap®“ (100 Hz), fiksuojant žymeklius: numatomą COM, platformos centro ir žemės atskaitos taškus; skaičiavimai atlikti „Python“ aplinkoje, projektavus judesius sagitalinėje plokštumoje.

Neurobiomachaniniame tyrime dalyvavo 25 sveiki asmenys (13 moterų, 12 vyrų). Vertinta stovėsena 16 pusiausvyros vertinimo užduočių metu (IL0–IL3 × 4 sensorinės strategijos, toliau – SIS), skiriant po 40 s kiekvienai užduočiai. Tarp IL blokų darytos 5 min pertraukos. Naudoti šeši žymekliai (galva, krūtinė, petys, kelis, čiurna, platforma) su „Qualisys“ (100 Hz) ir „Wii Balance Board COP“ signalui. Užtikrinta pastovi pėdų padėtis ir sinchroninis duomenų įrašas. Pusiausvyros atskaitai vertinti išmatuota kiekvieno tiriamojo YBT, FRT. Pirminiai rodikliai: segmentų TMV ir EV95 %, COP TMV ir COP A95. Analizė atlikta Python“ („NumPy“, „Pandas“, „SciPy“, „Matplotlib“).

Konstrukcija ir sisteminė integracija. Sukurta ir pagaminta mechatroninė platforma. Valdymas – dviejų lygių uždaro ciklo architektūra (kompiuteris ir mikrovaldiklis), su automatine kalibracija, laipsniškai didinamo nestabilumo lygio valdymu ir sauga - kritinių slenksčių detekcija. Užbaigto prototipo elektronikos mazgas ir surinkta sistema pateikta nuotraukose.

Mokslinis naujumas

1. Nustatyta, kad platformos pakabos geometrija reikšmingai lemia platformos ir ant jos stovinčio žmogaus viršutinės kūno dalies judesių sąveiką. Keičiant pakabos ilgį, kinta tiek poslinkio jėgos slenksčiai, tiek svyravimų slopinimo koeficientai. Šių mechaninių parametrų visuma apibrėžia skirtingus nestabilumo lygius, todėl nestabilumas nėra vieno parametro funkcija – tai daugiaparametris (kombinuotas) rodiklis.
2. Sukurtas ir įvertintas pasyvaus pusiausvyros destabilizavimo metodas, kuris, valdomai didinant platformos nestabilumą ir ribojant sensorinę informaciją, didina pusiausvyros trikdymo sudėtingumą be papildomų išorinių jėgų. Metodas leidžia dozuoti trikdymo sudėtingumą ir pasirodė efektyvus net sveikiems jauniems asmenims.
3. Sukurta posturalinės kontrolės vertinimo sistema, kuri nuosekliai ir laipsniškai didina pusiausvyros trikdymo sunkumą, realiuoju laiku registruoja tiriamojo pusiausvyros parametrus ir automatiškai lygina juos su disertacijos metu nustatytais saugumo slenksčiais. Testavimas tęsiamas, kol pasiekiama funkcinė posturalinės kontrolės riba.

Ginamieji teiginiai

1. Statiniu ir dinaminiu modeliavimo būdu parodyta, kad kampinė platformos pakabinimo geometrija sukuria reikšmingą reaktyvių jėgų asimetriją tarp pakabos pusių. Dėl šios asimetrijos kinta platformos ir ant jos esančios apverstos švytuoklės tarpusavio dinamika (perdavimo savybės, faziniai ryšiai, parametrai).
2. Eksperimentais nustatyta, kad, keičiant pakabos ilgį, nuosekliai kinta platformos plokštės poslinkiui reikalingas jėgos slenkstis ir svyravimų slopinimo koeficientas. Šių parametrų visuma apibrėžia konkretų mechaninio nestabilumo lygį.
3. Nustatyta, kad skirtingi mechaninio nestabilumo lygiai suformuoja skirtingus kūno masės centro (p-COM) ir atramos ploto (BOS) sąveikos režimus, kurie skiriasi savo p-COM ir BOS fazių santykiu.
4. Parodyta, kad, derinant mechaninio nestabilumo lygius su sensorinės informacijos ribojimu, galima labai padidinti posturalinės kontrolės trikdymą be papildomų išorinių mechaninių perturbacijų net sveikiems jauniems asmenims.
5. Sukurtas ir išbandytas adaptuojamo, automatinio posturalinės kontrolės testavimo aparato prototipas, automatiškai keičiantis nestabilumo lygius ir realiuoju laiku registruojantis biomechaninių parametrų, kurie svarbūs griuvimo nuspėjimui, kitimą.

Praktinė vertė

Sukurta adaptyvi posturalinės kontrolės vertinimo ir treniravimo sistema leidžia individualizuotai parinkti pusiausvyros trikdymo mechanizmus, t. y. mechaninio nestabilumo lygius ir sensorinės informacijos strategijas (SIS: *Basic, Proprioception, Visual, Vestibular*). Šie veiksniai derinami tarpusavyje testavimo ar treniravimo metu, todėl galima laipsniškai didinti sudėtingumą, objektyviai palyginti tiriamuosius ir ilgainiui sekti paciento būklės pokyčius tomis pačiomis sąlygomis. Be to, automatizuotas algoritmas realiuoju laiku taiko COP greičio įspėjimo / kritinius slenksčius ir pats sustabdo testą, kas užtikrina saugų ir vienodą procedūros vykdymą bei lengvą rezultatų pakartojimą. Rezultatai saugomi ir lyginami su norminiu intervalu, todėl galima patikimai atlikti pakartotinius įvertinimus. Jei reikia, mechaninį sudėtingumą galima sulyginti tarp skirtingo ūgio dalyvių naudojant santykinį mechaninio nestabilumo indeksą (angl. *Relative Instability Index*, RII).

Pritaikomumas

Klinikinė praktika (neurologija, geriatrinė reabilitacija). Individualizuotas SIS×IL dozavimas leidžia išryškinti sensorinės priklausomybės profilį (pvz., propriocepcijos ar vestibulinės įtakos) ir nustatyti kritinę kontrolės ribą. Progresas stebimas taikant tas pačias sąlygas ir automatinius slenksčius.

Diagnostika ir treniravimas. Sistema pateikia pusiausvyros trikdymo diapazoną nuo minimalaus iki didelio, leidžia tiksliai dozuoti krūvį, kol pasiekiama individuali kritinė posturalinės kontrolės riba.

Moksliniai tyrimai. Standartizuota IL×SIS schema, integruotas parametrų registravimas ir saugojimas bei apibrėžti saugos / baigimo kriterijai sudaro sąlygas kartoti eksperimentus tomis pačiomis sąlygomis, kas būtų naudinga lyginamajai analizei.

Darbo rezultatų aprobavimas

Rezultatai pristatyti dviejose tarptautinėse mokslinėse konferencijose (BIOMDLORE 2021, Vilnius; BIOMDLORE 2023, Bialystok) ir publikuoti dviejuose recenzuojamuose tarptautiniuose žurnaluose (*Web of Science / Scopus*): *Technology and Health Care* (2022) ir *Applied Sciences* (2024).

Disertacijos struktūra

Disertaciją sudaro įžanga, literatūros apžvalga, keturios tiriamosios dalys (mechaninė analizė, modeliavimas, biomechaninė ir neurobiomechaninė analizės), prototipo konstrukcija ir sistemos integracija bei išvados.

Literatūros apžvalga

Literatūroje posturalinė kontrolė apibrėžiama kaip gebėjimas palaikyti posturalinę orientaciją (kūno segmentų išsidėstymą gravitacijos atžvilgiu) ir posturalinį stabilumą. Ji apima tiek anticipacinius (iš anksto planuojamus) posturalinius sureguliavimus, lydimuosius valingus judesius, tiek reaktyvias, grįžtamuoju ryšiu pagrįstas korekcijas, atsirandančias sutrikus pusiausvyrai.

Stabilumas dažniausiai siejamas su kūno masės centro (COM) projekcijos padėtimi atramos plote (BOS): COM projekcija BOS viduje yra būtina, tačiau nepakankama sąlyga, nes realiame judėjime svarbu ne tik „kur yra“ COM, bet ir „kaip greitai“ jis juda. Dinaminis stabilumas priklauso nuo COM greičio, todėl literatūroje taikomos greičiu paremtos stabilumo sąvokos (pvz., stabilumo rezervas, paremtas COM padėtimi ir greičiu). Šios sąvokos leidžia aprašyti situacijas, kai COM dar yra BOS viduje, bet dėl didelio greičio artėja neišvengiamas pusiausvyros praradimas.

Literatūros analizė išryškino penkias spragas: 1) trūksta analizės, kaip pusiausvyros platformų pakabos geometrijos veikia žmogaus ir platformos sąveiką; 2) nėra universalių, tarpusavyje palyginamų mechaninio nestabilumo indeksų; 3) riboto atramos ploto judėjimo platformose nepakankamai aprašyta COM ir BOS sąveika; 4) retai kiekybiškai vertinama mechaninio nestabilumo ir jutiminės informacijos ribojimo sąveika (IL×SIS) be išorinių perturbacijų; 5) trūksta adaptacinių sistemų, kurios realiuoju laiku registruotų rodiklius ir taikytų automatinius saugos slenksčius.

Mechaninė analizė

Šiame disertacijos skyriuje buvo siekiama nustatyti platformos konfigūracijų parametrų reikšmes, kad būtų galima suformuoti nestabilumo indeksus, tinkamus lyginamajai mechaninių pusiausvyros platformų analizei ir sukeliamo nestabilumo lygiui apibūdinti. Tam eksperimentais apibrėžiami du pirminiai mechaniniai rodikliai: horizontalus standumas (išorinės jėgos kiekis platformos plokštei patraukti iš neutralaus taško) ir laisvųjų svyravimų slopinimas (amplitudės gesimo greitis). Šie rodikliai sudaro metodiką, leidžiančią parametrizuotai palyginti nestabilumo lygius (IL1–IL3) tarpusavyje.

Tirta „Abili Balance“ platforma, kuri sudaryta iš 0,60×0,50 m plokštės, kuri pakabinta keturiomis grandinėmis ant rėmo kolonų. Kiekvienoje kolonoje – trys grandinių prikabinimo laikikliai, leidžiantys pakopiškai keisti aktyvų grandinės ilgį ir taip sudaryti tris iš anksto nustatytus nestabilumo lygius (IL1–IL3). Grandinės prie kolonų pritvirtintos pasuktos 45° kryptimi į vidų, vertinant iš platformos rėmo perspektyvos. Taikytos dvi metodikos dviem mechaniniams parametrams matuoti:

1. Horizontaliam standumui nustatyti buvo matuota, kiek jėgos $F(x)$ reikia, kad platformos plokštė, apkrauta svoriu m, būtų palaikoma patraukta nuo centro atstumu x. Ant plokštės centro buvo uždėtas 20 kg svoris. Buvo matuotas jėgos poreikis plokštei išlaikyti neutralioje padėtyje, ją patraukiant numatytais intervalais. Tai atlikta visiems trims nestabilumo lygiams (IL1–IL3). Iš gautų jėgos ir atstumo duomenų nustatyti standumo koeficientai k_{exp} (N/m^{-1}) (55 lentelė).

Standumo bandymai parodė aiškią tiesinę jėgos ir atstumo priklausomybę visiems nestabilumo lygiams. Lyginant lygius vienu skaičiumi patogiausia naudoti K_{IL}.(standumas vienam kūno masės kilogramui, N/m/kg) Gauti dydžiai yra tokie: IL1 = 168,7 $N \cdot m^{-1} \cdot kg^{-1}$, IL2 = 65,8 $N \cdot m^{-1} \cdot kg^{-1}$, IL3 = 28,9 $N \cdot m^{-1} \cdot kg^{-1}$. Tai reiškia, kad konkrečiam tiriamajam standumo koeficientą galima tiesiog apskaičiuoti kaip $k = K_{IL} \cdot m$. Taigi trumpesnės grandinės (IL1) sukuria gerokai didesnį jėgos slenkstį, o ilgos (IL3) – mažesnį.

Kad į mechaninį vertinimą įtrauktume tiriamojo antropometrinius parametrus, naudojamas bedimensis santykinio nestabilumo indeksas. Konceptualiai jis nusako santykį $RII \approx \frac{\text{platformos mechaninis pasipriešinimas}}{\text{kūno sukelta gravitacinė grąžinamoji apkrova}}$. Matematiškai jis išreiškiamas taip: $RII = \frac{K_{IL}\, h_{COM}}{g}$, čia h_{COM} – masės centro aukštis, g – laisvojo kritimo pagreitis. Didesnis RII reiškia santykinai standesnę atramą tam konkrečiam asmeniui (mechaniniu požiūriu lengvesnę užduotį), mažesnis RII – didesnį santykinį nestabilumą.

2. Laisvųjų svyravimų slopinimas. Platformos plokštės (suminė apkrova – 50 kg) buvo atitraukiama ir paleidžiama laisvai svyruoti; poslinkiai fiksuojami integruotu 100 Hz akselerometru. Pradiniai atitraukimo dydžiai: 4,0 cm (IL3–IL2) ir 3,5 cm (IL1); registracijos trukmė – 60 s. Iš vibrogramų skaičiuotas logaritminis dekrementas, slopinimo santykis ζ ir efektyvus slopinimo koeficientas. Visų nestabilumo lygių vibrogramos pateiktos 54 pav., charakteristikos – 56 lentelė.

Laisvųjų svyravimų bandymai parodė, kad sistema yra silpnai slopinta ($0 < \zeta < 0{,}050$), o gesimo trukmė didėja didėjant nestabilumo lygiui. Su 20 kg apkrova pusinės slopimo trukmės buvo ~7 s (IL1), 15 s (IL2) ir 30 s (IL3). Ši efektą siekiant panaudoti prognozavimui prie skirtingų masių, slopinimo indeksas apibrėžiamas kaip $\psi_{IL} = \Delta T_{1/2}/\Delta m\ [s\ kg^{-1}]$. Praktikoje tai reiškia, kad $T_{1/2}$ didėja apytiksliai proporcingai masei, todėl, pvz., 70 kg tiriamajam numatomos trukmės būtų apie 24,5 s, 52,5 s ir 105 s atitinkamai IL1–IL3.

Taigi K_{IL} leidžia vertinti skirtingus nestabilumo lygius pagal jėgos slenkstį (IL1 > IL2 > IL3), o ψ_{IL} – pagal virpersių gesimo trukmę (IL1 < IL2 < IL3). Šie du indeksai svarbūs lyginamajai platformos konfigūracijų analizei ir elgsenos prognozėms esant skirtingoms masėms. Kai reikia atsižvelgti į kūno sandarą, pridedamas bedimensis RII.

55 lentelė. Teorinės ir eksperimentinės standumo koeficiento *k* reikšmės, esant 20 kg apkrovai

IL	Grandinės ilgis *l* (m)	Eksperimentinė nuolydžio reikšmė k_{exp} (N m⁻¹) †
3	0,445	579,7
2	0,255	1 316
1	0,125	3 382

56 lentelė. Kampinės pakabos platformos virpesių ir slopinimo charakteristikos esant trims iš anksto nustatytiems nestabilumo lygiams

Charakteristika	IL 1	IL 2	IL 3
Grandinės ilgis (m)	0,125	0,255	0,445
Platformos plokštės centro poslinkis nuo platformos rėmo centro (cm)	3,500	4,000	4,000
Jėga, reikalinga plokštei išlaikyti stabilios atitrauktos padėties prieš prasidedant svyravimams (N)	310	196	132
Periodas (s)	0,502	1,007	1,238
Ciklų skaičius (*n*)	20	20	20
Likusi pradinė amplitudė po *n* ciklų	0,143	0,500	0,700
Išmatuotas natūralus kampinis dažnis (ω_0) [$rad \cdot s^{-1}$]	10,649	6,243	5,077
Logaritminis dekrementas (δ) per *n* ciklų	1,946	0,693	0,357
Logaritminis dekrementas pirmame cikle	0,097	0,035	0,018
Slopinimo santykis (ζ)	0,015	0,006	0,003
Kritinis slopinimo konstanta (C_c)	1064,95	624,26	507,73
Efektyvus klampusis slopinimo koeficientas (C)	16,49	3,44	1,44
Slopinamas natūralus kampinis dažnis (ωd) [$rad \cdot s^{-1}$]	10,65	6,24	5,08

Pastaba. Lentelėje pateikiami: grandinės ilgis *l*, pradinis platformos plokštės centro poslinkis x_0, išlaikymo jėga F_0, virpesių periodas *T*, užfiksuotų ciklų skaičius *n*, santykinė likusi amplitudė po *n* ciklų, išmatuotas natūralus kampinis dažnis ω_0 (pagal *T*), logaritminis dekrementas δ, slopinimo santykis ζ, kritinė slopinimo konstanta Cc, efektyvus klampusis slopinimo koeficientas C ir slopinamas natūralus kampinis dažnis ω*d* (apskaičiuotas kaip $\omega_0\sqrt{(1-\zeta^2)}$). Vertės pateiktos, kai bendra plokštės apkrova *m* = 50 kg (≈40 kg išorinė apkrova + ~10 kg plokštės masė).

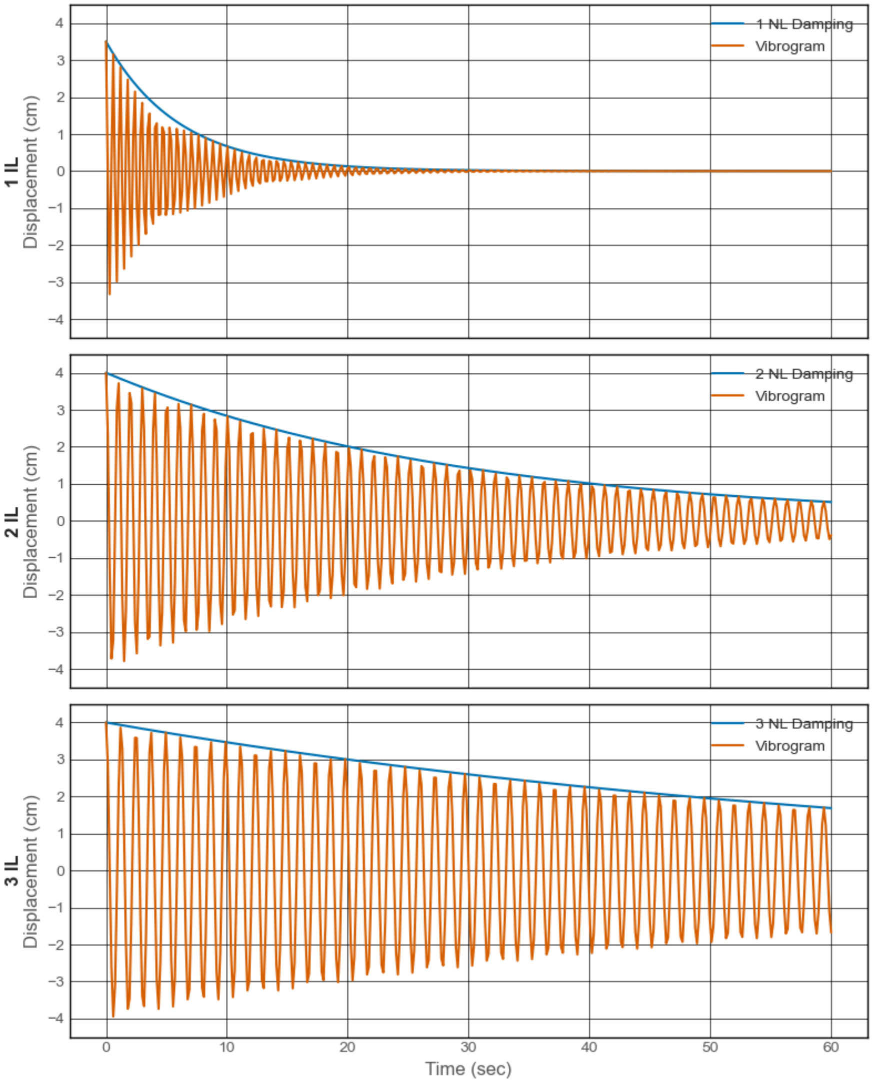

54 pav. Laisvojo gesimo vibrogramos trims nestabilumo lygiams (viršuje – IL 1; viduryje – IL 2; apačioje – IL 3). Oranžinės kreivės rodo išmatuotą plokštės poslinkį priekinės ir užpakalinės krypties atžvilgiu, mėlynos kreivės – vienos eksponentės apgaubas, naudotas slopinimo santykiui ζ nustatyti. Gesimo trukmė didėja augant nestabilumui

Modeliavimas

Šiame disertacijos skyriuje nagrinėjama, kaip platformos pakabos geometrija lemia sistemos mechaninį stabilumą ir pusiausvyros atkūrimą.

Modeliavimo tikslas – kiekybiškai įvertinti pakabos geometrijos poveikį stabilumui atliekant statinį ir dinaminį modeliavimą. Analizuojamos dvi pakabinimo geometrijos (∠ kampinė ir ‖ vertikali) ir trys grandinių (laikiklių) ilgiai (0,18 m, 0,24 m, 0,43 m), atitinkantys didėjantį nestabilumo lygį. Šie ilgiai parinkti pagal tipinių įrenginių konfigūracijas.

Statinė analizė. Sudarytos platformos ir pakabos sistemos pusiausvyros lygtys leidžia apskaičiuoti, kokios išorinės horizontaliosios jėgos reikia pasirinktam platformos plokštės poslinkiui ir kaip kinta kairės / dešinės grandinių įtempiai bei jų horizontaliosios projekcijos. Rezultatai rodo, kad: 1) tam pačiam poslinkiui kampinei pakabai reikia didesnės jėgos nei vertikaliai (129 vs 119 N); 2) neutraliame taške vertikali pakaba neturi horizontaliųjų projekcijų, o kampinė jas turi, todėl asimetrija atsiranda iš karto; 3) paslinkus plokštę, ∠ geometrijoje asimetrija sparčiai auga, o ‖ atveju pasiskirstymas išlieka beveik simetriškas. Vizualiai tai parodo 55 ir 56 pav. asimetrija esant neutraliai ir paslinktai padėčiai.

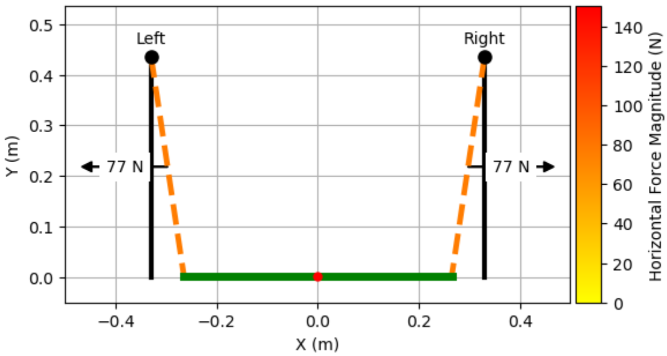

55 pav. Kampinė pakaba, neutrali padėtis (x = 0 m). Pradiniai grandinių kampai (9,01°) sukuria priešingas horizontaliąsias jėgas (~77 N kiekvienoje), kurios viena kitą kompensuoja. Grynoji išorinė stūmos jėga lygi nuliui

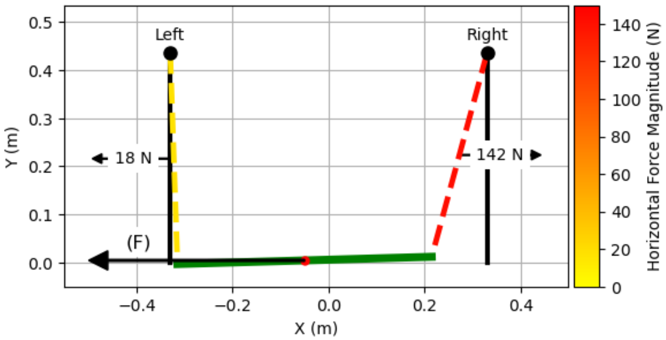

56 pav. Kampinė pakaba, paslinkta padėtis ($x = 0{,}05$ m). Grandinių kampai tampa asimetriški (2,09° ir 16,11°), todėl horizontaliosios komponentės labai nevienodos (17,8 N kairėje ir 142,3 N dešinėje). Stabilizacijai reikia ~125 N išorinės jėgos

Dinaminė analizės tikslas – nustatyti, kokio mažiausio vienkartinio korekcinio pagreičio reikia, kad kūnas (apversta švytuoklė) iš −20° padėties vėl pasiektų vertikalią poziciją neperžengusi leidžiamojo plokštės poslinkio. Taip įvertinama, kaip skiriasi pusiausvyros atkūrimo sąlygos priklausomai nuo pakabos geometrijos ir nestabilumo lygio.

Modeliuojant laikytasi prielaidos, kad platformos plokštė modeliuota kaip horizontaliai slenkantis vežimėlis, o žmogaus kūnas – kaip apversta švytuoklė ant vežimėlio (2 laisvės laipsnių sistema). Grandinių horizontaliosios reakcijos pakeistos dviejų šoninių spyruoklių modeliu; spyruoklių parametrai kalibruoti iš statinės analizės, kad atkartotų realią ∠ ir ∥ pakabų elgseną skirtingais IL (įskaitant *Free* ir *Rigid* kontrolinius režimus).

Protokolas. Pradinė būsena: plokštė centre ir nejuda; švytuoklė paleidžiama iš −20° be kampinio greičio. Nustatytos ribos: $|x| \leq 0{,}10$ m, $|\theta| \leq 10°$, slopinimo nėra. Sėkmės kriterijus – pirmasis $\theta = 0°$ kirtimas nepasiekus poslinkio ribos, tuomet fiksuojamas laikas, plokštės padėtis ir greitis bei kampinis greitis. Mažiausias sėkmei pakankamas pradinis pagreitis ieškomas iteracine paieška.

Geometrijos poveikis. Kampinė pakaba reikalauja didesnio pradinio pagreičio (apie ~ 7,8 m/s²), plokštė pasislenka nuo centrinės pozicijos (iki ≈ 0,09 m), todėl susidaro sąlygos, kai kūnas (švytuoklė) turi „vytis“ vis nuo jos tolstantį platformos atramos pagrindą. Vertikali pakaba – šiuo atveju pradinis pagreitis yra mažesnis (~4,5 m/s²), tačiau plokštė, priešingai nei kampinio pakabinimo atveju, linkusi apsigręžti ir judėti link neutralios padėties, todėl korekcija tampa palankesnė. Šie skirtumai vizualiai pateikti 57 pav., skaitinės vertės – 57 lentelėje.

Nestabilumo lygis (IL). Ilgėjant grandinėms, reikalingas pradinis pagreitis mažėja, tačiau ilgėja atsistatymo laikas ir didėja plokštės nuokrypis sėkmės momentu. Tendencijos abiejose geometrijose matomos 57 pav. ir 57 lentelėje.

57 lentelė. Minimalus pradinis korekcinis pagreitis ir kinematiniai kintamieji pirmojo švytuoklės vertikalios padėties kirtimo momentu (atsistatymo į statmeną padėtį) (pagal IL)

	Laisvas	**Standus**	**1 IL∠**	**2 IL∠**	**3 IL∠**	**1 IL‖**	**2 IL‖**	**3 IL‖**
$a_{c0,minimal}$	**6,8**	**1,5**	**9,6**	**8,5**	**7,8**	**1,6**	**1,8**	**4,5**
$t_{\theta=0}$ (s)	0,19	0,47	0,13	0,16	0,17	0,49	0,34	0,24
$x\ (t_{\theta=0})$ (m)	0,09	0,00	0,03	0,08	0,09	0,01	-0,05	0,08
$\dot{x}\ (t_{\theta=0})$ (m s^{-1})	0,88	0,00	1,38	2,10	1,56	-1,16	-0,89	-0,76
$\dot{\theta}(t_{\theta=0})$ (rad s^{-1})	1,46	0,78	1,52	0,59	1,00	1,66	1,51	2,51

Pastaba. ∠ – kampinė pakaba; ‖ – vertikali pakaba. IL1/IL2/IL3 atitinka grandinių ilgius ≈ 0,18 m, 0,24 m, 0,43 m. Laisva – be horizontalios grąžinamosios reakcijos; standus – efektyviai begalinis standumas.

Kampinėje (∠) pakaboje dėl horizontaliosios reakcijos jėgų asimetrijos plokštė greitai tolsta nuo centro, todėl, norint atkurti vertikalią padėtį, reikia didesnio pradinio korekcinio pagreičio. Vertikalioje (‖) pakaboje horizontaliosios jėgos pasiskirsto simetriškiau, plokštė linkusi ir vėl judėti link centro, todėl pakanka mažesnio impulso, o korekcija stabilesnė. Nestabilumo lygis (IL), nustatomas grandinių ilgiu, yra reguliuojamas dizaino parametru: ilgėjant grandinėms, pradinio pagreičio poreikis mažėja, tačiau ilgėja atsistatymo trukmė ir didėja plokštės nuokrypis sėkmės momentu.

Apibendrinant pakabos kampas ir laikiklių ilgis veikia kaip du pagrindiniai parametrai, lemiantys platformos kuriamą mechaninį nestabilumą. Didesnis kampas ir trumpesni laikikliai didina statinį standumą, bet kartu sukelia momentinę traukos asimetriją, todėl dinaminė korekcija reikalauja didesnių korekcinių impulsų. Mažesnis kampas ar ilgesni laikikliai standumą sumažina, tačiau sistema tampa atlaidesnė / laisvesnė.

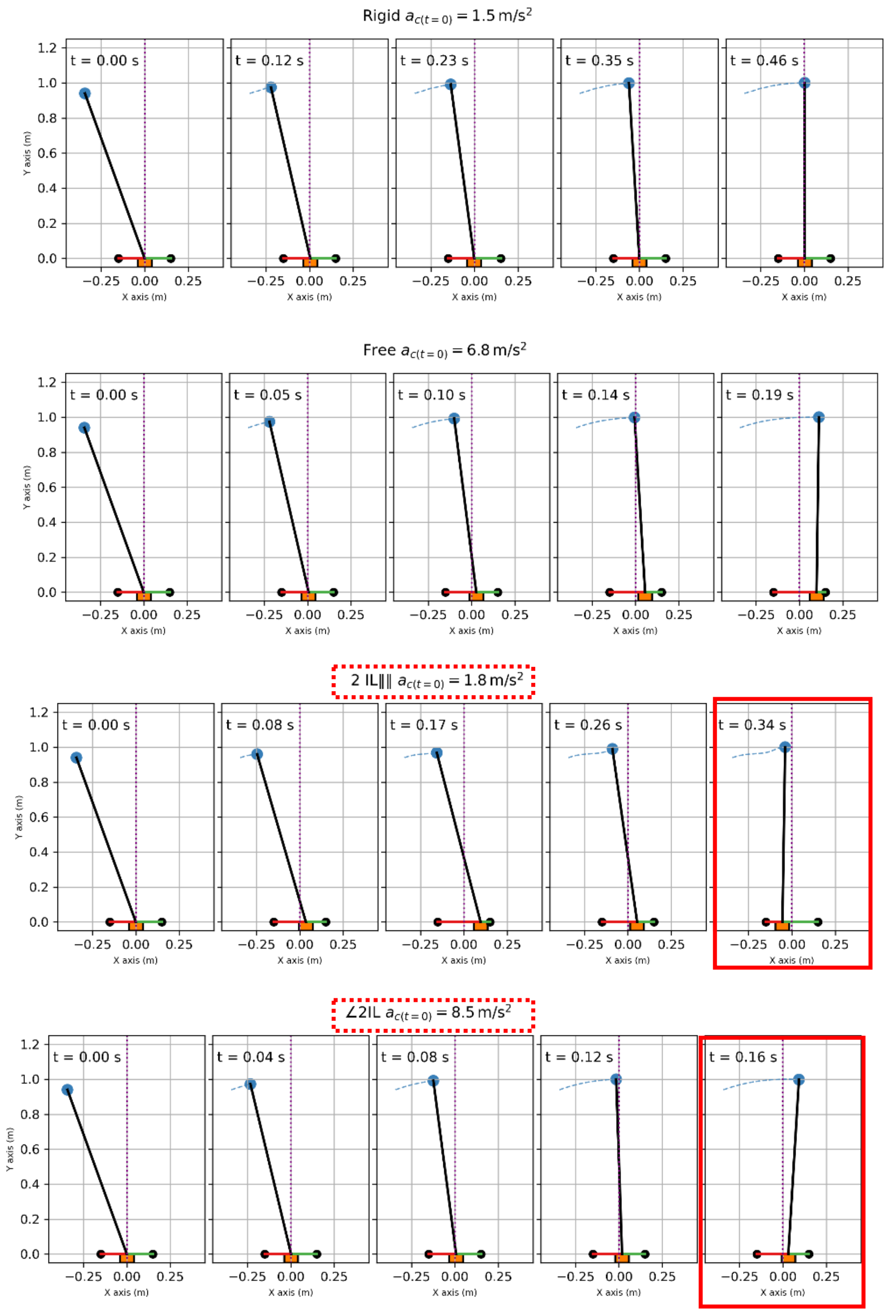

57 pav. Pakabos geometrijos įtaka atsistatymui. Vertikalioje pakaboje plokštė po pradinio impulso trumpam nutolsta, apsigręžia ir grįžta jau artėjant švytuoklės θ prie 0°, todėl atsistatymas vyksta mažesniu pradiniu pagreičiu. Kampinėje pakaboje reikalingas didesnis impulsas, o plokštė negrįžta link centro (dreifuoja iki ribos), todėl švytuoklės θ turi „vytis“ judantį atramos pagrindą. Prie vertikalios pakabos pasikeitusi plokštės judėjimo kryptis palengvina švytuoklės atsistatymą į vertikalią padėtį

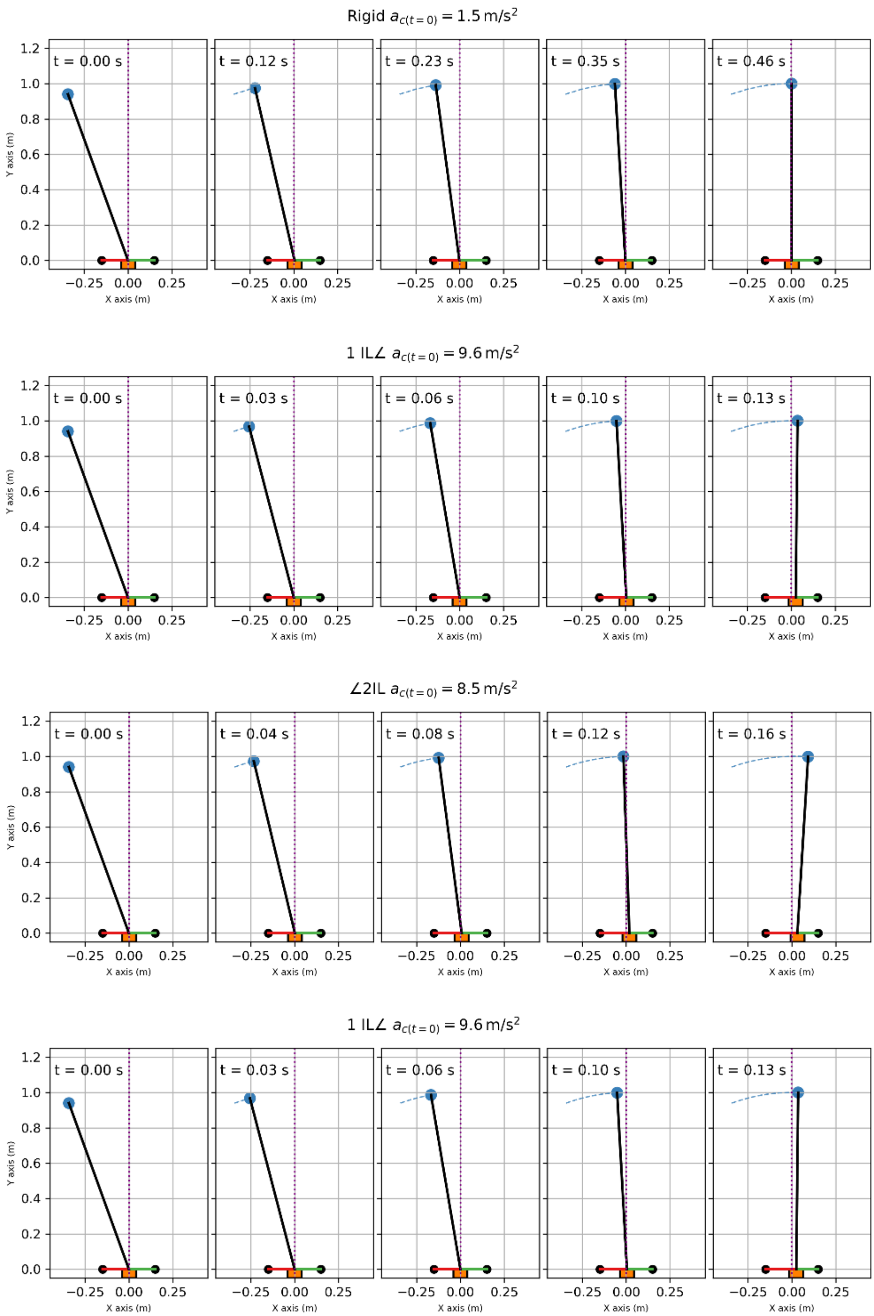

58 pav. Nestabilumo lygio įtaka atsistatymui. Didesnis nestabilumas (ilgesnės grandinės) sumažina reikalingą pradinį pagreitį, tačiau pailgina atsistatymo laiką ir padidina plokštės nuokrypį nuo centro vertikalios padėties kirtimo momentu

Biomechaninė analizė

Šiame skyriuje empiriškai įvertinta, kaip valingas kūno palinkimas į priekį keičia COM–BOS (kūno masės centro projekcijos ir atramos ploto) santykį ant mechaninį nestabilumą kuriančios platformos, kai nestabilumo lygis keičiamas trimis fiksuotomis konfigūracijomis (IL1–IL3). Tyrime dalyvavo vienas tiriamasis, kuris kiekviename lygyje atliko po tris maksimalius palinkimus. Judesiai registruoti 100 Hz optine judesių fiksavimo sistema („Qualisys Mocap®“). Buvo sekama p-COM (antropometrinis COM įvertis), platformos plokštės centro padėtis (šiame skyriuje ji atitinka BOS centrą) ir fiksuotas (nejudantis) grindų žymeklis kaip atskaitos nulis.

Naudoti du pagrindiniai dydžiai: BOS poslinkis (maksimalus platformos plokštės centro horizontalusis poslinkis nuo pradinės neutralios padėties; šis poslinkis įvyksta tik dėl jėgų, kurios atsiranda COM judėjimo metu) ir p-COM poslinkis (maksimalus p-COM poslinkis tiesia linija nuo pradinės neutralios padėties). Testo atlikimas pavaizduotas 59 pav., atliktų matavimų rezultatai – 60 pav.

59 pav. Dalyvis testą pradeda stovėdamas taip, kad p-COM (geltonas taškas), BOS (plokštės centras, mėlynas stačiakampis)) ir grindų atskaitos taškas (raudonas stačiakampis) būtų vertikaliai vienoje linijoje. Tuomet tiriamasis atlieka kontroliuojamą pasvirimą į priekį. Ši seka iliustruoja vienintelę leidžiamąją judėjimo laisvės laipsnio kryptį – apie čiurnos sąnarį

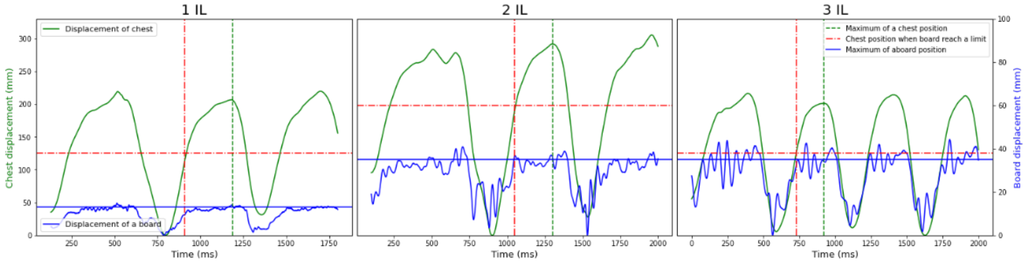

60 pav. p-COM ir BOS judėjimo sąsajos skirtinguose nestabilumo lygiuose. Žalia kreivė – COM poslinkis; mėlyna kreivė – plokštės poslinkis. Vertikali raudona punktyrinė linija žymi plokštės judėjimo ribos momentą, žalia punktyrinė linija – didžiausią COM poslinkį bandyme

Iš gautų duomenų buvo suskaičiuota p-COM poslinkio dalis, kai kartu judėjo ir BOS (vadinamoji susietoji fazė, nes p-COM ir BOS judėjo kartu), ir p-COM poslinkio dalis, kai judėjo tik p-COM, bet BOS nejudėjo (vadinamoji atsietoji fazė). Abu šie dydžiai yra bedimensiai, t. y. proporcijos. Taip pat skaičiuota BOS-per-p-COM koeficientas (kiek cm BOS poslinkio tenka 1 cm p-COM poslinkio). Vizualus fazių suskirstymas parodytas 61 pav., skaičiuotų parametrų vertės – 58 lentelėje.

58 lentelė. Parametrai, apibūdinantys, p-COM ir BOS sąveiką esant skirtingiems nestabilumo lygiams (IL1–IL3)

Parametras	**IL1**	**IL2**	**IL3**
BOS poslinkis (cm)	7,0	12,5	15,5
Maksimalus bendras p-COM poslinkis (cm)	18	19	16
p-COM poslinkis susietojoje fazėje (cm)	14	16	9
p-COM poslinkis atsietojoje fazėje (cm)	4	3	7
Susietosios fazės-COM / bendras maksimalus COM	0,78	0,84	0,56
Atsietosios fazės p-COM / bendras maksimalus COM	0,22	0,16	0,44
p-COM-per-BOS koeficientas (cm · cm^{-1})	0,5	0,78	1,72

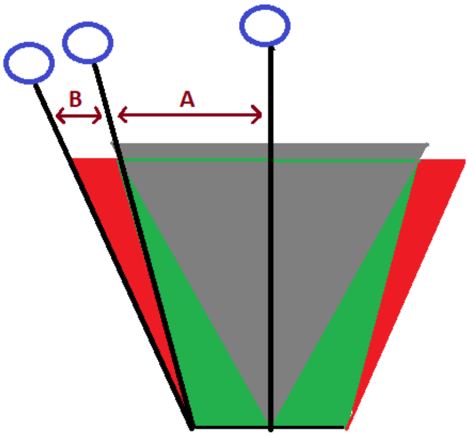

61 pav. Fazių segmentavimas. A – susietoji fazė: COM ir plokštės poslinkiai didėja kartu; B – atsietoji fazė: pasiekus plokštės judėjimo ribą COM toliau juda į priekį, o plokštė išlieka nejudri

Maksimalus p-COM poslinkis visais lygmenimis buvo panašus (apie 16–19 cm). BOS poslinkis didėjo didėjant nestabilumui: 7,0 cm (IL1), 12,5 cm (IL2) ir 15,5 cm (IL3). Tuo pat metu COM poslinkis susietoje fazėje buvo mažiausias didžiausiame IL, t. y. IL3 – tik ~9 cm, kai IL1 – 14 cm. Tad didžiausio nestabilumo sąlygomis mažesnis COM poslinkis sukelia didesnį BOS poslinkį.

Didėjant nestabilumo lygiui, matoma tendencija, kad, didėjant nestabilumo lygiui, didėja atsietosios fazės p-COM poslinkis: IL1 ~22 proc., o IL3 ~44 proc.

p-COM per BOS koeficientas (parametras, parodantis, kiek 1 cm p-COM judėjimo veikia BOS judėjimo) mažėjo, mažėjant IL: IL1 buvo 0,5, o IL3 1,72. Tai rodo, kad IL3 nestabilumo lygyje 1,72 cm p-COM poslinkio paveikė 1 cm BOS poslinkio, o IL1 1 cm p-COM poslinkis paveikė tik ~0,5 cm BOS poslinkio.

Skirtingų fazių proporcijos, esant skirtingiems nestabilumo lygiams, ir p-COM poslinkių dydžių skirtumas atsietoje fazėje lemia skirtingus biomechaninius platformos poveikius.

Didėjant nestabilumo lygiui, BOS poslinkis būna didesnis ir įvyksta esant mažesniam p-COM poslinkiui, o ir didesnė p-COM poslinkio dalis įvyksta jau nebejudant BOS. Skirtingų IL p-COM ir BOS judėjimo ryšių palyginimas pateiktas 62 pav.

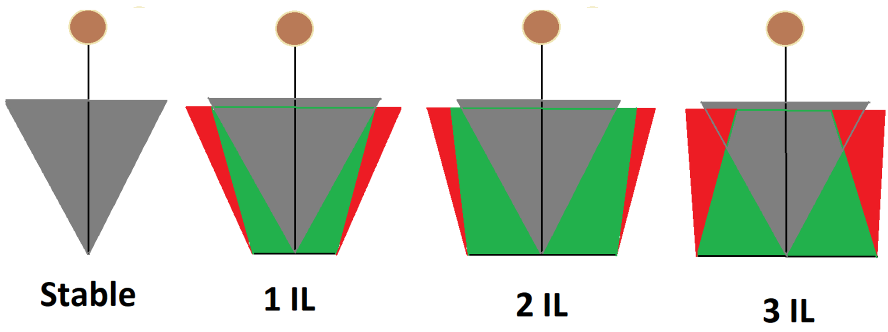

62 pav. p-COM–BOS judėjimo ryšių palyginimas esant skirtingiems nestabilumo lygiams. Pilki trikampiai – COM svyravimo apimtis stovint ant stabilaus pagrindo (naudojama tik kaip atskaitos taškas lyginti); žalios sritys – COM ir BOS poslinkis, kai juda kartu; raudonos sritys – COM poslinkis, kai BOS nebejuda

Neurobiomechaninė analizė

Taikant mechaninio nestabilumo (IL) ir jutiminės informacijos sumažinimo (SIS) manipuliacijas, buvo siekiama įvertinti, ar galima reikšmingai sutrikdyti žmogaus pusiausvyros kontrolę be išorinių trikdžių – tik sukuriant aplinkybes, kurios sustiprina natūralų kūno svyravimą. Šiuo tikslu tyrime dalyvavo 25 jauni suaugę asmenys, neturintys pusiausvyros ar eisenos sutrikimų. Ant pagrindinių jų kūno segmentų buvo pritvirtinti reflektoriniai žymekliai, o judesius erdvėje fiksavo optinė judesių registravimo sistema („MoCap Qualisys®“). Išmatuoti tiriamųjų antropometriniai rodikliai (ūgis, kūno masė, galūnių ilgiai) ir atlikti pradiniai funkciniai pusiausvyros vertinimo testai – Y pusiausvyros testas (YBT) ir funkcinio pasiekimo testas (FRT). Šių testų rezultatai atitiko amžiaus normos vertes, tuo patvirtinama, kad dalyviai turėjo įprastų pusiausvyros gebėjimų.

Pagrindinio bandymo metu kiekvienas tiriamasis atliko 16 skirtingo sudėtingumo stovėjimo užduočių rinkinį, sudarytą iš 4×4 matricos: keturios SIS derintos su keturiais mechaninio nestabilumo lygiais. SIS buvo parinktos analogiškai modifikuotam CTSIB protokolui, palaipsniui apribojant jutimų prieinamumą: 1) visos jutiminės sistemos veikė (*Basic*: atviros akys, kieta atrama); 2) eliminuota regos informacija (*Visual*: užmerktos akys, kieta atrama); 3) trikdoma proprioceptinė informacija atramos pagrinde (*Proprioceptive*: atviros akys, minkšta atrama); 4) maksimaliai apribota regos ir atramos jutimų informacija (*Vestibular*: užmerktos akys, minkšta atrama, pasikliaujant iš esmės vien vestibuline orientacija) (63 pav. viršutinė dalis).

Kiekviena iš šių SIS buvo testuojama esant skirtingam platformos mechaniniam nestabilumui: IL0 (stabilus) ir trimis didėjančio nestabilumo lygiais – IL1, IL2 ir IL3 (didžiausias nestabilumas) (63 pav. apatinė dalis).

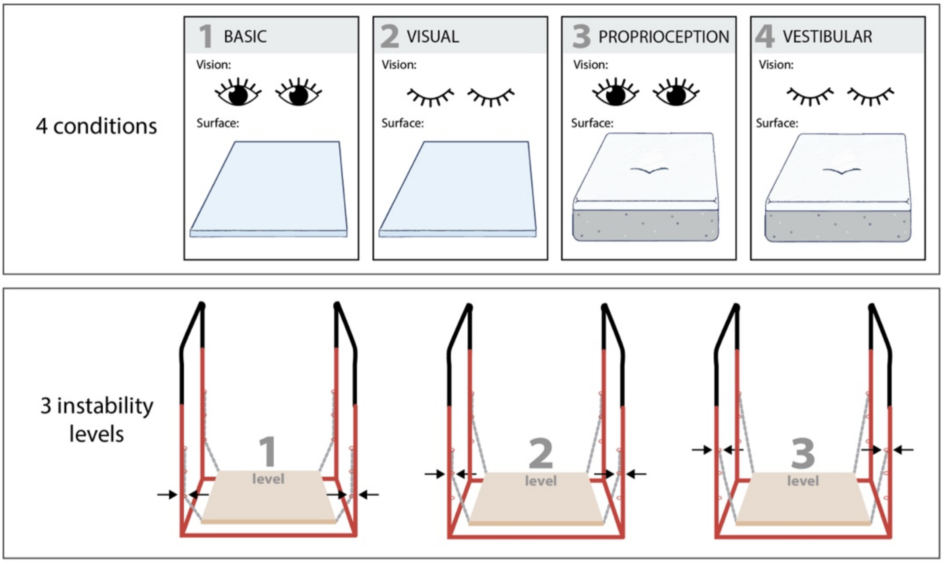

63 pav. Testavimo matricos IL×SIS sąlygoms schema. Viršutinėje dalyje pavaizduotos 4 SIS, apatinėje – 3 IL. Viršutinėje schemos dalyje piktogramos žymi SIS: atvira akis – regos informacija prieinama (*Basic*, *Proprioception*), užmerkta akis – regos informacija eliminuota (*Visual*, *Vestibular*). Atramos paviršiaus piktogramos: lygi plokštuma – kieta atrama; banguota pagalvėlė – minkšta atrama, keičianti pėdos padų / propriorecepcinius signalus. Apatinėje schemos dalyje pavaizduoti trys pakabinamos platformos nustatymai, naudojami palaipsniui didinant mechaninį nestabilumą; IL0 reiškia stabilų nejudantį pagrindą (schemoje nerodomas)

Tokiu būdu IL×SIS testavimo matrica apėmė užduotis nuo lengviausių (*Basic*–IL0) iki sunkiausių (*Vestibular*–IL3). Bandymų metu buvo registruojami kūno segmentų (galvos, krūtinės ir čiurnos) judesiai – jų padėties koordinatės ir greičiai.

Remiantis šiais duomenimis, kiekvienam bandymui apskaičiuoti du pagrindiniai posturalinio svyravimo rodikliai: EV95 % (95 % elipsinio judesių tūrio rodiklis cm^3, atspindintis kūno segmento svyravimo diapazoną erdvėje) ir TMV (trajektorijos vidutinio greičio rodiklis, cm/s, atspindintis judėjimo greitį). Šie rodikliai apskaičiuoti pagal krūtinės segmento judesius. Šis segmentas pasirinktas kaip artimiausias viso kūno masės centro (COM) atitikmuo ir reprezentatyviausias taškas pusiausvyros trikdymo intensyvumo analizei.

Po kiekvienos užduoties tiriamasis subjektyviai įvertino atlikimo sunkumą vizualinės analogijos skalėje (VAS) nuo 0 iki 10 balų, čia 0 reiškė „Visiškai lengva“, o 10 – „Labai sunku išlaikyti pusiausvyrą“.

Surinkus visų dalyvių duomenis, ekspertas medikas (nematydamas eksperimentinių sąlygų, atsitiktine tvarka vertindamas stebėdamas vaizdo įrašus) įvertino kiekvieno bandymo pusiausvyros išlaikymo kokybę pagal 0–100 balų skalę. Eksperto vertinimo rodikliai – 0 balų atitiko puikiai išlaikytą stabilią stovėseną (normalūs fiziologiniai kūno svyravimai), 100 balų rodė visišką nestabilumą (labai didelės amplitudės ir trūkčiojantys posvyriai, akivaizdi kritimo rizika). Pažymėtina, kad jeigu bandymo metu tiriamasis žengė korekcinį žingsnį ar prisilaikė turėklo, toks mėginimas buvo laikomas neįvykdytu (nepavykusiu) ir balais nevertintas.

Analizuojant tik *Basic* (bazines) sąlygas, vien tik didinant IL (nuo IL0 iki IL3) reikšmingai išauga EV95 %, o TMV kinta minimaliai. Pavyzdžiui, *Basic* sąlygoje krūtinės segmento EV95 % mediana padidėjo nuo ~179 cm³ esant IL0 iki ~693 cm³ esant IL3, t. y. beveik 4 kartus (59 lentelė). TMV pakilo tik nuo ~0,78 iki ~0,98 cm/s (60 lentelė), rodydamas menką posturalinio atsako pagreitėjimą idealiomis sensorinėmis sąlygomis.

59 lentelė. Krūtinės segmento EV95 % (cm³) skirtingomis IL×SIS sąlygomis; šviesoforo skalė (žalia = maža reikšmė, geltona = vidutinė, raudona = didelė)

SIS \ IL	**IL 0**		**IL 1**		**IL 2**		**IL 3**	
	Median	IQR	Median	IQR	Median	IQR	Median	IQR
Basic	179,5	261,7	561,5	551,8	771,6	833,6	692,9	855,7
Visual	186,1	188,7	653,5	683,6	3213,8	7806,3	2645,0	3163,6
Proprioception	855,7	726,5	1354,4	1117,9	1725,0	1389,9	1784,7	2104,5
Vestibular	1880,0	1633,2	4604,4	6535,5	9729,0	12,599,6	12,917,0	23,512,2

60 lentelė. Krūtinės segmento TMV (cm/s) skirtingomis IL×SIS sąlygomis; šviesoforo skalė (žalia = maža reikšmė, geltona = vidutinė, raudona = didelė)

SIS \ IL	IL 0		IL 1		IL 2		IL 3	
	Median	IQR	Median	IQR	Median	IQR	Median	IQR
Basic	0,78	0,21	0,88	0,18	1,07	0,32	0,98	0,28
Visual	0,86	0,23	1,08	0,46	2,20	2,33	1,93	0,95
Proprioception	1,20	0,18	1,22	0,36	1,46	0,44	1,54	0,35
Vestibular	2,00	0,50	2,95	0,93	4,19	1,77	4,53	1,87

Vertinant atskirai IL poveikį kiekvienai iš SIS, nustatyta, kad didėjantis IL nuosekliai didino tiek EV95 %, tiek TMV, tačiau šių rodiklių didėjimo mastas buvo skirtingas, ir kiekvienoje SIS, t. y. IL turėjo skirtingą efektą kiekvienai iš SIS: mažiausi pokyčiai fiksuoti esant visiškai sensorikai (*Basic*), o ryškiausi – *Vestibular* strategijoje, kai eliminuojami tiek regos, tiek propriocepcijos signalai. Pastaruoju atveju EV95% tūris padidėjo beveik 7 kartus (nuo ~1880 cm³ esant IL0 iki ~12 917 cm³ esant IL3), o TMV – daugiau nei dvigubai (nuo ~2,00 iki ~4,53 cm/s). *Visual* strategijoje (eliminuojant regėjimą) EV95 % tūris išaugo daugiau nei 10 kartų (nuo ~186 cm³ esant IL0 iki ~2645 cm³ esant IL3) kartu su ~ 2,2 karto didesniu TMV (nuo ~0,86 iki ~1,93 cm/s). *Proprioception* strategijoje (sutrikdžius propriorecepciją) pokyčiai buvo nuosaikesni: EV95 % tūris padvigubėjo (nuo ~856 cm³ esant IL0 iki ~1785 cm³ esant IL3), o TMV padidėjo tik apie 1,3 karto (nuo ~1,20 iki ~1,54 cm/s).

Visoje eksperimentinių sąlygų (IL×SIS) matricoje labiausiai išsiskiria kraštutinių situacijų palyginimas – *Basic* strategijos esant IL0 ir *Vestibular* strategijos esant IL3. Šis kontrastas atskleidžia, kaip smarkiai kompleksinis sensorinės ir mechaninės destabilizacijos poveikis padidina kūno svyravimus. *Basic* IL0 sąlygomis krūtinės segmento (COM atitikmens) posvyriai buvo minimalūs: EV95 % siekė ~180 cm³, o TMV – ~0,78 cm/s. *Vestibular* IL3 sąlygomis EV95 % išsiplėtė iki ~12 917 cm³, o TMV pasiekė ~4,53 cm/s. Kitaip tariant, posvyrio tūris padidėjo apie 71 kartą, o judėjimo greitis – maždaug 6 kartus. Šie radikalūs skirtumai parodo, kad didėjantis mechaninis nestabilumas kartu su labai apribota sensorine informacija sukelia didelį posturalinio atsako suintensyvėjimą: kūno masės centras svyruoja gerokai plačiau ir greičiau, atspindėdamas kur kas didesnę pusiausvyros kontrolės sistemos apkrovą (59 ir 60 lentelės).

Pažymėtina, jog tiek dalyvių subjektyvus užduoties sunkumo įvertinimas, tiek nepriklausomas eksperto vertinimas aiškiai atspindėjo tą pačią dėsningo didėjimo tendenciją. Pavyzdžiui, *Vestibular* strategijos subjektyvaus pusiausvyros sunkumo vertinimo vidurkis siekė ~6,3 balo esant IL3 lygiui, palyginti su ~ 0,97 balo *Basic* strategijoje (esant IL0), t. y. santykis apie ~6,4 karto, kas atitinka ir krūtinės TMV santykį ~6 kartai.

Analizuojant rezultatus matoma tendencija, kad posturalinio trikdymo efektas didėja nuo *Basic* link *Vestibular* sąlygų. Tačiau šis užduoties sunkumo kitimas nėra tiesinis. 64 pav. iliustruojama, kad užduoties sudėtingumas augo labiau logaritminiu dėsningumu nei tiesiniu – tai patvirtina ir statistinis modeliavimas: logaritminė funkcija puikiai atitiko empirinę kreivę (regresijos $R^2 = 0{,}943$. Taigi IL×SIS užduočių seka sudaro nuoseklų „sunkumo“ progresą, leidžiantį dozuoti pusiausvyros išlaikymo užduoties sudėtingumą.

Nebuvo gauta nuoseklios koreliacijos tarp IL×SIS rodiklių su pradiniais funkciniais pusiausvyros testais (FRT, Y-balanso) ar antropometriniais kintamaisiais. Platformos mechaniniai parametrai (RII, slopinimo koeficientas) rodė kryptingą ryšį su IL×SIS tik esant mažiausiam nestabilumo lygiui – sąlygai, artimai supaprastinto apverstos švytuoklės modelio prielaidoms; kai įsijungė ryškesnis neurobiomechaninės kontrolės komponentas (SIS taikymas ir IL2–IL3), šis ryšys išnyko.

Šiame tyrime pritaikyta IL×SIS strategija parodė, kad ji galėtų būti veiksminga metodika, skirta sistemingai didinti pusiausvyros užduoties sudėtingumą ir objektyviai įvertinti žmogaus posturalinės kontrolės galimybes. Laipsniškas vidinių svyravimų stiprinimas (be jokio išorinio stūmimo ar kitokio nenatūralaus išorinio trikdžio) galėtų būti laikomas „progresuojančio sunkumo“ testu. Tokios sąlygos yra artimos realioms situacijoms, pavyzdžiui, blogėjant jutiminei informacijai tamsoje arba esant nestabiliam pagrindui.

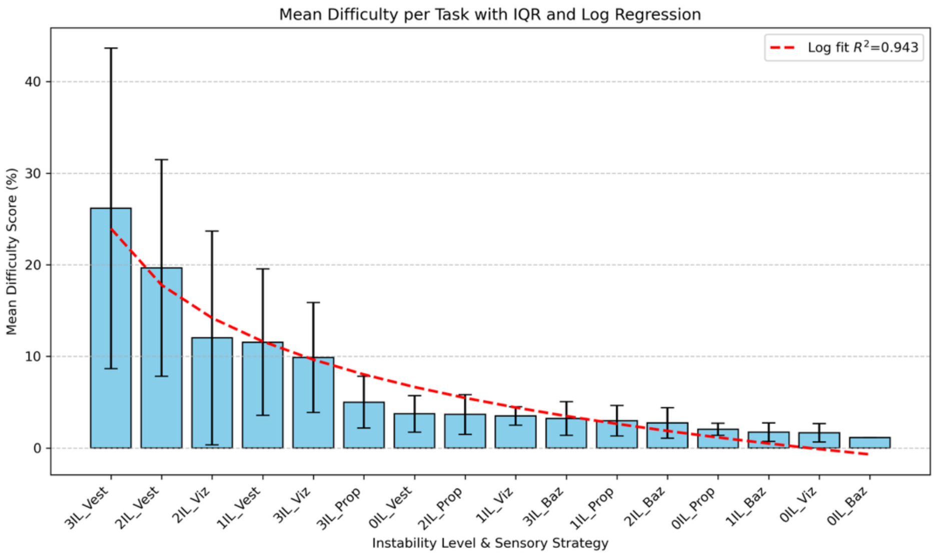

64 pav. Eksperto įvertintas užduoties sudėtingumas kirtingomis IL×SIS sąlygomis. Stulpeliai rodo vidutinį kiekvienos IL×SIS kombinacijos įvertinimą, taip pat pateiktas ir interkvartilinis diapazonas (IQR). Punktyrinė kreivė – sąlygų vidurkiams pritaikyta logaritminė priklausomybė ($R^2 = 0{,}943$). Sudėtingumas didėja didėjant IL ir ribojant jutiminę informaciją (pvz., *Vestibular* ir *Visual* sąlygos), o rezultatų sklaida išsiplečia (mėlyni stulpeliai – sąlygų vidurkiai; raudona punktyrinė linija – logaritminis pritaikymas)

IL×SIS posturalinės kontrolės trikdymo metodika gali tapti potencialia testavimo ir treniravimo priemone. Ji suteikia galimybę įvertinti žmogaus pusiausvyros kontrolę vis sudėtingėjančiomis sąlygomis ir gali būti pritaikoma kuriant personalizuotas balansavimo treniruočių programas. Pažymėtina, kad, taikant šią metodiką, nereikia sudėtingos išorinės įrangos ar dirbtinių posturalinių trikdžių.

Prototipo konstrukcija ir sistemos integracija

Sukurta platforma skirta žmogaus posturalinės kontrolės tyrimams. Tyrimų platformos plokštė pakabinta lynais prie keturių rėmo kampuose esančių kolonų. Prie kiekvienos iš kolonų sumontuota po linijinę pavarą, kuri, keičiant kiekvieno lyno pritraukimo vietą, keičia aktyvaus lyno ilgį, dėl ko kinta ir pakabinimo geometrija (65 pav.). Toks valdymas leidžia reguliuoti mechaninio nestabilumo parametrus, keičiant pakabos konfigūraciją.

65 pav. Automatizuotos tyrimų platformos CAD vaizdas. Pakabinama plokštė pritvirtinta plieniniais lynais prie rėmo kolonų. Prie kiekvienos kolonos sumontuota po linijinę pavarą, kurios reguliuoja aktyvaus lyno ilgį, taip keisdamos pakabos geometriją ir mechaninio nestabilumo lygį. Atviras aliumininis rėmas turi reguliuojamus apsauginius turėklus ir palieka laisvą prieigą prie jutiklių bei kabelių

Informatyviausio parametro parinkimas. Siekiant automatizuoti pusiausvyros testavimą, buvo atlikta analizė, kuris biomechaninis parametras geriausiai atspindi subjektyvų užduoties sudėtingumą. Koreliacijos tyrimas tarp ekspertų suteiktų užduoties sunkumo įverčių ir įvairių judesių rodiklių parodė, jog vidutinis kūno svyravimo greitis yra informatyviausias parametras. Stipriausias ryšys nustatytas būtent tarp spaudimo centro (COP) svyravimo greičio ir užduoties sudėtingumo – COP vidutinio greičio koreliacijos koeficientas su ekspertiniu sunkumo reitingu siekė r = 0,82, statistiškai patikimas (p < 0,001). Todėl COP vidutinis greitis pasirinktas kaip pagrindinis informatyviausias rodiklis tolesniam sistemos valdymui – jis jautriausiai atspindi subjektyvaus pusiausvyros iššūkio sunkumą ir gali būti naudojamas automatizuotai testavimo eigos kontrolei realiuoju laiku.

Slenkstinių reikšmių nustatymas. Automatiniam posturalinės kontrolės testavimo užduočių reguliavimui buvo nustatyta kritinė svyravimo greičio riba, kurią viršijus testavimas nutraukiamas arba pasirenkamas mažesnis nestabilumas. Tam iš visų vykdytų bandymų atrinkti tik visiškai saugiai atlikti bandymai, kad analizuojami duomenys atspindėtų toleruotinas nestabilumo ribas. Visi įtraukti testavimo bandymai buvo suskaidyti 1 s trukmės intervalais (>16 000 segmentų iš viso) ir kiekvienam intervalui apskaičiuotas 1 s COP vidutinis greitis. Sudarytas gautų verčių pasiskirstymas pagal dažnį. Kaip riba pasirinkta 95-oji procentilė – ji žymi didžiausio dar stabilaus svyravimo, kurią sveiki tiriamieji pagal testavimo rezultatus galėjo be papildomų veiksmų visiškai toleruoti, ribą. Taigi 95 % procentilės vertė priimta kaip slenkstis, virš kurio platformos testavimas automatiškai sustabdomas. Atlikus skaičiavimus nustatyta, kad COP vidutinio greičio 95% procentilė lygi ~8,95 cm/s. Ši riba naudojama realiuoju laiku: jei posturalinės kontrolės testavimo metu, taikant slankiojo lango metodą su 1 s trukmės intervalu, dalyvio COP greitis viršija 8,95 cm/s, sistema tai identifikuoja kaip grėsmingą nestabilumo būseną ir iš karto pereina į mažiausio nestabilumo lygmenį, užtikrindama dalyvio saugumą.

Sistemų surinkimas ir kalibravimas. Sujungus visas dalis – mechaninį rėmą, platformą su pavaromis, jutiklius ir valdymo elektroniką, buvo gautas veikiantis žmogaus posturalinės kontrolės testavimo prietaiso prototipas (66 pav.).

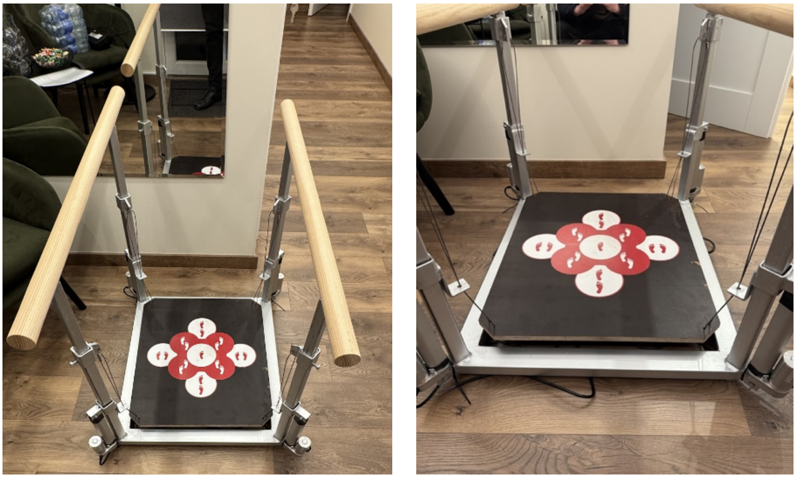

66 pav. Surinktas posturalinės kontrolės testavimo įrenginio prototipas. Priekinis ir įstrižinis baigto prototipo vaizdai su įrengtomis pavaromis, pakabos lynais, apsauginiais ranktūriais ir integruotais jutikliais

Integracijos funkcionalumo patikrinimas. Galutinai surinkto prototipo veikimas buvo patikrintas eksperimentiškai, testuojant patį darbo autorių. Pirmasis testavimas atliktas įprastomis sąlygomis, taikant standartinį pusiausvyros testą, gauti duomenys atitiko turimas referencines vertes. Antrasis testavimas atliktas su papildoma kognityvine apkrova – kartu su pusiausvyros testu vykdyta „Stroop“ užduotis. Šio bandymo metu pusiausvyra pablogėjo: užfiksuota didesnė kūno svyravimo amplitudė, o šis rezultatas atitinka literatūros duomenis, patvirtindamas prototipo jautrumą papildomai kognityvinei apkrovai (67 pav.). Sistema potencialiai leidžia saugiai kartoti standartizuotus testus, kaupti duomenis ir lyginti rezultatus tarp skirtingų sesijų ar su sveikų asmenų normomis, todėl ji galėtų būti tinkama ilgalaikiam posturalinės kontrolės stebėjimui.

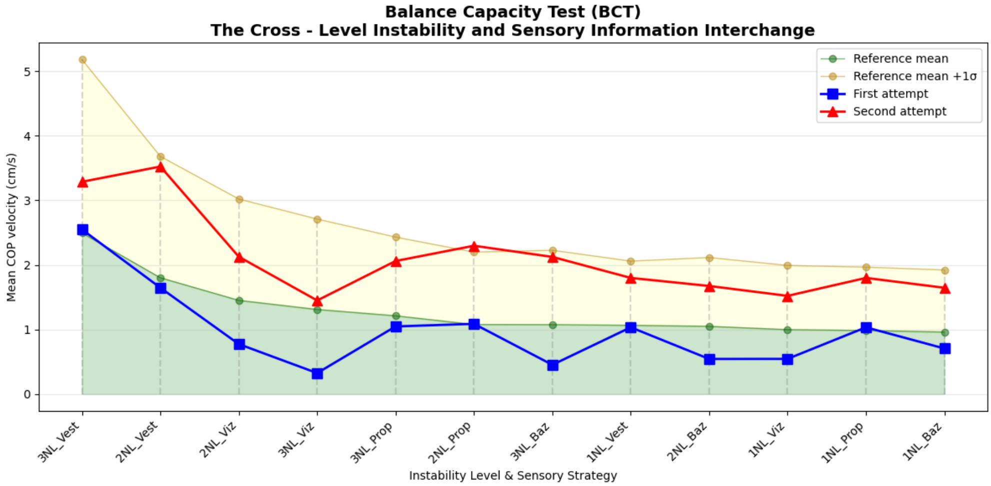

67 pav. COP vidutinio greičio palyginimas visomis testavimo sąlygomis tarp dviejų vieno dalyvio sesijų: 1-oji sesija – vienos užduoties testas (be kognityvinės apkrovos); 2-oji sesija – dviejų užduočių testas su spalvų ir žodžių *Stroop* užduotimi. Pateikta normatyvinė vertė ir ±1 SD sveikų asmenų rodikliai. Nors abiejų sesijų rezultatai išlieka normatyviniame intervale, dviejų užduočių (*Stroop*) sesijoje svyravimo greičiai yra didesni nei vienos užduoties sesijoje, o tai rodo išmatuojamą kognityvinės apkrovos poveikį posturalinei kontrolei. Legenda: „First attempt" = vienos užduoties testas, „Second attempt" = dviejų užduočių testas (*Stroop*)

Išvados

1. Taikant statinį ir dinaminį modeliavimą nustatyta, kad pakabos geometrija reikšmingai veikia platformos ir apverstos švytuoklės sąveiką bei pusiausvyros atkūrimo mechaniką. Kampinė pakaba sukuria asimetrinius grandinių įtempius ir netiesiškai didina atstojamąją horizontalią grąžinamąją jėgą, todėl tam pačiam plokštės poslinkiui ir pusiausvyros atkūrimui reikalinga didesnė horizontali korekcinė jėga / impulsas nei vertikalios pakabos atveju.
2. Eksperimentinių tyrimų metu nustatyti pusiausvyros vertinimo platformos mechaniniai parametrai ir sudaryti nestabilumo indeksai, tinkami lyginamajai analizei bei sukeliamam nestabilumui apibūdinti. Pagrindiniai parametrai: horizontaliojo poslinkio standumo koeficientas K_{IL} ir laisvųjų svyravimų slopinimo indeksas ψ_{IL}: $K_{IL1} = 168\, N\, m^{-1}\, kg^{-1}$ $\psi_{IL1} = 0{,}35\, [s\, kg^{-1}]$; $K_{IL3} = 28{,}9\, N\, m^{-1}\, kg^{-1}$, $\psi_{IL3} = 1{,}5\, [s\, kg^{-1}]$.
3. Biomechaninės analizės metu nustatyta, kad valingų judesių ant platformos metu išryškėja dvi fazės: 1) pirmoji (arba susietoji), kurios metu kūno masės centras juda kartu su platformos plokšte; 2) antroji (arba atsietoji fazė), kai juda

tik kūno masės centras, o platformos plokštė, pasiekusi savo kraštinę judėjimo ribą, nebejuda. Skirtingų fazių proporcijos, esant skirtingiems nestabilumo lygiams, ir kūno masės centro poslinkių dydžių skirtumas atsietoje fazėje lemia skirtingus biomechaninius platformos poveikius.

4. Laipsniškai didinant platformos nestabilumą ir ribojant jutiminę informaciją, posturalinio stabilumo rodikliai labai blogėja, o subjektyvus nestabilumo pojūtis smarkiai išauga (ekstremaliausiu atveju kūno svyravimų tūris padidėja ~71 kartą, judėjimo greitis ir suvokiamas užduoties sunkumas – daugiau nei 600 %). Šie pokyčiai nekoreliuoja su įprastinių funkcinių pusiausvyros testų rezultatais.

5. Sukurta ir pagaminta adaptyvi automatinė testavimo sistema. Ji leidžia saugiai ir tiksliai didinti užduoties sudėtingumą bei objektyviai vertinti posturalinės kontrolės efektyvumą realiuoju laiku. Sistema automatiškai kaupia ir vizualizuoja testavimo duomenis. Šis integruotas sprendimas tinkamas ilgalaikei posturalinės kontrolės stebėsenai, pakartotiniams standartizuotiems pusiausvyros testams ir paciento būklės pokyčiams sekti, lyginant rezultatus tarp skirtingų sesijų ar su sveikų asmenų normomis.

LIST OF REFERENCES

1. Horak FB. Postural orientation and equilibrium: what do we need to know about neural control of balance to prevent falls? Age Ageing. 2006 Sept;35 Suppl 2(suppl_2):ii7–11.
2. Pollock AS, Durward BR, Rowe PJ, Paul JP. What is balance? Clin Rehabil. 2000 Aug;14(4):402–6.
3. Winter DA. Human balance and posture control during standing and walking. Gait Posture. 1995 Dec;3(4):193–214.
4. Ivanenko Y, Gurfinkel VS. Human postural control. Front Neurosci. 2018 Mar 20;12:171.
5. Loram ID, Lakie M. Human balancing of an inverted pendulum: position control by small, ballistic-like, throw and catch movements. J Physiol. 2002 May 1;540(Pt 3):1111–24.
6. Asai Y, Tasaka Y, Nomura K, Nomura T, Casadio M, Morasso P. A model of postural control in quiet standing: robust compensation of delay-induced instability using intermittent activation of feedback control. PLoS One. 2009 July 8;4(7):e6169.
7. Bottaro A, Casadio M, Morasso PG, Sanguineti V. Body sway during quiet standing: is it the residual chattering of an intermittent stabilization process? Hum Mov Sci. 2005 Aug;24(4):588–615.
8. Hof AL, Gazendam MGJ, Sinke WE. The condition for dynamic stability. J Biomech. 2005 Jan;38(1):1–8.
9. Hertel J, Olmsted-Kramer LC, Challis JH. Time-to-boundary measures of postural control during single leg quiet standing. J Appl Biomech. 2006 Feb;22(1):67–73.
10. Hof AL. The “extrapolated center of mass” concept suggests a simple control of balance in walking. Hum Mov Sci. 2008 Feb;27(1):112–25.
11. Pai YC, Patton J. Center of mass velocity-position predictions for balance control. J Biomech. 1997 Apr;30(4):347–54.
12. Curtze C, Buurke TJW, McCrum C. Notes on the margin of stability. J Biomech. 2024 Mar;166(112045):112045.
13. Watson F, Fino PC, Thornton M, Heracleous C, Loureiro R, Leong JJH. Use of the margin of stability to quantify stability in pathologic gait - a qualitative systematic review. BMC Musculoskelet Disord. 2021 June 28;22(1):597.
14. Jasimi Zindashti N, Noamani A, Vette AH, Rouhani H. A narrative review on dynamic postural stability and neuromuscular control of balance. Trans Can Soc Mech Eng [Internet]. 2025 May 3; Available from: http://dx.doi.org/10.1139/tcsme-2024-0169
15. Dutt-Mazumder A, Slobounov SM, Challis JH, Newell KM. Postural stability margins as a function of support surface slopes. PLoS One. 2016 Oct 20;11(10):e0164913.
16. Richmond SB, Fling BW, Lee H, Peterson DS. The assessment of center of mass and center of pressure during quiet stance: Current applications and future directions. J Biomech. 2021 June 23;123(110485):110485.
17. Hof AL. The equations of motion for a standing human reveal three mechanisms for balance. J Biomech. 2007;40(2):451–7.
18. Gage WH, Winter DA, Frank JS, Adkin AL. Kinematic and kinetic validity of the inverted pendulum model in quiet standing. Gait Posture. 2004 Apr;19(2):124–32.
19. Morasso P. Centre of pressure versus centre of mass stabilization strategies: the tightrope balancing case. R Soc Open Sci. 2020 Sept;7(9):200111.
20. Sung JL, Hong CY, Liu CH, Lee P, Guo LY, Lin NH, et al. Characterizing the validity of the inverted pendulum model for quiet standing. J Healthc Eng. 2021 June 11;2021:8884614.

21. Sonobe M, Inoue Y. Center of mass estimation using a force platform and inertial sensors for balance evaluation in quiet standing. Sensors (Basel). 2023 May 20;23(10):4933.
22. Chen B, Liu P, Xiao F, Liu Z, Wang Y. Review of the upright balance assessment based on the force plate. Int J Environ Res Public Health. 2021 Mar 8;18(5):2696.
23. Masani K, Vette AH, Abe MO, Nakazawa K. Center of pressure velocity reflects body acceleration rather than body velocity during quiet standing. Gait Posture. 2014 Mar;39(3):946–52.
24. Lafond D, Corriveau H, Hébert R, Prince F. Intrasession reliability of center of pressure measures of postural steadiness in healthy elderly people. Arch Phys Med Rehabil. 2004 June;85(6):896–901.
25. Masani K, Popovic MR, Nakazawa K, Kouzaki M, Nozaki D. Importance of body sway velocity information in controlling ankle extensor activities during quiet stance. J Neurophysiol. 2003 Dec;90(6):3774–82.
26. Quijoux F, Nicolaï A, Chairi I, Bargiotas I, Ricard D, Yelnik A, et al. A review of center of pressure (COP) variables to quantify standing balance in elderly people: Algorithms and open-access code. Physiol Rep. 2021 Nov;9(22):e15067.
27. Rhea CK, Kiefer AW, Wright WG, Raisbeck LD, Haran FJ. Interpretation of postural control may change due to data processing techniques. Gait Posture. 2015 Feb;41(2):731–5.
28. Richmond SB, Otto G, Dames KD. Characterization of trial duration in traditional and emerging postural control measures. J Biomech. 2023 Jan;147(111438):111438.
29. Błaszczyk JW. The use of force-plate posturography in the assessment of postural instability. Gait Posture. 2016 Feb;44:1–6.
30. Scoppa F, Capra R, Gallamini M, Shiffer R. Clinical stabilometry standardization: basic definitions--acquisition interval--sampling frequency. Gait Posture. 2013 Feb;37(2):290–2.
31. Carpenter MG, Frank JS, Winter DA, Peysar GW. Sampling duration effects on centre of pressure summary measures. Gait Posture. 2001 Feb;13(1):35–40.
32. Sibley KM, Beauchamp MK, Van Ooteghem K, Straus SE, Jaglal SB. Using the systems framework for postural control to analyze the components of balance evaluated in standardized balance measures: a scoping review. Arch Phys Med Rehabil. 2015 Jan;96(1):122-132.e29.
33. Bergquist R, Weber M, Schwenk M, Ulseth S, Helbostad JL, Vereijken B, et al. Performance-based clinical tests of balance and muscle strength used in young seniors: a systematic literature review. BMC Geriatr. 2019 Jan 9;19(1):9.
34. Chiu AYY, Pang MYC. Assessment of psychometric properties of various balance assessment tools in persons with cervical spondylotic myelopathy. J Orthop Sports Phys Ther. 2017 Sept;47(9):673–82.
35. Ford-Smith CD, Wyman JF, Elswick RK Jr, Fernandez T, Newton RA. Test-retest reliability of the sensory organization test in noninstitutionalized older adults. Arch Phys Med Rehabil. 1995 Jan;76(1):77–81.
36. Peterka RJ. Sensorimotor integration in human postural control. J Neurophysiol. 2002 Sept;88(3):1097–118.
37. Teng YL, Chen CL, Lou SZ, Wang WT, Wu JY, Ma HI, et al. Postural stability of patients with schizophrenia during challenging sensory conditions: Implication of sensory integration for postural control. PLoS One. 2016 June 29;11(6):e0158219.
38. Chaudhary S, Saywell N, Taylor D. The differentiation of self-motion from external motion is a prerequisite for postural control: A narrative review of visual-vestibular interaction. Front Hum Neurosci. 2022 Feb 8;16:697739.

39. Karmali F, Goodworth AD, Valko Y, Leeder T, Peterka RJ, Merfeld DM. The role of vestibular cues in postural sway. J Neurophysiol. 2021 Feb 1;125(2):672–86.
40. Assländer L, Peterka RJ. Sensory reweighting dynamics in human postural control. J Neurophysiol. 2014 May;111(9):1852–64.
41. Carver S, Kiemel T, Jeka JJ. Modeling the dynamics of sensory reweighting. Biol Cybern. 2006 Aug;95(2):123–34.
42. Behtani L, Paromov D, Moïn-Darbari K, Houde MS, Bacon BA, Maheu M, et al. Sensory reweighting for postural control in older adults with age-related hearing loss. Brain Sci. 2023 Nov 23;13(12):1623.
43. Goble DJ, Conner NO, Nolff MR, Haworth JL, Kendall BJ. Test-retest reliability of the balance tracking system modified clinical test of sensory integration and balance protocol across multiple time durations. Med Devices (Auckl). 2021 Nov 15;14:355–61.
44. Goble DJ, Brar H, Brown EC, Marks CR, Baweja HS. Normative data for the Balance Tracking System modified Clinical Test of Sensory Integration and Balance protocol. Med Devices (Auckl). 2019 May 8;12:183–91.
45. Antoniadou E, Kalivioti X, Stolakis K, Koloniari A, Megas P, Tyllianakis M, et al. Reliability and validity of the mCTSIB dynamic platform test to assess balance in a population of older women living in the community. J Musculoskelet Neuronal Interact. 2020 June 1;20(2):185–93.
46. Seo JW, Kim JI, Kim T, Jang KM, Jeong Y, Do JH. Sensory interaction and balancing ability evaluation of the elderly using a simplified force plate system. Sensors (Basel). 2022 Nov 17;22(22):8883.
47. Young SN, Norris ES, Shifflett TB, Nisbet DB, Saunders BE, Driver CZ. Reliability of the instrumented modified Clinical Test of Sensory Interaction on balance using a virtual balance device. Int J Exerc Sci. 2024 Aug 1;17(1):1183–92.
48. Goble DJ, Brown EC, Marks CRC, Baweja HS. Expanded normative data for the balance tracking system modified clinical test of sensory integration and balance protocol. Med Devices Sens. 2020 June;3(3):e10084.
49. Morasso P. Integrating ankle and hip strategies for the stabilization of upright standing: An intermittent control model. Front Comput Neurosci. 2022 Nov 17;16:956932.
50. Runge CF, Shupert CL, Horak FB, Zajac FE. Ankle and hip postural strategies defined by joint torques. Gait Posture. 1999 Oct;10(2):161–70.
51. Hong S, Park S. Biomechanical optimization and reinforcement learning provide insight into transition from ankle to hip strategy in human postural control. Sci Rep. 2025 Apr 20;15(1):13640.
52. Maki BE, McIlroy WE. The Role of Limb Movements in Maintaining Upright Stance: The "Change-in-Support" Strategy. Phys Ther. 1997 May 1;77(5):488–507.
53. Monaghan AS, Takla T, Ofori E, Peterson DS, Wu W, Fritz NE, et al. The neural contributions to reactive balance control: A scoping review of EEG, fNIRS, MRI, and PET studies. Brain Sci. 2025 Dec 13;15(12):1330.
54. Cavallari P, Bolzoni F, Bruttini C, Esposti R. The organization and control of intra-limb anticipatory Postural Adjustments and their role in movement performance. Front Hum Neurosci. 2016 Oct 19;10:525.
55. Duarte MB, da Silva Almeida GC, Costa KHA, Garcez DR, de Athayde Costa E Silva A, da Silva Souza G, et al. Anticipatory postural adjustments in older versus young adults: a systematic review and meta-analysis. Syst Rev. 2022 Nov 23;11(1):251.
56. Horak FB, Nashner LM. Central programming of postural movements: adaptation to altered support-surface configurations. J Neurophysiol. 1986 June;55(6):1369–81.

57. Pardasaney PK, Latham NK, Jette AM, Wagenaar RC, Ni P, Slavin MD, et al. Sensitivity to change and responsiveness of four balance measures for community-dwelling older adults. Phys Ther. 2012 Mar;92(3):388–97.
58. Lima CA, Ricci NA, Nogueira EC, Perracini MR. The Berg Balance Scale as a clinical screening tool to predict fall risk in older adults: a systematic review. Physiotherapy. 2018 Dec;104(4):383–94.
59. Hebert JR, Manago MM. Reliability and validity of the computerized dynamic posturography sensory organization test in people with multiple sclerosis. Int J MS Care. 2017 May;19(3):151–7.
60. Saraiva M, Paszkiel S, Vilas-Boas JP, Castro MA. Influence of cognitive task difficulty in postural control and hemodynamic response in the prefrontal cortex during static postural standing. Appl Sci (Basel). 2022 June 22;12(13):6363.
61. Kusleikiene S, Pukenas K, Drozdova Statkeviciene M, Ziv G, Vints WAJ, Masiulis N, et al. Relationship between balance automaticity and dual-task interference in older adults. Motor Control. 2026 Jan 1;30(1):100–16.
62. Woollacott M, Shumway-Cook A. Attention and the control of posture and gait: a review of an emerging area of research. Gait Posture. 2002 Aug;16(1):1–14.
63. Dames KD, Richmond SB. Tall tales of balance: The influence of height on postural control measures. Motor Control. 2025 Apr 1;29(2):173–82.
64. Visser JE, Carpenter MG, van der Kooij H, Bloem BR. The clinical utility of posturography. Clin Neurophysiol. 2008 Nov;119(11):2424–36.
65. Podsiadlo D, Richardson S. The timed "Up & Go": a test of basic functional mobility for frail elderly persons. J Am Geriatr Soc. 1991 Feb;39(2):142–8.
66. Horak FB, Wrisley DM, Frank J. The Balance Evaluation Systems Test (BESTest) to differentiate balance deficits. Phys Ther. 2009 May;89(5):484–98.
67. Barry E, Galvin R, Keogh C, Horgan F, Fahey T. Is the Timed Up and Go test a useful predictor of risk of falls in community dwelling older adults: a systematic review and meta-analysis. BMC Geriatr. 2014 Feb 1;14(1):14.
68. Ban B, Sevšek F, Rugelj D. A comparison of the ceiling effect between Berg Balance Scale and Mini-BESTest in a group of balance trained community-dwelling older adults. Physiother Q. 2017;25(2):3–9.
69. Chen H, Smith SS. Item distribution in the berg balance scale: A problem for use with community-living older adults. J Geriatr Phys Ther. 2019 Oct;42(4):275–80.
70. Lesch KJ, Tuomisto S, Tikkanen HO, Venojärvi M. Validity and reliability of dynamic and functional balance tests in people aged 19-54: A systematic review. Int J Sports Phys Ther. 2024 Apr 1;19(4):381–93.
71. Plisky P, Schwartkopf-Phifer K, Huebner B, Garner MB, Bullock G. Systematic review and meta-analysis of the Y-Balance Test Lower Quarter: Reliability, discriminant validity, and predictive validity. Int J Sports Phys Ther. 2021 Oct 1;16(5):1190–209.
72. Hill MW, Wdowski MM, Rosicka K, Kay AD, Muehlbauer T. Exploring the relationship of static and dynamic balance with muscle mechanical properties of the lower limbs in healthy young adults. Front Physiol. 2023 May 26;14:1168314.
73. Nagymáté G, Orlovits Z, Kiss RM. Reliability analysis of a sensitive and independent stabilometry parameter set. PLoS One. 2018 Apr 17;13(4):e0195995.
74. O'Connor SM, Baweja HS, Goble DJ. Validating the BTrackS Balance Plate as a low cost alternative for the measurement of sway-induced center of pressure. J Biomech. 2016 Dec 8;49(16):4142–5.
75. Goble DJ, Khan E, Baweja HS, O'Connor SM. A point of application study to determine the accuracy, precision and reliability of a low-cost balance plate for center of pressure measurement. J Biomech. 2018 Apr 11;71:277–80.

76. Matłosz P, Wyszyńska J, Podgórska-Bednarz J, Leszczak J, Rachwał M, Przednowek K, et al. Agreement of three posturographic force plates in the assessment of postural stability. Int J Environ Res Public Health. 2020 May 4;17(9):3188.
77. Tipton N, Alderink G, Rhodes S. Approximate entropy and velocity of center of pressure to determine postural stability: A pilot study. Appl Sci (Basel). 2023 Aug 15;13(16):9259.
78. Janc M, Sliwinska-Kowalska M, Jozefowicz-Korczynska M, Marciniak P, Rosiak O, Kotas R, et al. A comparison of head movements tests in force plate and accelerometer based posturography in patients with balance problems due to vestibular dysfunction. Sci Rep. 2021 Sept 27;11(1):19094.
79. Escamilla-Martínez E, Gómez-Maldonado A, Gómez-Martín B, Castro-Méndez A, Díaz-Mancha JA, Fernández-Seguín LM. An assessment of balance through posturography in healthy about women: An observational study. Sensors (Basel). 2021 Nov 19;21(22):7684.
80. Prosperini L, Fortuna D, Giannì C, Leonardi L, Pozzilli C. The diagnostic accuracy of static posturography in predicting accidental falls in people with multiple sclerosis. Neurorehabil Neural Repair. 2013 Jan;27(1):45–52.
81. Griškevičius J, Jarmalienė E, Maskeliūnaitė I. Žmogaus pusiausvyros parametrų tyrimas. Moksl - Liet Ateitis. 2010 Aug 31;2(4):35–8.
82. Howcroft J, Lemaire ED, Kofman J, McIlroy WE. Elderly fall risk prediction using static posturography. PLoS One. 2017 Feb 21;12(2):e0172398.
83. Piirtola M, Era P. Force platform measurements as predictors of falls among older people - a review. Gerontology. 2006;52(1):1–16.
84. Batcir S, Gimmon Y, Kurz I, Edelman S, Levitsky Gil N, Adar R, et al. Effect of surface perturbation treadmill training program on strategies and kinematics of reactive stepping during standing in older adults: A single-blinded randomized controlled trial. Gerontology. 2025 Mar 28;71(6):439–52.
85. Batcir S, Livne K, Lehman RL, Berdichevsky Y, Maoz S, Shkedy LW, et al. Feedback-based perturbation balance training during stationary cycling improves reactive and proactive balance among older adults: a single-blinded randomised controlled trial. Age Ageing [Internet]. 2025 Aug 1;54(8). Available from: http://dx.doi.org/10.1093/ageing/afaf215
86. Mansfield A, Inness EL, Wong JS, Fraser JE, McIlroy WE. Is impaired control of reactive stepping related to falls during inpatient stroke rehabilitation? Neurorehabil Neural Repair. 2013 July;27(6):526–33.
87. Adams M, Brüll L, Lohkamp M, Schwenk M. The Stepping Threshold Test for reactive balance: Validation of two observer-based evaluation strategies to assess stepping behavior in fall-prone older adults. Front Sports Act Living. 2021 Oct 11;3:715392.
88. Kuo AD, Zajac FE. Human standing posture: multi-joint movement strategies based on biomechanical constraints. Prog Brain Res. 1993;97:349–58.
89. van Duijnhoven HJR, Roelofs JMB, den Boer JJ, Lem FC, Hofman R, van Bon GEA, et al. Perturbation-based balance training to improve step quality in the chronic phase after stroke: A proof-of-concept study. Front Neurol. 2018 Nov 22;9:980.
90. Mohapatra S, Krishnan V, Aruin AS. Postural control in response to an external perturbation: effect of altered proprioceptive information. Exp Brain Res. 2012 Mar;217(2):197–208.
91. Ferreira RN, Ribeiro NF, Figueiredo J, Santos CP. Provoking artificial slips and trips towards perturbation-based balance training: A narrative review. Sensors (Basel). 2022 Nov 28;22(23):9254.

92. Thrane G, Joakimsen RM, Thornquist E. The association between timed up and go test and history of falls: The Tromsø study. BMC Geriatr. 2007 Jan 12;7(1):1.
93. Neuls PD, Clark TL, Van Heuklon NC, Proctor JE, Kilker BJ, Bieber ME, et al. Usefulness of the Berg Balance Scale to predict falls in the elderly. J Geriatr Phys Ther. 2011 Jan;34(1):3–10.
94. Rosa MV, Perracini MR, Ricci NA. Usefulness, assessment and normative data of the Functional Reach Test in older adults: A systematic review and meta-analysis. Arch Gerontol Geriatr. 2019 Mar;81:149–70.
95. Whitney SL, Marchetti GF, Morris LO, Sparto PJ. The reliability and validity of the Four Square Step Test for people with balance deficits secondary to a vestibular disorder. Arch Phys Med Rehabil. 2007 Jan;88(1):99–104.
96. Herman T, Inbar-Borovsky N, Brozgol M, Giladi N, Hausdorff JM. The Dynamic Gait Index in healthy older adults: the role of stair climbing, fear of falling and gender. Gait Posture. 2009 Feb;29(2):237–41.
97. Wrisley DM, Kumar NA. Functional gait assessment: concurrent, discriminative, and predictive validity in community-dwelling older adults. Phys Ther. 2010 May;90(5):761–73.
98. Alsalaheen BA, Haines J, Yorke A, Stockdale K, Broglio SP. Reliability and concurrent validity of instrumented balance error scoring system using a portable force plate system. Phys Sportsmed. 2015 July;43(3):221–6.
99. Hansen C, Cushman D, Chen W, Bounsanga J, Hung M. Reliability testing of the Balance Error Scoring System in children between the ages of 5 and 14. Clin J Sport Med. 2017 Jan;27(1):64–8.
100. Clark RA, Bryant AL, Pua Y, McCrory P, Bennell K, Hunt M. Validity and reliability of the Nintendo Wii Balance Board for assessment of standing balance. Gait Posture. 2010 Mar;31(3):307–10.
101. Clark RA, Mentiplay BF, Pua YH, Bower KJ. Reliability and validity of the Wii Balance Board for assessment of standing balance: A systematic review. Gait Posture. 2018 Mar;61:40–54.
102. Pickerill ML, Harter RA. Validity and reliability of limits-of-stability testing: a comparison of 2 postural stability evaluation devices. J Athl Train. 2011 Nov;46(6):600–6.
103. Alqahtani BA, Sparto PJ, Whitney SL, Greenspan SL, Perera S, Brach JS. Psychometric properties of instrumented postural sway measures recorded in community settings in independent living older adults. BMC Geriatr. 2020 Feb 28;20(1):82.
104. Carty CP, Cronin NJ, Nicholson D, Lichtwark GA, Mills PM, Kerr G, et al. Reactive stepping behaviour in response to forward loss of balance predicts future falls in community-dwelling older adults. Age Ageing. 2015 Jan;44(1):109–15.
105. Lesch KJ, Lavikainen J, Hyrylä V, Vartiainen P, Venojärvi M, Karjalainen PA, et al. A perturbed postural balance test using an instrumented treadmill - precision and accuracy of belt movement and test-retest reliability of balance measures. Front Sports Act Living. 2021 Aug 27;3:688993.
106. Guadagnoli MA, Lee TD. Challenge point: a framework for conceptualizing the effects of various practice conditions in motor learning. J Mot Behav. 2004 June;36(2):212–24.
107. Mansfield A, Peters AL, Liu BA, Maki BE. A perturbation-based balance training program for older adults: study protocol for a randomised controlled trial. BMC Geriatr. 2007 May 31;7(1):12.
108. Sherrington C, Fairhall N, Wallbank G, Tiedemann A, Michaleff ZA, Howard K, et al. Exercise for preventing falls in older people living in the community: an abridged Cochrane systematic review. Br J Sports Med. 2020 Aug;54(15):885–91.

109. World Medical Association. World medical association declaration of Helsinki: Ethical principles for medical research involving human participants. JAMA [Internet]. 2024 Oct 19; Available from: http://dx.doi.org/10.1001/jama.2024.21972
110. Alnahdi AH, Alderaa AA, Aldali AZ, Alsobayel H. Reference values for the Y Balance Test and the lower extremity functional scale in young healthy adults. J Phys Ther Sci. 2015 Dec;27(12):3917–21.
111. Singh P, Hujon N. Normative data of Modified Functional Reach Test in younger and middle-aged North Eastern Indian population. Arch Med Health Sci. 2013;1(2):109.

CURRICULUM VITAE AND DESCRIPTION OF CREATIVE ACTIVITIES (CV)

Name, surname: Vaidotas Gudžiūnas

E-mail: [vaidotas.gudziunas@ktu.edu]

Current positions:

- Doctoral Candidate (PhD), Kaunas University of Technology (KTU)
- Clinical Neurologist, Tauragė Hospital
- Clinical Neurologist, V. Gudžiūnas Neurology Clinic

Education

- 2020–2025 – PhD studies, Kaunas University of Technology (KTU).
- 2014–2018 – Specialist training in Neurology**,** Lithuanian University of Health Sciences (LUHS).
- 2008–2014 **–** Master's degree in Medicine, Lithuanian University of Health Sciences (LUHS).

Key clinical competencies

- Extracranial vascular color duplex ultrasonography.
- Transcranial color duplex ultrasonography.
- Retrobulbar nerve and vascular assessment.
- EEG interpretation.
- Evoked potentials (VEP, BERA) interpretation.
- Static and dynamic posturography performance and interpretation.

Research interests

Dizziness, balance and gait disorders; quantitative postural control; vestibular assessment and rehabilitation; clinical biomechanics and neurophysiology.

LIST OF SCIENTIFIC PAPERS AND SCIENTIFIC CONFERENCES

The research results were presented at two international scientific conferences related to the dissertation topic:

1. “Quantitative Assessment of the Level of Instability of a Single-Plane Balance Platform”, October 22, 2021. 13th International Conference BIOMDLORE 2021, Vilnius, Lithuania.
2. “Instability Level and Sensory Information Interactions for Human Postural Control Adaptation”, October 22–24, 2023. 14th International Conference BIOMDLORE 2023, Białystok, Poland.

Two research articles related to the dissertation topic have been published in peer-reviewed international journals indexed in the Science Citation Index Expanded (Web of Science) and Scopus databases:

1. Gudziunas, Vaidotas; Domeika, Aurelijus; Puodžiukynas, Linas; Gustiene, Renata. Quantitative assessment of the level of instability of a single-plane balance platform // Technology and Health Care, 2022, vol. 30(1), pp. 291–307. [IF: 1.600; Q4 (Clarivate JCR SCIE); CiteScore: 2.00; Q3 (Scopus); Author contribution: 0.250]
2. Gudžiūnas, Vaidotas; Domeika, Aurelijus; Ylaitė, Berta; Daublys, Donatas; Puodžiukynas, Linas. Quantitative assessment of the effect of instability levels on reactive human postural control using different sensory organization strategies // Applied Sciences, 2024, vol. 14(22), art. no. 10311. [IF: 2.500; Q1 (Clarivate JCR SCIE); CiteScore: 5.30; Q1 (Scopus); Author contribution: 0.200]

ACKNOWLEDGEMENT

I sincerely thank everyone who directly or indirectly contributed to the preparation of this dissertation, the implementation of the scientific research, and supported me throughout this meaningful yet challenging journey.

First and foremost, I would like to express my special gratitude to my scientific supervisor, **Assoc. Prof. Dr. Aurelijus Domeika**. Only thanks to your energy, ideas, support, patience, and constant motivation was it possible to complete this journey. I am especially grateful for the trust you placed in me from the very beginning, which allowed me to believe in myself, face challenges with greater courage, and keep moving forward even when the path seemed difficult and insurmountable.

I am deeply grateful to the dear people I met along this journey, who inspired me, supported me, advised me, and helped me. I sincerely thank **Ieva Aleknaitė-Dambrauskienė**, my first mentor, to whom I could turn both for advice and for help. I thank **Donatas Daublys** for his help throughout the entire process, for contributing to the experimental research, data analysis, and for the good mood that made difficult stages easier to overcome. I am very grateful to **Berta Ylaitė** for her invaluable help, advice, and support. I thank **Justinas Krauleidis** for his assistance in preparing the technical part of the work. I would also like to express my great appreciation to **Prof. Valdas Eidukynas** for his help in preparing the 3D model.

I also sincerely thank **V. Cholomskienė**, for her endless patience, understanding, and help in balancing work and scientific studies. Your support and goodwill were very important during this stage.

My deepest gratitude goes to my family, without whom this journey would have been unimaginable. Thank you, **Dad Vygentas**, for always helping me, supporting me, and always finding time to make together yet another new prototype. Thank you, **Mom Vigilija**, for your moral support, protection, care, and the strength you gave me during the most difficult moments. Thank you, **my sister Vaiva**, for always being by my side when things were truly difficult. Thank you, my **wife Deimantė**, for your endless patience, support, understanding, and for being with me throughout this journey.

My son **Mykolas** - you have been and remain my compass.

APPENDICES

Appendix A - Python code for the static-equilibrium study

```
# ============================================================
#  Interactive static-equilibrium model
# ============================================================

# ---------- General imports ----------
import math, warnings, numpy as np, pandas as pd
import matplotlib.pyplot as plt
from IPython.display import display, HTML
import ipywidgets as w
from ipywidgets import FloatSlider, Layout, VBox, interactive_output

warnings.filterwarnings('ignore', category=RuntimeWarning)
# hide fsolve noise
plt.rcParams.update({'figure.autolayout': True})
# no "Figure n" tag
HTML("<style>.matplotlib-figure-number{display:none
!important;}</style>")  # remove caption

# ---------- 1. Geometry solver ------------------------------------
def solve_geometry(X, L, R, d, prev_phi=None, prev_Y=None):
    """Return (phi, Yc) so that both chains equal length R at board
shift X."""
    if prev_phi is None or prev_Y is None:      # first call –
symmetric seed
        horiz = abs(d-L)/2
        phi_guess, Y_guess = 0.0, math.sqrt(max(R**2 - horiz**2, 0))
    else:
        phi_guess, Y_guess = prev_phi, prev_Y

    def eq(v):
        Yc, phi = v
        eqL = (X+d/2 - (L/2)*math.cos(phi))**2 + (Yc -
(L/2)*math.sin(phi))**2 - R**2
        eqR = (X-d/2 + (L/2)*math.cos(phi))**2 + (Yc +
(L/2)*math.sin(phi))**2 - R**2
        return eqL, eqR

    from scipy.optimize import fsolve
    Yc, phi = fsolve(eq, (Y_guess, phi_guess), xtol=1e-12)
    return phi, Yc

# ---------- 2. Static equilibrium solver --------------------------
def solve_equilibrium_forces(X, Yc, phi, L, d, m, g=9.81):
    """Return chain tensions (TL, TR) and required axial push F."""
    xL, yL = X-(L/2)*math.cos(phi), Yc-(L/2)*math.sin(phi)
    xR, yR = X+(L/2)*math.cos(phi), Yc+(L/2)*math.sin(phi)

    rL = np.array([xL+d/2, yL]);   rR = np.array([xR-d/2, yR])
    uL = rL / np.linalg.norm(rL) if np.linalg.norm(rL) > 1e-12 else
np.zeros(2)
```

```
    uR = rR / np.linalg.norm(rR) if np.linalg.norm(rR) > 1e-12 else
np.zeros(2)

    rCL = np.array([xL-X, yL-Yc]); rCR = np.array([xR-X, yR-Yc])

    def eq(v):
        TL, TR, F = v
        TLv, TRv = -TL*uL, -TR*uR
        Fx = TLv[0] + TRv[0] + F
        Fy = TLv[1] + TRv[1] - m*g
        Mz = rCL[0]*TLv[1] - rCL[1]*TLv[0] + rCR[0]*TRv[1] -
rCR[1]*TRv[0]
        return Fx, Fy, Mz

    from scipy.optimize import fsolve
    TL, TR, F = fsolve(eq, (m*g/2, m*g/2, 0), xtol=1e-12)
    return TL, TR, F

# ---------- 3. Parameter sweep over X ------------------------------
def calculate_displacement_data(L, R, d, m):
    """Return arrays of forces, angles, etc., for X from 0 to
0.35 m."""
    if R**2 < ((d-L)/2)**2:                  # geometric
impossibility
        return None
    Xs = np.arange(0, 0.3501, 0.002)

    Fp, angL, angR, TLs, TRs, HxL, HxR = ([] for _ in range(7))
    prev_phi = 0
    prev_Y   = math.sqrt(max(R**2 - ((d-L)/2)**2, 0))

    for X in Xs:
        phi, Yc = (0, prev_Y) if abs(X) < 1e-9 else \
                   solve_geometry(X, L, R, d, prev_phi, prev_Y)

        TL, TR, F = solve_equilibrium_forces(X, Yc, phi, L, d, m)

        # rope angles vs. vertical column (90° is straight down)
        def rope_angle(rx, ry):
            return 90 + math.degrees(math.atan2(rx, ry)) if (rx or
ry) else 90
        rxL, ryL = X-(L/2)*math.cos(phi)+d/2,  Yc-(L/2)*math.sin(phi)
        rxR, ryR = X+(L/2)*math.cos(phi)-d/2,  Yc+(L/2)*math.sin(phi)
        angL.append(rope_angle(rxL, ryL));
angR.append(rope_angle(rxR, ryR))

        # horizontal chain loads (+ toward left column)
        uL = np.array([rxL, ryL]) / np.linalg.norm([rxL, ryL])
        uR = np.array([rxR, ryR]) / np.linalg.norm([rxR, ryR])
        FLx, FRx = (-TL*uL)[0], (-TR*uR)[0]

        Fp.append(F); TLs.append(TL); TRs.append(TR);
HxL.append(FLx); HxR.append(FRx)
        prev_phi, prev_Y = phi, Yc

    return Xs, Fp, angL, angR, TLs, TRs, HxL, HxR
```

```
# ---------- 4. Plotting and table output ----------------------------
last_df = None
def update_plot(L, R, d, m):
    """Callback for interactive sliders: draws plots and data
table."""
    global last_df
    data = calculate_displacement_data(L, R, d, m)
    if data is None:
        print("No static solution – increase R or adjust d/L.")
        return
    X, Fp, angL, angR, TL, TR, HxL, HxR = data
    Xcm = X * 100

    # sign convention: positive acts toward left column
    Fp, TL, TR, HxL, HxR = [[-v for v in arr] for arr in (Fp, TL, TR,
HxL, HxR)]

    fig, (axF, axH) = plt.subplots(2, 1, figsize=(7, 6), dpi=120)
    fig.suptitle("")                                      # no
auto-caption

    #  -  -  Axial push & angles  -  -
    axF.plot(Xcm, Fp, 'b', label='Required axial push force')
    axF.set(xlabel='Board displacement Δx (cm)', ylabel='Push force,
F (N)')
    axF.grid(True)

    axF2 = axF.twinx()
    axF2.plot(Xcm, angL, 'r--', label='Left chain inclination')
    axF2.plot(Xcm, angR, 'g--', label='Right chain inclination')
    axF2.set_ylabel('Chain inclination, θ (°)')

    h1, l1 = axF.get_legend_handles_labels()
    h2, l2 = axF2.get_legend_handles_labels()
    axF2.legend(h1 + h2, l1 + l2, loc='upper left', fontsize=8)
    axF.set_title('Axial push force and chain inclinations vs. board
displacement')

    #  -  -  Horizontal chain loads  -  -
    axH.plot(Xcm, HxL, 'm', label='Left chain horizontal load
(+→left)')
    axH.plot(Xcm, HxR, 'c', label='Right chain horizontal load
(+→left)')
    axH.set(xlabel='Board displacement Δx (cm)', ylabel='Horizontal
chain load, H (N)')
    axH.grid(True); axH.legend(fontsize=8)
    axH.set_title('Horizontal chain loads vs. board displacement')

    plt.show()

    #  -  -  Data table (first 50 rows)  -  -
    rows = 50
    last_df = pd.DataFrame({
        'Δx (cm)':          np.round(Xcm[:rows], 3),
        'Axial F (N)':      np.round(Fp [:rows], 1),
```

```
        'θ_left (°)':        np.round(angL[:rows], 2),
        'θ_right (°)':       np.round(angR[:rows], 2),
        'T_left (N)':        np.round(TL [:rows], 1),
        'T_right (N)':       np.round(TR [:rows], 1),
        'H_left (N)':        np.round(HxL[:rows], 1),
        'H_right (N)':       np.round(HxR[:rows], 1)
    })
    display(last_df.style.set_caption("Table 1 – Board equilibrium
outputs (first 50 rows)"))

# ---------- 5. Slider pane (centerd, full labels) ------------------
descr = {'description_width': '170px'}
track = Layout(width='600px')
pane  = Layout(align_items='center', border='2px solid #AAA',
               padding='8px 12px', width='100%')

L_slider = FloatSlider(value=1.0, min=0.5, max=2.0,  step=0.1,
                       description='Board length (m)',
                       style=descr, layout=track)
R_slider = FloatSlider(value=1.0, min=0.5, max=3.0,  step=0.1,
                       description='Chain length (m)',
                       style=descr, layout=track)
d_slider = FloatSlider(value=1.4, min=0.5, max=3.0,  step=0.1,
                       description='Anchor spacing (m)',
                       style=descr, layout=track)
m_slider = FloatSlider(value=100.0, min=1.0, max=300.0, step=1.0,
                       description='Mass m (kg)',
                       style=descr, layout=track)

sliders_box = VBox([L_slider, R_slider, d_slider, m_slider],
layout=pane)
out = interactive_output(update_plot, {'L': L_slider, 'R': R_slider,
                                       'd': d_slider, 'm': m_slider})
display(sliders_box, out)

# ---------- 6. Helper to fetch last DataFrame ----------------------
---
def get_last_df():
    """Return last populated DataFrame from update_plot()."""
    if last_df is None:
        print("No table yet – adjust any slider first."); return None
    return last_df
```

Appendix B - Python code of the coupled cart–pendulum simulation

```
 LIBRARIES
import math, csv
import numpy as np, pandas as pd
import matplotlib.pyplot as plt, matplotlib.animation as animation
from IPython.display import HTML, display

# Activate interactive canvases (classic + ipympl widget)
%matplotlib notebook
%matplotlib widget
```

```
# SPRING-SUSPENSION CALIBRATION
# The four forces below come from Table 7 of the dissertation.
#   • L0, R0  – baseline spring force (N) when the cart is centerd (x
= 0 m)
#   • Fleft_at_01, Fright_at_01 – spring forces (N) when the cart is
#     displaced −0.10 m and +0.10 m, respectively.
L0, R0            = -74.13,  74.13         # N
Fleft_at_01       = -38.68                 # N  at x = −0.10 m
Fright_at_01      = -203.75                # N  at x = +0.10 m

# INITIAL CONDITIONS: PENDULUM
# initial_centrip_acc (m s⁻²):
#     Desired centripetal acceleration of the bob at t = 0.
#     ‣ If > 0, the code computes theta_dot to match this value.
#     ‣ If  0, theta_dot (set below) is used verbatim.
initial_centrip_acc = 7          # m s⁻²; set 0 to disable

# theta_dot_sign (±1):
#     Direction of the initial rotation derived from the accel.
above.
#     −1 → counter-clockwise (tilt left), +1 → clockwise (tilt right)
theta_dot_sign      = -1         # unitless (±1 only)

# theta_dot (rad s⁻¹):
#     Explicit initial angular velocity. Ignored if
initial_centrip_acc > 0.
theta_dot           = 0          # rad s⁻¹

# theta (rad):
#     Initial tilt angle, positive right / negative left
theta = math.radians(+20)        # rad

# INITIAL CONDITIONS: CART
x, x_dot = 0.0, 0.0              # position (m) & velocity (m s⁻¹)

# SYSTEM CONSTANTS
M, m     = 10.0, 90.0            # kg   (cart mass, bob mass)
L        = 1.0                   # m    (pendulum length)
g        = 9.81                  # m s⁻² (gravity)

# MECHANICAL LIMITS
x_min, x_max           = -0.10, 0.10                # m  (rail
end-stops)
theta_min, theta_max   = map(math.radians, (-30,30)) # rad (tilt
limits)
Lpend = L                                          # alias used in
formulas

# DATA EXPORT PATH
csv_path = r"G:\My Drive\Dokt - pag\Python\simulation.csv"

# COMPUTE theta_dot IF ACCELERATION IS SPECIFIED
if initial_centrip_acc > 0:
```

```
    theta_dot = theta_dot_sign * math.sqrt(initial_centrip_acc /
Lpend)

# LINEAR SPRING CONSTANTS
# k_left, k_right  – N m⁻¹, derived from the two calibration points.
k_left  = (Fleft_at_01  - L0) / -0.10
k_right = (Fright_at_01 - R0) / -0.10

F_left   = lambda x: L0 + k_left  * x          # N, left spring
force
F_right  = lambda x: R0 + k_right * x          # N, right spring
force
F_springs = lambda x: F_left(x) + F_right(x)   # N, net horizontal
force

# Fixed wall anchor positions (visual only)
anchor_left_x, anchor_right_x = -0.15, 0.15    # m

# TIME GRID
dt, T        = 0.01, 0.5                       # s, s
num_frames   = int(T / dt)                     # animation length

# EQUATIONS OF MOTION (STATE-SPACE FORM)
def derivatives(x, x_dot, th, th_dot):
    """Return (ẋ, ẍ, θ˙, θ¨) for the coupled cart–pendulum system."""
    s, c      = math.sin(th), math.cos(th)
    D         = M + m * s**2
    Fs        = F_springs(x)
    x_dd      = (Fs + m*L*th_dot**2 * s - m*g*s*c) / D
    th_dd     = (g*s - c * x_dd) / L
    return x_dot, x_dd, th_dot, th_dd

def rk4_step(x, x_dot, th, th_dot, h):
    """Fourth-order Runge–Kutta integrator."""
    k1 = derivatives(x, x_dot, th, th_dot)
    k2 = derivatives(x+0.5*h*k1[0], x_dot+0.5*h*k1[1],
                     th+0.5*h*k1[2], th_dot+0.5*h*k1[3])
    k3 = derivatives(x+0.5*h*k2[0], x_dot+0.5*h*k2[1],
                     th+0.5*h*k2[2], th_dot+0.5*h*k2[3])
    k4 = derivatives(x+h*k3[0], x_dot+h*k3[1],
                     th+h*k3[2], th_dot+h*k3[3])
    frac = h/6
    f = lambda i: frac*(k1[i]+2*k2[i]+2*k3[i]+k4[i])
    return x+f(0), x_dot+f(1), th+f(2), th_dot+f(3)

# VISUAL SET-UP
fig, ax = plt.subplots(figsize=(8,6))
ax.set(xlim=(-.45,.45), ylim=(-.05, L+.25), aspect='equal',
       title="Dynamic interaction analysis",
       xlabel="Horizontal position (m)",
       ylabel="Vertical position (m)")
ax.plot(anchor_left_x, 0, 'ko'); ax.plot(anchor_right_x, 0, 'ko')

cart_w, cart_h  = .08, .05
cart            = plt.Rectangle((x-cart_w/2, -cart_h), cart_w,
cart_h, color='blue')
```

```
ax.add_patch(cart)
spr_L, = ax.plot([], [], 'r', lw=3)
spr_R, = ax.plot([], [], 'g', lw=3)
rod,   = ax.plot([], [], 'purple', lw=3)
bob_r  = .03
bob    = plt.Circle((0, L), bob_r, color='teal'); ax.add_patch(bob)
dbg    = ax.text(-.34, L+.15, '', fontsize=9, color='blue')
plt.tight_layout()

# GLOBAL STATE
gx, gxd, gth, gthd = x, x_dot, theta, theta_dot
dist, last_x       = 0.0, x

# Logging dictionary (keys = column headers)
log = {k: [] for k in ('t','x','bob_x','θ_deg','F_L','F_R',
                       'dist','F_p','a_c','x_dd','x_d','θ_d')}

# init()
def init():
    for line in (spr_L, spr_R, rod): line.set_data([],[])
    bob.set_center((0,L)); cart.set_x(gx-cart_w/2); dbg.set_text('')
    return spr_L, spr_R, rod, bob, cart, dbg

# update()
def update(frame):
    global gx, gxd, gth, gthd, dist, last_x
    gx, gxd, gth, gthd = rk4_step(gx, gxd, gth, gthd, dt)

    # Mechanical limits
    if gth > theta_max or gth < theta_min:
        gthd *= -1; gth = max(min(gth, theta_max), theta_min)
    if gx > x_max or gx < x_min:
        gxd *= -1; gx = max(min(gx, x_max), x_min)

    # Draw cart & springs
    cart.set_x(gx - cart_w/2)
    spr_L.set_data([anchor_left_x, gx], [0,0])
    spr_R.set_data([anchor_right_x, gx], [0,0])

    # Pendulum geometry
    s, c       = math.sin(gth), math.cos(gth)
    bob_x, bob_y = gx + L*s, L*c
    rod.set_data([gx, bob_x], [0, bob_y]); bob.set_center((bob_x,
bob_y))

    # Diagnostics
    _, x_dd, _, _ = derivatives(gx, gxd, gth, gthd)
    F_p      = m*L*gthd**2 * s - m*g*s*c
    a_c      = L * gthd**2
    dist    += abs(gx - last_x); last_x = gx
    t_now    = frame * dt

    # Log frame data
    log['t'].append(t_now)
    log['x'].append(gx)
    log['bob_x'].append(bob_x)
```

```
    log['θ_deg'].append(math.degrees(gth))
    log['F_L'].append(F_left(gx))
    log['F_R'].append(F_right(gx))
    log['dist'].append(dist)
    log['F_p'].append(F_p)
    log['a_c'].append(a_c)
    log['x_dd'].append(x_dd)
    log['x_d'].append(gxd)
    log['θ_d'].append(gthd)

    # Save CSV when the animation ends
    if frame == num_frames - 1:
        with open(csv_path, 'w', newline='', encoding='utf-8') as f:
            writer = csv.writer(f); writer.writerow(log.keys())
            rows = zip(*[log[k] for k in log]);
writer.writerows(rows)
        anim.event_source.stop(); plt.close(fig)

    return spr_L, spr_R, rod, bob, cart, dbg

# RUN ANIMATION
anim = animation.FuncAnimation(fig, update, init_func=init,
                               frames=range(num_frames),
                               interval=300, blit=False)
display(HTML(anim.to_jshtml()))
```

UDK 616.8-009.18+57.089+612.76](043.3)

SL344. 2026-07-20, 24 leidyb. apsk. l. Tiražas 14 egz. Užsakymas 120.
Išleido Kauno technologijos universitetas, K. Donelaičio g. 73, 44249 Kaunas
Spausdino leidyklos „Technologija“ spaustuvė, Studentų g. 54, 51424 Kaunas